Exciton Dynamics in π-Conjugated Polymer Systems

Jonathan Mannouch

University College
University of Oxford



A thesis submitted for the degree of
Doctor of Philosophy
at the University of Oxford

Hilary 2019

Exciton Dynamics in π-Conjugated Polymer Systems

Jonathan Mannouch
University College
University of Oxford

A thesis submitted for the degree of
Doctor of Philosophy
at the University of Oxford, Hilary 2019

Abstract

Experimentally, it is observed that upon photoexcitation, conjugated polymers undergo sub-picosecond coupled exciton-phonon dynamics, in which the nuclei distort to stabilise the new electronic state. Previously, such relaxation dynamics of highly excited electronic states of poly(p-phenylenevinylene) have been modelled using Ehrenfest dynamics. Rather than the system relaxing onto a single emissive chromophore as physically expected, the dynamics were seen to bifurcate into a quantum superposition of chromophore states.

In this thesis, the dynamics are instead modelled using a quantum mechanical treatment for the nuclei. In accordance with previous work, the excited electronic states of a polymer are described by a single Frenkel exciton and exciton-phonon coupling is explicitly included using the Frenkel-Holstein model. The time evolution of the system is then described by a Lindblad master equation, which includes damping of the internal nuclear degrees of freedom by the environment.

Firstly, the associated equations of motion are solved using the quantum jump trajectory and time evolving block decimation techniques. Within such a framework, we find that the unphysical bifurcation behaviour is corrected for and the dynamics reproduce the $\lesssim 50$ fs time scale observed in experiment. Processes such as exciton-polaron formation, exciton decoherence and exciton density localisation are also present within the model dynamics.

Secondly, the steady state solution associated with the dynamics is calculated using a Lindblad perturbation theory. Within this approach, the limited functional space (LFS) method is used to obtain numerical results for the steady state. These results confirm that our model dynamics do proceed into a 'chromophore like' steady state, with associated short-ranged exciton-phonon, exciton coherence and exciton localisation lengths.

Finally, we introduce two techniques designed to efficiently describe the time evolution of 'classical' torsional modes. These modes are thought to give rise to the ~ 100 fs time scale observed in experiments, which is currently absent from our model.

Statement of Originality

I, Jonathan Mannouch, hereby confirm that this thesis and the work to which it refers are the results of my own efforts. Any ideas, data, images, or text resulting from the work of others (whether published or unpublished) are fully identified as such within the work and attributed to their originator in the text, bibliography, or in footnotes. This thesis has not been submitted in whole or in part for any other academic degree or professional qualification.

Date:

Signature:

Acknowledgements

Firstly, I am hugely grateful to my supervisor, William Barford, for his support and encouragement during my DPhil. He has been patient, enthusiastic and understanding and has given me so much of his time, not least in reading and correcting the work produced in this thesis. I could not have asked for a better mentor.

I would like to acknowledge the financial support I have received from the EPSRC Centre for Doctoral Training, Theory and Modelling in Chemical Sciences under Grant No. EP/L015722/1 and through the Radcliffe Scholarship received from University College, Oxford. Without this funding I would not have been in a position to undertake this research. I am also very grateful to have been able to use the University of Oxford Advanced Research Computing (ARC) facility for obtaining the results presented in this thesis.

Many thanks go to the members of the Barford group and the TMCS CDT for the many laughs, as well as all the encouragement given during the thesis writing phase of my DPhil. I have also really appreciated all the work based conversations, which have no doubt helped further my understanding of the content presented in this thesis. I have obviously also enjoyed the many 'tea breaks' and pub trips.

As always, I am indebted to my parents. They have always gone the extra mile for me and their love and support has been unwavering. I definitely do not thank them enough for all they have done and continue to do.

Being a part of St Ebbe's Church has been one of the highlights of my time in Oxford. I am hugely thankful to the many friends I have made there, including past Focus and Thesis table members. I am so grateful for the conversations, care and love that they have shown me, as well as for their continual reminders of what ultimately matters. I feel truly privileged to have been a part of this family.

Finally, I would like to echo the small words on the title page of this thesis. *Dominus illuminatio mea.* He is indeed.

Publications

The work presented in this thesis has led to the following publications:

- Chapter 4:
  1. J. R. Mannouch, W. Barford, and S. Al-Assam; Ultra-Fast Relaxation, Decoherence, and Localization of Photoexcited States in π-Conjugated Polymers, *J. Chem. Phys.* **148**, 034901 (2018).
- Chapter 6:
  1. W. Barford, J. R. Mannouch; Torsionally Induced Exciton Localization and Decoherence in π-Conjugated Polymers, *J. Chem. Phys.* **149**, 214107 (2018).

The following papers are being prepared for publication:

- Chapter 5:
  1. Steady State Properties of the Exciton Relaxation Dynamics in π-Conjugated Polymers
- Chapter 6:
  1. The TEBD-Ehrenfest Method: Beyond Ehrenfest Dynamics using Matrix Product States

Glossary of Scaling and Units

Parameters:

Dimensionless Time: $\tilde{t} = \omega t$

Dimensionless External Dissipation Parameter: $\tilde{\gamma} = \dfrac{\gamma}{\omega}$

Exciton-Phonon Coupling Parameter: $\lambda = \dfrac{A^2 \hbar \omega}{2}$

Dimensionless Harmonic Oscillator Destruction Operator: $\hat{b}'_m = \sqrt{\dfrac{\hbar\omega}{2\lambda}}\, \hat{b}_m$

The operator $\hat{b}_m$ is another dimensionless harmonic oscillator destruction operator that satisfies:

$$\left[\hat{b}_m, \hat{b}_m^\dagger\right] = 1$$

Units:

Name	**Symbol**	**Unit**
Time	t	s
External Dissipation Parameter	γ	s^{-1}
Harmonic Oscillator Angular Frequency	ω	s^{-1}
Phonon Energy	$\hbar\omega$	eV
Exciton-Phonon Coupling Parameter	λ	eV

Abbreviations

Abbreviation:	Definition:
PPV	Poly(P-Phenylene Vinylene)
TEBD	Time Evolving Block Decimation
LFS	Limited Functional Space
HOMO	Highest Occupied Molecular Orbital
LUMO	Lowest Unoccupied Molecular Orbital
LEGS	Local Exciton Ground State
QEES	Quasi-Extended Exciton State
VRS	Vibrationally Relaxed State
MPS	Matrix Product State
SVD	Singular Value Decomposition
DMRG	Density Matrix Renormalisation Group
MPO	Matrix Product Operator
LEES	Local Excited Exciton State
vMCG	Variational Multi-Configurational Gaussian

Contents

Abstract iii

Statement of Originality v

Acknowledgements vii

Publications ix

Glossary of Scaling and Units xi

Abbreviations xiii

1 Introduction 1
- 1.1 Overview of Experimental Results . . . 2
- 1.2 Overview of Theoretical Results . . . 3
- 1.3 Thesis Structure . . . 4

2 Theoretical Background 7
- 2.1 The Two-Level Conical Intersection Model . . . 7
- 2.2 Coherent States . . . 12
- 2.3 Polymer Conformations and Coarse-Graining . . . 16
- 2.4 The Frenkel Model . . . 19
- 2.5 The Frenkel-Holstein Model . . . 24
  - 2.5.1 Adiabatic Limit . . . 29
  - 2.5.2 Anti-Adiabatic Limit . . . 33
- 2.6 The Lindblad Master Equation . . . 37
  - 2.6.1 Superoperator Formalism . . . 40

3 Computational Methods 43
- 3.1 Quantum Jump Trajectory Approach . . . 44
- 3.2 Ehrenfest Dynamics . . . 47
- 3.3 Time Evolving Block Decimation (TEBD) . . . 50
  - 3.3.1 Matrix Products States . . . 51
  - 3.3.2 Tensor Network Diagrams . . . 53
  - 3.3.3 Normalisation . . . 54
  - 3.3.4 Observables . . . 55
  - 3.3.5 Hilbert Space Truncation . . . 58

3.3.6 Matrix Product Operators . . . 60
3.3.7 Evolution Operator . . . 62
3.3.8 The Algorithm . . . 64
3.4 Limited Functional Space Approach . . . 66

4 Exciton Dynamics in Poly(p-phenylenevinylene) - a TEBD approach 71
4.1 Ehrenfest Dynamics . . . 74
4.2 Time Evolving Block Decimation . . . 76
4.2.1 Exciton-Polaron Formation . . . 80
4.2.2 Exciton Decoherence . . . 83
4.2.3 Exciton Density Localisation . . . 86
4.2.4 LEGS Dynamics . . . 92
4.2.5 Fluorescence Depolarisation . . . 92

5 Exciton Dynamics in Poly(p-phenylenevinylene) - the Steady State 99
5.1 Lindblad Perturbation Theory . . . 100
5.1.1 Zeroth-Order Term . . . 102
5.1.2 Off-Diagonal Zeroth-Order Eigenstates . . . 104
5.1.3 Diagonal Zeroth-Order Eigenstates . . . 105
5.2 Adiabatic Limit . . . 107
5.3 Anti-Adiabatic Limit . . . 113
5.3.1 Perturbation Theory about the Anti-Adiabatic Limit . . . 116
5.4 Limited Functional Space Approach . . . 121
5.5 Numerical Results . . . 126
5.5.1 Exciton-Polaron Formation . . . 130
5.5.2 Exciton Decoherence . . . 134
5.5.3 Exciton Density Localisation . . . 135

6 Correcting Ehrenfest Dynamics 141
6.1 TEBD-Ehrenfest . . . 142
6.1.1 The Effective Hamiltonian . . . 144
6.1.2 Generalised Coherent State Evolution . . . 145
6.1.3 The Frenkel-Holstein Model . . . 147
6.1.4 Numerical Results . . . 150
6.2 Bundle Trajectories . . . 155
6.2.1 A Conical Intersection in the Classical Limit . . . 157
6.2.1.1 The x Coordinate . . . 160
6.2.1.2 The y Coordinate . . . 162
6.2.1.3 The Nonadiabatic Transition . . . 165
6.2.2 Branching Bundle Trajectories . . . 169

7 Conclusion 177

Bibliography 181

A Superoperators in Liouville Space 191

A.1 Matrix Elements of Superoperators 192

B The TEBD Parameters **195**

C Nonadiabatic Derivative Coupling Vector **199**

D Generalised Coherent States **201**

1

Introduction

Interest in conjugated polymer materials over the last few decades has arisen for multiple reasons. Firstly, these materials are semiconductors, making them possible candidates for use in many electronic devices. While the large exciton binding energies associated with conjugated polymers poses a challenge for making efficient solar cells, this property makes these materials ideal for use in LEDs. In particular, it has been known since the 1990s that phenyl based polymers (such as poly(p-phenylene vinylene) (PPV)) undergo electroluminescence, with an optical band gap generally in the visible-UV region [1]. Such materials are also more flexible, lighter and easier to deposit as thin films compared to their inorganic counterparts.

Secondly, understanding the electronic properties of these materials poses a challenge to theorists. The quasi one-dimensional nature of polymer chains leads to weak screening of the electron-electron interactions, as well as an enhancement of the effects associated with electron-phonon coupling and disorder. The large electron-electron and electron-phonon interactions leads these materials to be strongly correlated and quantum many-body approaches are required to correctly describe the underlying physics. Obtaining the optical properties associated with conjugated polymers requires all these features to be taken into account, where drastically different behaviour can result from relatively small changes in the constituent moieties. For example, poly(p-phenylene) undergoes electroluminescence, while trans-polyacetylene does not [2].

Finally, the combined experimental and theoretical interest in these materials means

that there is a plethora of experimental data by which theoretical models and predictions can be tested. In particular, many spectroscopic studies have been performed which investigate the initial quantum dynamics induced by photoexcitation of a conjugated polymer to an electronically excited state (referred to as the exciton relaxation dynamics). We consider such spectroscopic studies in more detail now.

1.1 Overview of Experimental Results

The exciton relaxation dynamics have been investigated using a wide array of time-resolved spectroscopic techniques for the polymer PPV (the polymer particularly considered in this thesis). The first such experimental data was obtained using fluorescence depolarisation spectroscopy [3–5]. In this experiment, the polymer is first photoexcited using plane polarised light, with the polarisation of the subsequent emitted light (fluorescence) measured as a function of time. During the exciton relaxation dynamics, the transition dipole moment associated with the polymer chain is known to rotate, which is captured by this experimental measurement (the results of which are often presented using a quantity called the fluorescence anisotropy, r). Subsequently, more sophisticated pump-probe experiments have been used to investigate the relaxation dynamics in this system, such as three-pulse photon-echo [6–8] and coherent electronic two-dimensional spectroscopy [9], which are able to measure the dynamics with a much greater time resolution.

Within all of these experiments, three distinct time scales are observed. The largest time scale of $>$1 ps is widely accepted to correspond to the diffusion of the exciton between different chromophores [4,10]. The two shorter time scales of $\lesssim$50 fs and $\sim$100 fs, however, have been studied in less detail. While it has been suggested that these two time

scales correspond to the dynamic localisation of the exciton as it relaxes onto the low energy chromophores [3–9], to our knowledge this has yet to be confirmed by theoretical simulations. While the shortest of these time scales cannot be observed directly using fluorescence depolarisation spectroscopy, it can still be deduced from the fact that the initial anisotropy value measured is <0.4 (the theoretical value expected for a perfectly homogeneous sample), suggesting that an ultra-fast relaxation process is occurring with a time scale shorter than the time resolution of the experiment.

Although the exciton relaxation dynamics in these systems remains far from being fully understood, much progress has still been achieved in obtaining a theoretical description of such processes. We now consider the results produced from such theoretical studies.

1.2 Overview of Theoretical Results

The easiest time scale associated with the dynamics to theoretically model is the longest one of >1 ps. Two distinct processes are thought to contribute to the dynamics at these times. Migration of the exciton between chromophores on different polymer chains can be described as a Förster type exciton energy transfer process, induced by long range dipole-dipole interactions [4, 10–12]. In addition, intrachain exciton diffusion is induced by thermal fluctuations in the torsional modes of the polymer and can essentially be described correctly by treating these low frequency modes classically within the so-called Ehrenfest approximation [13, 14].

The shorter time scales are in contrast much harder to describe. One approach is again to treat the nuclear degrees of freedom classically. Indeed, this technique has been applied to study the ultra-fast exciton relaxation dynamics of photoexcited electronic states in PPV [15–17]. However, the Ehrenfest approximation fails in this case because

of the absence of exciton decoherence occurring during the time evolution induced by the exciton-phonon coupling [18–22], as well as its inability to correctly describe the splitting of a nuclear wave packet when passing through a conical intersection or avoided crossing [22, 23]. A full quantum treatment of all degrees of freedom is therefore needed to correctly describe the dynamics on these short time scales.

A full quantum treatment of the dynamics has been preformed within coarse-grained models, using a range of techniques including the time evolving block decimation [24–27], hierarchical equations of motion [28, 29] and the multi-layer multiconfigurational time-dependent Hartree techniques [30, 31]. However these calculations were limited to extremely short chain lengths and are therefore unrepresentative of physically realistic polymers. Full quantum calculations for realistic chain lengths have been performed on the Frenkel-Holstein model, to calculate static electronic absorption and emission spectra [32]. The obtained results showed good agreement with experiment [33–35]. Therefore in this thesis we aim to use the theoretical models that have already been successfully applied to calculate the static spectroscopic properties of conjugated polymer systems, to gain a correct theoretical description of the exciton relaxation dynamics on the ultra-fast time scales of interest.

1.3 Thesis Structure

In order to describe the exciton relaxation dynamics within polymer systems, a range of theoretical models will be employed, which are all introduced in Chapter 2. We first introduce the two-level conical intersection model, used to ascertain whether a particular quantum dynamics method is able to correctly describe evolution through such features. Nuclear coherent states are then introduced as a way of describing the dynamics of nu-

clear degrees of freedom close to the 'classical limit'. Within polymer systems the low lying excited electronic states are described by the Frenkel model. This constitutes to representing a single polymer chain as a one-dimensional array of sites (one for each moiety) and describing the electronic excitation as a single quasi-particle: a tightly-bound electron-hole pair referred to as a Frenkel exciton. The exciton-nuclear coupling, which induces the exciton relaxation dynamics, is then incorporated into the model by including a harmonic oscillator on each site, which couples locally to the exciton. This is the so-called Frenkel-Holstein model. The different types of eigenstates for the Frenkel and Frenkel-Holstein model are discussed, along with their analytical solutions in the adiabatic and anti-adiabatic limits. Finally, the Lindblad master equation is introduced, which describes the time evolution of the system, while accounting for the dissipation of the internal nuclear degrees of freedom by the environment.

In Chapter 3, the computational methods employed to obtain the quantum dynamics associated with these models are outlined. The Lindblad master equation can be solved using the quantum jump trajectory technique, which represents the system density matrix as an average over so-called quantum trajectories. The time evolution of each trajectory is then obtained from an effective time-dependent Schrödinger equation. One method for approximately solving the time-dependent Schrödinger equation is to use Ehrenfest dynamics, where the nuclei are treated classically. Additionally, a numerically exact solution of this time-dependent Schrödinger equation can be achieved by using the time evolving block decimation (TEBD) technique. For obtaining a large number of excited eigenstates of the Frenkel-Holstein model, the limited functional space (LFS) approach is introduced, in which the Hamiltonian is diagonalised in a reduced dimensional Hilbert space containing basis states which have solely short range exciton-phonon correlations.

The exciton relaxation dynamics associated with PPV polymer chains are obtained in Chapter 4 using the quantum jump trajectory and time evolving block decimation techniques. Certain processes associated with the dynamics will be discussed, such as polaron formation, exciton decoherence and exciton density localisation, where their corresponding time scales and mechanisms will also be elucidated. Finally, the model dynamics are then compared to experiment by calculating the fluorescence anisotropy decay associated with the time evolution.

In Chapter 5, the steady state solution to the Lindblad master equation is obtained using a Lindblad perturbation theory developed by us. An analytical solution for the steady state in the adiabatic and anti-adiabatic limits will be derived, while numerical results are obtained using variants of the limited functional space approach. Expected properties associated with the chromophore states of a polymer, such as polaron character and short ranged exciton coherence and exciton localisation lengths, will be discussed with regards to the steady state solutions. Finally, these results will be compared to the TEBD dynamics obtained in the previous chapter.

To describe 'classical' torsional modes within our model, we introduce suitable computational techniques in Chapter 6. The TEBD-Ehrenfest technique is first introduced, which is ideally suited to describe the adiabatic relaxation of an initial local exciton ground state, with the dynamics occurring on a single potential energy surface. Finally, the branching bundle trajectory technique is introduced, which is designed to describe the relaxation dynamics of high energy initial exciton states in the classical limit. The method is then tested on the two-level conical intersection model.

We conclude with a summary of the main results in this thesis, given in Chapter 7, along with possible avenues for future research.

2

Theoretical Background

To obtain a theoretical description of the exciton relaxation dynamics within polymers requires a model Hamiltonian, which contains the electronic and nuclear degrees of freedom within the system, from which the quantum dynamics can then be computed. In general, polymers contain many thousands of atoms, meaning that obtaining the dynamics from a full atomistic model is computationally infeasible. Coarse-grained models are therefore required, which contain only the most important degrees of freedom for describing the particular process of interest.

In this section, we identify the important polymer degrees of freedom needed for an accurate description of the exciton relaxation dynamics within these systems, as well as introducing the various model Hamiltonians used to describe them. Additionally, the equations of motion used to obtain the time evolution arising from these model Hamiltonians are given, which also includes the effect of weak system-environment coupling on the system dynamics in a perturbative manner.

2.1 The Two-Level Conical Intersection Model

Exciton relaxation dynamics are induced in a polymer by photoexcitation of the system into an excited electronic state. One important feature that strongly influences the resulting dynamics within this excited state manifold is the presence of conical intersections. These features occur when two or more potential energy surfaces cross (i.e., become degenerate in energy at a particular nuclear geometry) and during the dynamics give rise

to ultra-fast population transfer between the surfaces. It is also known that conical intersections are associated with strong nonadiabatic couplings, which require a quantum mechanical treatment of the nuclear degrees of freedom to correctly describe the time evolution of the system around these features.

One simple model used to describe a single conical intersection between two electronic potential energy surfaces is the two-level conical intersection model, whose Hamiltonian is given by [36, 37]:

$$\hat{H}_{\mathrm{CI}} = \frac{\hbar\omega}{2}\left(\hat{P}_x^2 + \hat{P}_y^2\right) + \hat{H}_{\mathrm{el}}(\hat{x},\, \hat{y}) \tag{2.1}$$

where $\hat{P}_x$ and $\hat{P}_y$ are the dimensionless momentum operators for the two nuclear degrees of freedom (x and y) which both have phonon energy $\hbar\omega$. Additionally, $\hat{H}_{\mathrm{el}}(\hat{x},\, \hat{y})$ is the electronic Hamiltonian, which in the diabatic basis depends on the dimensionless nuclear displacement operators $\hat{x}$ and $\hat{y}$ as follows:

$$\hat{H}_{\mathrm{el}}(\hat{x}, \hat{y}) = A\hbar\omega \begin{pmatrix} \hat{x} & \hat{y} \\ \hat{y} & -\hat{x} \end{pmatrix} + \frac{\hbar\omega}{2}\left(\hat{x}^2 + \hat{y}^2\right) \tag{2.2}$$

This model therefore corresponds to a two dimensional harmonic oscillator, which is linearly coupled to the electronic degrees of freedom through the first term in Eq. (2.2). The strength of this electron-nuclear coupling is determined by the dimensionless electron-phonon coupling parameter, A.

To identify the presence of a conical intersection in the model, the adiabatic potential energy surfaces are obtained as the eigenvalues of the electronic Hamiltonian. Using two dimensional polar coordinates:

$$r^2 = x^2 + y^2, \quad \phi = \tan^{-1}\left(\frac{y}{x}\right) \tag{2.3}$$

the potential energies of the two surfaces can be written as follows [37]:

$$E_+(r) = \frac{\hbar\omega}{2}\left[(r+A)^2 - A^2\right], \quad E_-(r) = \frac{\hbar\omega}{2}\left[(r-A)^2 - A^2\right] \tag{2.4}$$

These adiabatic energies are shown in Fig. 2.1 as a function of x, for $y = 0$ and $A = 10$. From this figure, a conical intersection between the two potential energy surfaces can be identified, characterised by a crossing point at $r = 0$. For completeness, the corresponding adiabatic basis states which diagonalise the electronic Hamiltonian are given by [37]:

$$|\psi_+(\phi)\rangle = \cos\left(\tfrac{\phi}{2}\right)|1\rangle + \sin\left(\tfrac{\phi}{2}\right)|2\rangle, \quad |\psi_-(\phi)\rangle = -\sin\left(\tfrac{\phi}{2}\right)|1\rangle + \cos\left(\tfrac{\phi}{2}\right)|2\rangle \tag{2.5}$$

where $|1\rangle$ and $|2\rangle$ are the diabatic basis states initially used to represent the electronic Hamiltonian in Eq. (2.2).

While this model does not provide an accurate description of the excited electronic states within complicated systems such as polymers, its simplicity does make it a useful tool to test whether a particular dynamics technique can correctly describe the time evolution through a conical intersection. To this end, we consider the following scenario. The system, initially at the energy minimum of the E_- surface (i.e., at $x = A$ in Fig. 2.1), undergoes photoexcitation to the upper E_+ surface under a static nuclear geometry. This process is illustrated by the black arrow in Fig. 2.1. The gradient of the upper E_+ surface at this nuclear geometry means that the subsequent dynamics will pass through the conical intersection (positioned at $x = 0$) at some later time, as illustrated by the dashed and dotted arrows in this figure. Numerically exact results for such a process within this model can be obtained using the exact diagonalisation technique, allowing the correct physics for passing through the conical intersection to be determined.

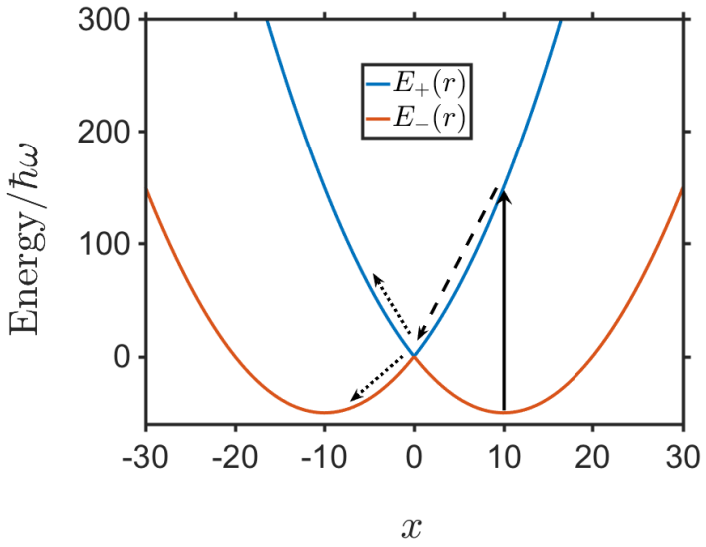


Figure 2.1: The potential energy surfaces for the two-level conical intersection model for $y = 0$ and $A = 10$, as a function of the nuclear displacement x. The solid arrow illustrates the photoexcitation process considered from the energy minimum of the lower E_- surface to the upper E_+ surface, from which the resulting quantum dynamics of interest occur. The resulting dynamics before the conical intersection is reached is labelled by the dashed arrow, while the dynamics after passing through the conical intersection is labelled by the dotted arrows.

Figure 2.2, shows the time dependence after photoexcitation of $P_1(\tilde{t})$ (the probability of the system being in the diabatic electronic state $|1\rangle$ during the dynamics) for $A = 10$ and $\hbar\omega = 0.01$ eV. In addition, $\tilde{t} = \omega t$ is the dimensionless time. For simplicity, the case where the initial nuclear geometry satisfies $y = 0$ and $|x| = r$ is chosen so that numerically it is observed that $\langle \hat{y} \rangle = \langle \hat{P}_y \rangle = 0$ during the resulting dynamics. This means that the adiabatic and diabatic basis states become identical (i.e., $|\psi_+\rangle = |1\rangle$ and $|\psi_-\rangle = |2\rangle$ for $x > 0$ and $|\psi_+\rangle = |2\rangle$ and $|\psi_-\rangle = |1\rangle$ for $x < 0$, as can be seen from Eqs. (2.3) and (2.5)). From this figure, it can be seen that away from the conical intersection, the population on each surface remains constant during the dynamics. However, a large population transfer between the two surfaces occurs at $\tilde{t} \sim 1$, which corresponds to the time at which the system passes through the conical intersection.

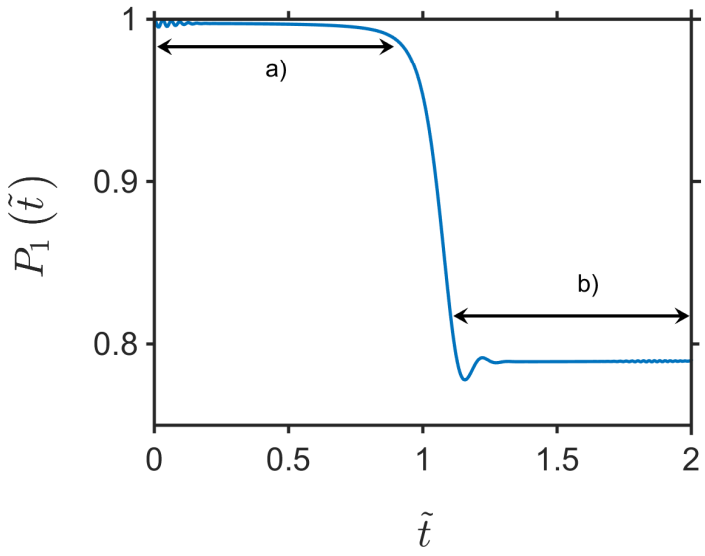


Figure 2.2: The probability of the system being in the $|1\rangle$ diabatic electronic state, $P_1(\tilde{t})$, during the dynamics as a function of the dimensionless time, $\tilde{t} = \omega t$, after the photoexcitation process has occurred. The parameters $A = 10$ and $\hbar\omega = 0.01$ eV were used. The a) and b) labels indicate whether the system has not or has passed through the conical intersection respectively.

One effect of this population transfer is the splitting of the nuclear trajectory on passing through the conical intersection [37]. This is shown in Fig. 2.3, which gives the probability distribution for the harmonic oscillator having a displacement x, $P(x, \tilde{t})$, as a function of the dimensionless time during the dynamics. Before the conical intersection is reached, the system evolves purely on the E_+ surface and therefore follows a single nuclear trajectory, as illustrated by arrow a) in Fig. 2.1. After the population transfer, the system now evolves independently on both surfaces, giving rise to two separate nuclear trajectories, as illustrated by the arrows b) in Fig. 2.1. It is this splitting of the nuclear trajectory on passing through the conical intersection which explains why a quantum treatment of the nuclear degrees of freedom is needed to correctly describe the time evolution of the system around these features.

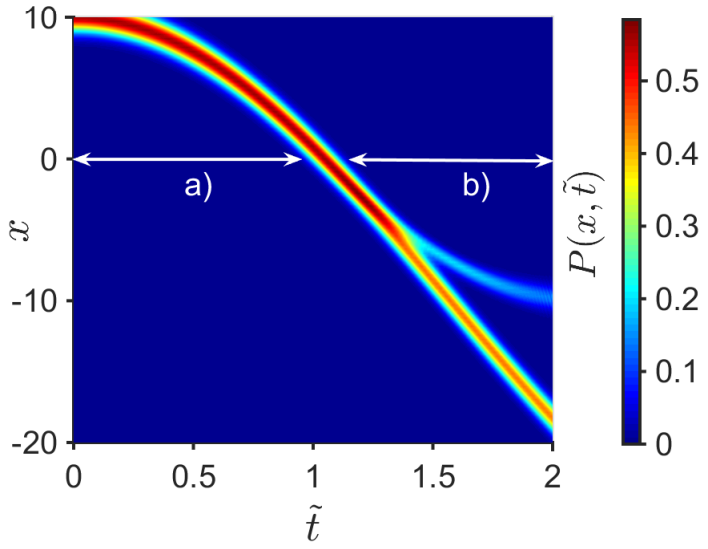


Figure 2.3: The probability distribution for the harmonic oscillator having a displacement x, $P(x, \tilde{t})$, as a function of the dimensionless time, $\tilde{t} = \omega t$, after the photoexcitation process has occurred. The parameters $A = 10$ and $\hbar\omega = 0.01$ eV were used. The a) and b) labels illustrate whether the system has not or has passed through the conical intersection respectively.

2.2 Coherent States

In the previous section, it was shown that for the two-level conical intersection model, the time dependent probability density for the harmonic oscillator having a displacement x took the form of a linear combination of multiple 'classical like' trajectories. This is known to be a more general result for the dynamics of the nuclear degrees of freedom in electron-nuclear coupled models close to the classical limit (i.e., where $\hbar\omega \to 0$). Hence to efficiently describe the time evolution of the nuclear degrees of freedom in this limit requires quantum states that have the form of frozen Gaussian wavepackets (i.e., a wavepacket with fixed width) and whose average displacements and momenta evolve along the correct 'classical like' trajectories. Coherent states satisfy both of these requirements.

Coherent states, $|\alpha\rangle$, are defined as the eigenstates of the harmonic oscillator destruc-

tion operator, $\hat{b}$, as follows [38, 39]:

$$\hat{b}\,|\alpha\rangle = \alpha\,|\alpha\rangle\,, \tag{2.6}$$

where α is the associated eigenvalue and is in general complex, as a result of $\hat{b}$ not being a Hermitian operator. Additionally, the harmonic oscillator destruction operator is defined as [40]:

$$\hat{b} = \frac{1}{\sqrt{2}}\left(\hat{Q} + i\hat{P}\right) \tag{2.7}$$

where $\hat{Q}$ and $\hat{P}$ are the dimensionless displacement and momentum operators respectively. From this definition of a coherent state, the following expression can be obtained in terms of the harmonic oscillator eigenstates, $|n\rangle$ [38, 39, 41]:

$$|\alpha\rangle = e^{-\frac{1}{2}|\alpha|^2} \sum_{n=0}^{\infty} \frac{\alpha^n}{\sqrt{n!}}\,|n\rangle \tag{2.8}$$

where it can be shown that Eq. (2.8) does indeed satisfy Eq. (2.6) by using the property of the harmonic oscillator destruction operator that $\hat{b}\,|n\rangle = \sqrt{n}\,|n-1\rangle$.

Coherent states have several convenient properties. One such property is that the eigenvalue of a coherent state encodes its average displacement and momentum. To see this, the following expressions for $\hat{Q}$ and $\hat{P}$ can be obtained using Eqs. (2.6) and (2.7) [39]:

$$\begin{aligned} \langle\alpha|\hat{Q}|\alpha\rangle &= \frac{\langle\alpha|(\hat{b}^\dagger + \hat{b})|\alpha\rangle}{\sqrt{2}} = \sqrt{2}\mathrm{Re}(\alpha) \\ \langle\alpha|\hat{P}|\alpha\rangle &= \frac{i\,\langle\alpha|(\hat{b}^\dagger - \hat{b})|\alpha\rangle}{\sqrt{2}} = \sqrt{2}\mathrm{Im}(\alpha) \end{aligned} \tag{2.9}$$

where $\hat{b}^\dagger$ is the harmonic oscillator creation operator and corresponds to the Hermitian conjugate of the analogous destruction operator.

Secondly, coherent states have the minimum uncertainty allowed by the Heisenberg uncertainty principle. To show this, expressions for $\langle \hat{Q}^2 \rangle$ and $\langle \hat{P}^2 \rangle$ can be obtained from Eqs. (2.6) and (2.7) [39]:

$$\begin{aligned} \langle \alpha | \hat{Q}^2 | \alpha \rangle &= \frac{\langle \alpha | (\hat{b}^\dagger + \hat{b})(\hat{b}^\dagger + \hat{b}) | \alpha \rangle}{2} = 2\left[\mathrm{Im}(\alpha)\right]^2 + \tfrac{1}{2} \\ \langle \alpha | \hat{P}^2 | \alpha \rangle &= \frac{-\langle \alpha | (\hat{b}^\dagger - \hat{b})(\hat{b}^\dagger - \hat{b}) | \alpha \rangle}{2} = 2\left[\mathrm{Re}(\alpha)\right]^2 + \tfrac{1}{2} \end{aligned} \tag{2.10}$$

where we have additionally used that $[\hat{b}, \hat{b}^\dagger] = 1$. Combining these results with Eq. (2.9) gives us the following expression, which is satisfied by coherent states [39]:

$$\Delta X \Delta P = \tfrac{1}{2} \tag{2.11}$$

where $\Delta A = \sqrt{\langle \hat{A}^2 \rangle - \langle \hat{A} \rangle^2}$ is the standard deviation for the observable corresponding to $\hat{A}$. The fact that coherent states have minimum uncertainty (confirmed by comparing Eq. (2.11) to the uncertainty principle $\Delta X \Delta P \geq \frac{1}{2}$) makes them ideally suited to describe any nuclear degrees of freedom close to the classical limit.

Finally, coherent states exactly solve the time-dependent Schrödinger equation for a linearly driven harmonic oscillator [42]. The Hamiltonian for such a system can be written as follows:

$$\hat{H}_{\mathrm{HO}} = \hbar\omega \left(\hat{b}^\dagger \hat{b} + \tfrac{1}{2} \right) - \frac{f\left(\tilde{t}\right)\hbar\omega}{\sqrt{2}} \left(\hat{b}^\dagger + \hat{b} \right) \tag{2.12}$$

where $\hbar\omega$ is the phonon energy and $f\left(\tilde{t}\right)$ is the time-dependent, dimensionless external force. For the following coherent state ansatz:

$$|\psi_{\mathrm{Coh}}\rangle = e^{i\chi} |\alpha\rangle \tag{2.13}$$

the associated time-dependent Schrödinger equation is then given by:

$$\frac{d\left|\psi_{\text{coh}}\right\rangle}{d\tilde{t}} = -\frac{i}{\hbar\omega}\hat{H}_{\text{HO}}\left|\psi_{\text{coh}}\right\rangle \tag{2.14}$$

where $\tilde{t} = \omega t$ is the dimensionless time. Inserting the definition of a coherent state given by Eq. (2.8) into this time-dependent Schrödinger equation results in the following expression:

$$\begin{aligned}\left(i\frac{d\chi}{d\tilde{t}} - \tfrac{1}{2}\frac{d\left|\alpha\right|^2}{d\tilde{t}}\right)\left|\psi_{\text{coh}}\right\rangle + e^{i\chi}e^{-\frac{1}{2}\left|\alpha\right|^2}\sum_{n=0}^{\infty}\left(\frac{d\alpha}{d\tilde{t}}\right)\frac{n\alpha^{n-1}}{\sqrt{n!}}\left|n\right\rangle = \\ -i\left(\frac{1}{2} - \frac{f\left(\tilde{t}\right)\alpha}{\sqrt{2}}\right)\left|\psi_{\text{coh}}\right\rangle - ie^{i\chi}e^{-\frac{1}{2}\left|\alpha\right|^2}\sum_{n=0}^{\infty}\left(\alpha - \frac{f\left(\tilde{t}\right)}{\sqrt{2}}\right)\frac{n\alpha^{n-1}}{\sqrt{n!}}\left|n\right\rangle\end{aligned} \tag{2.15}$$

where we have used the fact that a coherent state is an eigenstate of the harmonic oscillator destruction operator, $\hat{b}$, given by Eq. (2.6). In addition, the following expression for the application of the harmonic oscillator creation operator, $\hat{b}^\dagger$, to a coherent state has also been used:

$$\hat{b}^\dagger\left|\alpha\right\rangle = e^{-\frac{1}{2}\left|\alpha\right|^2}\sum_{n=0}^{\infty}\frac{\sqrt{n+1}\alpha^n}{\sqrt{n!}}\left|n+1\right\rangle = e^{-\frac{1}{2}\left|\alpha\right|^2}\sum_{n=0}^{\infty}\frac{n\alpha^{n-1}}{\sqrt{n!}}\left|n\right\rangle \tag{2.16}$$

where $\hat{b}^\dagger\left|n\right\rangle = \sqrt{n+1}\left|n+1\right\rangle$. To solve the expression in Eq. (2.15), we equate terms of similar form to give:

$$\begin{aligned}\frac{d\alpha}{d\tilde{t}} &= \frac{if\left(\tilde{t}\right)}{\sqrt{2}} - i\alpha \\ \frac{d\chi}{d\tilde{t}} &= -\frac{i}{2}\frac{d\left|\alpha\right|^2}{d\tilde{t}} + \frac{f\left(\tilde{t}\right)}{\sqrt{2}}\alpha - \frac{1}{2}\end{aligned} \tag{2.17}$$

This expression for χ can be simplified by using the first line in Eq. (2.17) to generate an

expression for $\frac{d|\alpha|^2}{d\tilde{t}}$, which leads to the final result:

$$\begin{aligned} \frac{d\alpha}{d\tilde{t}} &= \frac{if\left(\tilde{t}\right)}{\sqrt{2}} - i\alpha \\ \frac{d\chi}{d\tilde{t}} &= \frac{1}{2}\left(f\left(\tilde{t}\right)\langle\hat{Q}\rangle - 1\right) \end{aligned} \tag{2.18}$$

where we have used the equation for $\langle\hat{Q}\rangle$ given in Eq. (2.9). Therefore Eqs. (2.13) and (2.18) form the exact solution to the time-dependent Schrödinger equation for a linearly driven Harmonic oscillator. The physical interpretation of the first line in Eq. (2.18) can be identified by using Eq. (2.9) to obtain the time dependence of $\langle\hat{Q}\rangle$ and $\langle\hat{P}\rangle$:

$$\begin{aligned} \frac{d\langle\hat{Q}\rangle}{d\tilde{t}} &= \langle\hat{P}\rangle \\ \frac{d\langle\hat{P}\rangle}{d\tilde{t}} &= f\left(\tilde{t}\right) - \langle\hat{Q}\rangle \end{aligned} \tag{2.19}$$

which are identical to Newton's equations of motion for the classical driven Harmonic oscillator. Thus the time evolution of coherent states do indeed mimic 'classical like' trajectories as required.

2.3 Polymer Conformations and Coarse-Graining

Before we consider models which can be used to accurately describe the exciton relaxation dynamics within polymers, we first need to understand the structure of such materials. In this thesis we consider solely amorphous phases of poly(p-phenylene vinylene) (PPV), for which the individual polymer chains themselves occur in many quasi-random conformations, arising from fluctuations in the torsional angles around the single carbon-carbon bonds, as well as defects in the polymer chains themselves. While in the solid state these torsional angle fluctuations are quasi-static, in solution they give rise to dynamical dis-

order. However, as the time scale for exciton relaxation is much shorter than for the conformational dynamics, the observables associated with the exciton relaxation dynamics can be calculated by averaging over an ensemble of static polymer chain conformations for both phases.

Figure 2.4 illustrates how each polymer conformation of PPV is generated. With a phenylene unit as the starting moiety, the polymer chain is obtained using the parameter values given in Table 2.1, along with the following rules [15]:

- The torsional angles about the single carbon-carbon bonds, ϕ_m, are taken as Gaussian random variables, with a mean $\langle\phi\rangle$ and standard deviation σ_ϕ.
- With equal probability, the torsional angles, ϕ_m, and the vinylene bond angles, θ_m, can be positive or negative, corresponding to an anticlockwise or clockwise rotation respectively.
- For a pure polymer chain, all vinylene units take the lowest energy trans geometry. However, trans-cis defects are introduced randomly along the chain, with probability x_{cis}.

Parameter	**Value**	**Parameter**	**Value**
$\langle\phi\rangle$	15°	σ_ϕ	5°
x_{cis}	0.08	θ	60°

Table 2.1: Parameters used to generate the conformations associated with PPV polymer chains [15].

Such polymer chain conformations can then be used to aid the parametrisation of coarse-grained models.

As stated previously, the exciton relaxation dynamics of interest proceed initially from an excited electronic state of the polymer accessible by photoexcitation. Therefore a

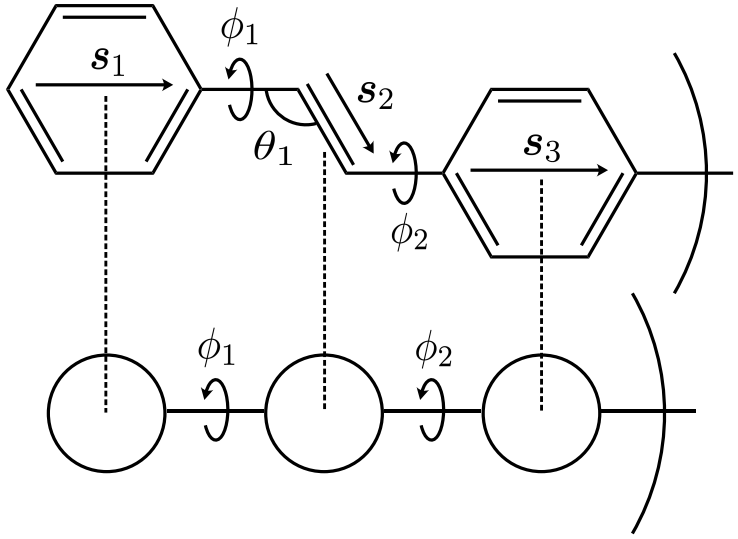


Figure 2.4: The mapping of a polymer chain conformation to a coarse-grained linear site model. Each site corresponds to a moiety along the polymer chain, with the connection between sites characterised by the torsional angle, ϕ_m. Also shown is the dipole unit vector, $\boldsymbol{s}_m$, associated with site/moiety m.

prerequisite of any model used in this thesis is that it can accurately describe such electronically excited states. Due to the photon energy associated with radiation in the visible to ultraviolet range of the electromagnetic spectrum, the photoexcitation process in conjugated polymers will involve a $\pi^* \rightarrow \pi$ transition. Within this description, the orbitals which make up the fully occupied π band are formed from the highest occupied molecular orbital (HOMO) on each moiety of the polymer chain, while the orbitals which make up the unoccupied π^* band are analogously formed from the lowest unoccupied molecular orbital (LUMO) on each moiety. The resulting excited electronic state can then be described by an electron in the unoccupied π^* band and a hole (i.e., the absence of an electron) in the fully occupied π band. Together, this electron-hole pair is commonly referred to as an exciton.

An exciton state can be characterised in terms of two coordinates; the centre of mass coordinate of the exciton, R, and the electron-hole separation, r. These coordinates are

defined as follows [43]:

$$R = \tfrac{1}{2}\left(r_{\mathrm{e}} + r_{\mathrm{h}}\right), \qquad r = r_{\mathrm{e}} - r_{\mathrm{h}} \tag{2.20}$$

where r_e and r_h are the coordinates of the electron and hole respectively. Due to the large electron-electron interactions present in conjugated polymer systems and one-dimensionality, an exciton in general has a large binding energy on the order of ~ 1 eV [2, 44], such that the electron and hole typically occupy the same moiety of the polymer chain. This is known as a Frenkel exciton [45]. This feature suggests that an advantageous way to coarse-grain the electronic degrees of freedom is to represent the polymer chain as a linear array of sites, where each site corresponds to one of the moieties of the polymer [15]. This mapping is illustrated in Fig. 2.4. The advantage of such a coarse-grained model is that now we only need to consider how the centre of mass of the Frenkel exciton, R, propagates along the array of sites. In creating the model, a single Frenkel exciton state is kept per site, corresponding to the lowest energy excitation of each moiety (i.e., the LUMO to HOMO transition), such that in principle all physically relevant transitions between the fully occupied π band to the fully unoccupied π^* band are included. Additionally, only the singlet spin state of the exciton is considered, such that the spin selection rules are satisfied for its formation during the photoexcitation process.

2.4 The Frenkel Model

Within the Hilbert space associated with the linear site model introduced above, the initial exciton state of a PPV polymer generated after photoexcitation can be described by the Frenkel Hamiltonian [2, 46, 47]:

$$\hat{H}_{\mathrm{F}} = \sum_m \epsilon_m \hat{a}_m^\dagger \hat{a}_m + \sum_m J_m \left(\hat{a}_{m+1}^\dagger \hat{a}_m + \hat{a}_m^\dagger \hat{a}_{m+1}\right) \tag{2.21}$$

where $\hat{a}_m^\dagger$ ($\hat{a}_m$) is the exciton creation (destruction) operator, which creates (destroys) a Frenkel exciton on site/moiety m of the polymer chain. For PPV, the odd and even sites, m, correspond to phenylene and vinylene moieties respectively. Within this Hamiltonian, the on-site energy is given by:

$$\epsilon_m = E_0 + (-1)^m \frac{\Delta}{2} + \alpha_m \tag{2.22}$$

where $E_0 - \Delta/2$ and $E_0 + \Delta/2$ are the respective LUMO-HOMO excitation energies for phenylene and vinylene moieties. In addition, α_m represents the diagonal disorder, with standard deviation σ_α. This diagonal disorder arises physically from density fluctuations in the environment around the polymer chain, due to the inhomogeneity of the material [11, 48].

The final term in the Frenkel Hamiltonian gives rise to the migration of the Frenkel exciton between nearest-neighbour sites/moieties, through the hopping integral given by [43, 49]:

$$J_m = J^{\mathrm{DD}} + J^{\mathrm{SE}} \cos^2 \phi_m \tag{2.23}$$

where ϕ_m is the torsional angle between moieties m and $m+1$, which is obtained from the generated polymer conformations discussed in the previous section. From Eq. (2.23), we see that there are two contributions to the nearest-neighbour hopping integral. The first contribution arises from a through space dipole-dipole interaction, which is incorporated through the term $J_{n,m}^{\mathrm{DD}}$:

$$J_{n,m}^{\mathrm{DD}} = \frac{\kappa_{n,m}\mu_0^2}{4\pi\epsilon_r\epsilon_0 R_{n,m}^3} \tag{2.24}$$

where μ_0 is the magnitude of the transition dipole moment on any given moiety and $R_{n,m}$ is the distance between the centres of moieties n and m. In addition, $\kappa_{n,m}$ is a structure

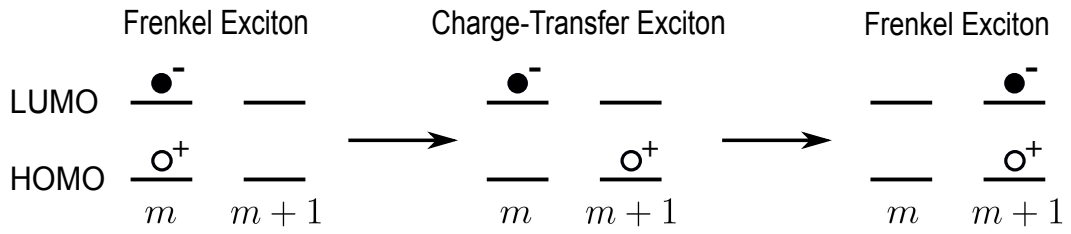


Figure 2.5: A schematic diagram illustrating the migration of the Frenkel exciton from site m to site $m+1$ via the through bond superexchange mechanism. The solid circle represents the electron, while the open circle represents the hole, which together form the exciton. The superexchange mechanism results in an intermediate charge-transfer exciton state, in which the electron and hole occupy different moieties along the polymer chain.

factor given by:

$$\kappa_{n,m} = \boldsymbol{s}_m \cdot \boldsymbol{s}_n - 3\left(\boldsymbol{R}_{n,m} \cdot \boldsymbol{s}_m\right)\left(\boldsymbol{R}_{n,m} \cdot \boldsymbol{s}_n\right) \tag{2.25}$$

where $\boldsymbol{s}_m$ is the dipole unit vector on site/moiety m (illustrated in Fig. 2.4) and $\boldsymbol{R}_{n,m}$ is a unit vector which points between the centres of moieties m and n. While in principle this interaction term is non-zero between all moieties in the polymer chain, the rapidly decaying nature of $1/R^3_{n,m}$ in Eq. (2.24) means that we only include the largest nearest-neighbour interactions within the Hamiltonian (i.e., $J^{\mathrm{DD}} = J^{\mathrm{DD}}_{m,m+1} = J^{\mathrm{DD}}_{m+1,m}$).

The second contribution to the hopping integral arises from a through bond superexchange interaction, in which the system passes through an intermediate charge-transfer exciton state [2]. This process is illustrated pictorially in Fig. 2.5, where the Frenkel exciton moves to a nearest-neighbour moiety by successive migrations of the electron and hole (in either order) through the π bond linking the two moieties. An expression for the hopping integral associated with such a process is given by:

$$J^{\mathrm{SE}}_{m,m+1} = -\frac{2t_m^2}{\Delta E} \tag{2.26}$$

where t_m is the electron/hole transfer integral linking moieties m and $m+1$, ΔE is

the energy difference between the charge-transfer and Frenkel exciton states and the factor of 2 occurs because there are two pathways through which the superexchange process can proceed, differing by which particle (i.e., the electron or hole) moves first. The electron/hole transfer integral t_m has a $\cos\phi_m$ dependence, arising from the overlap between the p_z orbitals on neighbouring moieties through which the electron and hole are transferred. This leads to the expression for the superexchange contribution to the nearest-neighbour hopping integral given by the second term in Eq. (2.23). Thus from Eq. (2.23), torsional fluctuations in the polymer chain give rise to disordered hopping integrals in the Frenkel Hamiltonian.

For the Frenkel Hamiltonian containing L sites, the eigenstates and associated energy eigenvalues can be obtained using the exact diagonalisation technique, for a particular instance of the disorder. These energy eigenvalues can be visualised using the associated density of states, which is given in Fig. 2.6 and corresponds to the thermodynamic limit (when $L \to \infty$). Figure 2.6 has also been averaged over many instances of the disorder. The two distinct bands present in the spectrum correspond to the different exciton energies for the phenylene and vinylene moieties, while the divergent nature of the density of states at the band edges is a symptomatic feature of one-dimensional systems [50]. The presence of disorder in the model, which enters through the site energies and hopping integrals, gives rise to the band asymmetry in the spectrum.

This disorder also leads to the Frenkel Hamiltonian having two forms of eigenstates. The low energy states of the Hamiltonian are Anderson localized [51], non-overlapping and nodeless states, called local exciton ground states (LEGSs) [52–55]. A LEGS is quantified

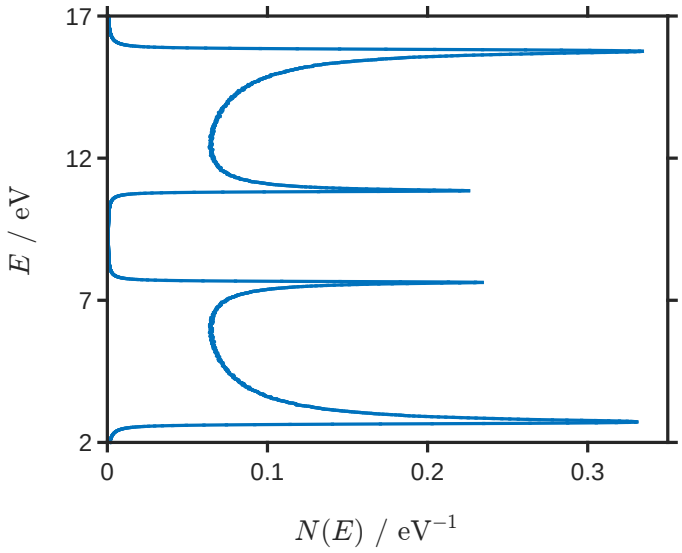


Figure 2.6: The density of states, $N(E)$, for the Frenkel Hamiltonian eigenstates, as a function of the energy eigenvalues E. The density of states is averaged over several instances of the disorder and corresponds to the thermodynamic limit, when $L \to \infty$.

by a signed-value parameter, α, defined as:

$$\alpha = \left| \sum_m |\psi_m| \, \psi_m \right| \tag{2.27}$$

where ψ_m is the probability amplitude of the Frenkel exciton being on site m. In accord with previous work, we define a LEGS as satisfying $\alpha \geq 0.95$ [52,55]. The exciton density for three LEGSs corresponding to a particular conformation of a 99 moiety PPV polymer chain are given in Fig. 2.7. It is the width of these states that define the size of the polymer's absorbing chromophores [56]. In addition, the Frenkel Hamiltonian has higher energy eigenstates that are delocalised over several chromophores, called quasi-extended exciton states (QEES) [2]. The exciton density for a QEES on the same 99 moiety PPV polymer chain is given in Fig. 2.8.

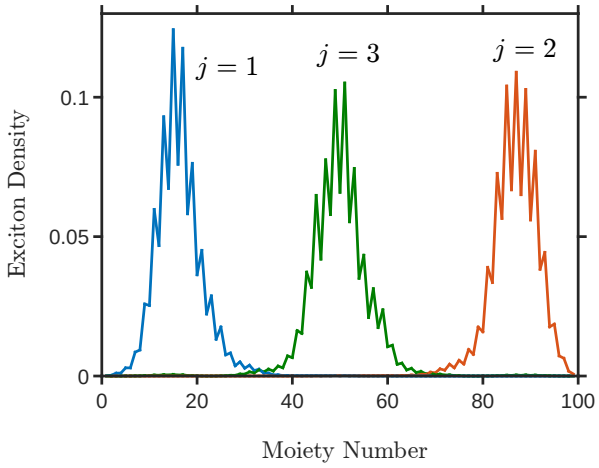


Figure 2.7: The three local exciton ground states (LEGSs) for one particular conformation of a PPV polymer chain made up of 99 moieties. The exciton centre-of-mass quantum number, j, for each state is also given.

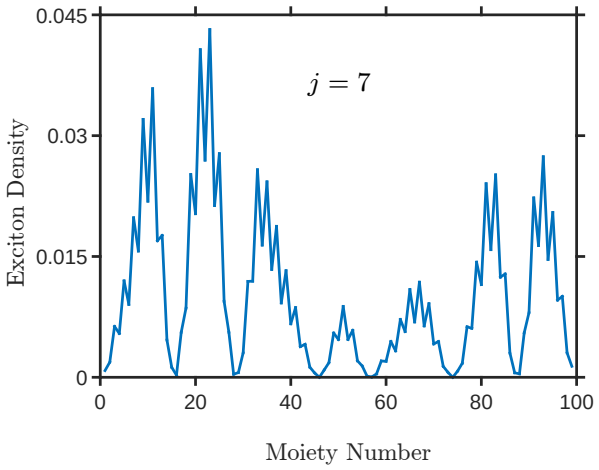


Figure 2.8: The associated exciton density of a QEES, with quantum number $j = 7$, for one particular conformation of a PPV polymer chain made up of 99 moieties.

2.5 The Frenkel-Holstein Model

Relaxation of a LEGS or QEES is physically induced by exciton-nuclear coupling, which allows the nuclear geometry of the polymer to distort so that it best stabilises the newly formed excited electronic state. Most vibrational normal modes in a polymer, such as in PPV, can be neglected within our model, because they either couple weakly to the exciton or have a low vibrational frequency, such that they do not strongly influence the exciton dynamics on the ultra-fast time scale of interest. As in previous work, we thus consider the Frenkel exciton coupling to a single high frequency normal mode per moiety (the benzenoid-quinoid distortion in the phenylene unit and the C-C double bond stretch in the vinylene unit). These vibrational modes are illustrated in Fig. 2.9 and are shown to couple strongly to the exciton degrees of freedom by quantum chemistry calculations [2]. The exciton and nuclear degrees of freedom within such a framework can be modelled

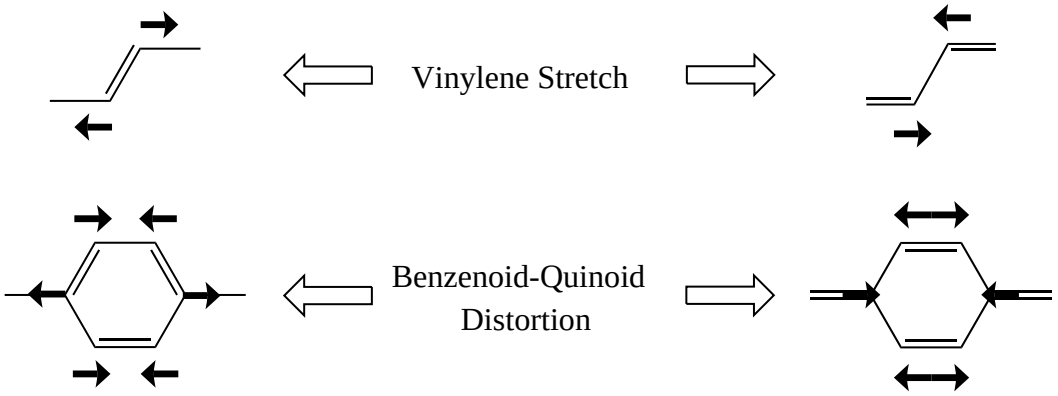


Figure 2.9: A schematic diagram illustrating the vibrational mode associated with the vinylene stretch and the benzenoid-quinoid distortion, occurring on the corresponding moiety of the PPV polymer chain. Both normal modes couple strongly to the Frenkel exciton degrees of freedom and have high vibrational frequencies of $\sim 1800\text{cm}^{-1}$.

using the Frenkel-Holstein Hamiltonian [32, 57, 58]:

$$\hat{H}_{\text{FH}} = \hat{H}_{\text{F}} - \frac{A\hbar\omega}{\sqrt{2}} \sum_m \hat{a}_m^\dagger \hat{a}_m \left(\hat{b}_m^\dagger + \hat{b}_m \right) + \hbar\omega \sum_m \left(\hat{b}_m^\dagger \hat{b}_m + \tfrac{1}{2} \right) \tag{2.28}$$

where A is the dimensionless exciton-nuclear coupling parameter, which determines the strength of the exciton-phonon coupling, and $\hbar\omega$ is the phonon energy associated with the vibrational normal modes. Within the Frenkel-Holstein model, the vibrational normal mode on moiety/site m is represented by a harmonic oscillator, where $\hat{b}_m^\dagger$ ($\hat{b}_m$) is the associated dimensionless harmonic oscillator creation (destruction) operator. The values for the Frenkel-Holstein Hamiltonian parameters that we used to model PPV [15] are given in Table 2.2.

Parameter	**Value**	**Parameter**	**Value**
E_0	9.24 eV	J^{DD}	-1.35 eV
Δ	3.20 eV	$\hbar\omega$	0.2 eV
σ_α	65 meV	A	4.00
J^{SE}	-1.96 eV	$\tilde{\gamma}$	0.033

Table 2.2: Parameters used in the Frenkel-Holstein Hamiltonian [15].

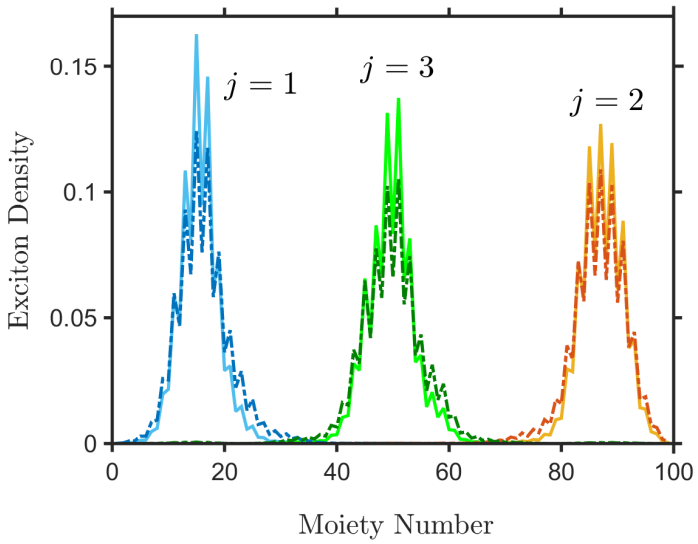


Figure 2.10: The three local exciton ground states (LEGSs, dashed lines) and the three vibrationally relaxed states (VRSs, solid lines) for one particular conformation of a PPV polymer chain made up of 99 moieties. The exciton centre-of-mass quantum number, j, for each state is also given. The VRSs were obtained using the density matrix renormalisation group technique [61], allowing a maximum of two phonons per site.

One effect of the exciton-nuclear coupling term in this Hamiltonian is to further localise the exciton density of the low energy LEGSs, to create so-called vibrationally relaxed states (VRSs) [59]. These VRSs are the low energy eigenstates of the Frenkel-Holstein Hamiltonian [60], with their associated exciton densities given by the solid curves in Fig. 2.10 for a 99 moiety PPV polymer chain. Comparing these VRSs with their associated LEGSs (given by the dashed curves) shows that the degree of self-localisation arising from coupling to the high frequency vibrational modes is small, leading to the spatial extent of the VRSs still being largely determined by the disorder in the Frenkel Hamiltonian [59,60]. It is the width of these VRSs that define the size of the polymer's emissive chromophores [15].

One additional feature associated with the vibrationally relaxed states is that they exhibit exciton-polaron character. An exciton-polaron is a quasiparticle consisting of an

exciton 'dressed' by local displacements of the nuclei. The effective size of the exciton-polaron can be described by the exciton-phonon correlation function [62]:

$$C_n^{\text{ex-ph}} = \frac{1}{A}\sum_m \langle \hat{a}_m^\dagger \hat{a}_m \hat{Q}_{m+n} \rangle \tag{2.29}$$

where the factor $\frac{1}{A}$ normalises the function for eigenstates of the Frenkel-Holstein Hamiltonian [63] (i.e., $\sum_n C_n^{\text{ex-ph}} = 1$). Physically, this correlation function corresponds to the average nuclear displacement n sites away from the exciton. The exciton-phonon correlation function is given in Fig. 2.11 for the lowest energy VRS of a 99 moiety polymer chain, for several values of the phonon energy, $\hbar\omega$. The exciton-phonon correlation function shows an exponential dependence on the exciton-phonon separation n, which is a signature of exciton-polarons [60, 64]. Deviations from this exponential behaviour arise due to the disorder in the model, which leads to non uniform exciton density distributions among the moieties/sites, which enter the correlation function through the density operator $\hat{a}_m^\dagger \hat{a}_m$. From this figure, the size of the exciton-polaron is shown to depend strongly on the phonon energy, $\hbar\omega$, with the exciton-phonon correlation length increasing with decreasing phonon energy. This arises because as $\hbar\omega$ decreases, the time scale associated with the nuclear motion decreases relative to the exciton. Therefore the nuclei cannot respond as quickly to the exciton propagation, leading on average to a larger exciton-phonon separation [60].

In practice, the physics of the model can be best controlled by using the adiabatic parameter, which is defined as follows [60]:

$$\omega' = \frac{\hbar\omega}{|\langle J \rangle|} \tag{2.30}$$

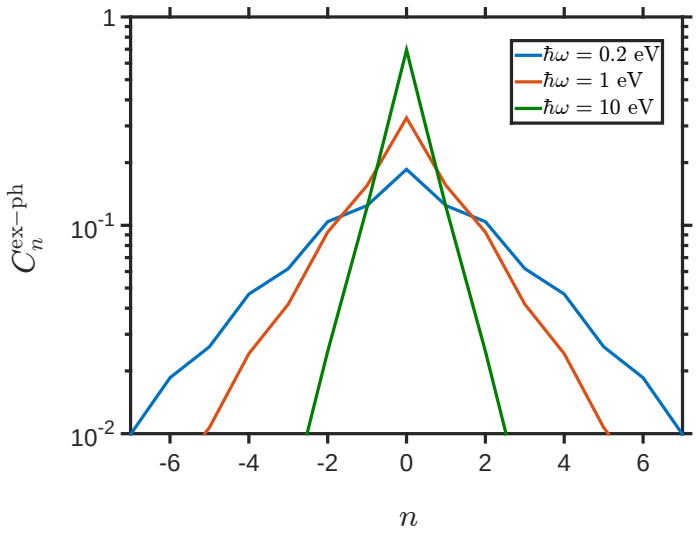


Figure 2.11: The exciton-phonon correlation function, $C_n^{\text{ex-ph}}$, which corresponds to the average nuclear displacement n sites away from the Frenkel exciton and is defined in Eq. (2.29). This correlation function is given for the lowest energy VRS of a PPV polymer chain conformation made up of 99 moieties, for several values of the phonon energy, $\hbar\omega$.

where $\langle J \rangle$ is the exciton nearest-neighbour hopping integral averaged over all sites. Physically, the adiabatic parameter gives the ratio of the exciton and nuclear time scales. Using this parameter, we can define two limits. The adiabatic limit is defined by $\omega' \to 0$ and corresponds to the nuclei being essentially stationary on the time scale of the exciton, while the opposite anti-adiabatic limit is defined by $\omega' \to \infty$ and corresponds to the nuclear dynamics being much faster than that of the exciton.

For both limits to be well defined, all the terms in the Frenkel-Holstein Hamiltonian, given by Eq. (2.28), must remain finite. For the harmonic oscillator part of the Hamiltonian, this can be ensured by defining new scaled harmonic oscillator destruction operators equal to $\sqrt{\hbar\omega}\,\hat{b}_m$. Therefore for the exciton-phonon coupling term in the Frenkel-Holstein Hamiltonian, given by Eq. (2.28), to have a finite contribution with these new scaled harmonic oscillator destruction operators, the following exciton-phonon coupling parameter

must remain constant [60]:

$$\lambda = \frac{A^2 \hbar\omega}{2} \tag{2.31}$$

This parameter physically corresponds to the exciton-polaron relaxation energy in the atomic limit. Keeping λ constant also ensures that the exciton localisation length remains static as the adiabatic limit is approached (as will be shown in Section 2.5.1) [60]. Instead of using the scaled harmonic oscillator destruction operators, $\sqrt{\hbar\omega}\,\hat{b}_m$, it is often more convenient to use the following dimensionless operators:

$$\hat{b}'_m = \sqrt{\frac{\hbar\omega}{2\lambda}}\,\hat{b}_m \tag{2.32}$$

As the average nuclear displacement for an eigenstate of the Frenkel-Holstein Hamiltonian satisfies $\langle \hat{Q}_m \rangle = A \langle \hat{a}_m^\dagger \hat{a}_m \rangle$, using these dimensionless operators therefore results in the primary dependence of the exciton-phonon coupling parameter being removed from such expectation values.

Analytic solutions for the eigenstates of the Frenkel-Holstein model exist in both the adiabatic and anti-adiabatic limits. We now consider these two cases in turn.

2.5.1 Adiabatic Limit

In the adiabatic limit, the nuclear degrees of freedom behave classically and the Born-Oppenheimer approximation becomes valid [40]:

$$|\psi_\beta\rangle = |\psi_{\beta,\,\mathrm{ex}}(\mathbf{Q}')\rangle \otimes |\phi_{\mathrm{ph},\,1}\rangle \otimes \cdots \otimes |\phi_{\mathrm{ph},\,L}\rangle \tag{2.33}$$

Within this mean-field ansatz, $|\phi_{\mathrm{ph},\,m}\rangle$ is the nuclear quantum state associated with the harmonic oscillator on site m. In addition, $|\psi_{\beta,\,\mathrm{ex}}(\mathbf{Q}')\rangle$ is the quantum state associated

with the exciton degrees of freedom, with quantum number β, which in general also depends on the nuclear coordinates, $Q'_m = \langle \phi_{\mathrm{ph},m} | \hat{Q}'_m | \phi_{\mathrm{ph},m} \rangle$. This excitonic quantum state can be written in the exciton site basis:

$$|\psi_{\beta,\mathrm{ex}}(\mathbf{Q}')\rangle = \sum_m \psi_{\beta,m} \, |m\rangle \tag{2.34}$$

where $|m\rangle$ is the quantum state associated with the exciton residing on site m and $\psi_{\beta,m}$ is the corresponding probability amplitude.

From the expression for the Frenkel-Holstein Hamiltonian given in Eq. (2.28), the following Born-Oppenheimer Hamiltonian can be obtained:

$$\hat{H}_{\mathrm{BO}} = \hat{H}_{\mathrm{F}} - 2\lambda \sum_m Q'_m \hat{a}^\dagger_m \hat{a}_m + \lambda \sum_m \left(Q'_m\right)^2 \tag{2.35}$$

where Q'_m is the classical nuclear displacement for the oscillator on site m, given in terms of the new dimensionless coordinates introduced in Eq. (2.32). The eigenvalues, E_β, of this Hamiltonian correspond to the adiabatic potential energy surfaces for the Frenkel-Holstein model:

$$\hat{H}_{\mathrm{BO}} \, |\psi_{\beta,\mathrm{ex}}(\mathbf{Q}')\rangle = E_\beta(\mathbf{Q}') \, |\psi_{\beta,\mathrm{ex}}(\mathbf{Q}')\rangle \tag{2.36}$$

Of particular interest are the minimum points of these surfaces, which correspond to the stable equilibrium geometries of the system. Using the Hellmann-Feynman theorem, the following expression can be obtained for the surface gradients [40]:

$$\frac{dE_\beta}{dQ'_m} = \left\langle \psi_{\beta,\mathrm{ex}}(\mathbf{Q}') \left| \frac{d\hat{H}_{\mathrm{BO}}}{dQ'_m} \right| \psi_{\beta,\mathrm{ex}}(\mathbf{Q}') \right\rangle \tag{2.37}$$

Inserting Eq. (2.35) into Eq. (2.37) then leads to the following constraint that is satisfied

for the stationary points of the adiabatic surfaces [15]:

$$Q'_m = |\psi_{\beta,m}|^2 \tag{2.38}$$

Imposing this constraint by inserting Eqs. (2.35) and (2.38) into Eq. (2.36) results in a non-linear eigenvalue equation for the probability amplitudes, $\psi_{\beta,m}$, associated with these stationary points. In the case where the Frenkel Hamiltonian contains no disorder (i.e., $\hat{H}_{\mathrm{F}}$ corresponds to the Hamiltonian for a continuum tight binding model with uniform nearest-neighbour hopping integrals, $\langle J \rangle$), this non-linear eigenvalue equation has the following analytic solutions [57, 65, 66]:

$$\psi_{\beta,m} = \sqrt{\frac{\lambda}{4\,|\langle J \rangle|}}\,\mathrm{sech}\left[\frac{\lambda\,(m - m_0)}{2\,|\langle J \rangle|}\right] \tag{2.39}$$

These correspond to the VRSs of the model and describe the exciton becoming self-localised around the site m_0, with a spatial extent inversely proportional to the exciton-nuclear coupling strength. In addition, all these states (each corresponding to a different value of m_0) are degenerate, arising from the translational invariance of the system in the case where no disorder is present in the model. Adding disorder breaks this translational symmetry and 'pins' these solutions to certain specific values for the central site, m_0. This can be seen by obtaining the stationary points of the adiabatic surfaces numerically, for a particular instance of the disorder within the Frenkel-Holstein Hamiltonian, by iteratively solving Eq. (2.36) while simultaneously imposing the constraint given by Eq. (2.38).

For the 99 site Frenkel-Holstein model considered previously, five adiabatic VRSs exist, with their associated exciton densities and centre-of mass quantum numbers, j, given in Fig. 2.12. The exciton densities for all these adiabatic VRSs are much further localised

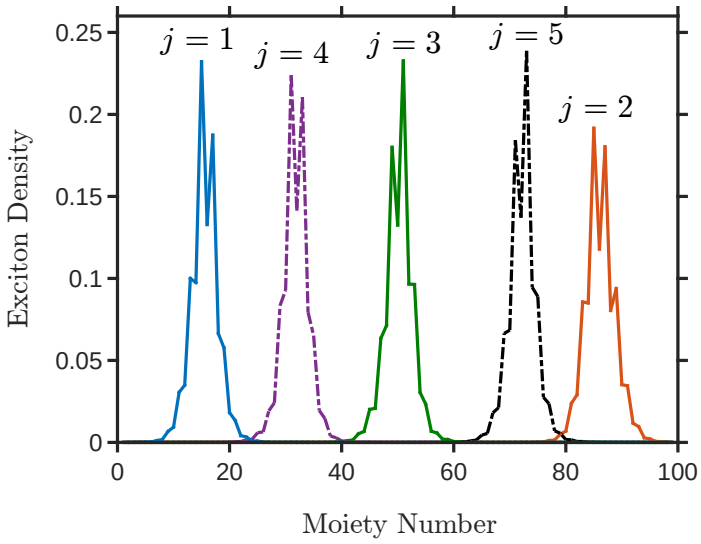


Figure 2.12: The five vibrationally relaxed states (VRSs) for one particular conformation of a PPV polymer chain made up of 99 moieties, calculated in the adiabatic limit. The exciton centre-of-mass quantum number, j, for each state is also given. The VRSs given by the solid curves in this figure each have an associated LEGS in the underlying Frenkel model, all of which are given in Fig. 2.7. In contrast, the VRSs given by the dashed curves have no associated localised state in the Frenkel model and arise solely as a result of the exciton-nuclear coupling.

than for the VRSs corresponding to the system with quantum nuclei of $\hbar\omega = 0.2$ eV (whose exciton densities are given in Fig. 2.10). This is because coupling the exciton to static classical nuclei is known to have a much greater localisation effect compared to the Anderson localisation arising from the disorder in the model, giving rise to so called Landau polarons [59, 67, 68]. Of these adiabatic VRSs, those given by the solid curves in Fig. 2.12 are 'pinned' in the same location as a LEGS (whose exciton densities are given in Fig. 2.7), while those VRSs given by the dashed curves have no corresponding localised state in the underlying Frenkel model. To understand the origin of the adiabatic VRSs given by the dashed curves, we consider the strong coupling limit of the Born-Oppenheimer Hamiltonian, where $\lambda / \langle J \rangle \to \infty$. In this limit, the effect of the nearest-neighbour exciton hopping term in $\hat{H}_{\mathrm{F}}$ becomes vanishingly small, giving rise to L adiabatic VRSs which

correspond to $|\psi_{\beta,\mathrm{ex}}\rangle = |m\rangle$ (i.e., the VRSs correspond to the exciton becoming self-localised onto a single site within the model) [69]. Hence the number of adiabatic VRSs for a given Frenkel-Holstein model must be between n_{LEGs} (the number of LEGSs) and L and solely depends on the value of $\lambda/\langle J\rangle$.

Additionally, for the adiabatic VRSs, the exciton-phonon correlation function is given by:

$$C_n^{\text{ex-ph}} = \sum_m |\psi_{\beta,m}|^2 \, |\psi_{\beta,m+n}|^2 \tag{2.40}$$

The exciton-polaron therefore has maximal size in the adiabatic limit, with the range of exciton-phonon correlations only limited by the spatial extent of the exciton density [60, 64].

2.5.2 Anti-Adiabatic Limit

In the limit $\omega' \to \infty$ (while the exciton-phonon coupling parameter, λ, is kept constant) the Frenkel-Holstein Hamiltonian can be diagonalised by performing the so-called Lang-Firsov transformation [70, 71]. This unitary transformation is defined as follows:

$$\hat{\tilde{H}}_{\mathrm{FH}} = e^{-\hat{S}} \hat{H}_{\mathrm{FH}} e^{\hat{S}} \tag{2.41}$$

where $\hat{S}$ is an anti-Hermitian operator given by:

$$\hat{S} = -i\sqrt{\frac{2\lambda}{\hbar\omega}} \sum_m \hat{a}_m^\dagger \hat{a}_m \hat{P}_m \tag{2.42}$$

and $\hat{P}_m = \frac{i}{\sqrt{2}}(\hat{b}_m^\dagger - \hat{b}_m)$ is the dimensionless momentum operator, for the oscillator on site m. Physically, the Lang-Firsov transformation corresponds to a shift in the displacement of the oscillator on the exciton site, by an amount given by the dimensionless exciton-

phonon coupling parameter, A.

To simplify this expression for the transformed Frenkel-Holstein Hamiltonian, the commutator $\left[\hat{H}_{\mathrm{FH}}, e^{\hat{S}}\right]$ must be evaluated. While a simple expression for $\left[\hat{A}, e^{\hat{S}}\right]$ for an arbitrary operator $\hat{A}$ does not exist, in the case where $[\hat{A}, \hat{S}]$ commutes with $\hat{S}$ (i.e., $[[\hat{A}, \hat{S}], \hat{S}] = 0$), the following equation is valid:

$$\left[\hat{A}, e^{\hat{S}}\right] = \left[\hat{A}, \hat{S}\right] e^{\hat{S}} \tag{2.43}$$

which is obtained by inserting the Taylor expansion of $\exp[\hat{S}]$ into the left-hand side of Eq. (2.43). From Eq. (2.43), the following expression for the transformed operator, $\hat{\tilde{A}} = e^{-\hat{S}} \hat{A} e^{\hat{S}}$, can be obtained [38, 72]:

$$\hat{\tilde{A}} = \hat{A} + \left[\hat{A}, \hat{S}\right] \tag{2.44}$$

One such operator that satisfies the requirement that $[[\hat{A}, \hat{S}], \hat{S}] = 0$ is the harmonic oscillator destruction operator for site m, $\hat{b}_m$. As a result, this operator has the following form, after the Lang-Firsov transformation has been applied:

$$\hat{\tilde{b}}_m = \hat{b}_m + \frac{A}{\sqrt{2}} \hat{a}_m^\dagger \hat{a}_m \tag{2.45}$$

The Lang-Firsov transformed Hamiltonian can now be obtained by inserting Eq. (2.45) into the Frenkel-Holstein Hamiltonian, given by Eq. (2.28) [73]:

$$\hat{\tilde{H}}_{\mathrm{FH}} = e^{-\hat{S}} \hat{H}_{\mathrm{F}} e^{\hat{S}} + \hbar\omega \sum_m \left(\hat{b}_m^\dagger \hat{b}_m + \tfrac{1}{2} \right) - \lambda \tag{2.46}$$

From Eq. (2.46), we see that the only term not to be brought into diagonal form is

that which involves the Frenkel Hamiltonian, $\hat{H}_{\mathrm{F}}$. In this Frenkel Hamiltonian term, the additional exponential factors, $e^{\hat{S}}$, physically correspond to the presence of a vibrational overlap contribution to the exciton nearest-neighbour hopping [74], as a result of the applied transformation. However in the anti-adiabatic limit, when $\hbar\omega \to \infty$ while λ and $\langle J \rangle$ remain constant, $e^{-\hat{S}}\hat{H}_{\mathrm{F}}e^{\hat{S}} \simeq \hat{H}_{\mathrm{F}}$ and as a result the Lang-Firsov transformation fully diagonalises the Frenkel-Holstein Hamiltonian:

$$\hat{\tilde{H}}_{\mathrm{FH}} \simeq \hat{H}_{\mathrm{F}} + \hbar\omega \sum_{m} \left(\hat{b}_{m}^{\dagger}\hat{b}_{m} + \tfrac{1}{2} \right) - \lambda \tag{2.47}$$

Therefore in the anti-adiabatic limit, the eigenvalues of the Frenkel-Holstein Hamiltonian for a L site chain are given by:

$$E_{k,\, n_{\mathrm{phon}}} = \epsilon_k + \hbar\omega \left(n_{\mathrm{phon}} + \tfrac{1}{2} \right) - \lambda \tag{2.48}$$

where ϵ_k is the eigenvalue of the Frenkel Hamiltonian corresponding to the state with quantum number k and n_{phon} is the total number of phonons present. Additionally, the corresponding eigenkets have the following form in the transformed basis:

$$|\tilde{\psi}_{k,\, n_1,\, n_2,\, ..,\, n_L}\rangle = |k\rangle \otimes |n_1\rangle \otimes |n_2\rangle \otimes \cdots \otimes |n_L\rangle \tag{2.49}$$

where $|k\rangle$ is the eigenket of the Frenkel Hamiltonian, with quantum number k, $|n_m\rangle$ is the harmonic oscillator eigenket for site m, with quantum number n_m and the untransformed and transformed eigenkets of the Frenkel-Holstein Hamiltonian are related as follows:

$$|\psi_{k,\, n_1,\, n_2,\, ..,\, n_L}\rangle = e^{\hat{S}}\, |\tilde{\psi}_{k,\, n_1,\, n_2,\, ..,\, n_L}\rangle \tag{2.50}$$

Hence in the anti-adiabatic limit, any observables solely associated with the exciton are unaffected by the presence of the exciton-phonon coupling term in the Frenkel-Holstein Hamiltonian.

Additionally, for the eigenstates of the Frenkel-Holstein Hamiltonian in their vibrational ground state, the exciton-phonon correlation function is given by [64]:

$$C_n^{\text{ex-ph}} = \delta_{n,\,0} \tag{2.51}$$

where $\delta_{n,\,0}$ is the Kronecker delta. The exciton-polaron therefore has minimal size in the anti-adiabatic limit. This result can be confirmed from the expression for the associated anti-adiabatic eigenkets within the untransformed basis, obtained using Eqs. (2.49) and (2.50). Firstly, the exponential operator, $\exp[\hat{S}]$, can be simplified using the Baker-Hausdorff formula [75, 76]:

$$e^{\hat{A}+\hat{B}} = e^{\hat{A}} e^{\hat{B}} e^{-[\hat{A},\,\hat{B}]/2} \tag{2.52}$$

which is valid if the operators $\hat{A}$ and $\hat{B}$ commute with their commutator, $[\hat{A}, \hat{B}]$. Using this expression, along with that for the operator $\hat{S}$ given in Eq. (2.42), leads to the following expression for the exponential transformation operator [38, 72]:

$$e^{\hat{S}} = e^{\sqrt{\frac{2\lambda}{\hbar\omega}} \sum_m \hat{a}_m^\dagger \hat{a}_m \hat{b}_m^\dagger} e^{-\sqrt{\frac{2\lambda}{\hbar\omega}} \sum_m \hat{a}_m^\dagger \hat{a}_m \hat{b}_m} e^{-\frac{\lambda}{2\hbar\omega}} \tag{2.53}$$

Finally, an expression for the eigenstates of the Frenkel-Holstein model in their vibrational ground state, $|\psi_{k,\,0_1,..,\,0_L}\rangle$, can then be obtained by inserting Eq. (2.53) into Eqs. (2.49)

and (2.50), as well as using $\hat{b}_m |0_m\rangle = 0$ [38, 72]:

$$\begin{aligned} |\psi_{k,0_1,..,0_L}\rangle &= \sum_m \psi_{k,m} |m\rangle \otimes |0_1\rangle \otimes \cdots \otimes \left(e^{-\frac{\lambda}{2\hbar\omega}} \sum_{q_m=0}^{\infty} \frac{\left(\sqrt{\frac{\lambda}{\hbar\omega}}\right)^{q_m} |q_m\rangle}{\sqrt{q_m!}} \right) \otimes \cdots \otimes |0_L\rangle \\ &= \sum_m \psi_{k,m} |m\rangle \otimes |0_1\rangle \otimes \cdots \otimes \left| \alpha_m = \sqrt{\frac{\lambda}{\hbar\omega}} \right\rangle \otimes \cdots \otimes |0_L\rangle \end{aligned} \tag{2.54}$$

In this expression, $\psi_{k,m}$ is the probability amplitude for the exciton residing on site m, for the Frenkel eigenstate with quantum number k and $|q_m\rangle$ is the harmonic oscillator eigenstate for the oscillator on site m, with quantum number q_m. Hence the quantum state associated with the oscillator on the exciton site corresponds to a displaced coherent state (as defined in Eq. (2.8)), confirming that the exciton-phonon correlations are purely local in the anti-adiabatic limit.

2.6 The Lindblad Master Equation

To describe the time evolution of a Frenkel exciton (initially prepared in a high energy QEES or LEGS) relaxing into the low energy VRSs of the polymer chain, the model must allow the system to lose excess energy to the environment (where throughout this thesis, the system is defined as containing both the exciton and internal phonon degrees of freedom and is described by the Hamiltonian given in Eq. (2.28), whereas the environment is defined as anything external to the polymer chain of interest). Dissipation of energy arising from system-environment coupling is commonly accounted for by describing the

time evolution of the quantum system by a Lindblad master equation [77–79]:

$$\frac{\partial\hat{\rho}}{\partial\tilde{t}} = -\frac{i}{\hbar\omega}\left[\hat{H},\hat{\rho}\right] - \frac{\tilde{\gamma}}{2}\sum_{m}\left(\hat{b}_m^{\dagger}\hat{b}_m\hat{\rho} + \hat{\rho}\hat{b}_m^{\dagger}\hat{b}_m - 2\hat{b}_m\hat{\rho}\hat{b}_m^{\dagger}\right) \tag{2.55}$$

where $\tilde{t} = t\omega$ is the dimensionless time. Such an equation describes the time dependence of the system density matrix, $\hat{\rho}$, which for a system with a Hilbert dimension of size N, becomes a $N \times N$ matrix. From the system density matrix, the expectation value of any operator corresponding to a system observable, $\hat{O}$, can be calculated [80]:

$$\langle\hat{O}\rangle = \mathrm{Tr}\left[\hat{\rho}\hat{O}\right] \tag{2.56}$$

where $\mathrm{Tr}[\cdots]$ corresponds to taking the trace of the quantity inside the brackets. One desirable feature of the Lindblad master equation is that it ensures that the physical constraints imposed on the reduced density matrix are preserved throughout the time evolution (i.e., that the density matrix remains Hermitian, positive-definite and continues to have a trace of one).

From Eq. (2.55), we see that the time dependence of the system density matrix depends on two terms. The first term on the right of Eq. (2.55) corresponds to the unitary evolution of the system density matrix under the Hamiltonian, $\hat{H}$, given by:

$$\hat{H} = \hat{H}_{\mathrm{FH}} + \hat{H}_{\Delta} \tag{2.57}$$

where:

$$\hat{H}_{\Delta} = \frac{\tilde{\gamma}\hbar\omega}{4}\sum_{m}\left(\hat{Q}_m\hat{P}_m + \hat{P}_m\hat{Q}_m\right) \tag{2.58}$$

In this equation, $\hat{Q}_m = \frac{1}{\sqrt{2}}(\hat{b}_m^{\dagger} + \hat{b}_m)$ is the dimensionless displacement operator and

$\hat{P}_m = \frac{i}{\sqrt{2}}(\hat{b}_m^\dagger - \hat{b}_m)$ is the dimensionless momentum operator, for the oscillator on site m and physically this correction term, given by Eq. (2.58), corresponds to the damping correction to the harmonic oscillator frequency induced by the external dissipation [81]. The second term in Eq. (2.55) accounts for energy dissipation of the system induced by the system-environment coupling. The effect of the system-environment coupling is controlled by the dimensionless dissipation parameter $\tilde{\gamma} = \frac{\gamma}{\omega}$, as well as the Lindblad operator for site m, $\hat{b}_m$, which for the system considered in this thesis becomes the dimensionless harmonic oscillator destruction operator.

While the Lindblad master equation only approximately describes dissipation effects due to system-environment coupling, the perturbative nature of its derivation means that we expect the master equation to describe the dynamics of systems in which the system-environment coupling is weak (i.e., when $\tilde{\gamma}$ is small). Such a situation is indeed physically relevant to the exciton relaxation dynamics in polymer chains, in which the exciton-phonon coupling strength is much larger that any coupling terms to the environment.

It is not necessarily obvious why the harmonic oscillator destruction operator is a good choice for the Lindblad operator in our master equation in Eq. (2.55). To show that it is, we can derive the following equations of motion for the dimensionless nuclear displacement and momentum, using equations (2.55) and (2.56):

$$\begin{aligned} \frac{d\langle \hat{Q}_m \rangle}{d\tilde{t}} &= \langle \hat{P}_m \rangle \\ \frac{d\langle \hat{P}_m \rangle}{d\tilde{t}} &= A\langle \hat{a}_m^\dagger \hat{a}_m \rangle - \langle \hat{Q}_m \rangle - \tilde{\gamma}\langle \hat{P}_m \rangle \end{aligned} \tag{2.59}$$

which have the form of Newton's equations of motion for a damped harmonic oscillator [79, 81] and are the identical equations of motion used previously for modelling exciton relaxation dynamics for classical nuclei [15]. The dissipation terms in Eq. (2.55) thus

result in an effective frictional damping force which is experienced by the internal nuclear degrees of freedom of the polymer.

2.6.1 Superoperator Formalism

The differential equation given be Eq. (2.55) has a complicated form and a general solution for $\hat{\rho}(\tilde{t})$ does not exist. The Lindblad master equation can however be simplified by writing it in Liouville space. In this space, the system density matrix becomes a N^2 column vector:

$$|\vec{\rho}\rangle = \begin{pmatrix} \rho_{11} \\ \rho_{21} \\ \rho_{31} \\ \vdots \end{pmatrix} \tag{2.60}$$

where ρ_{ij} are the various matrix elements of the system density matrix. This process of converting a matrix into a column vector is known as vec-ing [82]. In this Liouville space representation, the Lindblad master equation takes the following Schrödinger like form:

$$\frac{d\,|\vec{\rho}\rangle}{d\tilde{t}} = -i\hat{\hat{L}}\,|\vec{\rho}\rangle \tag{2.61}$$

where $\hat{\hat{L}}$ is a $N^2 \times N^2$ matrix called the Lindblad superoperator, which is given by [83]:

$$\hat{\hat{L}} = \frac{1}{\hbar\omega}\left(\hat{\mathbb{1}} \otimes \hat{H} - \hat{H}^T \otimes \hat{\mathbb{1}}\right) - \frac{i\tilde{\gamma}}{2}\sum_m \left(\hat{\mathbb{1}} \otimes \hat{b}_m^\dagger \hat{b}_m + \left(\hat{b}_m^\dagger \hat{b}_m\right)^T \otimes \hat{\mathbb{1}} - 2\left(\hat{b}_m^\dagger\right)^T \otimes \hat{b}_m\right) \tag{2.62}$$

where $\hat{\mathbb{1}}$ is the $N \times N$ unit matrix, $A \otimes B$ refers to the Kronecker product between matrices A and B and A^T is the transpose of matrix A. The proof that Eqs. (2.55) and (2.61) are equivalent is given in Appendix A. A general solution to Eq. (2.61) can be obtained by writing the system density matrix in the basis of the Lindblad superoperator eigenstates. The Lindblad superoperator is in general non-Hermitian, leading it to have

complex eigenvalues, λ_μ, as well as associated left and right eigenvectors, $|\vec{w}_\mu\rangle$ and $|\vec{u}_\mu\rangle$, which are not the same. These quantities are obtained from the following eigenvalue equations [82]:

$$\hat{\hat{L}}\,|\vec{u}_\mu\rangle = \lambda_\mu\,|\vec{u}_\mu\rangle\,, \qquad \hat{\hat{L}}^\dagger\,|\vec{w}_\mu\rangle = \lambda_\mu^*\,|\vec{w}_\mu\rangle \tag{2.63}$$

where the left and right eigenvectors can be normalised so that they obey the following bi-orthogonality relation:

$$\langle\vec{w}_\mu|\vec{u}_\nu\rangle = \delta_{\mu,\nu} \tag{2.64}$$

The fact that the right eigenvectors of the Lindblad superoperator are not themselves orthogonal raises the question as to whether these states form a complete basis. While the Lindblad superoperator cannot in general be brought into diagonal form, under an appropriate similarity transformation S, the superoperator can always be transformed into Jordan canonical form, $\hat{\hat{L}}_J$, given by [82]:

$$\hat{\hat{L}}_J = S^{-1}\hat{\hat{L}}S = J_{n_1}(\lambda_1) \oplus J_{n_2}(\lambda_2) \oplus ... \oplus J_{n_p}(\lambda_p) \tag{2.65}$$

The Jordan canonical form given by Eq. (2.65) corresponds to a direct sum of Jordan blocks, $J_{n_\mu}(\lambda_\mu)$, of dimension n_μ, such that the total dimension of $\hat{\hat{L}}_J$, $n = n_1+n_2+...+n_p$, is equal to the size of the Liouville space of the system. Each eigenvalue of the Lindblad superoperator λ_μ has an associated Jordan block, given by:

$$J_{n_\mu}(\lambda_\mu) = \begin{pmatrix} \lambda_\mu & 1 & & & \\ & \lambda_\mu & 1 & & \\ & & \ddots & \ddots & \\ & & & \lambda_\mu & 1 \\ & & & & \lambda_\mu \end{pmatrix} \tag{2.66}$$

where all other elements in the matrix are zero. We will write the states which transform the Lindblad superoperator into Jordan canonical form as follows. The vector $|u_{\mu,k}\rangle$ is the state associated with the kth row or column of the Jordan block associated with eigenvalue λ_μ. In this notation, $|\vec{u}_{\mu,0}\rangle$ is then the right eigenvector of the Lindblad superoperator associated with eigenvalue λ_μ. The states $|\vec{u}_{\mu,k}\rangle$ therefore form a complete basis of the Liouville space of the system. Using these basis states, it can be shown that the solution to the Lindblad master equation given in Eq. (2.61) can be written as follows [84, 85]:

$$|\vec{\rho}\left(\tilde{t}\right)\rangle = \sum_{\mu=1}^{p}\sum_{k=0}^{n_\mu}\sum_{\alpha=0}^{k} a_{\mu,(k-\alpha)}\left[-i\tilde{t}\right]^\alpha e^{-i\lambda_\mu \tilde{t}}\,|\vec{u}_{\mu,k}\rangle \tag{2.67}$$

where $a_{\mu,(k-\alpha)}$ are coefficients which can be determined from the system density matrix at $\tilde{t} = 0$.

Of particular interest is the form of the system density matrix in the limit $\tilde{t} \to \infty$, at which point the system has reached equilibrium. From Eq. (2.67), we see that only states which satisfy the following relation contribute to the system density matrix in this limit:

$$\hat{\tilde{L}}\,|\vec{u}_{\rm s}\rangle = 0, \quad \text{i.e.,} \quad \lambda_s = 0 \tag{2.68}$$

which are known as the steady state solutions of the system.

3

Computational Methods

In the previous section, model Hamiltonians were introduced which include the necessary electronic and nuclear degrees of freedom needed to accurately describe the exciton relaxation dynamics within polymer systems. In addition, the Lindblad master equation was shown to describe the time evolution of the system under a given model Hamiltonian, while also including the effects of the system-environment coupling in a perturbative manner. To obtain dynamical observables which can be compared to experiment, computational methods are therefore needed which can solve the Lindblad master equation for a suitable model Hamiltonian.

For electron-nuclear coupled models, the Hilbert space is known to scale exponentially with the system size (i.e., for the Frenkel-Holstein model, the Hilbert space scales as $\sim d^L$, where L is the number of sites/moieties in the model and d is the size of the Hilbert space associated with a single site). Therefore the Frenkel-Holstein model Hilbert space becomes too large to manipulate on a computer for a number of sites/moieties physically relevant for modelling realistic polymer chains. Additionally the system density matrix, which is the quantity used in the Lindblad master equation, has a size equal to the square of the system Hilbert space. To circumvent these issues, we first introduce the quantum jump trajectory method, which allows the Lindblad master equation to be solved by using standard time-dependent Schrödinger equation based methods. For the rest of the section, we introduce various techniques that solve the time-dependent Schrödinger equation for the Frenkel-Holstein model, all of which use a truncated Hilbert space to do so.

3.1 Quantum Jump Trajectory Approach

The Lindblad master equation, which describes the time evolution of the system and was previously introduced in Section 2.6, is given by [77–79]:

$$\frac{\partial\hat{\rho}}{\partial\tilde{t}} = -\frac{i}{\hbar\omega}\left[\hat{H},\hat{\rho}\right] - \frac{\tilde{\gamma}}{2}\sum_{m}\left(\hat{b}_m^\dagger\hat{b}_m\hat{\rho} + \hat{\rho}\hat{b}_m^\dagger\hat{b}_m - 2\hat{b}_m\hat{\rho}\hat{b}_m^\dagger\right) \tag{3.1}$$

where $\hat{H}$ is the system Hamiltonian, $\tilde{\gamma}$ is the dimensionless dissipation parameter and $\hat{b}_m$ is the Lindblad operator for site m. For a system with Hilbert space size N, the system density matrix, $\hat{\rho}\left(\tilde{t}\right)$, is a $N \times N$ matrix that contains all known information about the system at time $\tilde{t}$. Observables associated with a system operator, $\hat{O}$, can be obtained from this system density matrix as follows [80]:

$$\langle\hat{O}\rangle = \mathrm{Tr}\left[\hat{\rho}\hat{O}\right] \tag{3.2}$$

where $\mathrm{Tr}[\cdots]$ corresponds to taking the trace of the quantity inside the brackets. For a system in a pure state (i.e., one that can be fully described by a single quantum state $|\psi\rangle$), the system density matrix takes the following form [80]:

$$\hat{\rho} = |\psi\rangle\langle\psi| \tag{3.3}$$

Within the quantum jump trajectory method, observables associated with the density matrix solution of a Lindblad master equation are obtained by averaging over many so-called quantum jump trajectories. In other words, a set of N_{traj} trajectories, $|\psi_j\rangle$, are

used to represent the system density matrix as follows:

$$\hat{\rho} = \frac{1}{N_{\text{traj}}} \sum_{j=1}^{N_{\text{traj}}} |\psi_j\rangle \langle\psi_j| \tag{3.4}$$

such that from Eq. (3.2), the expectation value of an observable associated with the system operator $\hat{O}$ is obtained as an average over the individual trajectories:

$$\langle \hat{O} \rangle = \frac{1}{N_{\text{traj}}} \sum_{j=1}^{N_{\text{traj}}} \langle\psi_j|\hat{O}|\psi_j\rangle \tag{3.5}$$

The time evolution of a single quantum jump trajectory is obtained using the following procedure [86–89]:

- *Step 1:* The total time evolution of a single trajectory is divided into several small time steps of length $\delta\tilde{t}$. Next, the effective Hamiltonian for the system is defined as follows [90]:

$$\hat{H}_{\text{eff}} = \hat{H} - \frac{i\tilde{\gamma}\hbar\omega}{2} \sum_m \hat{b}_m^\dagger \hat{b}_m \tag{3.6}$$

  Evolving this single quantum trajectory, initially in state $|\psi(\tilde{t})\rangle$, under the effective Hamiltonian gives us a trial state for the trajectory at time $\tilde{t} + \delta\tilde{t}$:

$$|\psi_{\text{trial}}(\tilde{t} + \delta\tilde{t})\rangle = e^{-\frac{i\hat{H}_{\text{eff}}\delta\tilde{t}}{\hbar\omega}} |\psi(\tilde{t})\rangle \tag{3.7}$$

- *Step 2:* As the effective Hamiltonian in Eq. (3.6) is non-Hermitian, the time evolution in Eq. (3.7) does not conserve the quantum state's norm:

$$\langle\psi_{\text{trial}}(\tilde{t} + \delta\tilde{t})|\psi_{\text{trial}}(\tilde{t} + \delta\tilde{t})\rangle = 1 - \delta p \tag{3.8}$$

where δp is the decay in the norm over the time step $\delta\tilde{t}$. From the Taylor expansion of the evolution operator, $\exp[-i\hat{H}_{\text{eff}}\delta\tilde{t}/\hbar\omega]$:

$$e^{-\frac{i\hat{H}_{\text{eff}}\delta\tilde{t}}{\hbar\omega}} = 1 - \frac{i\hat{H}_{\text{eff}}\delta\tilde{t}}{\hbar\omega} + \mathrm{O}(\delta\tilde{t}^2) \tag{3.9}$$

the following expression for δp can be obtained valid in the limit $\delta\tilde{t} \to 0$:

$$\delta p = \sum_m \delta p_m \,, \qquad \delta p_m = \tilde{\gamma}\delta\tilde{t}\,\langle\psi\left(\tilde{t}\right)|\hat{b}_m^\dagger\hat{b}_m|\psi\left(\tilde{t}\right)\rangle \tag{3.10}$$

where the expression for $\hat{H}_{\text{eff}}$ in Eq. (3.6) has also been used. Using Eq. (3.8), the state of the single quantum trajectory at time $\tilde{t}+\delta\tilde{t}$ is determined probabilistically as follows:

a) With probability $1-\delta p$, the state at time $\tilde{t}+\delta\tilde{t}$ is:

$$|\psi\big(\tilde{t}+\delta\tilde{t}\big)\rangle = \frac{e^{-\frac{i\hat{H}_{\text{eff}}\delta\tilde{t}}{\hbar\omega}}\,|\psi\big(\tilde{t}\big)\rangle}{\sqrt{1-\delta p}} \tag{3.11}$$

b) With probability δp_m, the state at time $\tilde{t}+\delta\tilde{t}$ is:

$$|\psi\big(\tilde{t}+\delta\tilde{t}\big)\rangle = \frac{\hat{b}_m\,|\psi\big(\tilde{t}\big)\rangle}{\sqrt{\delta p_m/\tilde{\gamma}\delta\tilde{t}}} \tag{3.12}$$

which is commonly referred to as the trajectory undergoing a quantum jump.

It can be shown that time evolving the trajectories in this way leads to Eq. (3.4) being an exact solution to the Lindblad master equation in the limit $N_{\text{traj}} \to \infty$. To see this, the system density matrix at time $\tilde{t}+\delta\tilde{t}$ can be written within the quantum jump trajectory

approach as follows, using Eq. (3.4) [90]:

$$\hat{\rho}\big(\tilde{t}+\delta\tilde{t}\big) = (1-\delta p)\,\frac{e^{-\frac{i\hat{H}_{\text{eff}}\delta\tilde{t}}{\hbar\omega}}\,|\psi\big(\tilde{t}\big)\rangle}{\sqrt{1-\delta p}}\,\frac{\langle\psi\big(\tilde{t}\big)|\,e^{\frac{i\hat{H}^{\dagger}_{\text{eff}}\delta\tilde{t}}{\hbar\omega}}}{\sqrt{1-\delta p}} + \sum_m \delta p_m \frac{\hat{b}_m\,|\psi\big(\tilde{t}\big)\rangle}{\sqrt{\delta p_m/\tilde{\gamma}\delta\tilde{t}}}\,\frac{\langle\psi\big(\tilde{t}\big)|\,\hat{b}^{\dagger}_m}{\sqrt{\delta p_m/\tilde{\gamma}\delta\tilde{t}}} \quad (3.13)$$

where the two terms in this expression correspond to the two ways in which the trajectory can be evolved during the time step $\delta\tilde{t}$ (given by Eqs. (3.11) and (3.12)), along with their associated probabilities. Inserting in the expressions for $\hat{\rho}\big(\tilde{t}\,\big)$ in Eq. (3.3), δp and δp_m in Eq. (3.10), as well as using the Taylor expansion for $\exp[-i\hat{H}_{\text{eff}}\delta\tilde{t}/\hbar\omega]$, the above expression can be simplified into the following form:

$$\hat{\rho}\big(\tilde{t}+\delta\tilde{t}\big) = \hat{\rho}\big(\tilde{t}\,\big) - \frac{i\delta\tilde{t}}{\hbar\omega}\Big(\hat{H}_{\text{eff}}\hat{\rho}\big(\tilde{t}\,\big) - \hat{\rho}\big(\tilde{t}\,\big)\hat{H}^{\dagger}_{\text{eff}}\Big) + \tilde{\gamma}\delta\tilde{t}\sum_m \hat{b}_m\hat{\rho}\big(\tilde{t}\,\big)\hat{b}^{\dagger}_m \quad (3.14)$$

which is indeed the time discretised version of the Lindblad master equation given by Eq. (3.1).

Hence, we now need a technique by which to apply the time step evolution operator, $\exp[-i\hat{H}_{\text{eff}}\delta t/\hbar\omega]$, for the system of interest. This is the focus for the remainder of this section.

3.2 Ehrenfest Dynamics

In this thesis, we will predominately use the Frenkel-Holstein Hamiltonian, introduced in Section 2.5, to model the exciton relaxation dynamics within polymer systems. Using the quantum jump trajectory approach introduced above, this amounts to solving the following time-dependent Schrödinger equation (ignoring the $\tilde{\gamma}$ dependent terms in the

effective Hamiltonian, which can be incorporated using the same methodology):

$$\frac{d\left|\psi\right\rangle}{d\tilde{t}} = -\frac{i}{\hbar\omega}\hat{H}_{\mathrm{FH}}\left|\psi\right\rangle \tag{3.15}$$

where $\hbar\omega$ is the phonon energy of the harmonic oscillator, $\tilde{t} = \omega t$ is the dimensionless time and the Frenkel-Holstein Hamiltonian, $\hat{H}_{\mathrm{FH}}$, is given by [32, 57, 58]:

$$\hat{H}_{\mathrm{FH}} = \hat{H}_{\mathrm{F}} - \frac{A\hbar\omega}{\sqrt{2}}\sum_m \hat{a}_m^\dagger \hat{a}_m \left(\hat{b}_m^\dagger + \hat{b}_m\right) + \hbar\omega\sum_m \left(\hat{b}_m^\dagger \hat{b}_m + \tfrac{1}{2}\right) \tag{3.16}$$

where $\hat{H}_F$ is the Frenkel Hamiltonian, which was introduced in Section 2.4 and contains solely exciton operators. The Hilbert space associated with the Frenkel-Holstein Hamiltonian grows exponentially with the number of sites/moieties in the system and therefore to solve the associated time-dependent Schrödinger equation, we must employ techniques which use a reduced dimensional, truncated Hilbert space.

One option is to use a mean-field ansatz for the quantum state of the system [91]:

$$\left|\psi_{\mathrm{MF}}\right\rangle = e^{-iA\sum_m \int_0^{\tilde{t}} \langle \hat{a}_m^\dagger \hat{a}_m\rangle \langle \hat{Q}_m\rangle dt} \left|\psi_{\mathrm{ex}}\right\rangle \otimes \left|\psi_{\mathrm{ph},1}\right\rangle \otimes \cdots \otimes \left|\psi_{\mathrm{ph},L}\right\rangle \tag{3.17}$$

where the exciton and nuclear degrees of freedom are restricted to a product state during the entire time evolution. In this expression, $\left|\psi_{\mathrm{ex}}\right\rangle$ corresponds to the quantum state of the exciton, while $\left|\psi_{\mathrm{ph},m}\right\rangle$ corresponds to the quantum state of the harmonic oscillator on site m, for a Frenkel-Holstein model containing L sites. The time-dependence of the quantum states for the exciton and harmonic oscillators are given by the following:

$$\frac{d\left|\psi_{\mathrm{ex}}\right\rangle}{d\tilde{t}} = -\frac{i}{\hbar\omega}\left(\hat{H}_{\mathrm{F}} - A\hbar\omega\sum_m \hat{a}_m^\dagger \hat{a}_m \left\langle \hat{Q}_m\right\rangle\right)\left|\psi_{\mathrm{ex}}\right\rangle \tag{3.18}$$

$$\frac{d\left|\psi_{\mathrm{ph},m}\right\rangle}{d\tilde{t}} = -i\left(\hat{b}_m^\dagger \hat{b}_m + \tfrac{1}{2} - \frac{A}{\sqrt{2}}\left\langle \hat{a}_m^\dagger \hat{a}_m \right\rangle \left(\hat{b}_m^\dagger + \hat{b}_m\right)\right)\left|\psi_{\mathrm{ph},m}\right\rangle \tag{3.19}$$

where $\langle \hat{Q}_m \rangle = \langle \psi_{\mathrm{ph},m} | \hat{Q}_m | \psi_{\mathrm{ph},m} \rangle$, $\langle \hat{a}_m^\dagger \hat{a}_m \rangle = \langle \psi_{\mathrm{ex}} | \hat{a}_m^\dagger \hat{a}_m | \psi_{\mathrm{ex}} \rangle$ and $\hat{Q}_m = \frac{1}{\sqrt{2}}(\hat{b}_m^\dagger + \hat{b}_m)$ is the dimensionless displacement operator for the harmonic oscillator on site m. Together, Eqs. (3.17), (3.18) and (3.19) are referred to as the time-dependent self-consistent field equations [91–93]. Taking the time derivative of the mean-field ansatz given in Eq. (3.17) results in the following Schrödinger like equation:

$$\frac{d\left|\psi_{\mathrm{MF}}\right\rangle}{d\tilde{t}} = -\frac{i}{\hbar\omega}\hat{H}_{\mathrm{FH}}\left|\psi_{\mathrm{MF}}\right\rangle - iA\sum_m \left(\hat{a}_m^\dagger \hat{a}_m - \langle \hat{a}_m^\dagger \hat{a}_m \rangle\right)\left(\hat{Q}_m - \langle \hat{Q}_m \rangle\right)\left|\psi_{\mathrm{MF}}\right\rangle \tag{3.20}$$

While the mean-field ansatz does not exactly solve the time-dependent Schrödinger equation for the Frenkel-Holstein model, as can be seen by comparing Eqs. (3.15) and (3.20), it does approximately do so in the limit where quantum fluctuations about the mean nuclear displacements, $\langle \hat{Q}_m \rangle$, vanish. This is indeed the case in the limit where the nuclear degrees of freedom behave classically.

To proceed, we notice that Eq. (3.19) has the form of the time-dependent Schrödinger equation for a linearly driven harmonic oscillator. In Section 2.2, it was shown that such an equation can be solved exactly using a coherent state ansatz. Using the equations associated with the exact solution derived in that section, it can be shown that $|\psi_{\mathrm{ph},m}\rangle$ is given by:

$$\begin{aligned} \left|\psi_{\mathrm{ph},m}\right\rangle &= e^{-\frac{i}{2}\int_0^{\tilde{t}}\left[1 - A\langle \hat{a}_m^\dagger \hat{a}_m \rangle \langle \hat{Q}_m \rangle\right] dt}\left|\alpha_m\right\rangle \\ \frac{d\alpha_m}{d\tilde{t}} &= -i\alpha_m + \frac{iA}{\sqrt{2}}\left\langle \hat{a}_m^\dagger \hat{a}_m \right\rangle \end{aligned} \tag{3.21}$$

where $|\alpha_m\rangle$ is a coherent state of the harmonic oscillator on site m. Using the expressions for the average dimensionless nuclear displacement and momentum associated with the

coherent state, given by Eq. (2.9), the second term in Eq. (3.21) can be turned into the following:

$$\begin{aligned} \frac{d\langle \hat{Q}_m \rangle}{d\tilde{t}} &= \langle \hat{P}_m \rangle \\ \frac{d\langle \hat{P}_m \rangle}{d\tilde{t}} &= A\langle \hat{a}_m^\dagger \hat{a}_m \rangle - \langle \hat{Q}_m \rangle \end{aligned} \tag{3.22}$$

which is exactly Newtons equations of motion for the harmonic oscillator on site m. Therefore the approximation associated with the dynamics of the mean-field ansatz can be thought of as a classical treatment of the nuclear degrees of freedom in the model. The mean-field dynamics of the system can equally be performed using Eqs. (3.18) and (3.22), with this alternative procedure referred to as Ehrenfest dynamics [94].

3.3 Time Evolving Block Decimation (TEBD)

For many situations, the nuclear degrees of freedom in a system cannot be accurately described by classical displacements and momenta, meaning a quantum treatment is required to describe the dynamics. In such circumstances, we must find a procedure for truncating the exponentially large Hilbert space such that the states required to describe the properties of interest are retained. For one-dimensional strongly correlated systems, the density matrix renormalisation group technique has been successful in obtaining accurate numerical results for properties associated with the ground state of the system [61, 64, 95, 96]. Using the same Hilbert space truncation scheme, the time evolving block decimation (TEBD) technique [97–99] is an efficient and accurate method for computing the short time dynamics of such systems. The essential features of this technique involve efficiently representing the time evolving quantum state using a matrix products state (MPS), truncating the Hilbert space associated with this matrix product state through singular value

decompositions (SVDs) and partitioning the evolution operator into manageable parts using a Trotter decomposition. We now consider all of these elements in more detail.

3.3.1 Matrix Products States

For a one-dimensional system containing L sites, any quantum state can be described using the following form:

$$|\psi\rangle = \sum_{\sigma_1,...,\sigma_L} C_{\sigma_1,...,\sigma_L} |\sigma_1, ..., \sigma_L\rangle \tag{3.23}$$

where σ_m are referred to as the physical indices and correspond to the quantum numbers associated with the local Hilbert space basis on site m. The size of this index, d, therefore corresponds to the size of the corresponding local Hilbert space. In addition, $|\sigma_1, ..., \sigma_L\rangle$ is the product state basis corresponding to the set of quantum numbers, $\sigma = \{\sigma_1, ..., \sigma_L\}$, given by:

$$|\sigma_1, .., \sigma_L\rangle = |\sigma_1\rangle \otimes \cdots \otimes |\sigma_L\rangle \tag{3.24}$$

and $C_{\sigma_1,...,\sigma_L}$ is the probability amplitude tensor. As the size of this tensor, d^L, grows exponentially with the number of sites, this quantum state representation soon becomes impractical for realistic system sizes.

Alternatively, a quantum state can be described using matrix product states (MPSs) [61]:

$$|\psi\rangle = \sum_{\sigma_1,...,\sigma_L} \sum_{\alpha_1,...,\alpha_{L-1}} M^{\sigma_1}_{1,\alpha_1} M^{\sigma_2}_{\alpha_1,\alpha_2} \cdots M^{\sigma_{L-1}}_{\alpha_{L-2},\alpha_{L-1}} M^{\sigma_L}_{\alpha_{L-1},1} |\sigma_1, ..., \sigma_L\rangle \tag{3.25}$$

which corresponds to the probability amplitude tensor being decomposed into a matrix product of smaller site tensors, $M^{\sigma_m}_{\alpha_{m-1},\alpha_m}$. Within this new definition, α_m, are referred

to as the internal indices, which have size χ_m. Matrix product states can be used to represent any arbitrary quantum state of a one-dimensional system, as long as the size of the internal index associated with 'bond' m, χ_m, is given by [61]:

$$\chi_m = \begin{cases} d^m, & \text{for} \quad m < \frac{L}{2} \\ d^{L-m}, & \text{for} \quad m \geq \frac{L}{2} \end{cases} \tag{3.26}$$

In other words, the internal index dimensions must be exponentially large.

Physically, the internal index can be understood by considering the entanglement entropy between two partitioned parts of a system [97]. Forming two sub-systems that are separated by 'bond' m, the von Neumann entropy associated with each sub-system is [100]:

$$E(\rho_{A,m}) = -\text{Tr}\left[\rho_{A,m}\log(\rho_{A,m})\right] = E(\rho_{B,m}) \tag{3.27}$$

where $\rho_{A,m}$ and $\rho_{B,m}$ are the reduced density matrices for the left and right sub-systems respectively. For a matrix product state, it can be shown that the maximum possible encoded entanglement entropy across 'bond' m is given by:

$$E_{\max}(\rho_{A,m}) = \log(\chi_m) \tag{3.28}$$

This means that MPSs can efficiently describe minimally entangled states (i.e., these states can be accurately described by a MPS with small internal index dimensions). To illustrate this, consider the set of MPSs which have $\chi_m = 1$. From Eq. (3.25), the MPS ansatz in this case can be written as:

$$|\psi_{\text{MF}}\rangle = \left(\sum_{\sigma_1} M_{1,1}^{\sigma_1} |\sigma_1\rangle\right) \otimes \cdots \otimes \left(\sum_{\sigma_L} M_{1,1}^{\sigma_L} |\sigma_L\rangle\right) \tag{3.29}$$

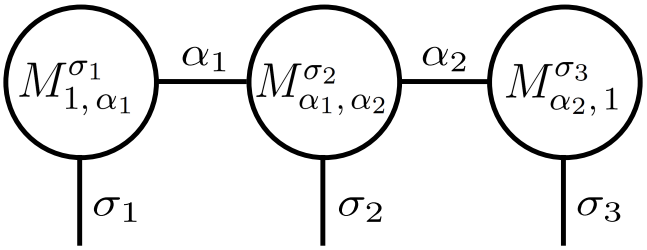


Figure 3.1: Tensor network diagram corresponding to a three site MPS.

which corresponds to all possible uncorrelated mean-field product states, with $E(\rho_{A,m}) = 0$. 'Truncating' the size of the internal index in a MPS therefore allows for an accurate reduced Hilbert space representation of a quantum state with an entanglement entropy less than the upper bound given in Eq. (3.28).

3.3.2 Tensor Network Diagrams

MPSs can be helpfully represented and manipulated using tensor network diagrams [101]. Figure 3.1 shows the tensor network diagram for a three site MPS. In these diagrams, the circles (or nodes) represent the site tensors in the MPS, $M^{\sigma_m}_{\alpha_{m-1},\alpha_m}$, the vertical lines correspond to their physical indices and the horizontal lines correspond to their internal indices. If a line is 'closed', then the index it represents is implicitly summed over.

Using these rules, other objects can be constructed in diagrammatic form. For example, the Hermitian conjugate of a site tensor, $M^{\sigma_m\dagger}_{\alpha_{m-1},\alpha_m}$, can be illustrated as a reflected node, where the physical index now points 'up' rather than 'down'. This is shown in Fig. 3.2. Finally, operators O_{σ_m,σ'_m} can be represented by objects which have an equal number of physical indices that point 'up' and 'down', as also shown in Fig. 3.2. The advantage of using such diagrams is that it circumvents the complicated algebra behind algorithms involving MPSs and makes these procedures easier to understand.

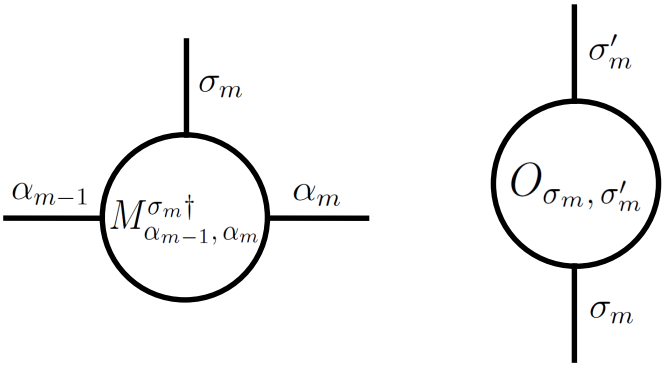


Figure 3.2: Tensor network diagrams corresponding to the conjugate transpose of a site tensor, $M^{\sigma_m\dagger}_{\alpha_{m-1},\alpha_m}$, and a single site operator, O_{σ_m,σ'_m}.

3.3.3 Normalisation

For a given state $|\psi\rangle$, a unique MPS representation does not exist. This is because a unit operator, $\mathbb{1} = \mathbf{X}\mathbf{X}^{-\mathbf{1}}$, can always be inserted in between any of the site tensors within the MPS, which gives rise to:

$$M^{\sigma_m}_{\alpha_{m-1},\alpha_m} \rightarrow \sum_{\alpha'_m} M^{\sigma_m}_{\alpha_{m-1},\alpha'_m} X_{\alpha'_m,\alpha_m}, \qquad M^{\sigma_{m+1}}_{\alpha_m,\alpha_{m+1}} \rightarrow \sum_{\alpha'_m} X^{-1}_{\alpha_m,\alpha'_m} M^{\sigma_{m+1}}_{\alpha'_m,\alpha_{m+1}} \tag{3.30}$$

and overall leaves the quantum state unchanged. This gauge degree of freedom can be exploited to convert the MPS into different canonical forms. Firstly the site tensors, $A^{\sigma_m}_{\alpha_{m-1},\alpha_m}$, can be left-normalised, such that [102]:

$$\sum_{\sigma_m}\sum_{\alpha_{m-1}} A^{\sigma_m\dagger}_{\alpha_m,\alpha_{m-1}} A^{\sigma_m}_{\alpha_{m-1},\alpha'_m} = \delta_{\alpha_m,\alpha'_m} \tag{3.31}$$

Site tensors which have this property are denoted by 'A' and a MPS consisting entirely of such tensors is referred to as left-canonical. Secondly the site tensors, $B^{\sigma_m}_{\alpha_{m-1},\alpha_m}$, can

be right-normalised, such that [102]:

$$\sum_{\sigma_m}\sum_{\alpha_m} B^{\sigma_m}_{\alpha_{m-1},\,\alpha_m} B^{\sigma_m\dagger}_{\alpha_m,\,\alpha'_{m-1}} = \delta_{\alpha_{m-1},\,\alpha'_{m-1}} \tag{3.32}$$

Site tensors which have this property are denoted by 'B' and a MPS consisting entirely of such tensors is referred to as right-canonical. The reason that left and right normalised site tensors differ is because the α_m and α_{m-1} internal indices in general having different dimensions, so that the tensors $M^{\sigma_m}_{\alpha_m,\alpha_{m-1}}$ are rectangular. These orthonormality properties of the site tensors ensure that for these two canonical forms, the full MPS is normalised. A final useful MPS canonical form is the following [103]:

$$|\psi\rangle = \sum_{\sigma_1,...,\,\sigma_L}\sum_{\alpha_1,...,\,\alpha_{L-1}} A^{\sigma_1}_{1,\,\alpha_1}\cdots A^{\sigma_{m-1}}_{\alpha_{m-2},\,\alpha_{m-1}} M^{\sigma_m}_{\alpha_{m-1},\,\alpha_m} B^{\sigma_{m+1}}_{\alpha_m,\,\alpha_{m+1}}\cdots B^{\sigma_L}_{\alpha_{L-1},1}\,|\sigma_1,...,\,\sigma_L\rangle \tag{3.33}$$

where the left of the MPS is formed of left-normalised site tensors and the right of the MPS is formed of right-normalised site tensors. The boundary between the two types of site tensors, in this case at site m, is called the orthogonality centre and has a site tensor which is neither left or right normalised, denoted by 'M'. Such a MPS is referred to as mixed-canonical and is in practice the most useful canonical form for numerical algorithms considered in this thesis. We now show how these MPS properties can be used to perform useful calculations.

3.3.4 Observables

Within this thesis, observables of interest can always be separated into expectation values involving products of single site operators. Such expectation values can be efficiently calculated using MPSs. Consider the observable $\langle\psi|\hat{O}_2|\psi\rangle$ corresponding to a local op-

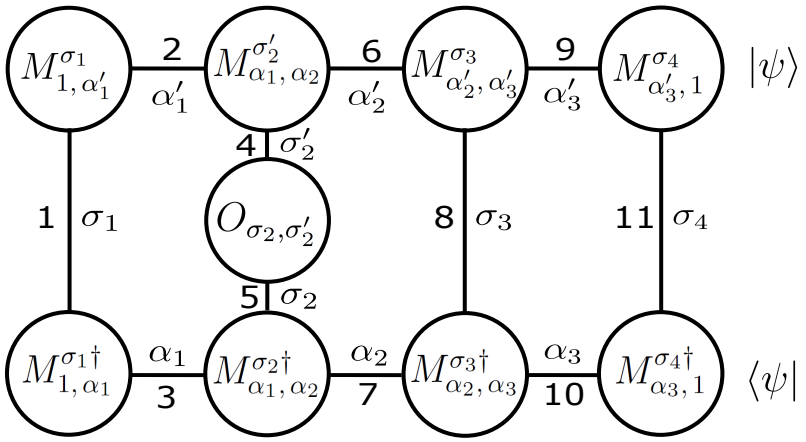


Figure 3.3: Tensor network diagram corresponding to the expectation value, $\langle\psi|\hat{O}_2|\psi\rangle$ for a four-site MPS given by $|\psi\rangle$. The operator $\hat{O}_2$ is a single-site operator that acts on the local Hilbert space of site two. The most efficient way of contracting the indices within this object are given by the numbers 1-11.

erator, $\hat{O}_2$, which acts on the Hilbert space of site two. If $|\psi\rangle$ is given by a four node MPS, then this expectation value corresponds to the object represented in the tensor network diagram given in Fig. 3.3. Within this tensor network diagram, the upper MPS corresponds to $|\psi\rangle$ and the lower MPS corresponds to $\langle\psi|$ (i.e., a conjugate transpose of the upper MPS). In addition, the observable tensor $O_{\sigma_2,\,\sigma'_2}$ contains the following local operator matrix elements:

$$O_{\sigma_2,\,\sigma'_2} = \langle\sigma_2|\hat{O}_2|\sigma'_2\rangle \tag{3.34}$$

For expectation values containing products of multiple local operators, the appropriate tensor network diagram is similar to Fig. 3.3, but with the observable tensor for each operator applied at the appropriate physical index.

For such an object, there are multiple ways in which the various indices can be contracted. The most efficient way to do so is illustrated in Fig. 3.3, where the order of index contractions is given by the numbers 1-11. Algebraically, this corresponds to first

performing the sum over the physical index, σ_1, in the following expression [103]:

$$\begin{aligned}\langle\psi|\hat{O}_m|\psi\rangle = &\sum_{\sigma_L}\sum_{\alpha_{L-1},\,\alpha'_{L-1}} M^{\sigma_L\dagger}_{1,\,\alpha_{L-1}}\Bigg(\cdots \\ &\left(\sum_{\sigma_m}\sum_{\alpha_{m-1},\,\alpha'_{m-1}} M^{\sigma_m\dagger}_{\alpha_m,\,\alpha_{m-1}}\left(\cdots\left(\sum_{\sigma_1} M^{\sigma_1\dagger}_{\alpha_1,\,1}M^{\sigma_1}_{1,\,\alpha'_1}\right)\cdots\right)E^{\sigma_m}_{\alpha'_{m-1},\,\alpha'_m}\right) \\ &\cdots\Bigg)M^{\sigma_L}_{\alpha'_{L-1},\,1}\end{aligned} \tag{3.35}$$

and then performing successive summations on moving out from the centre. In this expression, $E^{\sigma_m}_{\alpha'_{m-1},\,\alpha'_m}$ is the tensor given by:

$$E^{\sigma_m}_{\alpha'_{m-1},\,\alpha'_m} = \sum_{\sigma'_m}\langle\sigma_m|\hat{O}_m|\sigma'_m\rangle\, M^{\sigma'_m}_{\alpha'_{m-1},\,\alpha'_m} \tag{3.36}$$

and contains the operator contribution to the expectation value. Performing the index contractions in this order has an overall cost of $\mathrm{O}\left(2(L-1)\chi^3 d\right)$ (where χ is the average internal index dimension) and therefore scales linearly with the number of sites in the system. This means that it is computationally feasible to calculate expectation values involving local operators for even large systems.

The calculation of such expectation values is even more efficient for a MPS in mixed canonical form. Consider the expectation value of a single local site operator, $\hat{O}_m$, which acts on the orthogonality centre of a MPS given by:

$$|\psi\rangle = \sum_{\sigma_1,\ldots,\sigma_L}\sum_{\alpha_1,\ldots,\alpha_{L-1}} A^{\sigma_1}_{1,\,\alpha_1}\cdots A^{\sigma_{m-1}}_{\alpha_{m-2},\,\alpha_{m-1}} M^{\sigma_m}_{\alpha_{m-1},\,\alpha_m} B^{\sigma_{m+1}}_{\alpha_m,\,\alpha_{m+1}}\cdots B^{\sigma_L}_{\alpha_{L-1},\,1}\,|\sigma_1,\ldots,\,\sigma_L\rangle \tag{3.37}$$

Using the orthonormality properties of the left and right-normalised site tensors, given in Eqs. (3.31) and (3.32), the expectation value in this case reduces down to the following

simplified form:

$$\langle\psi|\hat{O}_m|\psi\rangle = \sum_{\sigma_m,\,\sigma'_m} \sum_{\alpha_{m-1},\,\alpha_m} \langle\sigma_m|\hat{O}_m|\sigma'_m\rangle\, M^{\sigma_m\dagger}_{\alpha_m,\,\alpha_{m-1}} M^{\sigma'_m}_{\alpha_{m-1},\,\alpha_m} \tag{3.38}$$

and only requires four index contractions to be performed, irrespective of the number of nodes in the MPS.

3.3.5 Hilbert Space Truncation

For large systems, the Hilbert space is too big to allow for the manipulation and storage of any possible MPS on a computer. Therefore, an algorithm is needed to truncate the internal indices, α_m, of a MPS so that an approximate and reduced dimensional representation of the original quantum state can be obtained. As shown in Section 3.3.1, the size of the internal index dimension corresponds to the maximum possible site entanglement that can be described by a given MPS. Truncating the internal index of a MPS will therefore only be a valid procedure for minimally entangled states.

To truncate the dimension of internal index α_m, the MPS must first be converted into the following form:

$$|\psi\rangle = \sum_{\sigma_1,\ldots,\sigma_L} \sum_{\alpha_1,\ldots,\alpha_{m-1}} \sum_{\alpha_{m+1},\ldots,\alpha_{L-1}} A^{\sigma_1}_{1,\,\alpha_1} \cdots D^{\sigma_m,\,\sigma_{m+1}}_{\alpha_{m-1},\,\alpha_{m+1}} \cdots B^{\sigma_L}_{\alpha_{L-1},\,1} \,|\sigma_1, \ldots, \sigma_L\rangle \tag{3.39}$$

This for example could be achieved as a result of applying a two-site operator to an mixed-canonical MPS with an orthogonality centre either on site m or $m+1$. Additionally, for a mixed-canonical MPS given by Eq. (3.37), the form given by Eq. (3.39) is achieved by

contracting the α_m internal index as follows:

$$D^{\sigma_m,\,\sigma_{m+1}}_{\alpha_{m-1},\,\alpha_{m+1}} = \sum_{\alpha_m} M^{\sigma_m}_{\alpha_{m-1},\alpha_m} B^{\sigma_{m+1}}_{\alpha_m,\,\alpha_{m+1}} \tag{3.40}$$

The state given in Eq. (3.40) can be converted back into MPS form by first applying a singular value decomposition (SVD) on the tensor $D^{\sigma_m,\,\sigma_{m+1}}_{\alpha_{m-1},\,\alpha_{m+1}}$ [104]:

$$D^{\sigma_m,\,\sigma_{m+1}}_{\alpha_{m-1},\,\alpha_{m+1}} = \sum_{\alpha_m} A^{\sigma_m}_{\alpha_{m-1},\alpha_m} S_{\alpha_m,\,\alpha_m} B^{\sigma_{m+1}}_{\alpha_m,\,\alpha_{m+1}} \tag{3.41}$$

where $A^{\sigma_m}_{\alpha_{m-1},\,\alpha_m}$ and $B^{\sigma_{m+1}}_{\alpha_m,\,\alpha_{m+1}}$ are left and right-normalised tensors respectively (defined in Eqs. (3.31) and (3.32)) and $S_{\alpha_m,\,\alpha_m}$ is a diagonal matrix containing the positive singular values, S_{α_m}. The diagonal matrix $S_{\alpha_m,\,\alpha_m}$ can then either be incorporated into $A^{\sigma_m}_{\alpha_{m-1},\,\alpha_m}$ to reform the MPS in Eq. (3.37) or can be incorporated into $B^{\sigma_{m+1}}_{\alpha_m,\,\alpha_{m+1}}$ to give a mixed-canonical MPS with the orthogonality centre on site $m+1$.

Alternatively, inserting Eq. (3.41) into Eq. (3.39) converts the quantum state $|\psi\rangle$ into the Schmidt decomposed form [105]:

$$|\psi\rangle = \sum_{\alpha_m} S_{\alpha_m} |\alpha_m\rangle_{\mathrm{A}} |\alpha_m\rangle_{\mathrm{B}} \tag{3.42}$$

where $|\alpha_m\rangle_{\mathrm{A}}$ are orthonormal states of sub-system A, which corresponds to sites 1 through m, and are given by [90]:

$$|\alpha_m\rangle_{\mathrm{A}} = \sum_{\sigma_1,\ldots,\sigma_m} \sum_{\alpha_1,\ldots,\alpha_{m-1}} A^{\sigma_1}_{1,\,\alpha_1} \cdots A^{\sigma_m}_{\alpha_{m-1},\,\alpha_m} |\sigma_1, \ldots, \sigma_m\rangle \tag{3.43}$$

while $|\alpha_m\rangle_{\mathrm{B}}$ are orthonormal states of sub-system B, which corresponds to sites $m+1$

through L, and are given by [90]:

$$|\alpha_m\rangle_{\mathrm{B}} = \sum_{\sigma_{m+1},...,\sigma_L} \sum_{\alpha_{m+1},...,\alpha_{L-1}} B^{\sigma_{m+1}}_{\alpha_m,\,\alpha_{m+1}} \cdots B^{\sigma_L}_{\alpha_{L-1},\,1} \,|\sigma_{m+1},...,\sigma_L\rangle \tag{3.44}$$

In particular, the reduced density matrix for sub-system A (as well as the reduced density matrix for sub-system B) has a simple form within the Schmidt decomposition basis [105]:

$$\hat{\rho}_{\mathrm{A}} = \mathrm{Tr}_B \,|\psi\rangle \langle\psi| = \sum_{\alpha_m} S^2_{\alpha_m} \,|\alpha_m\rangle_{\mathrm{A}} \langle\alpha_m| \tag{3.45}$$

Within the density matrix renormalisation group technique (DMRG), it is known that the optimum Hilbert space truncation scheme for one-dimensional systems is to retain the eigenstates of the reduced density matrix with the largest eigenvalues. From Eq. (3.45), this is therefore equivalent to retaining the internal index 'states' with the largest singular values [105]. For the work in this thesis, the degree of truncation performed for each SVD is determined using two different measures. Firstly, we impose a maximum internal index dimension, χ, so that only the χ largest singular values are ever retained. Secondly, additional singular values, S_{α_m}, are discarded if they satisfy:

$$\frac{S_{\alpha_m}}{S_{\mathrm{large}}} < S_{\mathrm{ratio}} \tag{3.46}$$

where S_{large} is the largest singular value for that particular SVD and S_{ratio} is a parameter set in the algorithm to determine the extent of truncation.

3.3.6 Matrix Product Operators

In a similar way to the MPS scheme discussed so far, any operator which acts on the full Hilbert space of a one-dimensional system can be expressed as a matrix product operator

(MPO) [102]:

$$\hat{V} = \sum_{\sigma_1,...,\sigma_L} \sum_{\sigma'_1,...,\sigma'_L} \sum_{\beta_1,...,\beta_{L-1}} N^{\sigma_1,\sigma'_1}_{1,\beta_1} N^{\sigma_2,\sigma'_2}_{\beta_1,\beta_2} \cdots N^{\sigma_L,\sigma'_L}_{\beta_{L-1},1} |\sigma_1, ..., \sigma_L\rangle \langle\sigma'_1, ..., \sigma'_L| \tag{3.47}$$

where β_m is the internal index for 'bond' m, while σ'_m and σ_m are the incoming and outgoing physical indices for site m, respectively. For certain types of operators, expressions for these MPO site tensors are easily obtainable. In particular if an operator, $\hat{V}$, is given as a linear combination of single-site operators, $\hat{O}_m$:

$$\hat{V} = \sum_m c_m \hat{O}_m \tag{3.48}$$

then $\hat{V}$ can be written as an MPO with an internal index dimension of $\chi = 2$, whose site tensors are obtained by [102]:

$$\mathbf{N}^{\sigma_m,\sigma'_m} = \begin{pmatrix} \delta_{\sigma_m,\sigma'_m} & 0 \\ c_m O_{\sigma_m,\sigma'_m} & \delta_{\sigma_m,\sigma'_m} \end{pmatrix} \tag{3.49}$$

where O_{σ_m,σ'_m} are the single-site operator matrix elements:

$$O_{\sigma_m,\sigma'_m} = \langle\sigma_m|\hat{O}_m|\sigma'_m\rangle \tag{3.50}$$

As the first and last site tensors only have a single internal index, they are instead given by the following vectors:

$$\mathbf{N}^{\sigma_1,\sigma'_1} = \begin{pmatrix} c_1 O_{\sigma_1,\sigma'_1} & \delta_{\sigma_1,\sigma'_1} \end{pmatrix}, \qquad \mathbf{N}^{\sigma_L,\sigma'_L} = \begin{pmatrix} \delta_{\sigma_L,\sigma'_L} \\ c_L O_{\sigma_L,\sigma'_L} \end{pmatrix} \tag{3.51}$$

In addition to MPOs offering a compact way of storing such operators (they contain

$Ld^2\chi^2$ elements, which is much less than the expected d^{2L}), MPOs are also easily applied to MPSs. Applying $\hat{V}$, given by the MPO in Eq. (3.47), to the following MPS:

$$|\psi\rangle = \sum_{\sigma_1,...,\sigma_L} \sum_{\alpha_1,...,\alpha_{L-1}} M^{\sigma_1}_{1,\alpha_1} M^{\sigma_2}_{\alpha_1,\alpha_2} \cdots M^{\sigma_L}_{\alpha_{L-1},1} |\sigma_1, ..., \sigma_L\rangle \tag{3.52}$$

leads to a new MPS, whose site tensors are obtained by the following [106]:

$$M^{\sigma_m}_{(\alpha_{m-1}\beta_{m-1}),(\alpha_m\beta_m)} = \sum_{\sigma'_m} N^{\sigma_m,\sigma'_m}_{\beta_{m-1},\beta_m} M^{\sigma'_m}_{\alpha_{m-1},\alpha_m} \tag{3.53}$$

Hence the internal index dimensions of this new MPS are the product of the corresponding internal index dimensions of the MPO and the original MPS.

While MPOs have many useful properties, not all operators can easily be converted into this form. In particular for a general time step evolution operator, $\exp[-i\hat{H}\delta\tilde{t}/\hbar\omega]$, an analytic expression for the site tensors within a MPO representation does not exist. For the TEBD technique, the exponentially large evolution operator is instead dealt with in the following way.

3.3.7 Evolution Operator

In order to obtain the quantum dynamics for a system, the evolution operator for a time step, $\exp[-i\hat{H}\delta\tilde{t}/\hbar\omega]$, must first be computed. For systems that have a large Hilbert space, this is not possible. Within the TEBD technique, this issue is circumvented by using the Trotter decomposition to expand the evolution operator into several smaller and more manageable terms.

For Hamiltonians that contain solely on-site and nearest-neighbour terms, it can be

shown that the full Hamiltonian can be written as the following sum:

$$\hat{H} = \sum_{m=1}^{L-1} \hat{H}_{m,\,m+1} \tag{3.54}$$

where $\hat{H}_{m,\,m+1}$ is the Hamiltonian for the 'bond' m. Using Eq. (3.54), the Trotter decomposition for the evolution operator is given by [107]:

$$e^{-i\hat{H}\delta\tilde{t}/\hbar\omega} \simeq e^{-i\hat{H}_{1,\,2}\delta\tilde{t}/2\hbar\omega} e^{-i\hat{H}_{2,\,3}\delta\tilde{t}/2\hbar\omega} \cdots e^{-i\hat{H}_{2,\,3}\delta\tilde{t}/2\hbar\omega} e^{-i\hat{H}_{1,\,2}\delta\tilde{t}/2\hbar\omega} + \mathrm{O}(\delta\tilde{t}^{\,3}) \tag{3.55}$$

The Trotter decomposition given in Eq. (3.55) is not exact, as the Hamiltonian terms $\hat{H}_{m,\,m+1}$ in general do not commute with each other. However, the error associated with this Trotter decomposition is of $\mathrm{O}(\delta\tilde{t}^{\,3})$, which becomes negligible if the time steps are chosen to be small. For a single time step, the form of this Trotter decomposition gives rise to a forward and backward 'sweep' process [103, 107]. The last $L-1$ terms in Eq. (3.55) are first applied successively in a forward 'sweep' along the MPS from site 1 to site L, while the first $L-1$ terms are then applied on the reverse 'sweep' on going from sites L to 1. Repeating this process allows the dynamics to be obtained for many time steps.

Other possible Trotter decompositions of the evolution operator exist, many of which have a smaller associated error. The disadvantage of these decompositions are that they contain more terms that have to be applied to the quantum state for each time step. The Trotter decomposition given in Eq. (3.55) is therefore generally seen as the optimum choice.

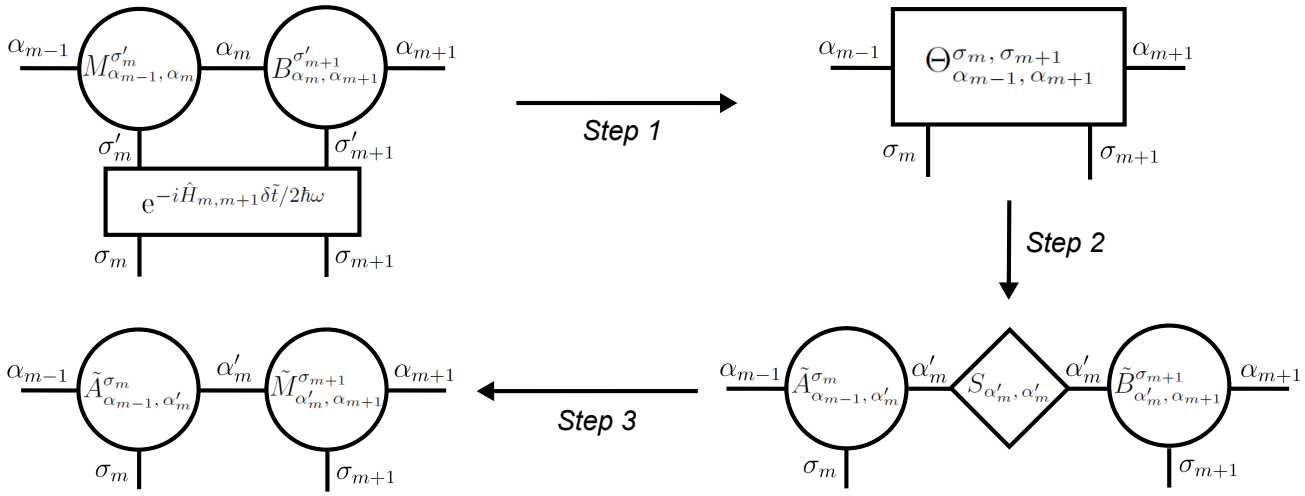


Figure 3.4: Diagram outlining the TEBD procedure.

3.3.8 The Algorithm

Now that the various elements of the TEBD technique have been introduced, we now consider the algorithm itself. The procedure for applying a single Trotter decomposition evolution operator onto a MPS in the forward (left to right) 'sweep' within the TEBD algorithm is illustrated in Fig. 3.4, with the first tensor network diagram in this figure corresponding to the object $\exp[-i\hat{H}_{m,m+1}\delta\tilde{t}/2\hbar\omega]\,|\psi\rangle$. The state $|\psi\rangle$ is in mixed-canonical form, with the orthogonality centre on site m. This figure illustrates the following steps:

- *Step 1:* The closed indices α_m, σ'_m and σ'_{m+1} are summed over to form the new tensor $\Theta^{\sigma_m,\,\sigma_{m+1}}_{\alpha_{m-1},\,\alpha_{m+1}}$. From Fig. 3.4, we see that this new tensor is given by [97]:

$$\Theta^{\sigma_m,\sigma_{m+1}}_{\alpha_{m-1},\alpha_{m+1}} = \sum_{\sigma'_m,\,\sigma'_{m+1}} \sum_{\alpha_m} U^{\sigma_m,\,\sigma_{m+1}}_{\sigma'_m,\,\sigma'_{m+1}} M^{\sigma'_m}_{\alpha_{m-1},\,\alpha_m} B^{\sigma'_{m+1}}_{\alpha_m,\,\alpha_{m+1}} \tag{3.56}$$

  where

$$U^{\sigma_m,\,\sigma_{m+1}}_{\sigma'_m,\,\sigma'_{m+1}} = \langle \sigma_m,\, \sigma_{m+1}|\, e^{-i\hat{H}_{m,m+1}\delta\tilde{t}/2\hbar\omega}\, |\sigma'_m,\, \sigma'_{m+1}\rangle \tag{3.57}$$

- *Step 2:* A singular value decomposition is applied on the tensor $\Theta^{\sigma_m,\,\sigma_{m+1}}_{\alpha_{m-1},\,\alpha_{m+1}}$ to obtain three new tensors, as well as a new internal index α'_m [97, 104]:

$$\Theta^{\sigma_m,\,\sigma_{m+1}}_{\alpha_{m-1},\,\alpha_{m+1}} = \tilde{A}^{\sigma_m}_{\alpha_{m-1},\,\alpha'_m} S_{\alpha'_m,\,\alpha'_m} \tilde{B}^{\sigma_{m+1}}_{\alpha'_m,\,\alpha_{m+1}} \tag{3.58}$$

  If the size of the original internal index α_m was χ, then the new internal index α'_m has grown to size χd on completion of the procedure outlined above, where d is the size of the site basis. To keep the internal indices constant in size, we truncate the α'_m index by discarding the α'_m 'states' associated with the smallest values of the singular values (as discussed in Section 3.3.5) [97]. The error associated with this truncation procedure can be quantified by computing the sum of the discarded singular values, $S_{\alpha'_m}$, which gives a bound on the error associated with the time evolved quantum state. It is this truncation procedure that keeps the total Hilbert space of the system finite and manageable throughout the dynamics.

- *Step 3:* The resulting tensor network diagram is transformed back into MPS form by creating the new tensor $\tilde{M}^{\sigma_{m+1}}_{\alpha'_m,\,\alpha_{m+1}}$:

$$\tilde{M}^{\sigma_{m+1}}_{\alpha'_m,\,\alpha_{m+1}} = S_{\alpha'_m,\,\alpha'_m} \tilde{B}^{\sigma_{m+1}}_{\alpha'_m,\,\alpha_{m+1}} \tag{3.59}$$

  This leads to the orthogonality centre of the MPS moving to site $m+1$ and is now in the correct location for applying the next term of the Trotter decomposed evolution operator in the forward (left to right) 'sweep'.

Hence to complete a dynamics time step within the TEBD algorithm, the same three step procedure outlined above is performed for every evolution operator in the Trotter decomposition, given in Eq. (3.55).

The process for the backward (right to left) 'sweep' is almost identical to the forward 'sweep' shown in Fig. 3.4. The only differences are that the orthogonality centre of the starting MPS is now on site $m+1$ and on reforming the MPS in Step 3, the diagonal $S_{\alpha'_m,\alpha'_m}$ matrix is instead incorporated into the left-hand site tensor, $\tilde{A}^{\sigma_m}_{\alpha_{m-1},\alpha'_m}$, with the resulting orthogonality centre now on site m.

3.4 Limited Functional Space Approach

One simple method for solving the time-dependent Schrödinger equation is to obtain the full eigenstate spectrum of the associated Hamiltonian. While several methods exist for calculating the ground state of the Frenkel-Holstein Hamiltonian, such as the density matrix renormalisation group (DMRG) technique [61, 95], few methods are able to calculate large numbers of excited eigenstates.

The excited eigenstates of the Frenkel-Holstein Hamiltonian exist within several vibronic manifolds, involving coupled electronic and vibrational excitations. While in general these excited eigenstates can have arbitrarily large exciton-phonon separations, the low energy states of each manifold are known to exhibit exciton-polaron character and are characterised by having solely short ranged exciton-phonon correlations, as discussed in Section 2.5. As we will show in this thesis, it is these excited states that are important in describing the steady state associated with the exciton relaxation dynamics within polymer systems. One way to target such eigenstates is to use a truncated Hilbert space, in which only states with short exciton-phonon separations are included. This is the premise of the limited functional space (LFS) approach [108].

Within the LFS approach, the starting Hilbert space is the Frenkel Hamiltonian basis, $|m\rangle$, which corresponds to the exciton residing on the various sites, m, of the model, with

the harmonic oscillators in their ground state. Therefore this Hilbert space contains L states, where L is the number of sites in the model. The Hilbert space associated with the LFS approach is then generated in a series of steps, where the collection of states associated with the Hilbert space after n_{step} steps is given by [109]:

$$\sum_{q=0}^{n_{\text{step}}} \left(\hat{H}_{\text{coup}} + \hat{H}_{\text{kin}} \right)^q |m\rangle \tag{3.60}$$

The state generation shown in Eq. (3.60) is then repeated for every possible starting Frenkel Hamiltonian basis state $|m\rangle$. This procedure corresponds to applying two different terms in the Frenkel-Holstein Hamiltonian, $\hat{H}_{\text{kin}}$ and $\hat{H}_{\text{coup}}$, to all generated states in the previous step of the LFS approach and removing any duplicate terms. The first term, $\hat{H}_{\text{coup}}$ is the exciton-phonon coupling part of the Hamiltonian, given by:

$$\hat{H}_{\text{coup}} = -\frac{A\hbar\omega}{\sqrt{2}} \sum_m \hat{a}_m^\dagger \hat{a}_m \left(\hat{b}_m^\dagger + \hat{b}_m \right) \tag{3.61}$$

and physically gives rise to new states in which a phonon has been added to the site in which the exciton resides. The second term, $\hat{H}_{\text{kin}}$, corresponds to the exciton hopping part of the Hamiltonian, given by:

$$\hat{H}_{\text{kin}} = \sum_m J_m \left(\hat{a}_{m+1}^\dagger \hat{a}_m + \hat{a}_m^\dagger \hat{a}_{m+1} \right) \tag{3.62}$$

and physically gives rise to new states in which the exciton-phonon separation is increased by one. Therefore, the maximum possible exciton-phonon separation for a state generated in the LFS approach after n_{step} steps is given by $n_{\text{step}} - 1$.

Pictorially, this process is illustrated in Fig. 3.5, for the generation of states where the

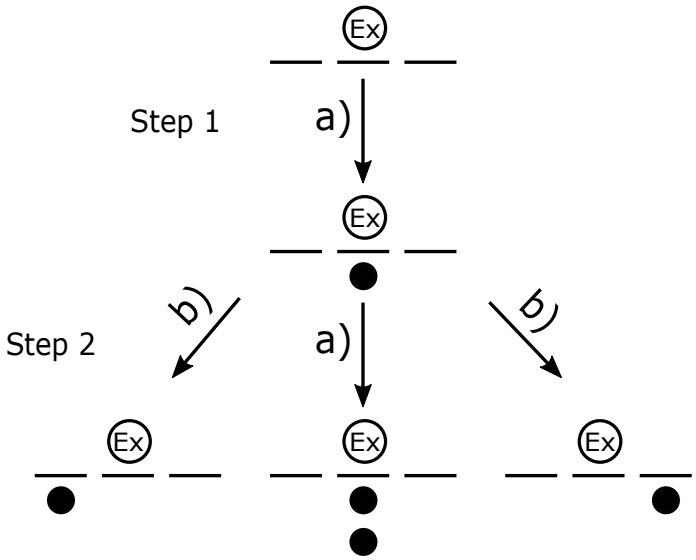


Figure 3.5: A schematic diagram illustrating how Hilbert space states for the Frenkel-Holstein Hamiltonian are generated within the LFS approach. The 'Ex' illustrates the site on which the exciton is located, while the solid circles represents a phonon present on the corresponding site. These states are generated in successive steps, where at each step either a phonon can be created on the exciton site, a), or all phonons can 'hop' left or right to a neighbouring site, b).

exciton resides on the middle site. In this diagram, process a) corresponds to applying the exciton-phonon coupling part of the Hamiltonian, while process b) has an analogous effect to applying the exciton hopping part of the Hamiltonian, where the exciton-phonon separation increases by one. Once the Hilbert space is generated from the required number of steps in the LFS approach, the associated eigenstates are obtained by diagonalising the Hamiltonian in this basis.

Table 3.1 shows the growth in the Hilbert space size as a function of the number of steps in the LFS generation procedure for a 99 moiety/site Frenkel-Holstein model. While the Hilbert space size grows exponentially with the number of steps in the procedure, it still remains manageable for a reasonably large number of steps. Therefore, as long as the excited electronic eigenstates converge to their "exact" form in a reasonable number of LFS generation steps, the technique will be effective.

$\mathbf{n_{step}}$	**Hilbert Space Size**
0	99
1	198
2	493
3	1178
4	2639
5	5741
6	12301
7	26030

Table 3.1: The growth of the Hilbert Space size as a function of the number of steps in the LFS generation procedure for a 99 moiety/site Frenkel-Holstein model.

The convergence of the ground state energy to its "exact" value as a function of the number of steps in the LFS generation routine, n_{step} is given in Fig. 3.6, for a 99 site Frenkel-Holstein Hamiltonian. The "exact" ground state energy is obtained using the density matrix renormalisation group (DMRG) technique. For large values of the phonon energy, $\hbar\omega$, the energy obtained from the LFS approach rapidly converges to the "exact" value with only a few generation steps [110]. As the phonon energy decreases, the LFS approach becomes less effective and more generation steps are required to converge. This is a result of the exciton-phonon correlation length associated with the exciton-polaron increasing as $\hbar\omega$ decreases, as discussed in Section 2.5. Overall, the LFS approach has been effective in obtaining time-dependent and static properties associated with the Frenkel-Holstein model in previous work [24, 109, 111–113].

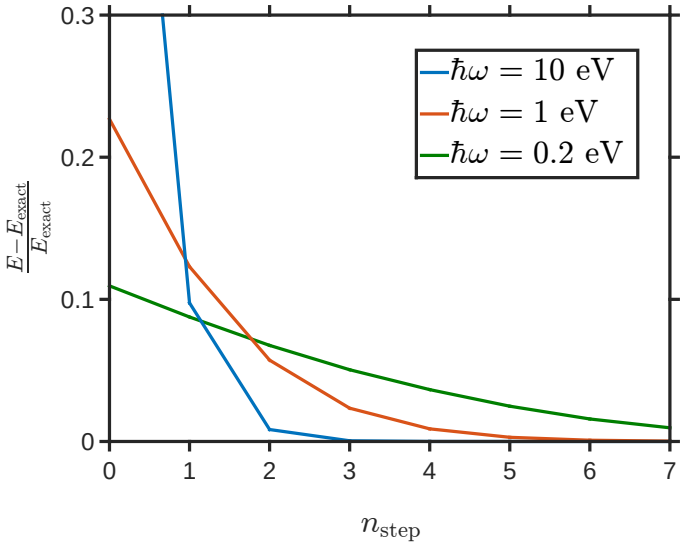


Figure 3.6: The relative error in the ground state energy of the Frenkel-Holstein Hamiltonian associated with using the incomplete Hilbert space generated from the LFS approach involving n_{step} steps for a model containing 99 sites/moieties. The "exact" ground state energy is obtained using the density matrix renormalisation group (DMRG) technique. This relative error in the ground state energy is given for different values for the phonon energy, $\hbar\omega$.

4

Exciton Dynamics in Poly(p-phenylenevinylene) - a TEBD approach

In Chapter 2, the ingredients for describing the exciton relaxation dynamics within polymer systems were introduced. Namely it was postulated that the system, which must contain the necessary exciton and nuclear degrees of freedom, could be adequately described using the Frenkel-Holstein model, while the associated time evolution could be adequately described using a Lindblad master equation. It is however *a priori* unclear whether such a coarse-grained approach will be successful in producing physically sensible dynamics, along with reproducing the experimental time scales introduced in Section 1.1. To ascertain whether this is the case, numerical solutions to the underlying equations of motion will be obtained in this chapter.

To theoretically obtain the exciton relaxation dynamics within conjugated polymer systems, a good description of the starting quantum state is needed, from which the dynamics then proceed. In an experiment, the initial exciton state is formed by photoexcitation from the electronic ground state. On application of this pulse, the nuclear degrees of freedom remain static (i.e., the harmonic oscillators remain in their ground state), while the exciton is created as a linear combination of the eigenstates of the Frenkel Hamiltonian, which were introduced in Section 2.4. The probability that an eigenstate of the Frenkel Hamiltonian with energy E contributes to this initial exciton state is given by the spectral

function:

$$I(E) = \left\langle \sum_{\alpha} f_k \delta(E - \epsilon_k) \right\rangle_{\text{Disorder}} \tag{4.1}$$

where ϵ_k is the energy eigenvalue associated with eigenstate $|\psi_k\rangle$ of the Frenkel Hamiltonian. In addition, f_k is the associated oscillator strength for this eigenstate, given by:

$$f_k = \left(\frac{2m_e\epsilon_k}{3e^2\hbar^2}\right) \sum_{s=x,y,z} |\langle\psi_k|\hat{\mu}_s|0\rangle|^2 \tag{4.2}$$

where $|0\rangle$ corresponds to the electronic ground state of the system. The Frenkel Hamiltonian contains disordered parameters, the values of which are generated from polymer conformations obtained using the process described in Section 2.3. On calculating the spectral function using Eq. (4.1), we average our result over the various instances of the disorder in the Frenkel Hamiltonian, as well as over all possible conformations of the polymer chain. For a particular conformation, the transition dipole moment operator, $\hat{\boldsymbol{\mu}}$, takes the form:

$$\hat{\boldsymbol{\mu}} = \mu_0 \sum_m \boldsymbol{s}_m \left(\hat{a}_m^\dagger + \hat{a}_m\right) \tag{4.3}$$

where μ_0 is the magnitude of the transition dipole moment for a Frenkel exciton localised on a single moiety of the polymer and $\hat{a}_m^\dagger$ ($\hat{a}_m$) is the exciton creation (destruction) operator for site/moiety m. Additionally, $\boldsymbol{s}_m$ is the dipole unit vector that points along the polymer axis at moiety m, which is illustrated in Fig. 2.4.

Figure 4.1 shows the calculated spectral function for PPV, using the parameter values given in Tables 2.1 and 2.2. In this work, we chose to perform our relaxation dynamics for initial Frenkel exciton energies of 2.68 eV and 2.88 eV, shown by the dotted lines in Fig. 4.1. Both of these Frenkel exciton energies have appreciable formation probabilities and also allow us to investigate the differing relaxation dynamics for different Frenkel

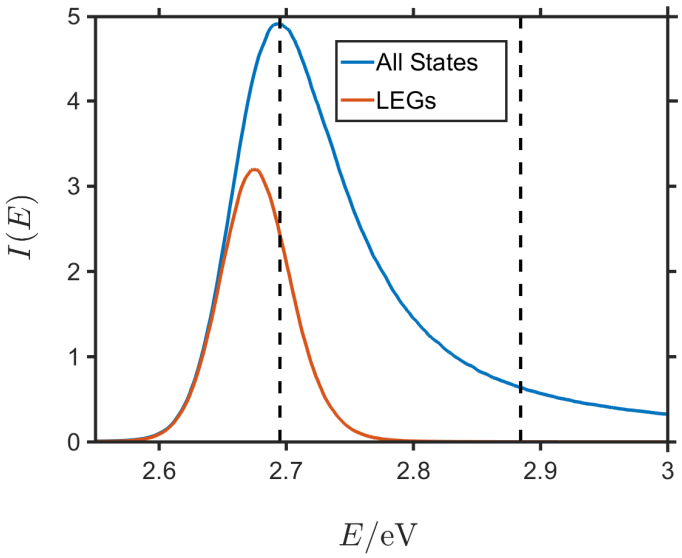


Figure 4.1: The theoretically obtained spectral function, $I(E)$, for PPV polymers, that corresponds to the probability that Frenkel exciton states with energy E are produced by a broadband photoexcitation pulse. The low energy part of the spectrum is dominated by the LEGSs, whose spatial extent define the size of the polymers absorbing chromophores. The dotted lines at 2.68 eV and 2.88 eV illustrate the initial Frenkel exciton energies from which the exciton relaxation dynamics are simulated.

eigenstates, such as LEGSs, low energy QEESs and high energy QEESs.

Within the theoretical framework outlined in Chapter 2, the exciton relaxation dynamics, proceeding from an initial quantum state generated as above, can be modelled by solving the Linblad master equation introduced in Section 2.6. Computationally, this can be achieved by using the quantum jump trajectory technique, introduced in Section 3.1, in tandem with a method to solve the time-dependent Schrödinger equation, examples of which are given in Chapter 3. How do we know if the dynamics obtained from such a procedure are correct? Experimentally, fluorescence is known to occur from the emissive chromophores of the polymer, which correspond to the VRSs within the polymer model considered in this thesis (i.e., the low energy eigenstates of the Frenkel-Holstein model, introduced in Section 2.5). For the theoretically obtained exciton relaxation dynamics to be physically sensible, the time evolution must cause the system to relax into a single

VRS of the polymer chain. To test whether this is the case, we preform the dynamics using two different time-dependent Schrödinger equation solvers.

4.1 Ehrenfest Dynamics

We first consider the dynamics within the Ehrenfest approximation, introduced previously in Section 3.2. Within this method, the nuclei are treated classically, such that the time evolution of each degree of freedom is described by a single classical displacement and momentum. In other words, the nuclear degrees of freedom are described by coherent states (introduced in Section 2.2), whose average displacement and momentum are evolved using Newton's equations of motion. As coherent states are eigenstates of the harmonic oscillator destruction operator, quantum jumps within the quantum jump trajectory technique have no effect on the dynamics and the time evolution is solely described by the effective Hamiltonian. This corresponds to evolving the electronic degrees of freedom under the standard electronic Hamiltonian, while the time dependence of the classical nuclear coordinates are given as follows:

$$\begin{aligned} \frac{d\langle \hat{Q}_m \rangle}{d\tilde{t}} &= \langle \hat{P}_m \rangle \\ \frac{d\langle \hat{P}_m \rangle}{d\tilde{t}} &= A\langle \hat{a}_m^\dagger \hat{a}_m \rangle - \langle \hat{Q}_m \rangle - \tilde{\gamma}\langle \hat{P}_m \rangle \end{aligned} \tag{4.4}$$

This expression can also be obtained directly from the Lindblad master equation, as in Eq. (2.59).

Consider an initial QEES with $E = 2.88$ eV and an exciton density given in Fig. 4.2. Under Ehrenfest dynamics, this QEES evolves such that the exciton density at 100 fs is given by the solid blue curve in Fig. 4.3. In this same figure, the dashed curves correspond to the three VRSs for this particular polymer chain conformation. Rather than the system

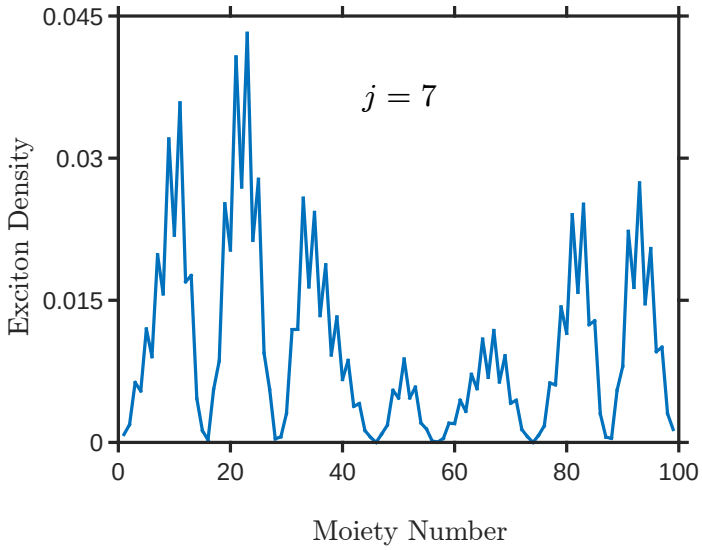


Figure 4.2: The associated exciton density of a QEES, with quantum number $j = 7$, for one particular conformation of a PPV polymer chain made up of 99 moieties.

relaxing onto a single emissive chromophore, as physically expected, the exciton density 'bifuricates' under Ehrenfest dynamics and becomes a superposition of multiple VRSs. Additionally, while the peaks in the exciton density at $t = 100$ fs are broadly located in the same positions as the VRSs, their shape is substantially different. Such a calculation has been performed in previous work, with similar findings [15].

Ultimately Ehrenfest dynamics fails in this case, because it cannot correctly describe the branching of a nuclear wavepacket on passing through a conical intersection. Such branching processes are illustrated in Section 2.1 for a two-level conical intersection model and are important in describing excited electronic state dynamics. It is unclear, however, whether the unphysical result given in Fig. 4.3 is solely due to the failure of Ehrenfest dynamics to correctly describe the coupled exciton-nuclear dynamics, or whether the model is defective as well. To ascertain whether the coarse-grained model is valid, the exciton dynamics are now calculated by treating the nuclear degrees of freedom quantum mechanically.

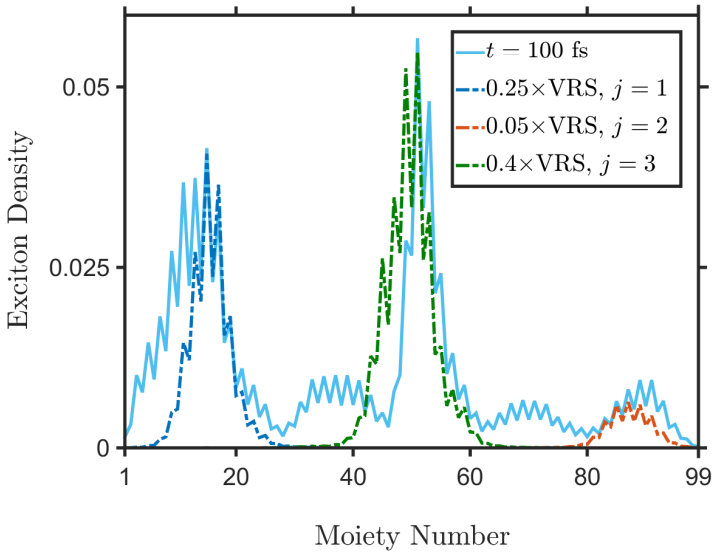


Figure 4.3: The exciton density at $t = 100$ fs, given by the solid blue curve, for an initial QEES given in Fig. 4.2. The exciton density was evolved using Ehrenfest dynamics. Also present are the scaled exciton densities for the three VRSs of the polymer chain, given by the dashed curves.

4.2 Time Evolving Block Decimation

The time evolving block decimation technique (TEBD) was introduced earlier in Section 3.3 and is ideally suited to solving the time-dependent Schrödinger equation for one-dimensional systems. To apply this technique, the starting quantum state must first be written in matrix product state form. Consider the site basis given by:

$$(|0_m\rangle + |1_m\rangle) \otimes \sum_{n_m=0}^{n_{\max}} |n_m\rangle$$

where $|1_m\rangle$ and $|0_m\rangle$ corresponds to site m being occupied or unoccupied by a Frenkel exciton, respectively and $\sum_{n_m=0}^{n_{\max}} |n_m\rangle$ corresponds to a truncated harmonic oscillator eigenstate basis, containing the lowest $n_{\max} + 1$ eigenstates. Within this site basis, a Frenkel

eigenstate with quantum number k can be written as:

$$|\psi_k\rangle = \sum_{m=1}^{L} \psi_{k,m} \hat{a}_m^\dagger |0\rangle \tag{4.5}$$

where $\hat{a}_m^\dagger$ is the Frenkel exciton creation operator, which creates a Frenkel exciton on site m of a L site chain. Additionally, $\psi_{k,m}$ is the probability amplitude for finding an exciton on site m for a Frenkel eigenstate with quantum number k and $|0\rangle$ is the vacuum, corresponding to the state of the system with no Frenkel exciton and all harmonic oscillators in their ground state. The vacuum, $|0\rangle$, is a product state and can easily be written in matrix product state form, while the operator $\sum_{m=1}^{L} \psi_{k,m} \hat{a}_m^\dagger$ is a sum of on-site terms and can be constructed as a matrix product operator (MPO), using the formalism in Section 3.3.6. A Frenkel eigenstate can thus be constructed as a matrix product state with an internal index dimension of $\chi = 2$ (the same internal index dimension as the MPO used to form it). As the dynamics proceed, this internal index dimension must increase to accurately describe the time evolving state, with the rate at which the internal index dimension grows determining the time, t, for which the dynamics can feasibly be obtained. In practice, we have found that $t \simeq 100$ fs is feasible for polymer chains made up of 99 sites/moieties.

To use the TEBD technique for the Frenkel-Holstein model, sensible values must be obtained for the dimensionless time step, $\delta\tilde{t}$, the maximum internal index dimension, χ, the ratio of the smallest retained singular value in each SVD step compared to the largest value, S_{ratio} and the maximum number of phonons used in the truncated harmonic oscillator eigenstate basis, n_{max}. In addition, the number of trajectories needed to generate accurate observables within the quantum jump trajectory technique is also required. For the results obtained in this thesis, the parameter values used are given in Table 4.1,

while Appendix B gives the necessary justification for why these values were chosen. The code used to perform the TEBD dynamics for this system was written within the Tensor Network Theory library [114].

Parameter	**Value**	**Parameter**	**Value**
$\delta\tilde{t}$	$5\,\mathrm{e}^{-4}$	χ	150
S_{ratio}	$2\,\mathrm{e}^{-5}$	n_{max}	2
n_{traj}	160		

Table 4.1: Parameters used in the time evolving block decimation technique (TEBD).

As discussed previously, for the model dynamics obtained using TEBD to be correct, the total energy of the system must decrease, approaching the energies of the VRSs. We indeed find that the system energy does decrease in our model dynamics, as shown by the time evolution of the total energy of the system for two different initial Frenkel exciton energies given in Fig. 4.4. This confirms that the form of the external dissipation in our model, described by the damping terms in the Lindblad master equation, is having the desired effect. Also shown in this figure are the energies associated with the VRSs, for various instances of the disorder, given by the dotted curves. The fact that the total system energy at $t = 60$ fs is greater than the energy of these VRSs for both initial Frenkel exciton energies, as well as dE/dt being non-zero at this time, suggests that the dynamics are far from equilibrium. This is not surprising, since the value of the exponential dissipation time scale, $\gamma^{-1} \sim 100$ fs, means that the system will only reach equilibrium at times much longer than computationally practical simulations of $\sim$100 fs.

We observe a separation of time scales within our computed dynamics. This is illustrated in Fig. 4.5, which shows the time-dependent phonon energy for two different initial Frenkel exciton energies, with and without external dissipation. For very short times, the evolution of the system observables depend on the Frenkel-Holstein parameters and are

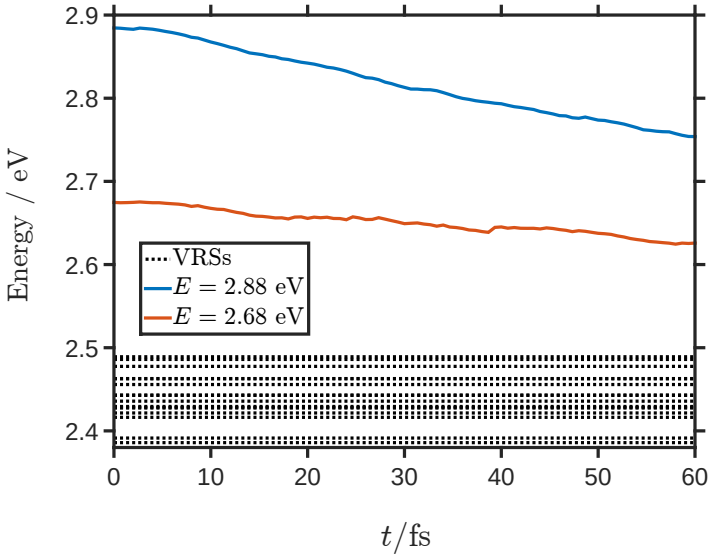


Figure 4.4: The time dependence of the total system energy. The blue curve corresponds to an initial Frenkel exciton energy of 2.88 eV, while the orange curve corresponds to an initial Frenkel exciton energy of 2.68 eV. The black dotted lines show the corresponding system energy for the VRSs of the polymer chain for different instances of the disorder.

largely independent of the external dissipation, $\tilde{\gamma}$. From Fig. 4.5, we see that the phonon energy initially increases during the dynamics, suggesting that this ultra-fast time scale is characterised by energy transfer from the exciton to the internal nuclear degrees of freedom (i.e., the phonon degrees of freedom act as a heat bath for the exciton). Eventually, the energy associated with the nuclear degrees of freedom saturates, with the time evolution of the observables now dependent on the longer external dissipation time scale. Figure 4.5 shows that for $\tilde{\gamma} \neq 0$, the phonon energy decreases at long times, suggesting that the long time scale dynamics are characterised by dissipation of the phonon energy to the environment (i.e., the environment acts as a heat bath for the internal nuclear degrees of freedom).

Even though the system is far from equilibrium for the times considered in our relaxation dynamics simulation, we should expect the time evolution of observables to still exhibit features associated with the steady states (i.e., the state of the system as $\tilde{t} \to \infty$).

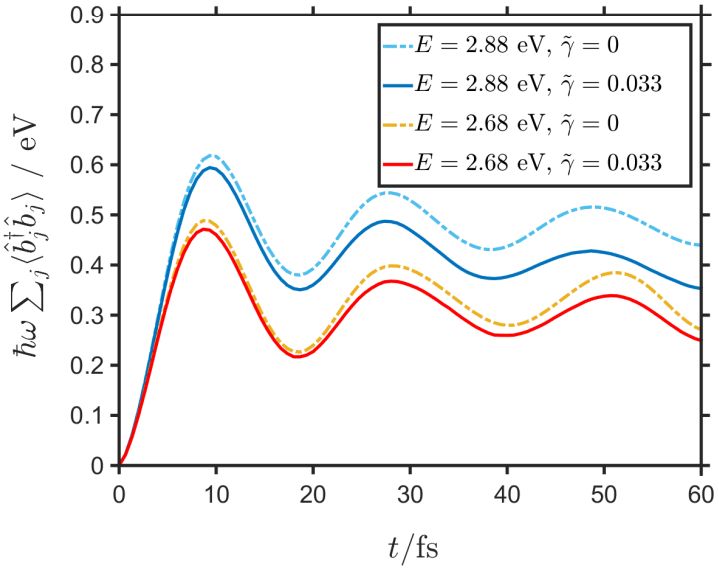


Figure 4.5: The time dependence of the phonon energy. The blue curves correspond to an initial Frenkel exciton energy of 2.88 eV, while the red curves correspond to an initial Frenkel exciton energy of 2.68 eV. In addition, the dashed curves correspond to the relaxation dynamics with no energy dissipation to the environment, while the solid curves correspond to the dynamics with $\tilde{\gamma} = 0.033$.

Indeed, if the system does relax to the low energy VRSs as physically expected, processes such as exciton-polaron formation, exciton decoherence and exciton density localisation should be present in the short time dynamics. We now consider each of these processes.

4.2.1 Exciton-Polaron Formation

In systems with strong exciton-phonon interactions, the low energy excitations of the system are described by exciton-polarons, which are quasiparticles consisting of an exciton 'dressed' or 'self-trapped' by local displacements of the nuclei [67]. The effective size of the exciton-polaron can be described by the exciton-phonon correlation function [62]:

$$C_n^{\text{ex-ph}} = \frac{1}{A} \sum_m \langle \hat{a}_m^\dagger \hat{a}_m \hat{Q}_{m+n} \rangle \tag{4.6}$$

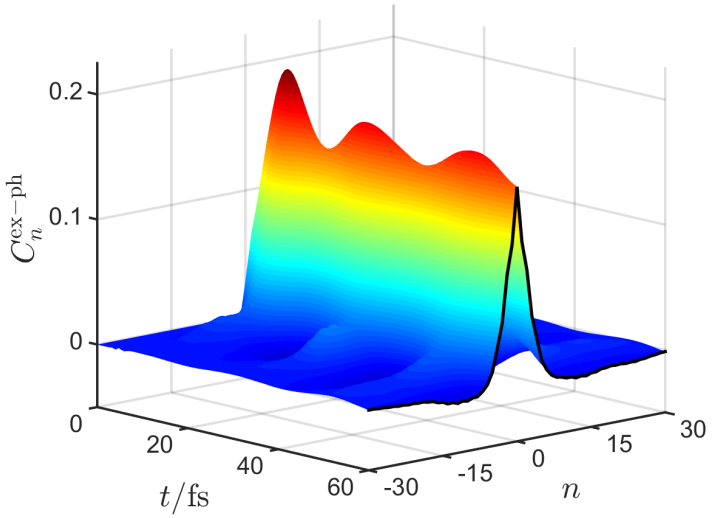


Figure 4.6: The time dependence of the exciton-phonon correlation function, $C_n^{\text{ex-ph}}$, for an initial high energy QEES given in Fig. 4.2.

where the factor $1/A$ normalises the function for eigenstates of the Frenkel-Holstein Hamiltonian (i.e., $\sum_n C_n^{\text{ex-ph}} = 1$) [63]. Physically, this correlation function corresponds to the average nuclear displacement n sites away from the exciton. As discussed in Section 2.5, it is known that for the VRSs of the Frenkel-Holstein model, the exciton-phonon correlation function has an exponential form, with a correlation length that is a function of the parameters $\hbar\omega$, A and $\langle J \rangle$ [60]. If the system does evolve to the VRSs, then we would expect the exciton-phonon correlation function to acquire this exponential behaviour during the exciton relaxation dynamics.

Figure 4.6 shows the time evolution of the exciton-phonon correlation function for an initial high energy QEES given in Fig. 4.2. This correlation function acquires an exponential form during the dynamics, confirming that exciton-polaron formation is occurring within our model. Exciton-polaron formation occurs on an ultra-fast time scale (∼10 fs), with the dynamics being largely independent of the external dissipation. Indeed, we find that the time scale associated with exciton-polaron formation solely depends on the pa-

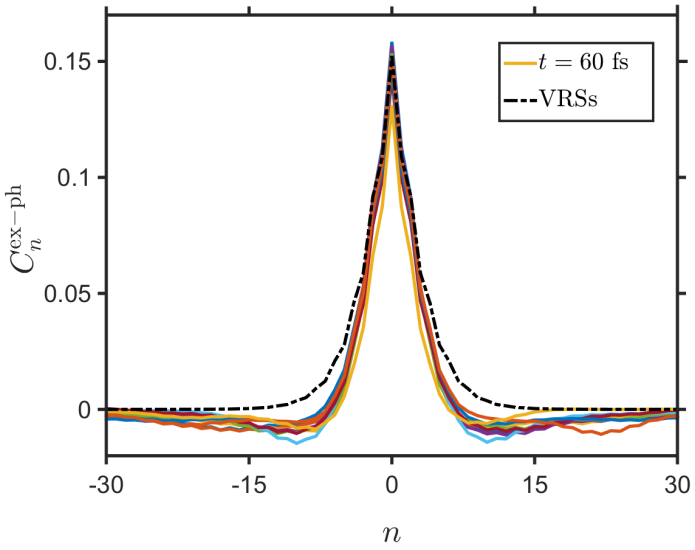


Figure 4.7: The exciton-phonon correlation function, $C_n^{\text{ex-ph}}$, at $t = 60$ fs for two initial photoexcitation energies (2.68 eV and 2.88 eV) as well as several instances of the disorder in the Frenkel-Holstein Hamiltonian (given by the solid curves). Also shown is the exciton-phonon correlation function for the VRSs, given by the dashed curve and averaged over the same instances of the disorder.

rameter $\hbar\omega$, with the local exciton-phonon correlations present within half a vibrational time period. In addition, persisting oscillations occur in the exciton-phonon correlation function with a time period (∼20 fs) that matches the vibrational time period of the harmonic oscillators in the model. These oscillations thus arise from the time evolution of the nuclear displacements $\hat{Q}_m$, which physically correspond to the C-C bond oscillations.

We now consider whether the correlation length associated with the dynamical exciton-phonon correlation function given in Fig. 4.6 is the same as for the VRSs. The solid curves in Fig. 4.7, which correspond to the exciton-phonon correlation functions at $t = 60$ fs for two initial Frenkel exciton energies (2.68 eV and 2.88 eV), as well as several instances of the disorder, all coincide. This is to be expected, as the parameters $\hbar\omega$, A and $\langle J \rangle$ have the same values for all these curves, giving rise to an identical exciton-polaron formation time scale and exciton-phonon correlation length. Also shown in Fig. 4.7 is

the exciton-phonon correlation function associated with the VRSs, given by the dashed curve and averaged over the same instances of the disorder. The form of the dynamical exciton-phonon correlation functions at $t = 60$ fs shows good agreement with the same function for the VRSs, which is consistent with the system evolving to these states during the dynamics. However the agreement is not perfect, with deviations arising due to the persistent oscillations in the dynamical correlation function, which are symptomatic of the time evolution having not yet reached the steady state.

4.2.2 Exciton Decoherence

An exciton confined to a one-dimensional polymer chain in general can have long range quantum coherences between the moieties, which physically give rise to interference effects in the calculated observables. While the range of these coherences are often limited by the presence of disorder in the system, for QEESs the exciton coherences can still persist over a distance of several chromophores. If the exciton localises onto a single chromophore during the relaxation dynamics, then these long range coherences will decay.

One way to quantify the magnitude of the exciton coherences is from the off-diagonal elements of the exciton reduced density matrix, $\hat{\rho}_{\text{ex}}$:

$$\hat{\rho}_{\text{ex}} = \sum_{v} \langle v|\hat{\rho}|v\rangle \tag{4.7}$$

which is obtained by taking the trace of the system density matrix over the nuclear degrees of freedom (characterised by the quantum number v). The following exciton coherence correlation function can then be defined, which gives the average magnitude of the exciton

coherences between moieties/sites a distance n apart [115, 116]:

$$C_n^{\mathrm{coh}} = \sum_m |\langle m|\hat{\rho}_{\mathrm{ex}}|m+n\rangle| \tag{4.8}$$

where $|m\rangle$ is the ket corresponding to the exciton on site m.

Figure 4.8 shows the time dependence of the exciton coherence correlation function for an initial high energy QEES given in Fig. 4.2. The correlation function rapidly localises, showing that within our model, decoherence of the exciton occurs on an ultra-fast time scale. This time scale is more evident from the time dependence of the exciton coherence number, N_{coh}:

$$N_{\mathrm{coh}} = \sum_n C_n^{\mathrm{coh}} \tag{4.9}$$

which corresponds to the average number of moieties over which exciton coherences persist and is given in the inset of Fig. 4.8. Indeed, we find that the coherence number reaches its equilibrium value within ∼10 fs. As for exciton-polaron formation, the short time scale associated with this decoherence leads to the associated dynamics being largely independent of the external dissipation and depending solely on the Frenkel-Holstein parameters.

The exciton decoherence mechanism present within our model can be elucidated by considering the following state representation for the Frenkel-Holstein model:

$$|\psi\rangle = \sum_m \psi_m |m\rangle |V_m\rangle \tag{4.10}$$

Within this representation, ψ_m corresponds to the probability amplitude for the Frenkel exciton residing on site/moiety m, given by $|m\rangle$, while the ket $|V_m\rangle$ corresponds to the state of the L harmonic oscillators when the exciton is on this site. Using this state

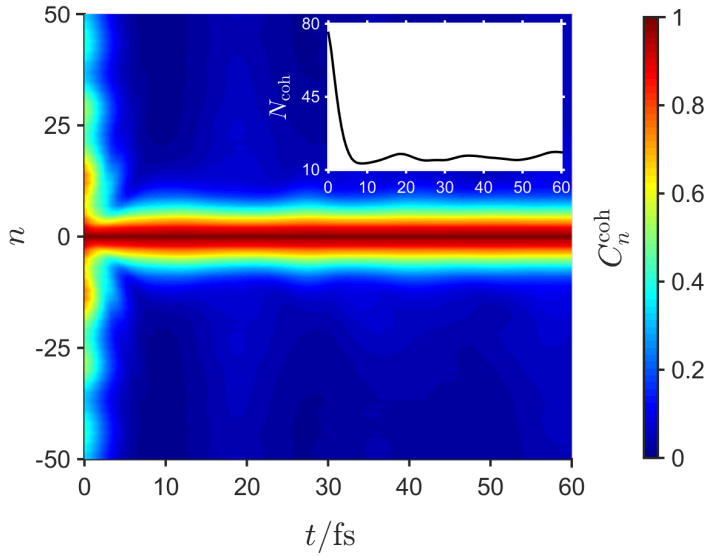


Figure 4.8: The time dependence of the exciton coherence correlation function, C_n^{coh}, for an initial high energy QEES given in Fig. 4.2. In addition, the time dependence of the associated coherence number, N_{coh}, is given in the inset figure.

representation, the exciton coherence correlation function takes the form:

$$C_n^{\mathrm{coh}} = \sum_m \left| \psi_m \psi_{m+n}^* \langle V_{m+n} | V_m \rangle \right| \tag{4.11}$$

This expression contains two terms. The first term, $\psi_m \psi_{m+n}^*$, corresponds to the exciton wavefunction overlap between the two sites/moieties. As shown in Sec. 4.2.3, this term remains essentially stationary over the time scale of exciton decoherence. The second term, $\langle V_{m+n} | V_m \rangle$, corresponds to the overlap of the vibrational states associated with the exciton being on sites/moieties $m+n$ and m. In Sec. 4.2.1, we saw that during the exciton relaxation dynamics, exciton-polaron formation occurs on an ultra-fast time scale, leading to the nuclear displacements of the polymer becoming locally correlated to the exciton. This means that during the dynamics, the vibrational state $|V_m\rangle$ will only have nuclear displacements spatially close to moiety/site m (where the exciton resides), thus causing the vibrational overlap $\langle V_{m+n} | V_m \rangle$ to decrease with increasing site separation n.

It is this local nature of the vibrational overlap that accounts for the local nature of the exciton coherence correlation function in Fig. 4.8. Exciton-polaron formation is therefore the mechanism by which the exciton decoheres, which is consistent with decoherence mechanisms found in other electron-nuclear coupled systems [19–21].

Knowledge of the exciton decoherence mechanism now gives insight into the dependence of the associated time scale on the Frenkel-Holstein parameters. Based on this mechanism, we would expect the exciton decoherence time scale to be identical to that for exciton-polaron formation, depending solely on $\hbar\omega$ and with decoherence occurring within half a vibrational time period. While this is consistent with our results, we find that the exciton decoherence time scale additionally depends on the exciton-phonon coupling strength, A, with the time scale decreasing with increasing A. This arises, because increasing A leads to an increase in the nuclear displacements associated with the exciton-polaron, which results in a more rapid decay of the vibrational overlaps that lead to decoherence.

4.2.3 Exciton Density Localisation

In Sec. 4.2.2, we saw that rapid exciton decoherence occurs during the relaxation dynamics, driven by the decay in the overlap of the vibrational states associated with exciton-polaron formation. As exciton decoherence arises from the vibrational configuration of the system, the exciton density can in principle be delocalised along the polymer chain, even if the exciton coherences between different sites/moieties are short ranged. Therefore, if the system does relax to the low energy VRSs, the exciton density must also localise during the time evolution.

In Fig. 4.9, the solid blue curve corresponds to the exciton density at time $t = 100$ fs for an initial high energy QEES given in Fig. 4.2. Also shown are the scaled exciton densities for the three VRSs of the polymer chain, given by the dashed curves. Three of the peaks

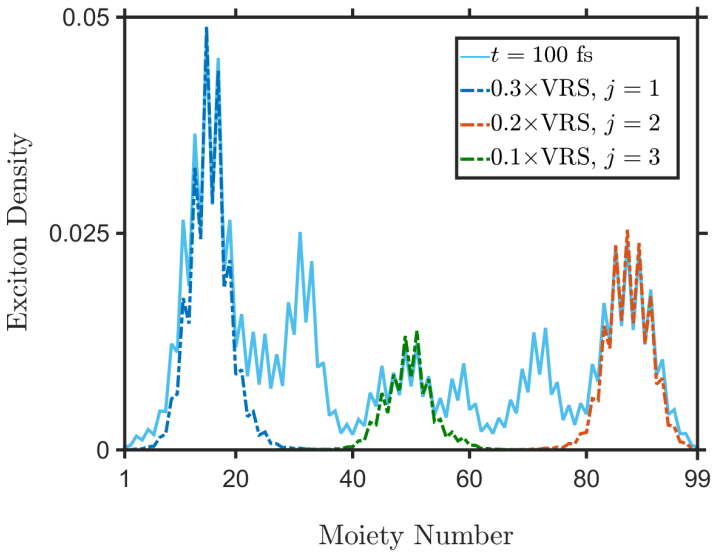


Figure 4.9: The exciton density at $t = 100$ fs, given by the solid blue curve, for an initial QEES given in Fig. 4.2. Also present are the scaled exciton densities for the three VRSs of the polymer chain, given by the dashed curves.

in the exciton density at $t = 100$ fs match those corresponding to the VRSs, suggesting that the system is relaxing into these low energy states during the time evolution. The presence of additional peaks in the time evolved exciton density are probably a result of the system having not reached the steady state at $t = 100$ fs, but could also signify that the steady state solutions of our Lindblad master equation do not correspond to the VRSs. This potential issue is pursued in the next chapter.

While the time evolved exciton density contains peaks corresponding to the VRSs of the polymer chain, the solid blue curve in Fig. 4.9 seems to show that the exciton density remains quasi-delocalised during the dynamics. However, as the system is described by a mixed state density matrix, the associated observables physically correspond to an ensemble average over many different environment configurations (or alternatively, over many quantum trajectories). This means that it is not *a priori* obvious whether the non-local nature of the ensemble averaged exciton density is symptomatic of an actual

absence of exciton density localisation in our model or whether it is simply a consequence of ensemble averaging over exciton density that has localised onto different chromophores. To distinguish between these two possibilities requires a correlation function that measures the spatial extent of the exciton for a single environment configuration, such as [117,118]:

$$C_n^{\mathrm{loc}} = \frac{\sum_m |\langle m,0|\hat{\rho}|m+n,0\rangle|}{\sum_m |\langle m,0|\hat{\rho}|m,0\rangle|} \tag{4.12}$$

where the scaling factor is chosen so that $C_0^{\mathrm{loc}} = 1$. In this definition, the ket $|m,0\rangle$ corresponds to the exciton being on site/moiety m, while all the L harmonic oscillators are in their ground state, signified by the '0' index.

The physical interpretation of this exciton localisation correlation function can be understood by considering the state representation for the Frenkel-Holstein model, given in Eq. (4.10). Using this state representation, the correlation function takes the form:

$$C_n^{\mathrm{loc}} = \frac{\sum_m \left|\psi_m \psi_{m+n}^* \langle V_{m+n}|0\rangle \langle 0|V_m\rangle\right|}{\sum_m |\psi_m|^2 |\langle V_m|0\rangle|^2} \tag{4.13}$$

where ψ_m is the probability amplitude for the exciton being on moiety/site m, $|V_m\rangle$ corresponds to the state of the nuclear degrees of freedom when the exciton resides on site m and $|0\rangle$ corresponds to the ground state of the L harmonic oscillators in the system. To a good approximation, the quantity $\langle V_m|0\rangle$ will be independent of the exciton site index m. This is because the spatial distribution of the oscillator displacements around the exciton depend on the exciton-phonon correlation length, which will be largely independent of the exciton site index. Applying this approximation to Eq. (4.13) leads to

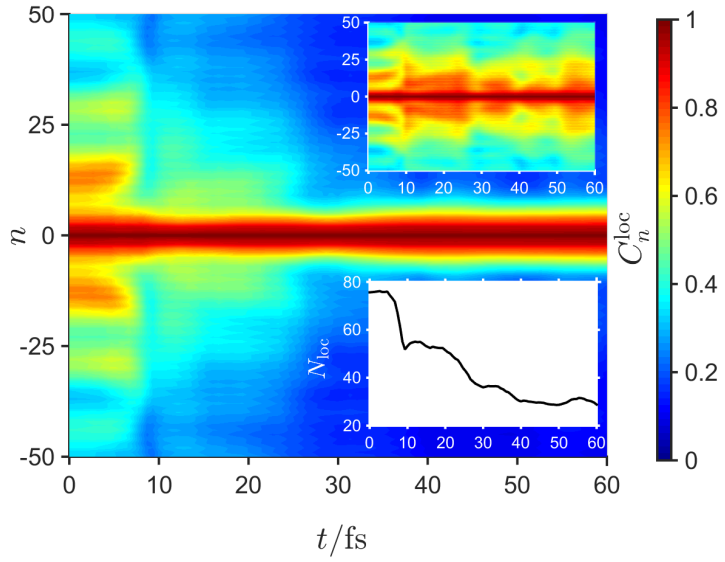


Figure 4.10: The time dependence of the exciton localisation correlation function, C_n^{loc}, for an initial high energy QEES given in Fig. 4.2. The main figure corresponds to the time evolution with $\tilde{\gamma} = 0.033$, while the upper inset figure corresponds to the time evolution without external dissipation. In addition, the time dependence of the associated exciton localisation number, N_{loc}, with $\tilde{\gamma} = 0.033$ is given in the lower inset figure.

the following simplified form for the exciton localisation correlation function:

$$C_n^{\mathrm{loc}} \approx \sum_m \left|\psi_m \psi_{m+n}^*\right| \tag{4.14}$$

This expression shows that the correlation function can be regarded as giving the average magnitude of the exciton wavefunction overlap between moieties/sites a distance n apart and therefore gives a measure of the spatial extent of the exciton on a polymer chain.

Figure 4.10 shows the time dependence of the exciton localisation correlation function for an initial high energy QEES given in Fig. 4.2. The main figure corresponds to the time evolution with the standard external dissipation parameter of $\tilde{\gamma} = 0.033$, while the upper inset corresponds to the time evolution without external dissipation to the environment. When external dissipation is present, this correlation function does localise, confirming

that exciton density localisation is present within our model of the relaxation dynamics. However, the time scale associated with this process appears substantially different from the ultra-fast exciton-polaron formation and exciton decoherence time scales studied previously. Indeed, the exciton localisation correlation function remains essentially static for initial times on the order of the ultra-fast time scale (∼10 fs) with the function only starting to localise at longer times. This time scale is more evident from the time dependence of the exciton localisation number, $N_{\rm loc}$ [118]:

$$N_{\rm loc} = \sum_n C_n^{\rm loc} \tag{4.15}$$

which corresponds to the average number of moieties over which the exciton wavefunction overlap remains non-zero and is given in the lower inset of Fig. 4.10. The exciton localisation number continues to decrease for $t > 60$ fs, illustrating the much longer time scale associated with this process. This suggests that the exciton density localisation is driven by the external dissipation to the environment. Further confirmation of this is given in the upper inset of Fig. 4.10, which shows that without external dissipation, the correlation function remains delocalised during the time evolution.

The mechanism by which external dissipation drives this exciton density localisation can be understood by investigating the time evolution of individual trajectories within the quantum jump trajectory method. Figure 4.11 shows the time dependence of the exciton density for a typical trajectory associated with this technique, where the system is initially in a high energy QEES given in Fig. 4.2. For $t < 20$ fs, the dynamics correspond to time evolution under the effective Hamiltonian, $\hat{H}_{\rm eff}$, where the figure shows that during this evolution, the exciton density remains quasi-delocalised along the polymer chain. The discontinuity in the exciton density at $t \sim 20$ fs corresponds to a 'quantum jump', in

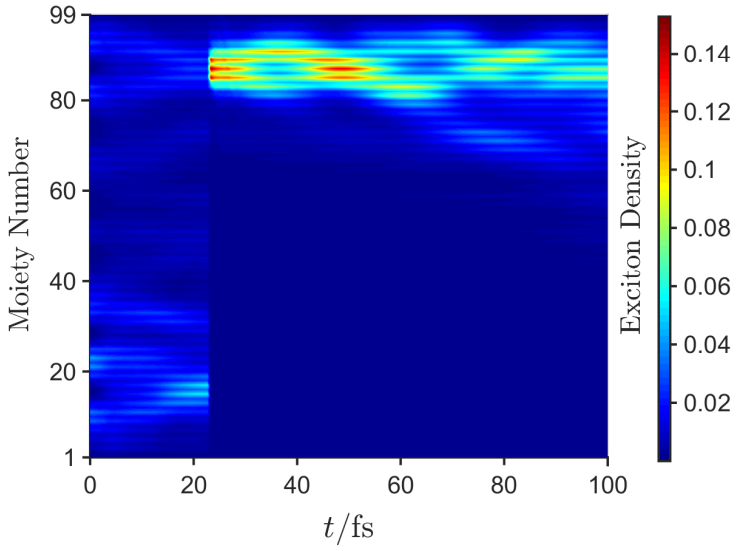


Figure 4.11: The time dependence of the exciton density for a single trajectory of the quantum jump trajectory method. The discontinuity in the density at ca. 20 fs is a 'quantum jump' caused by the stochastic application of a Lindblad jump operator. The dynamics were performed for an initial high energy QEES given in Fig. 4.2, with $\tilde{\gamma} = 0.033$.

which one of the harmonic oscillator destruction operators, $\hat{b}_m$, is randomly applied to the system. The effect of this 'quantum jump' process is to cause an immediate localisation of the exciton density, as seen in Fig. 4.11. This arises because only states of the harmonic oscillator on site m with a non-zero displacement remain after application of the operator, $\hat{b}_m$. As these nuclear displacements are locally correlated to the exciton through exciton-polaron formation, application of $\hat{b}_m$ therefore leads to a state with the exciton localised around site m. Physically this process corresponds to 'wavefunction collapse', where local environment interactions with the internal phonon degrees of freedom act as a quantum measurement. Hence, it is the position of these local environment interactions that determines the particular chromophore that the exciton density relaxes onto during the time evolution.

Overall, comparing Sections 4.2.2 and 4.2.3 , these results show that exciton decoher-

ence and exciton density localisation, which are terms that are often used interchangeably in the literature, are different physical processes that occur on different time scales.

4.2.4 LEGS Dynamics

In the preceding analysis, the main focus has been on understanding the short time exciton relaxation dynamics of initial QEESs. However, the features of the dynamics, as well as their associated time scales, are largely identical for initial LEGSs, with a few important differences. For QEESs, we saw that the system evolves to become a mixed state combination of the various VRSs on the polymer chain, as seen in the time evolved exciton density. In contrast, we find that an initial LEGS adiabatically relaxes almost entirely onto a single VRS, with the exciton density remaining on the same chromophore throughout the time evolution. This finding is in agreement with previous work on the relaxation dynamics of LEGSs and is why Ehrenfest dynamics is found to give physically sensible results for the relaxation of these states [15, 119]. Finally, as the spatial extent of LEGSs and VRSs are very similar (see Fig. 2.10) the extent of exciton decoherence and exciton density localisation during the time evolution is much less pronounced compared to that for an initial QEES, resulting in a smaller time dependence of the associated correlation functions.

4.2.5 Fluorescence Depolarisation

So far, we have outlined many features present in our model of the exciton relaxation dynamics in polymer systems, such as exciton-polaron formation, exciton decoherence and exciton density localisation. We now consider whether such features can be seen in experimental observables used to study the dynamics.

One such experimental technique is the measurement of the time-dependent decay in

the fluorescence anisotropy after photoexcitation. It is known experimentally that as the exciton relaxes, the polarisation axis associated with the fluorescence rotates from that of the incident radiation, caused by a rotation of the transition dipole moment of the polymer. This can be quantified using the fluorescence anisotropy, r [120]:

$$r = \frac{I_{\parallel} - I_{\perp}}{I_{\parallel} + 2I_{\perp}} \tag{4.16}$$

where $I_{\parallel}$ and $I_{\perp}$ are the intensities of the fluorescence radiation polarised parallel and perpendicular to the incident radiation, respectively.

For an arbitrary state of a quantum system, $|\psi\rangle$, the fluorescence intensity polarised along the x axis is related to the x component of the transition dipole operator, $\hat{\mu}_x$, by:

$$I_x \propto \sum_v |\langle\psi|\hat{\mu}_x|0, v\rangle|^2 \tag{4.17}$$

where $|0, v\rangle$ corresponds to the system in the ground electronic state, with the nuclear degrees of freedom in the state characterised by the quantum number v. In principle, the expression for I_x also has an energy dependent term. However, as long as the variance of the energy associated with the system remains small during the time evolution, this term just becomes a multiplicative constant that can be neglected in Eq. (4.17). The expression given in Eq. (4.17) can be generalised for a mixed state density matrix, $\hat{\rho}$, as follows [121]:

$$\begin{aligned} I_x &\propto \sum_v \langle 0, v|\hat{\mu}_x\hat{\rho}\hat{\mu}_x|0, v\rangle \\ &\propto \sum_{m,n} s_{m,x}s_{n,x} \langle m|\hat{\rho}_{\text{ex}}|n\rangle \end{aligned} \tag{4.18}$$

where the final equation is obtained by using the expression for the transition dipole moment given in Eq. (4.3). In this equation, $\hat{\rho}_{\mathrm{ex}}$ corresponds to the exciton reduced density matrix, defined in Eq. (4.7), while $|m\rangle$ is the ket corresponding to the exciton residing on site m. In addition, $s_{m,x}$ is the x component of the unit vector that points along the polymer axis at site m, illustrated in Fig. 2.4. Inserting the required intensity components, given in Eq. (4.18), into Eq. (4.16) allows the fluorescence anisotropy to be obtained for a specific polymer conformation. The fluorescence anisotropy can then be averaged over several different polymer conformations and initial exciton states using the following expression [120]:

$$\langle r\left(t\right)\rangle = 0.4 \times \frac{\sum_j I_j\left(t\right) r_j\left(t\right)}{\sum_j I_j\left(t\right)} \tag{4.19}$$

where $I_j\left(t\right)$ is the total fluorescence intensity and $r_j\left(t\right)$ is the fluorescence anisotropy, both associated with conformation j at time t. The factor of 0.4 is included on the assumption that the polymers are oriented uniformly in the bulk material [120].

Figure 4.12 shows the calculated time dependence of the fluorescence anisotropy for two different initial Frenkel exciton energies. The mechanism for the decay of the fluorescence anisotropy can be understood by comparing the expression for the components of the fluorescence intensity, given in Eq. (4.18), with the expression for the exciton coherence correlation function, given in Eq. (4.8). While the fluorescence intensity components cannot be directly written in terms of the exciton coherence correlation function, since both quantities depend on the elements of the exciton reduced density matrix, the time dependence of the two quantities are related. Indeed, we find numerically that the time dependence of the fluorescence intensity components are dominated by the decay of the off diagonal elements of the exciton reduced density matrix, which also give rise to the

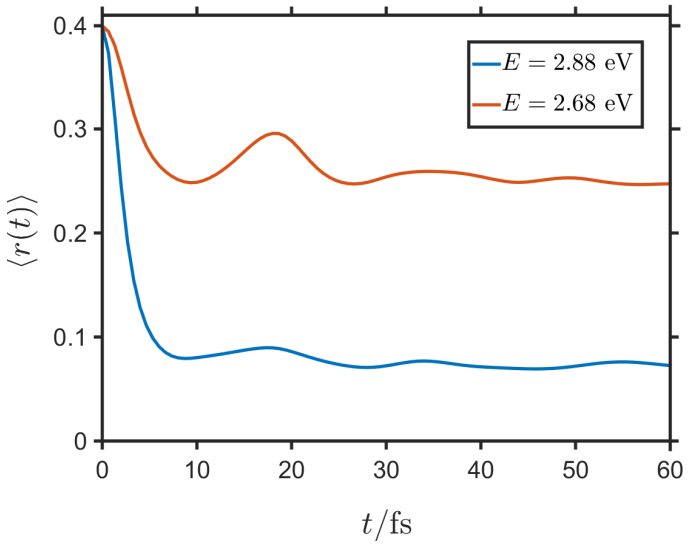


Figure 4.12: The time dependence of the fluorescence anisotropy, $\langle r\,(t) \rangle$, for two initial Frenkel exciton energies. The orange curve corresponds to an initial Frenkel exciton energy of 2.68 eV, while the blue curve corresponds to an initial Frenkel exciton energy of 2.88 eV

localisation of the exciton coherence correlation function. The decay in the fluorescence anisotropy can therefore be attributed to the decoherence of the exciton during the relaxation dynamics, induced by exciton-polaron formation. This is also consistent with the observations that the decay of the fluorescence anisotropy is independent of $\tilde{\gamma}$ and also occurs on a time scale equal to the exciton decoherence time scale from Fig. 4.8.

The difference in the magnitude of the fluorescence anisotropy decay for the two initial Frenkel exciton energies can now be explained in terms of this exciton decoherence mechanism. For the lower initial Frenkel exciton energy of 2.68 eV, Fig. 4.1 shows that a large fraction of the initial Frenkel exciton states are LEGSs. As the exciton is already localised onto a single chromophore in a LEGS, the extent of exciton decoherence during the relaxation dynamics is much reduced for an initial LEGS compared to an initial QEES. This therefore explains why the magnitude of the fluorescence anisotropy decay is smaller for the lower initial Frenkel exciton energy in Fig. 4.12, consistent with

experimental observations [3].

We now attempt to interpret experimental observations in the light of these simulations. As stated in Section 1.1, experimental studies of the exciton relaxation dynamics in PPV observe two sub picosecond time scales ($\lesssim$50 fs and $\sim$100 fs). Fluorescence depolarisation experiments on PPV observe that the initial anisotropy value is $<$0.4, suggesting that an ultra-fast relaxation process is occurring with a time scale shorter than the time resolution of the experiment. This is consistent with the anisotropy decay time scale in our model and therefore we assign this ultra-fast process to the exciton decoherence arising from coupling to the high frequency C-C bond oscillations.

We also noted, however, that our calculated fluorescence anisotropy decay is essentially independent of the dissipation time scale, γ^{-1}, and therefore our simulation cannot account for the time scale of $\sim$100 fs observed in fluorescence depolarisation experiments. As suggested in previous work [5], we predict that this further decay in the anisotropy arises from coupling of the exciton to the low frequency torsional modes in the polymer, which have an oscillation period of $\sim$ 100 fs [17, 122]. Indeed, as these torsional modes behave classically, they would be expected to form self-localised Landau polarons [59,60] (see Section 2.5.1) and therefore cause further exciton decoherence in addition to that arising from coupling to the high frequency C-C bond oscillations. However, because classical normal modes give rise to a diverging exciton-phonon correlation length, the exciton decoherence and exciton density localisation processes will occur via different mechanisms than for the high frequency modes. As most spectroscopic quantities depend on the exciton reduced density matrix, it is likely that the two time scales seen in these experiments arise from exciton decoherence through coupling of the exciton to these two different normal modes. How to incorporate these torsional modes into our model, and therefore account for both

experimental time scales, is addressed in Chapter 6.

5

Exciton Dynamics in Poly(p-phenylenevinylene) - the Steady State

In the previous chapter, we showed that exciton-polaron formation, exciton decoherence and exciton density localisation all occur during the exciton relaxation dynamics within our model, which is consistent with the system relaxing into the low energy chromophore states of the polymer chain, as physically expected. However, the relaxation dynamics can only be obtained for relatively short times of $t \sim 100$ fs within the TEBD technique and it is therefore difficult to come to any definitive conclusions about what the steady state solution of the dynamics is (i.e the state of the system when $t \to \infty$). In this chapter, the steady state solution of the exciton relaxation dynamics is obtained to identify whether the system does indeed relax into the emissive chromophore states of the polymer chain at long times.

In Section 2.6.1, it was shown that the steady state solution of a Lindblad master equation can be obtained from the Lindblad superoperator, $\hat{\hat{L}}$, using the following equation:

$$\hat{\hat{L}} \left| \vec{u}_{\mathrm{s}} \right\rangle = 0 \tag{5.1}$$

i.e., the steady state solution is an eigenstate of the Lindblad superoperator, with eigenvalue $\lambda_s = 0$. The Lindblad superoperator is a $N^2 \times N^2$ matrix, where N is the size of the Hilbert space associated with the system. Since the system of interest in this thesis has

an exponentially large Hilbert space, the Lindblad superoperator is too large to generate and hence its eigenstates cannot be determined directly. To circumvent this issue, we have developed a Lindblad perturbation theory, which is introduced in the following section.

5.1 Lindblad Perturbation Theory

Perturbation theory is a commonly used technique to solve eigenvalue problems, such as the following:

$$\hat{\hat{L}} \left|\vec{u}_\mu\right\rangle = \lambda_\mu \left|\vec{u}_\mu\right\rangle \tag{5.2}$$

in which the operator (in this case the Lindblad superoperator) is partitioned into an unperturbed part, $\hat{\hat{L}}_0$, and a perturbation, $\hat{\hat{V}}$:

$$\hat{\hat{L}} = \hat{\hat{L}}_0 + \alpha\hat{\hat{V}} \tag{5.3}$$

where α is a book-keeping parameter introduced to keep track of the order of the perturbation and is set to one at the end of the calculation. The partitioning of the superoperator in Eq. (5.3) is chosen so that $\hat{\hat{L}}_0$ has known eigenstates and eigenvalues and $\hat{\hat{V}}$ corresponds to a small correction to $\hat{\hat{L}}_0$, meaning that the exact eigenvalues and eigenstates of $\hat{\hat{L}}$ can be written as a convergent Taylor expansion in the perturbation:

$$\begin{aligned} \lambda_\mu &= \lambda_\mu^{(0)} + \alpha\lambda_\mu^{(1)} + \alpha^2\lambda_\mu^{(2)} + \cdots \\ \left|\vec{u}_\mu\right\rangle &= \left|\vec{u}_\mu^{(0)}\right\rangle + \alpha\left|\vec{u}_\mu^{(1)}\right\rangle + \alpha^2\left|\vec{u}_\mu^{(2)}\right\rangle + \cdots \end{aligned} \tag{5.4}$$

where the superscripts signify the order of the perturbation. Perturbation theory has already been successfully applied to Lindblad master equations, for any arbitrary partitioning of the Lindblad superoperator for which the eigenvalues of $\hat{\hat{L}}_0$ are non-degenerate

[123–126].

Our approach differs from this previous work by considering a particular partitioning of the Lindblad superoperator (the expression for which is given by Eq. (2.62)) such that the unperturbed part contains the terms that involve the system Hamiltonian (in this case the Frenkel-Holstein Hamiltonian, $\hat{H}_{\mathrm{FH}}$) [127]:

$$\hat{\hat{L}}_0 = \frac{1}{\hbar\omega}\left(\hat{\mathbb{1}} \otimes \hat{H}_{\mathrm{FH}} - \hat{H}_{\mathrm{FH}}^T \otimes \hat{\mathbb{1}}\right) \tag{5.5}$$

while the perturbation contains all the terms that involve the system-environment coupling [127]:

$$\hat{\hat{V}} = \tilde{\gamma}\left[\frac{1}{\hbar\omega}\left(\hat{\mathbb{1}} \otimes \hat{H}_{\Delta} - \hat{H}_{\Delta}^T \otimes \hat{\mathbb{1}}\right) - \frac{i}{2}\sum_m \left(\hat{\mathbb{1}} \otimes \hat{b}_m^\dagger \hat{b}_m + \left(\hat{b}_m^\dagger \hat{b}_m\right)^T \otimes \hat{\mathbb{1}} - 2\left(\hat{b}_m^\dagger\right)^T \otimes \hat{b}_m\right)\right] \tag{5.6}$$

where $\tilde{\gamma}$ is the dimensionless dissipation parameter, which controls the strength of the system-environment coupling and $\hat{H}_{\Delta}$ (given by Eq. (2.58)) is the Hamiltonian that describes the damping correction to the harmonic oscillator frequency induced by the external dissipation. We think that this is the most natural partitioning of the Lindblad superoperator, since the Lindblad master equation is only valid for systems in which the system-environment coupling is weak (i.e., when $\tilde{\gamma}$ is small), as discussed previously in Section 2.6. This particular partitioning of the Lindblad superoperator is also advantageous, because the unperturbed part of the superoperator, $\hat{\hat{L}}_0$, is Hermitian, ensuring that the unperturbed eigenstates form a complete orthonormal basis. This property leads to much simpler expressions for the perturbative corrections to the eigenvalues and eigenstates.

To obtain expressions for these perturbative corrections, we first insert Eqs. (5.3) and

(5.4) into the Lindblad superoperator eigenvalue equation, given by Eq. (5.2):

$$\left(\hat{\hat{L}}_0 + \alpha\hat{\hat{V}}\right)\left(|\vec{u}_\mu^{(0)}\rangle + \alpha\,|\vec{u}_\mu^{(1)}\rangle + \cdots\right) = \left(\lambda_\mu^{(0)} + \alpha\lambda_\mu^{(1)} + \cdots\right)\left(|\vec{u}_\mu^{(0)}\rangle + \alpha\,|\vec{u}_\mu^{(1)}\rangle + \cdots\right) \quad (5.7)$$

in analogous fashion to conventional perturbation theory [80]. Grouping together terms with identical powers of α then leads to the following result:

$$\left[\left(\hat{\hat{L}}_0 - \lambda_\mu^{(0)}\right)|\vec{u}_\mu^{(0)}\rangle\right] + \alpha\left[\left(\hat{\hat{L}}_0 - \lambda_\mu^{(0)}\right)|\vec{u}_\mu^{(1)}\rangle + \left(\hat{\hat{V}} - \lambda_\mu^{(1)}\right)|\vec{u}_\mu^{(0)}\rangle\right] + \cdots = 0 \quad (5.8)$$

The eigenvalue and eigenstate corrections for a particular order of perturbation can then be obtained by solving the corresponding term in Eq. (5.8).

For our system of interest, the internal exciton-phonon interactions dominate the much weaker system-environment coupling, making it sufficient to calculate the Lindblad superoperator eigenvalues to first order in the perturbation, while only considering the zeroth-order eigenstates. However, it is indeed possible to calculate the eigenstates and eigenvalues to any order in the perturbation, using the same method employed in conventional perturbation theory for the time-independent Schrödinger equation. The required perturbative terms are now derived in the following sub-sections.

5.1.1 Zeroth-Order Term

From Eq. (5.8), the zeroth-order term gives rise to the following eigenvalue equation for the zeroth-order eigenvalues and eigenstates:

$$\hat{\hat{L}}_0\,|\vec{u}_\mu^{(0)}\rangle = \lambda_\mu^{(0)}\,|\vec{u}_\mu^{(0)}\rangle \quad (5.9)$$

To solve this equation, it proves beneficial to work in the Hilbert space basis given by the eigenstates of the Frenkel-Holstein Hamiltonian, $\hat{H}_{\mathrm{FH}}$:

$$\hat{H}_{\mathrm{FH}} |\psi_j\rangle = E_j |\psi_j\rangle \tag{5.10}$$

where j corresponds to the quantum number associated with the eigenstate $|\psi_j\rangle$. The analogous Liouville space basis states are then $|\vec{\rho}_{l,\,j}\rangle$, which correspond to the matrix elements of the system density matrix in this Hilbert space basis. Using the form of the unperturbed part of the Lindblad superoperator, given by Eq. (5.5), the eigenstates of $\hat{\hat{L}}_0$ are shown to be:

$$|\vec{u}^{(0)}_{l,\,j}\rangle = |\vec{\rho}_{l,\,j}\rangle \tag{5.11}$$

while the corresponding zeroth-order eigenvalues are:

$$\lambda^{(0)}_{l,\,j} = \begin{cases} \frac{E_l - E_j}{\hbar\omega}, & \text{for} \quad l \neq j \\ 0, & \text{for} \quad l = j \end{cases} \tag{5.12}$$

where E_j is the eigenvalue of the Frenkel-Holstein Hamiltonian with quantum number j, as defined in Eq. (5.10).

Now that the zeroth-order eigenvalues and eigenstates have been determined, the first-order correction to the eigenvalues, $\lambda^{(1)}_{\mu}$, can be obtained by solving the first-order term in Eq. (5.8):

$$\left(\hat{\hat{L}}_0 - \lambda^{(0)}_{\mu}\right) |\vec{u}^{(1)}_{\mu}\rangle + \left(\hat{\hat{V}} - \lambda^{(1)}_{\mu}\right) |\vec{u}^{(0)}_{\mu}\rangle = 0 \tag{5.13}$$

There are two situations to consider. For the 'off-diagonal' zeroth-order eigenstates ($|\vec{u}^{(0)}_{l,j}\rangle$, where $l \neq j$), the zeroth-order eigenvalues (given by Eq. (5.12)) are non-degenerate, meaning that Eq. (5.13) must be solved using non-degenerate perturbation theory. In

contrast, for the 'diagonal' zeroth-order eigenstates ($|\vec{u}_{l,j}^{(0)}\rangle$, where $l = j$), the zeroth-order eigenvalues are degenerate, meaning that Eq. (5.13) must be solved using degenerate perturbation theory. We now consider each case in turn.

5.1.2 Off-Diagonal Zeroth-Order Eigenstates

For non-degenerate eigenstates, $|\vec{u}_{\mu}^{(0)}\rangle$, Eq. (5.13) can be solved by pre-multiplying by $\langle\vec{u}_{\mu}^{(0)}|$ to give:

$$\langle\vec{u}_{\mu}^{(0)}|\left(\hat{\hat{L}}_0 - \lambda_{\mu}^{(0)}\right)|\vec{u}_{\mu}^{(1)}\rangle + \langle\vec{u}_{\mu}^{(0)}|\left(\hat{\hat{V}} - \lambda_{\mu}^{(1)}\right)|\vec{u}_{\mu}^{(0)}\rangle = 0 \tag{5.14}$$

This term can be simplified as follows. Applying Eq. (5.9) shows that the first term in the above equation is zero. Additionally, the orthonormality of the zeroth-order eigenstates (i.e., $\langle\vec{u}_{\mu}^{(0)}|\vec{u}_{\nu}^{(0)}\rangle = \delta_{\mu,\nu}$) leads to the following expression for the first-order eigenvalues, valid for non-degenerate states:

$$\lambda_{\mu}^{(1)} = \langle\vec{u}_{\mu}^{(0)}|\hat{\hat{V}}|\vec{u}_{\mu}^{(0)}\rangle \tag{5.15}$$

Applying Eq. (5.15) to the off-diagonal zeroth-order eigenstates ($|\vec{u}_{l,j}^{(0)}\rangle$, where $l \neq j$) leads to the following expression for the corresponding first-order eigenvalue:

$$\lambda_{l,j}^{(1)} = \tilde{\gamma}\left[\frac{1}{\hbar\omega}\left(\langle\psi_l|\hat{H}_{\Delta}|\psi_l\rangle - \langle\psi_j|\hat{H}_{\Delta}|\psi_j\rangle\right)\right.$$
$$\left. -\frac{i}{2}\sum_m\left(\langle\psi_l|\hat{b}_m^{\dagger}\hat{b}_m|\psi_l\rangle + \langle\psi_j|\hat{b}_m^{\dagger}\hat{b}_m|\psi_j\rangle - 2\langle\psi_l|\hat{b}_m|\psi_l\rangle\langle\psi_j|\hat{b}_m|\psi_j\rangle\right)\right] \tag{5.16}$$

where $|\psi_j\rangle$ is the Frenkel-Holstein eigenstate with quantum number j. A detailed derivation for this expression is given in Appendix A.1. From Eqs. (5.12) and (5.16), we see

that for the off-diagonal zeroth-order eigenstates, the corresponding zeroth and first-order eigenvalues are generally non-zero, meaning that none of these states correspond to the steady state solution of the Lindblad master equation, which is defined in Eq. (5.1).

5.1.3 Diagonal Zeroth-Order Eigenstates

From Eq. (5.12), all the diagonal zeroth-order eigenstates, $|\vec{u}^{(0)}_{j,j}\rangle$, are shown to have the same zeroth-order eigenvalue, $\lambda^{(0)}_{j,j} = 0$. Therefore, any linear combination of these diagonal states, $|u^{(0)}_{j,j}\rangle$, also forms a valid zeroth-order eigenstate with the same eigenvalue:

$$|\vec{u}^{(0)}_{\mu}\rangle = \sum_{j} a_{\mu,j} \, |\vec{u}^{(0)}_{j,j}\rangle \tag{5.17}$$

where $a_{\mu,j}$ are the coefficients for the new zeroth-order eigenstate, $|\vec{u}^{(0)}_{\mu}\rangle$, with $\lambda^{(0)}_{\mu} = 0$. To obtain the first-order eigenvalues for these degenerate states, we insert Eq. (5.17) into Eq. (5.13), as well as pre-multiply by $\langle\vec{u}^{(0)}_{l,l}|$, to give:

$$\langle\vec{u}^{(0)}_{l,l}| \left(\hat{\hat{L}}_0 - \lambda^{(0)}_{\mu}\right) |\vec{u}^{(1)}_{\mu}\rangle + \sum_{j} \langle\vec{u}^{(0)}_{l,l}| \left(\hat{\hat{V}} - \lambda^{(1)}_{\mu}\right) |\vec{u}^{(0)}_{j,j}\rangle \, a_j = 0 \tag{5.18}$$

This term can be simplified as follows. Applying Eq. (5.9) shows that the first term in the above equation is zero. Additionally, the orthonormality of the zeroth-order eigenstates (i.e., $\langle\vec{u}^{(0)}_{l,l}|\vec{u}^{(0)}_{j,j}\rangle = \delta_{l,j}$) leads to the following expression for the first-order eigenvalues, valid for degenerate states:

$$\sum_{j} \langle\vec{u}^{(0)}_{l,l}|\hat{\hat{V}}|\vec{u}^{(0)}_{j,j}\rangle \, a_j = \lambda^{(1)}_{\mu} a_l \tag{5.19}$$

Hence the first-order eigenvalues, $\lambda_{\mu}^{(1)}$, are obtained as the eigenvalues of the perturbation matrix, $\langle \vec{u}_{l,l}^{(0)} | \hat{\hat{V}} | \vec{u}_{j,j}^{(0)} \rangle$, formed in the basis of the diagonal zeroth order-eigenstates, $|\vec{u}_{j,j}^{(0)}\rangle$. Additionally, the coefficients for these zeroth-order states ($|\vec{u}_{\mu}^{(0)}\rangle$), defined in Eq. (5.17), are obtained as the corresponding eigenvectors of this perturbation matrix. From the expression for the perturbation superoperator given by Eq. (5.3), the diagonal elements of this perturbation matrix are given by:

$$\langle \vec{\rho}_{j,j} | \hat{\hat{V}} | \vec{\rho}_{j,j} \rangle = -i\tilde{\gamma} \sum_{m} \left(\langle \psi_j | \hat{b}_m^{\dagger} \hat{b}_m | \psi_j \rangle - \left| \langle \psi_j | \hat{b}_m | \psi_j \rangle \right|^2 \right) \tag{5.20}$$

while the off-diagonal elements are given by:

$$\langle \vec{\rho}_{l,l} | \hat{\hat{V}} | \vec{\rho}_{j,j} \rangle = i\tilde{\gamma} \sum_{m} \left| \langle \psi_l | \hat{b}_m | \psi_j \rangle \right|^2 \tag{5.21}$$

where $|\vec{u}_{j,j}^{(0)}\rangle = |\vec{\rho}_{j,j}\rangle$ (as given by Eq. (5.11)) and $|\psi_j\rangle$ are the eigenstates of the Frenkel-Holstein Hamiltonian, with quantum number j. A detailed derivation of these results is given in Appendix A.1. This perturbation matrix has size N, where N is the size of the system Hilbert space.

As stated before, all these diagonal zeroth order eigenstates satisfy $\lambda_{\mu}^{(0)} = 0$. Therefore, the steady state solution of the Lindblad master equation corresponds to the state which also satisfies $\lambda_{\mu}^{(1)} = 0$. It can be proved that such a state must exist. To this end, we consider the following result for the sum of all the elements within a single column of the perturbation matrix:

$$\sum_{l} \langle \vec{\rho}_{l,l} | \hat{\hat{V}} | \vec{\rho}_{j,j} \rangle = -i\tilde{\gamma} \sum_{m} \left(\langle \psi_j | \hat{b}_m^{\dagger} \hat{b}_m | \psi_j \rangle - \sum_{l} \left| \langle \psi_l | \hat{b}_m | \psi_j \rangle \right|^2 \right) = 0 \tag{5.22}$$

where we have used that $\langle\psi_l|\hat{b}_m|\psi_j\rangle^* = \langle\psi_j|\hat{b}_m^\dagger|\psi_l\rangle$ (i.e., $\hat{b}_m^\dagger$ is the Hermitian conjugate of $\hat{b}_m$) as well as that $\hat{1} = \sum_l |\psi_l\rangle\langle\psi_l|$ is the unit operator. Equation (5.22) can be interpreted as showing that the following row vector:

$$\langle\vec{u}_\mu^{(0)}| = \begin{pmatrix} 1 & 1 & 1 & \cdots \end{pmatrix} \tag{5.23}$$

is a left eigenvector of the perturbation matrix, with eigenvalue $\lambda_\mu^{(1)} = 0$ (where the left eigenvector of a matrix is defined by the right-hand side of Eq. (2.63)). As a result, the perturbation matrix must contain at least one zero eigenvalue.

We have shown that within the perturbation theory outlined above, the steady state solution of the Lindblad master equation can be obtained from the eigenstates of the perturbation matrix, of size N. While this is an advantageous method compared to obtaining the steady state solution from the eigenstates of the full Lindblad superoperator, of size N^2, for systems with an exponentially large Hilbert space, such as the Frenkel-Holstein model, the perturbation matrix is still too large to generate and determine its eigenstates directly. To proceed, we first consider the adiabatic and anti-adiabatic limits, introduced initially in Section 2.5, for which the eigenstates of the Frenkel-Holstein Hamiltonian can be obtained analytically.

5.2 Adiabatic Limit

Consider the solution of the Lindblad master equation obtained with the quantum jump trajectory technique, discussed previously in Section 3.1. In the adiabatic limit (where $\hbar\omega/\langle J\rangle \to 0$), the time evolution for an individual trajectory (away from conical intersections) is exactly described by the following mean-field ansatz (introduced previously

in Section 3.2):

$$|\psi_{\mathrm{MF}}\rangle = e^{-\frac{i2\lambda}{\hbar\omega}\sum_m \int_0^{\tilde{t}} \langle \hat{a}_m^\dagger \hat{a}_m \rangle \langle \hat{Q}'_m \rangle dt} \, |\psi_{\mathrm{ex}}\rangle \otimes |\psi_{\mathrm{ph},1}\rangle \otimes \cdots \otimes |\psi_{\mathrm{ph},L}\rangle \tag{5.24}$$

where $\hat{Q}'_m$ is the dimensionless displacement operator for the harmonic oscillator on site m, defined as:

$$\hat{Q}'_m = \sqrt{\frac{\hbar\omega}{2\lambda}}\, \hat{Q}_m \tag{5.25}$$

From Section 3.2, the time dependence of the quantum state associated with the harmonic oscillator on site m, $|\psi_{\mathrm{ph},m}\rangle$, corresponds to a coherent state for the Frenkel-Holstein model. As coherent states are eigenstates of the harmonic oscillator destruction operator:

$$\hat{b}'_m \, |\alpha'_m\rangle = \alpha'_m \, |\alpha'_m\rangle \tag{5.26}$$

the quantum trajectories defined by Eq. (5.24) are unaffected by quantum jumps, with their time dependence solely determined by the effective Hamiltonian, $\hat{H}_{\mathrm{eff}}$, of the system.

The steady state solution in the adiabatic limit is therefore a mixed state density matrix consisting of the various minima on the adiabatic potential energy surfaces (i.e., the points on the surface where the nuclear force is zero, so that a stationary solution of the Ehrenfest equations of motion results). For the ground state potential energy surface, the minima correspond to the adiabatic VRSs, which were introduced in Section 2.5.1. In addition, minima also exist on the excited potential energy surfaces, corresponding to 'nodeful' exciton states. The exciton density associated with one such example of this is shown in Fig. 5.1, which corresponds to a minimum on the first excited potential energy surface and hence contains a single node in the exciton wavefunction. Such states are analogous to local excited exciton states (LEES), which are sometimes formed as

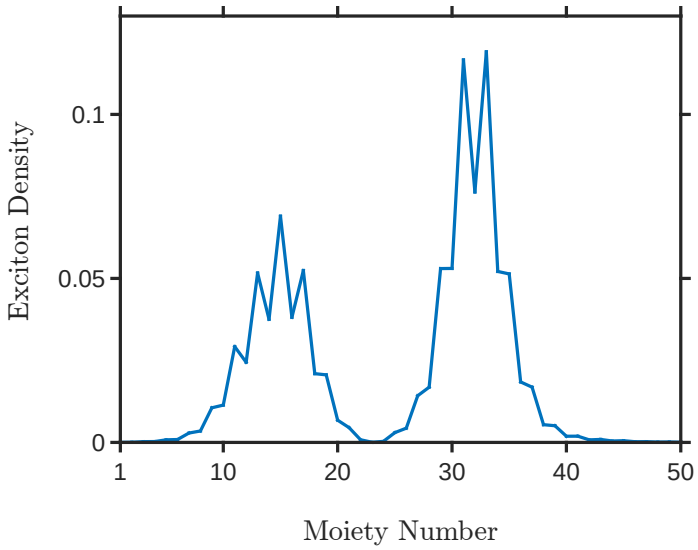


Figure 5.1: The exciton density associated with the state corresponding to a minima on the first excited adiabatic potential energy surface of the Frenkel-Holstein model, for one particular conformation of a PPV polymer chain made up of 99 moieties. The corresponding exciton wavefunction contains a single node.

eigenstates of the Frenkel Hamiltonian [56].

To ascertain the stability of the exciton states associated with these surface minima, we derive an expression for the transition probability rate between two adiabatic surfaces, at an instantaneous nuclear geometry $\mathbf{Q'_0}$. To begin, the time dependent quantum state associated with the exciton degrees of freedom is given in the adiabatic basis [80]:

$$|\psi_{\mathrm{ex}}(\tilde{t}\,)\rangle = \sum_{\beta} a_{\beta}\, \mathrm{e}^{-i\int_0^{\tilde{t}} \tilde{E}_{\beta}(\mathbf{Q'})dt}\, |\psi_{\beta,\mathrm{ex}}(\mathbf{Q'_0})\rangle \tag{5.27}$$

where a_β is the probability amplitude associated with the adiabatic state $|\psi_{\beta,\mathrm{ex}}(\mathbf{Q'_0})\rangle$ and $\tilde{E}_\beta(\mathbf{Q'})$ is the associated adiabatic surface energy:

$$\hat{H}_{\mathrm{BO}}\, |\psi_{\beta,\mathrm{ex}}(\mathbf{Q'})\rangle = E_\beta(\mathbf{Q'})\, |\psi_{\beta,\mathrm{ex}}(\mathbf{Q'})\rangle \tag{5.28}$$

where $\hat{H}_{\mathrm{BO}}$ is the Born-Oppenheimer Hamiltonian for the Frenkel-Holstein model, defined in Eq. (2.35). These eigenvalues are then made dimensionless by scaling them with the phonon energy, $\hbar\omega$:

$$\tilde{E}_\beta(\mathbf{Q}') = \frac{E_\beta(\mathbf{Q}')}{\hbar\omega} \tag{5.29}$$

Inserting Eq. (5.27) into the time-dependent Schrödinger equation and rearranging leads to the following expression for the time derivative of the probability amplitude, a_β [80]:

$$\frac{da_\beta}{d\tilde{t}} = \sum_{\beta'} \sum_m p'_m d_m(\boldsymbol{\beta},\, \mathbf{Q}'_{\mathbf{0}})\, \mathrm{e}^{-i\int_0^{\tilde{t}} \left(\tilde{E}_{\beta'}(\mathbf{Q}') - \tilde{E}_\beta(\mathbf{Q}')\right) dt} a_{\beta'} \tag{5.30}$$

where the transition probability to state $|\psi_{\beta,\mathrm{ex}}(\mathbf{Q}'_{\mathbf{0}})\rangle$ is obtained as $P_\beta = |a_\beta|^2$. In this expression, $p'_m = dQ'_m/d\tilde{t}$ is the classical momentum associated with the harmonic oscillator on site m and $d_m(\boldsymbol{\beta},\, \mathbf{Q}'_{\mathbf{0}})$ is the nonadiabatic derivative coupling vector between states $|\psi_{\beta,\mathrm{ex}}(\mathbf{Q}'_{\mathbf{0}})\rangle$ and $|\psi_{\beta',\mathrm{ex}}(\mathbf{Q}'_{\mathbf{0}})\rangle$, induced by the oscillator on site m. This quantity is given by:

$$d_m(\boldsymbol{\beta},\, \mathbf{Q}'_{\mathbf{0}}) = \left\langle \psi_{\beta',\mathrm{ex}} \left| \frac{\partial \psi_{\beta,\mathrm{ex}}}{\partial Q'_m} \right\rangle \right|_{\mathbf{Q}'=\mathbf{Q}'_{\mathbf{0}}} \tag{5.31}$$

where $\boldsymbol{\beta} = (\beta,\, \beta')$ is a vector containing the quantum numbers associated with the two coupled surfaces. From Eq. (5.30), the magnitudes of the nonadiabatic couplings associated with a state $|\psi_{\beta,\mathrm{ex}}(\mathbf{Q}'_{\mathbf{0}})\rangle$ therefore determine the transition rate from that particular surface. Hence a state associated with a surface minima must have small nonadiabatic derivative couplings to have a large contribution to the steady state solution.

An exact expression for the nonadiabatic derivative coupling vector can be obtained using time-independent perturbation theory [80]:

$$d_m(\boldsymbol{\beta},\, \mathbf{Q}'_{\mathbf{0}}) = \frac{-2\lambda \psi^*_{\beta',m} \psi_{\beta,m}}{E_\beta(\mathbf{Q}'_{\mathbf{0}}) - E_{\beta'}(\mathbf{Q}'_{\mathbf{0}})} \qquad \text{for} \quad \beta' \neq \beta \tag{5.32}$$

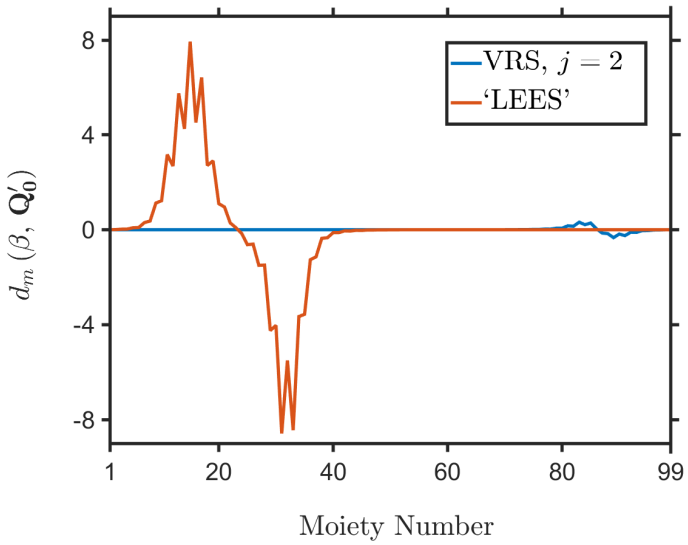


Figure 5.2: The nonadiabatic derivative coupling vector for two states corresponding to minima on the adiabatic potential energy surfaces. The solid blue curve corresponds to the adiabatic VRS with quantum number $j = 2$ (see Fig. 2.12), while the solid orange curve corresponds to a minima on the first excited surface, with associated exciton density given by Figure 5.1. For these two states, the value of β' is chosen such that the elements of the derivative coupling vector have their largest values.

where $\psi_{\beta,m}$ is the probability amplitude associated with site m, for the state $|\psi_{\beta,\mathrm{ex}}(\mathbf{Q}_0')\rangle$ and λ is the exciton-phonon coupling parameter given by:

$$\lambda = \frac{A^2\hbar\omega}{2} \tag{5.33}$$

A derivation of this expression is given in Appendix C. Using this expression, the nonadiabatic derivative coupling vectors can be calculated for minima of the potential energy surfaces within the Frenkel-Holstein model, some of which are given in Fig. 5.2. In this figure, the solid blue curve corresponds to the adiabatic VRS with quantum number $j = 2$ (see Fig. 2.12), while the solid orange curve corresponds to a minima on the first excited surface, with the corresponding exciton density given by Fig. 5.1. For these two states, the value of β' is chosen such that the elements of the derivative coupling vector have

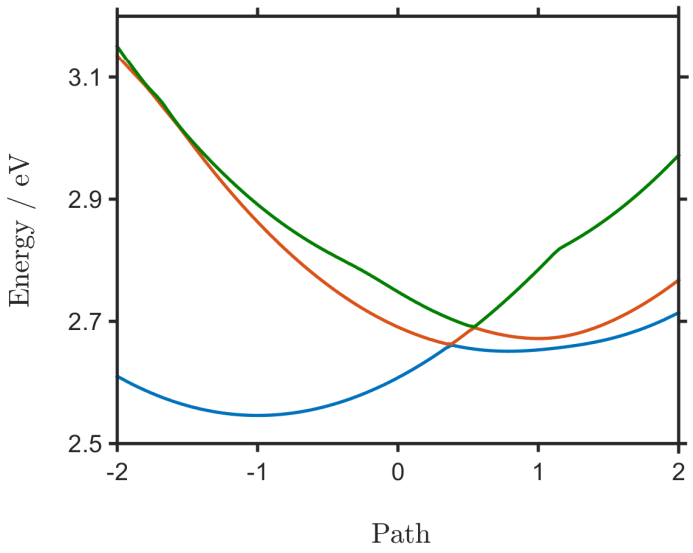


Figure 5.3: The three lowest energy adiabatic potential energy surfaces corresponding to a linear path between the nuclear geometries associated with the $j = 2$ adiabatic VRS and the 'LEES' given in Fig. 5.1. The minima in the lowest energy surface (blue) at Path $= -1$ corresponds to this adiabatic VRS, while the minima in the first excited surface (orange) at Path $= 1$ corresponds to the 'LEES'.

their largest values. The nonadiabatic derivative coupling vector associated with the 'LEES' (the state on an excited potential energy surface) is much larger than that for the adiabatic VRS, meaning that the adiabatic VRSs dominate the steady state solution in the adiabatic limit. Indeed numerical results presented later in this chapter will confirm that the disparity between the magnitudes of these derivative couplings is so large that essentially the steady state solution consists entirely of the adiabatic VRSs in this case.

The reason why the excited state minima have large associated derivative coupling vectors can be understood by considering the form of the potential energy surfaces within the model. Figure 5.3 gives the energies associated with the three lowest energy adiabatic potential energy surfaces, for a linear path between the nuclear geometries associated with the $j = 2$ adiabatic VRS and the 'LEES' given in Fig. 5.1. The minima in the lowest energy surface (blue) at Path $= -1$ corresponds to this adiabatic VRS, while the

minima in the first excited surface (orange) at Path = 1 corresponds to the 'LEES'. From Eq. (5.32), the large nonadiabatic derivative coupling vector for the 'LEES' hence arises from the small energy gap between the ground and first excited potential energy surface at this nuclear geometry, which induces a large population loss from this minimum to the lower surface.

Overall, this result for the steady state solution shows that the exciton relaxation dynamics do indeed proceed into the low energy chromphore states of the polymer (i.e., the VRSs) in the adiabatic limit, as physically expected.

5.3 Anti-Adiabatic Limit

In Section 2.5.2, it was shown that in the anti-adiabatic limit (where $\hbar\omega/\langle J\rangle \to \infty$) the Frenkel-Holstein Hamiltonian can be diagonalised by performing the Lang-Firsov transformation. In this transformed basis, the Frenkel-Holstein Hamiltonian for the anti-adiabatic limit is given by [73]:

$$\hat{\tilde{H}}_{\mathrm{FH}} \simeq \hat{H}_{\mathrm{F}} + \hbar\omega \sum_m \left(\hat{b}_m^\dagger \hat{b}_m + \tfrac{1}{2}\right) - \lambda \tag{5.34}$$

where $\lambda = A^2\hbar\omega/2$ corresponds to the exciton-polaron relaxation energy in the atomic limit and A is the dimensionless exciton-phonon coupling parameter. In addition, $\hat{H}_F$ is the Frenkel Hamiltonian (introduced in Section 2.4), which in the eigenstate basis is given by:

$$\hat{H}_F = \sum_k \epsilon_k \hat{c}_k^\dagger \hat{c}_k \tag{5.35}$$

where ϵ_k is the energy of the Frenkel eigenstate with quantum number k and $\hat{c}_k^\dagger/\hat{c}_k$ are the corresponding creation/destruction operators respectively. From Eqs. (5.34) and (5.35), the eigenstates in the anti-adiabatic limit of the Frenkel-Holstein Hamiltonian are given

by the following equation in the transformed basis:

$$|\tilde{\psi}_{k,\,n_1,\,n_2,..,\,n_L}\rangle = |k\rangle \otimes |n_1\rangle \otimes |n_2\rangle \otimes \cdots \otimes |n_L\rangle \tag{5.36}$$

where $|k\rangle$ is the eigenket of the Frenkel Hamiltonian with quantum number k and $|n_m\rangle$ is the harmonic oscillator eigenket on site m, with quantum number n_m. The corresponding eigenvalues are then:

$$E_{k,\,n_{\text{phon}}} = \epsilon_k + \hbar\omega\left(n_{\text{phon}} + \tfrac{1}{2}\right) - \lambda \tag{5.37}$$

where $n_{\text{phon}} = \sum_m n_m$ is the total number of phonons associated with the corresponding eigenstate.

To generate the perturbation matrix, given by Eq. (5.20) and (5.21), from which the steady state solution of the Lindblad superoperator can be obtained, we need an expression for the harmonic oscillator destruction operator in the Lang-Firsov basis, $\hat{\tilde{b}}_m$. This was already determined in Section 2.5.2 and is given by:

$$\hat{\tilde{b}}_m = \hat{b}_m + \frac{A}{\sqrt{2}}\hat{a}_m^\dagger \hat{a}_m \tag{5.38}$$

Consider the anti-adiabatic Frenkel-Holstein Hamiltonian eigenstates in their vibrational ground state (i.e., those with $n_m = 0$ for all m). Applying the harmonic oscillator destruction operator to these states gives the following:

$$\hat{\tilde{b}}_m\,|\tilde{\psi}_{k,\,0_1,..,\,0_L}\rangle = \frac{A}{\sqrt{2}}\psi_{k,m}\,|m\rangle \otimes |0_1\rangle \otimes |0_2\rangle \otimes \cdots \otimes |0_L\rangle \tag{5.39}$$

where $|m\rangle$ is the state which corresponds to the Frenkel exciton residing on site m and $\psi_{k,m}$ is the associated probability amplitude, for an eigenstate of the Frenkel Hamiltonian

with quantum number k. From Eq. (5.39), we see that applying the harmonic oscillator destruction operator keeps a state within the vibrational ground state manifold. As the harmonic oscillator destruction operator introduces no vibrational excitations in the anti-adiabatic limit, only eigenstates in their vibrational ground state make any contribution to the steady state solution. We thus only need to consider the subspace of these states when calculating the perturbation matrix in this limit. Using Eqs. (5.20), (5.21) and (5.39), the required elements of the perturbation matrix are:

$$\langle \vec{\rho}_{k',k'} | \hat{\hat{V}} | \vec{\rho}_{k',k'} \rangle = -\frac{i\tilde{\gamma}A^2}{2} \sum_m \left(1 - |\psi_{k',m}|^4\right) \tag{5.40}$$

$$\langle \vec{\rho}_{k',k'} | \hat{\hat{V}} | \vec{\rho}_{k,\,k} \rangle = \frac{i\tilde{\gamma}A^2}{2} \sum_m |\psi_{k',m}|^2 \, |\psi_{k,\,m}|^2 \tag{5.41}$$

where we have used that $\sum_m |\psi_{k,\,m}|^2 = 1$ (i.e., the eigenstates of the Frenkel Hamiltonian are normalised). From Eqs. (5.40) and (5.41), $\sum_{k'} \langle \vec{\rho}_{k',k'} | \hat{\hat{V}} | \vec{\rho}_{k,\,k} \rangle = 0$ within the subspace of the vibrational ground state eigenstates, which means that this matrix has a zero eigenvalue (as shown in Section 5.1.3) and as such confirms that the steady state solution consists solely of these states.

Additionally, from Eq. (5.41) we see that the perturbation matrix in this subspace is anti-Hermitian, which means that the left and right eigenvectors of the perturbation matrix are identical in this case. In Section 5.1.3, it was shown that the left eigenvector for the steady state solution is always given by Eq. (5.23), so that the elements of the corresponding right eigenvector in the anti-adiabatic limit are given by:

$$\rho_{k,\,k} \sim \begin{cases} 1, & \text{for} \quad n_{\text{phon}} = 0 \\ 0, & \text{for} \quad n_{\text{phon}} \neq 0 \end{cases} \tag{5.42}$$

This steady state solution physically corresponds to an 'infinite temperature' thermal exciton state, showing that the exciton relaxation dynamics do not proceed solely into the VRSs in this limit.

Now that the steady state solution is understood in the anti-adiabatic limit, in the following we consider perturbative corrections away from this limit, to see how the steady state solution is altered.

5.3.1 Perturbation Theory about the Anti-Adiabatic Limit

In Section 2.5.2, it was shown that applying the Lang-Firsov transformation to the Frenkel-Holstein Hamiltonian results in the following [73]:

$$\hat{\tilde{H}}_{\mathrm{FH}} = e^{-\hat{S}}\hat{H}_{\mathrm{F}}e^{\hat{S}} + \hbar\omega\sum_{m}\left(\hat{b}_{m}^{\dagger}\hat{b}_{m} + \tfrac{1}{2}\right) - \lambda \tag{5.43}$$

where the only remaining non-diagonal contribution to this Hamiltonian is that which involves the Frenkel Hamiltonian, $\hat{H}_F$. To obtain the Frenkel-Holstein Hamiltonian valid in the anti-adiabatic limit (as given previously by Eq. (5.34)) the limit $\hbar\omega/\langle J\rangle \to \infty$ is taken, which results in $e^{-\hat{S}}\hat{H}_{\mathrm{F}}e^{\hat{S}} \to \hat{H}_F$. Therefore, by Taylor expanding the exponential operators in this Frenkel Hamiltonian term, we can obtain the following correction to the anti-adiabatic Frenkel-Holstein Hamiltonian [128]:

$$e^{-\hat{S}}\hat{H}_{\mathrm{F}}e^{\hat{S}} \simeq \hat{H}_{\mathrm{F}} + \hat{V}_1 + \cdots \tag{5.44}$$

where $\hat{V}_1$ is the first-order perturbation operator:

$$\hat{V}_1 = \left[\hat{H}_{\mathrm{F}}, \hat{S}\right] \tag{5.45}$$

and $\hat{S}$ is an anti-Hermitian operator given by:

$$\hat{S} = -i\sqrt{\frac{2\lambda}{\hbar\omega}}\sum_m \hat{a}_m^\dagger \hat{a}_m \hat{P}_m \tag{5.46}$$

where $\hat{P}_m = \frac{1}{\sqrt{2}}(\hat{b}_m^\dagger - \hat{b}_m)$ is the dimensionless harmonic oscillator momentum operator for site m. From Eq. (5.44), we identify the second term in this expression as the largest perturbative correction to the anti-adiabatic Frenkel-Holstein Hamiltonian in the limit $\hbar\omega/\langle J\rangle \to \infty$. Noting that the Frenkel exciton creation operator for site m can be written in terms of the creation operators for the Frenkel Hamiltonian eigenstates:

$$\hat{a}_m^\dagger = \sum_k \psi_{k,m}^* \hat{c}_k^\dagger \tag{5.47}$$

we obtain the following expression for this first-order perturbation operator:

$$\hat{V}_1 = iA\sum_m \sum_{k,k',k''} \epsilon_k \psi_{k'',m}^* \psi_{k',m} \left(\hat{c}_{k''}^\dagger \hat{c}_{k'} \hat{c}_k^\dagger \hat{c}_k - \hat{c}_k^\dagger \hat{c}_k \hat{c}_{k''}^\dagger \hat{c}_{k'}\right) \hat{P}_m \tag{5.48}$$

where we have also used the expression for the Frenkel Hamiltonian given in Eq. (5.35), as well as the definition $A = 2\lambda/\hbar\omega$. In this thesis, we consider solely the single Frenkel exciton subspace of the system. Therefore, for an operator to give a non-zero contribution in this subspace, any Frenkel exciton destruction operators present must act on the same state that the Frenkel exciton is created in previously, meaning that:

$$\hat{c}_k^\dagger \hat{c}_p \hat{c}_q^\dagger \hat{c}_r = \hat{c}_k^\dagger \hat{c}_r \delta_{q,p} \tag{5.49}$$

Inserting this relation into the expression for the first-order perturbation operator (given by Eq. (5.48)) and rearranging leads to the following simplified expression for this term:

$$\hat{V}_1 = iA \sum_m \sum_{k,\,k'} (\epsilon_k - \epsilon_{k'})\, \psi^*_{k',m} \psi_{k,\,m} \hat{c}^\dagger_{k'} \hat{c}_k \hat{P}_m \tag{5.50}$$

We now have all the necessary ingredients to apply standard perturbation theory to ascertain how the steady state solution of the Lindblad master equation changes away from the anti-adiabatic limit. The unperturbed Hamiltonian, $\hat{H}_0$, is the anti-adiabatic Frenkel-Holstein Hamiltonian given by Eq. (5.34), while the perturbation is given by Eq. (5.50). Hence to first order in perturbation theory, the eigenstates of the Frenkel-Holstein Hamiltonian that correspond to the vibrational ground state (i.e., those with $n_j = 0$ for all sites j), are given by:

$$|\tilde{\psi}_{k,\,0_1,..,\,0_L}\rangle = |\tilde{\psi}^{(0)}_{k,\,0_1,..,\,0_L}\rangle - \frac{A}{\sqrt{2}} \sum_m \sum_{k'} \frac{(\epsilon_k - \epsilon_{k'})\, \psi^*_{k',m} \psi_{k,\,m}}{(\epsilon_k - \epsilon_{k'} - \hbar\omega)}\, |\tilde{\psi}^{(0)}_{k',0_1,..,\,1_m,..,\,0_L}\rangle \tag{5.51}$$

where this expression is given in the transformed basis and is valid close to the anti-adiabatic limit.

To generate the steady state solution of the Lindblad superoperator, the perturbation matrix (given by Eqs. (5.20) and (5.21)) must be obtained. To this end, consider the Frenkel-Holstein Hamiltonian eigenstates in their vibrational ground state. Applying the harmonic oscillator destruction operator in the Lang-Firsov basis (given by Eq. (5.38)) to these states gives the following:

$$\hat{\tilde{b}}_m\, |\tilde{\psi}_{k,\,0_1,..,\,0_L}\rangle \simeq \frac{A}{\sqrt{2}} \left[\psi_{k,\,m}\, |m\rangle \otimes |0_1\rangle \otimes .... \otimes |0_L\rangle - \sum_{k'} \frac{(\epsilon_k - \epsilon_{k'})\, \psi^*_{k',m} \psi_{k,\,m}}{(\epsilon_k - \epsilon_{k'} - \hbar\omega)}\, |\tilde{\psi}^{(0)}_{k',\,0_1,..,\,0_L}\rangle \right] \tag{5.52}$$

where we have only retained terms to first-order in the dimensionless exciton-phonon coupling constant, A, which is consistent with the order of perturbation used for the Frenkel-Holstein eigenstates given by Eq. (5.51). Additionally, $|m\rangle$ is the state which corresponds to the Frenkel exciton residing on site m. From Eq. (5.52), we see that applying the harmonic oscillator destruction operator will keep a state within the vibrational ground state manifold. Therefore, as in the beginning of Section 5.3, we only need to consider the subspace of these states when calculating the perturbation matrix in this limit. Using Eqs. (5.52), (5.20) and (5.21), the required elements of the perturbation matrix are:

$$\langle \vec{\rho}_{k,\,k} | \hat{\hat{V}} | \vec{\rho}_{k,\,k} \rangle = -\frac{i\tilde{\gamma} A^2 \sum_m \sum_{k' \neq k} |\psi_{k,\,m}|^2 \, |\psi_{k',m}|^2}{2\left(\tilde{\epsilon}_{k'} - \tilde{\epsilon}_k + 1\right)^2} \tag{5.53}$$

$$\langle \vec{\rho}_{k,\,k} | \hat{\hat{V}} | \vec{\rho}_{k',k'} \rangle = \frac{i\tilde{\gamma} A^2 \sum_m |\psi_{k,\,m}|^2 \, |\psi_{k',m}|^2}{2\left(\tilde{\epsilon}_k - \tilde{\epsilon}_{k'} + 1\right)^2} \tag{5.54}$$

where $\tilde{\epsilon}_k = \epsilon_k / \hbar\omega$ are the dimensionless eigenvalues of the Frenkel Hamiltonian. Inserting these expressions for the elements of the perturbation matrix into the eigenvalue equation for the zeroth-order Lindblad superoperator eigenstates (given by Eq. (5.19)) results in the following equation for the steady state:

$$\frac{i\tilde{\gamma} A^2}{2} \sum_m \sum_{k' \neq k} |\psi_{k,\,m}|^2 \, |\psi_{k',m}|^2 \left[\frac{-\rho_{k,\,k}}{\left(\tilde{\epsilon}_{k'} - \tilde{\epsilon}_k + 1\right)^2} + \frac{\rho_{k',k'}}{\left(\tilde{\epsilon}_k - \tilde{\epsilon}_{k'} + 1\right)^2} \right] = 0 \tag{5.55}$$

where $\rho_{k,\,k}$ is the diagonal steady state density matrix coefficient, corresponding to the eigenstate of the Frenkel-Holstein Hamiltonian with eigenvalue k. Hence the diagonal steady state density matrix elements must satisfy:

$$\rho_{k',k'} = \rho_{k,\,k} f(\tilde{\epsilon}_k - \tilde{\epsilon}_{k'}) \tag{5.56}$$

where:

$$f(x) = \left(\frac{x+1}{x-1}\right)^2 \tag{5.57}$$

Expanding this function then leads to the following representation:

$$f(x) = 1 + \frac{4}{x-1} + \frac{4}{(x-1)^2} \tag{5.58}$$

The expression given in Eq. (5.56) is valid near the anti-adiabatic limit, when $\hbar\omega/\langle J\rangle \to \infty$. This is the same limit in which the Taylor expansion of $f(x)$ is valid, given by:

$$f(x) = 1 + 4x + \frac{(4x)^2}{2} + \cdots \simeq \mathrm{e}^{4x} \tag{5.59}$$

As the first three terms in the Taylor expansion of $f(x)$ are identical to that of $\exp(4x)$, we can replace the function in Eq. (5.56) with this exponential. Finally, noting that the eigenvalues of the Frenkel-Holstein Hamiltonian in the anti-adiabatic limit are given by:

$$E_{k,\,n_{\mathrm{phon}}} = \epsilon_k + \hbar\omega\left(n_{\mathrm{phon}} + \tfrac{1}{2}\right) - \lambda \tag{5.60}$$

the solution to Eq. (5.56), valid close to this limit, is hence:

$$\rho_{k,k} \sim \begin{cases} \exp[-4E_{k,\,0}/\hbar\omega], & \text{for} \quad n_{\mathrm{phon}} = 0 \\ 0, & \text{for} \quad n_{\mathrm{phon}} \neq 0 \end{cases} \tag{5.61}$$

Therefore, this steady state solution physically corresponds to a thermal exciton state, with temperature $T = \hbar\omega/4$. This is indeed consistent with the result given in Eq. (5.42), which corresponds to the anti-adiabatic limit, when $\hbar\omega/\langle J\rangle \to \infty$.

5.4 Limited Functional Space Approach

Away from the adiabatic and anti-adiabatic limits, analytical solutions for the eigenstates of the Frenkel-Holstein model are not known to exist and the associated steady state solution can only be obtained numerically. To obtain a representative Lindblad perturbation matrix, from which the steady state solution is obtained, requires a method that is able to generate a large number of excited eigenstates of the Frenkel-Holstein Hamiltonian. The limited functional space (LFS) approach, which has already been introduced in Section 3.4, is well suited for this task.

To calculate the steady state solution of the Lindblad master equation using the LFS approach, a reduced dimensional Hilbert space is first generated for the Frenkel-Holstein model using a set number of LFS 'steps'. Within this reduced dimensional Hilbert space, the Frenkel-Holstein eigenstates are obtained by diagonalising the Hamiltonian matrix. The Lindblad perturbation matrix can then be calculated from these energy eigenstates using Eqs. (5.20) and (5.21), from which the steady state solution corresponds to the perturbation matrix eigenstate with an eigenvalue of zero. This procedure is then repeated using larger Hilbert spaces generated with a greater number of LFS 'steps', until the obtained steady state solution converges.

In some cases, the reduced dimensional Hilbert space grows too large for the Frenkel-Holstein Hamiltonian to be diagonalised, before convergence of the steady state solution is reached. To numerically obtain the steady state solution in this situation, we introduce a modified LFS method developed by us, which calculates the Frenkel-Holstein eigenstates with the lowest N_{eig} energies, within a reduced dimensional Hilbert space. This reduced dimensional Hilbert space is generated from N_{step} 'steps' within the standard LFS approach. The basis states associated with this Hilbert space can be characterised using the

following notation:

$$|m,\, q\rangle = |m\rangle \otimes |V_{m,\,q}\rangle \tag{5.62}$$

where $|m\rangle$ is the exciton basis state corresponding to the exciton residing on site m and q is a quantum number which distinguishes the various D_m vibrational states, $|V_{m,\,q}\rangle$, associated with this particular exciton configuration. For example in Section 3.4, Fig. 3.5 gives a subset of the basis states generated by the LFS approach with $N_{\text{step}} = 2$, which correspond to all of the $D_2 = 5$ states associated with the exciton residing on site 2 (i.e., states $|2, q\rangle$ corresponding to all possible quantum numbers q).

For the modified LFS method, 'trial' solutions for the eigenstates, $|\psi_k\rangle$, with the lowest N_{eig} energies must firstly be supplied:

$$|\psi_k\rangle = \sum_{m=1}^{L} \sum_{q=1}^{D_m} c^k_{m,\,q}\, |m,\, q\rangle \tag{5.63}$$

In practice, these trial solutions can be initially chosen as the lowest energy eigenstates from a previous smaller Hilbert space LFS calculation. The method then optimises these coefficients, $c^k_{m,\,q}$, so that the eigenstates converge to their "exact" values. To optimise these coefficients, the reduced dimensional Hilbert space is partitioned into a 'system' and an 'environment', as illustrated in Fig. 5.4. The 'system' corresponds to one of the sites within the model (i.e., site p in the figure) and its Hilbert space consists of all states for which the exciton resides on this site (i.e., the states $|p, q\rangle$ corresponding to all possible quantum numbers q). The 'environment' then consists of the remaining Hilbert space. Rather than including all of the basis states contained within the 'environment', only the

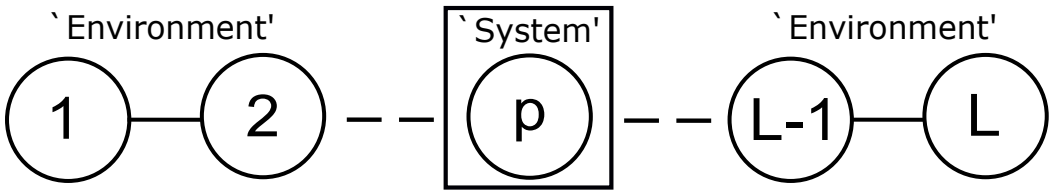


Figure 5.4: A schematic diagram to illustrate the partitioning of the Hilbert space into the 'system' and the 'environment'. The system consists of all the basis states associated with the exciton residing on site p (i.e., the states $|p, q\rangle$ corresponding to all possible quantum numbers q), while the environment consists of the remaining Hilbert space. Within this modified LFS method, the 'environment' then represented by N_{eig} 'trial' solutions. The system site then 'sweeps' backwards and forwards along the chain as the procedure is repeated at each new iteration.

N_{eig} 'trial' solutions are included, with their system basis coefficients set to zero:

$$c^k_{m,\,q} = \begin{cases} c^k_{m,\,q}, & \text{for} \quad m \neq p \\ 0, & \text{for} \quad m = p \end{cases} \tag{5.64}$$

This means that the total Hilbert space considered is now only of size $D_p + N_{\text{eig}}$.

For the Frenkel-Holstein model, the Hamiltonian can be written as follows:

$$\hat{H} = \sum_{m=1}^{L} \hat{h}_m + \sum_{m=1}^{L-1} \hat{h}_{m,\,m+1} \tag{5.65}$$

where $\hat{h}_m$ corresponds to the Hamiltonian terms which involve the exciton on site m and $\hat{h}_{m,\,m+1}$ corresponds to the nearest-neighbour Hamiltonian terms which link exciton sites m and $m+1$. In other words, for the Frenkel-Holstein Hamiltonian:

$$\begin{aligned} \hat{h}_m &= \left(\epsilon_m - A\hbar\omega\hat{Q}_m + \hbar\omega \sum_j \hat{b}^\dagger_j \hat{b}_j \right) \hat{a}^\dagger_m \hat{a}_m \\ \hat{h}_{m,\,m+1} &= J_m \left(\hat{a}^\dagger_{m+1} \hat{a}_m + \hat{a}^\dagger_m \hat{a}_{m+1} \right) \end{aligned} \tag{5.66}$$

Using Eq. (5.65), the Hamiltonian within the reduced 'environment' basis, $|\psi_k\rangle$, is given

by:

$$E_{k,\,k'} = E_k \delta_{k,\,k'} - \langle \psi_k | \hat{h}_p + \hat{h}_{p,\,p+1} + \hat{h}_{p-1,\,p} | \psi_{k'} \rangle \tag{5.67}$$

where E_k are the energies associated with the initial 'trial' solutions. Eq. (5.67) corresponds to removing the energy contributions to E_k arising from the 'system' site p. As the system basis coefficients have been set to zero in the 'trial' solutions, $|\psi_k\rangle$, these states are no longer orthonormal. An orthonormal basis, $|\tilde{\psi}_k\rangle$ can be obtained from these states using the Gram-Schmidt orthogonalisation procedure:

$$\begin{aligned}
|u_1\rangle &= |\psi_1\rangle\,, & |\tilde{\psi}_1\rangle &= \frac{|u_1\rangle}{\sqrt{\langle u_1|u_1\rangle}} \\
|u_2\rangle &= |\psi_2\rangle - \langle \tilde{\psi}_1|\psi_2\rangle\,|\tilde{\psi}_1\rangle\,, & |\tilde{\psi}_2\rangle &= \frac{|u_2\rangle}{\sqrt{\langle u_2|u_2\rangle}} \\
&\vdots & & \\
|u_k\rangle &= |\psi_k\rangle - \sum_{s=1}^{k-1} \langle \tilde{\psi}_s|\psi_k\rangle\,|\tilde{\psi}_s\rangle\,, & |\tilde{\psi}_k\rangle &= \frac{|u_k\rangle}{\sqrt{\langle u_k|u_k\rangle}}
\end{aligned} \tag{5.68}$$

The Hamiltonian within the 'environment' basis can then be updated as follows:

$$\tilde{\mathbf{E}} = \mathbf{U}^{\mathrm{T}}\mathbf{E}\mathbf{U} \tag{5.69}$$

where $U_{k,\,k'}$ is the transformation matrix which transforms states $|\tilde{\psi}_{k'}\rangle$ to states $|\psi_k\rangle$:

$$U_{k,\,k'} = \frac{\langle \psi_k | u_{k'} \rangle}{\sqrt{\langle u_{k'} | u_{k'} \rangle}} \tag{5.70}$$

The full Hamiltonian matrix can now be constructed using the 'system' states, $|p, q\rangle$

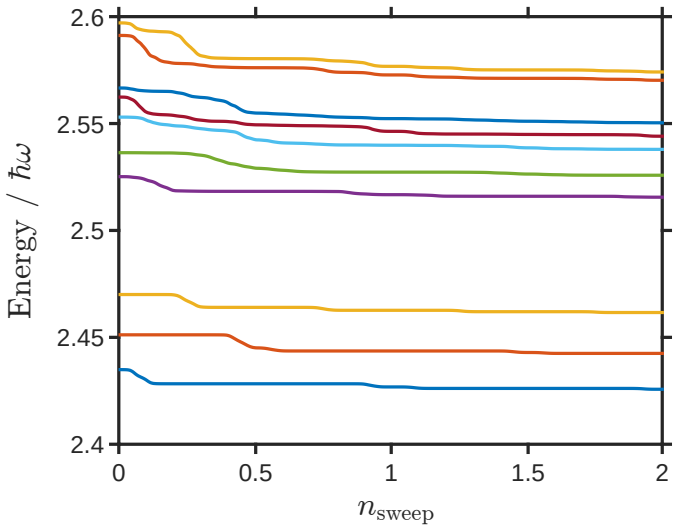


Figure 5.5: The lowest $N_{\text{eig}} = 10$ energies of a $L = 99$ Frenkel-Holstein model, with parameters $\hbar\omega = 0.2$ eV and $A = 4$, for a reduced dimensional Hilbert space generated with $N_{\text{step}} = 8$ steps of the LFS scheme. These energies were calculated using the modified LFS method and are given as a function of the number of full 'sweeps', N_{sweep}, of the procedure. The initial 'trial' solutions for these eigenstates were chosen as the lowest energy eigenstates of the standard LFS approach, with $N_{\text{step}} = 7$.

and the 'environment' states, $|\tilde{\psi}_k\rangle$ as the basis:

$$\mathbf{H} = \begin{pmatrix} \langle p,\, q|\hat{h}_p|p,\, q'\rangle & \cdots & \langle p,\, q|\hat{h}_{p,\,p+1} + \hat{h}_{p-1,\,p}|\tilde{\psi}_{k'}\rangle \\ \vdots & \ddots & \vdots \\ \langle\tilde{\psi}_k|\hat{h}_{p,\,p+1} + \hat{h}_{p-1,\,p}|p,\, q'\rangle & \cdots & \tilde{E}_{k,\,k'} \end{pmatrix} \tag{5.71}$$

The size of this Hamiltonian matrix is $D_p + N_{\text{eig}}$ and hence if only a relatively few number of energy eigenstates need to be obtained (i.e., N_{eig} is not too large) then this matrix is much smaller than the full Hilbert space and is easily diagonalisable. From this matrix, the lowest N_{eig} eigenvalues become the new energies, E_k, and the corresponding eigenvectors become the new 'trial' solutions, $|\psi_k\rangle$. Physically the process described so far corresponds to optimising the system site coefficients for the 'trial' solutions, while keeping the environment coefficients fixed.

This process is then repeated for a new system site in a 'sweeping' algorithm. In other words, for the forward (left to right) 'sweep', the new system site would become site $p+1$, while for the backward (right to left) 'sweep', the new system site would become site $p-1$. This is repeated until the N_{eig} energies and eigenstates have converged. The convergence of the energies of the 'trial' solutions, E_k, as a function of the number of full 'sweeps', N_{sweep}, of the procedure are given in Fig. 5.5. These results were obtained for a $L = 99$ system, with parameters $\hbar\omega = 0.2$ eV and $A = 4$. The Hilbert space used consisted of 54502 states (generated using $N_{\text{step}} = 8$ steps of the LFS scheme), in which $N_{\text{eig}} = 10$ eigenstates were calculated. The 'trial' solutions were initially chosen as the lowest energy eigenstates of the standard LFS approach, with $N_{\text{step}} = 7$. Convergence of the energies is shown to be stable within this technique and generally requires only a few full 'sweeps' of the algorithm. Additionally, as the size of the diagonalised Hamiltonian matrix grows linearly with N_{eig}, a relatively large number of eigenstates can in principle be calculated using this technique. Practically, calculations involving $N_{\text{eig}} \sim 5000$ for systems containing $L = 99$ sites are feasible.

5.5 Numerical Results

In this section, both the standard and modified LFS approaches are used to numerically obtain properties associated with the steady state solution of the exciton relaxation dynamics. For a steady state density matrix, $\hat{\rho}$, any property associated with a system operator, $\hat{O}$, can be calculated as follows:

$$\langle \hat{O} \rangle = \text{Tr}\left[\hat{\rho}\hat{O}\right] \tag{5.72}$$

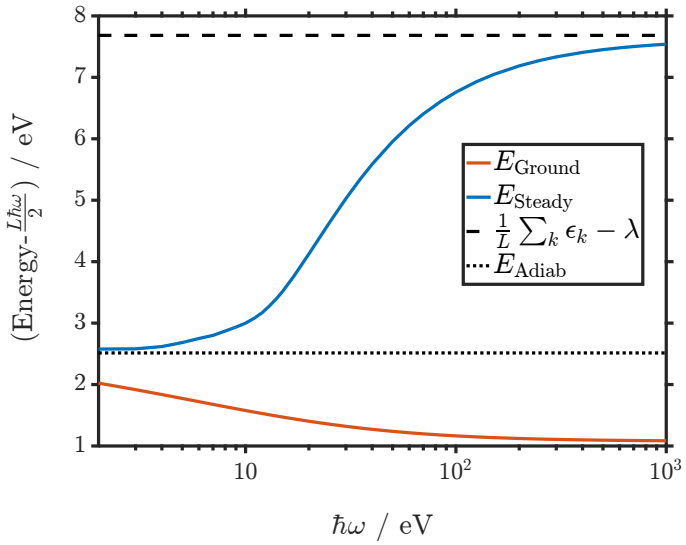


Figure 5.6: The dependence of the steady state energy, E_{Steady}, on the harmonic oscillator phonon energy, $\hbar\omega$, for a $L = 99$ site Frenkel-Holstein model with $\lambda = 1.6$ eV. The numerical result is given by the solid blue curve, while the analytical result, valid in the anti-adiabatic limit, is given by the dashed black line. Additionally, the ground state energy, E_{Ground}, which corresponds to the lowest energy eigenvalue of the model, is given by the solid orange curve in this figure, while the same quantity in the adiabatic limit, E_{Adiab}, is given by the dotted black line.

All results presented here are for to a $L = 99$ site Frenkel-Holstein model, with parameters which correspond to a PPV polymer chain (values of which are given in Table 2.2) and an exciton-phonon coupling parameter of $\lambda = 1.6$ eV. This value for the exciton-phonon coupling parameter was chosen so as to be consistent with the parameters $A = 4$ and $\hbar\omega = 0.2$ eV, as used in Chapter 4.

To begin, we check that our numerical results for the steady state solution are consistent with the previously obtained analytical results valid in the adiabatic and anti-adiabatic limits. In Section 5.2, it was suggested that in the adiabatic limit (where $\hbar\omega/\langle J\rangle \to 0$), the steady state solution consists solely of the adiabatic VRSs. To confirm whether this is the case, the energy associated with the lowest energy adiabatic VRS, E_{Adiab}, is given by the dotted black line in Fig. 5.6, while the numerically obtained steady state energy,

E_{Steady}, is given by the solid blue curve. The two results do indeed coincide as the adiabatic limit is approached, confirming that only the potential energy surface minima corresponding to the adiabatic VRSs contribute to the steady state solution in this limit, as was initially thought in Section 5.2. Additionally, away from the adiabatic limit, the numerically obtained steady state energy is always greater than the ground state energy of the model (i.e., the lowest energy eigenvalue of the Frenkel-Holstein Hamiltonian), which is given by the solid orange curve. This means that it is only in the adiabatic limit for which the exciton relaxation dynamics proceed solely into the low energy VRSs of the polymer.

In the anti-adiabatic limit (where $\hbar\omega/\langle J\rangle \to \infty$), it was shown in Section 5.3 that the analytical solution for the steady state density matrix corresponds to $\rho_{k,k} \sim 1$, where k are the quantum numbers associated with the eigenstates of the Frenkel-Holstein model in the vibrational ground state (i.e., the eigenstates where the oscillator quantum numbers satisfy $n_m = 0$ for all sites m). Using the expression for the associated eigenvalues of these states, given by Eq. (5.37), the steady state energy in the anti-adiabatic limit is as follows:

$$E_{\text{Steady}} = \frac{1}{L}\sum_k \epsilon_k - \lambda \tag{5.73}$$

where ϵ_k are the eigenvalues of the Frenkel Hamiltonian, with quantum number k. The value of this quantity for the $L = 99$ site Frenkel-Holstein model is given by the dashed black line in Fig. 5.6. Indeed the numerical result for the steady state energy, given by the solid blue curve, coincides with this analytical result as the anti-adiabatic limit is approached, confirming that the two results are consistent with one another.

In Section 5.3 it was shown that close to the anti-adiabatic limit, the diagonal steady state density matrix elements associated with the eigenstates of the Frenkel-Holstein

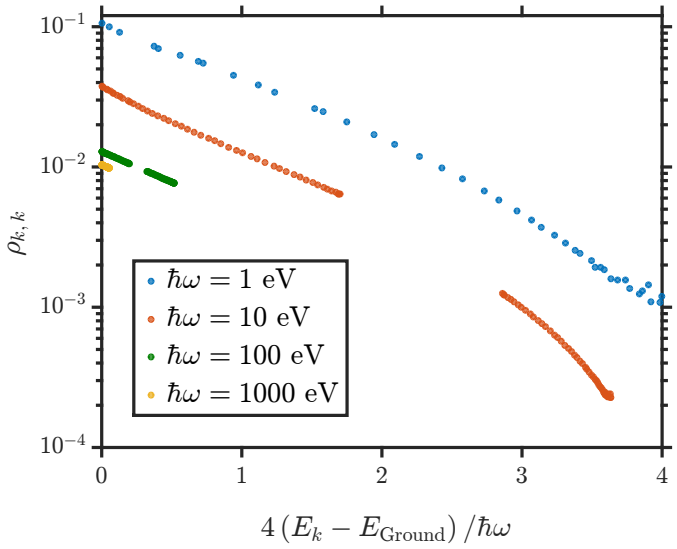


Figure 5.7: The dependence of the diagonal steady state density matrix elements, $\rho_{k,k}$, on the Boltzmann exponent, $4(E_k - E_{\mathrm{ground}})/\hbar\omega$ for a $L = 99$ site Frenkel-Holstein model with $\lambda = 1.6$ eV. The different coloured data points correspond to different values of the phonon energy, $\hbar\omega$.

model in the vibrational ground state, take the following Boltzmann form:

$$\rho_{k,k} \sim \exp[-E_{k,0}/T] \tag{5.74}$$

where the effective temperature, T, is proportional to the harmonic oscillator phonon energy, $\hbar\omega$:

$$T = \frac{\hbar\omega}{4} \tag{5.75}$$

These diagonal density matrix elements can be computed numerically to ascertain their energy dependence away from the anti-adiabatic limit, the results of which are given in Fig. 5.7, for several values of the phonon energy, $\hbar\omega$. The diagonal density matrix elements are given on a semi-log plot against $(E_k - E_{\mathrm{Ground}})/T$, to help identify deviations from Boltzmann behaviour. As expected, for large values of $\hbar\omega$, the numerically obtained diagonal density matrix elements are "exactly" described by Eq. (5.74). However, far

away from the anti-adiabatic limit, the numerically obtained diagonal density matrix elements still appear to exhibit this Boltzmann behaviour for $E_k \ll \hbar\omega$, with deviations only appearing at higher energies (for example, in the 'bending' of the coefficients in the upper band of the $\hbar\omega = 10$ eV result). The fact that Eq. (5.74) appears to hold for $E_k \ll \hbar\omega$, irrespective of the value of the phonon energy, is entirely consistent with the analytical solution for the steady state in the adiabatic limit, which can be thought of as a zero temperature Boltzmann state (i.e., it consists entirely of the ground state adiabatic VRSs).

Experimentally it is known that during the exciton relaxation dynamics within polymer systems, the exciton relaxes onto a single chromophore along the polymer chain. The steady state solution of the exciton relaxation dynamics therefore describes these possible chromophore states. For the chromophore states described by this theory to be physically realistic, they must have associated with them short ranged exciton-phonon, exciton coherence and exciton localisation lengths (as discussed previously in Chapter 4). We now consider each of these properties in turn, with regards to the Lindblad steady state.

5.5.1 Exciton-Polaron Formation

In real polymer systems, the low energy chromophore states are associated with short-ranged exciton-phonon correlations and are therefore referred to as exhibiting exciton-polaron character. As discussed in Section 4.2.1, the effective size of the exciton-polaron (i.e., the range of these exciton-phonon correlations) can be described by the exciton-phonon correlation function [62]:

$$C_n^{\text{ex-ph}} = \sum_m \langle \hat{a}_m^\dagger \hat{a}_m \hat{Q}'_{m+n} \rangle \tag{5.76}$$

where $\hat{Q}'_m$ is the nuclear displacement operator for the harmonic oscillator on site m, given in dimensionless units defined by Eq. (2.32). As achieved previously for the exciton coherence and exciton localisation correlation functions (see Chapter 4), an exciton-phonon correlation number can be defined:

$$N_{\text{ex-ph}} = \frac{1}{C_0^{\text{ex-ph}}} \sum_n C_n^{\text{ex-ph}} \tag{5.77}$$

As the exciton-phonon correlation function is normalised (i.e., $\sum_n C_n^{\text{ex-ph}} = 1$) for eigenstates of the Frenkel-Holstein model, this expression can be simplified as follows:

$$N_{\text{ex-ph}} = \left[\sum_m \langle \hat{a}_m^\dagger \hat{a}_m \hat{Q}'_m \rangle \right]^{-1} \tag{5.78}$$

Physically, this quantity corresponds to the average number of sites/moieties over which the exciton-phonon correlations persist.

The orange curve in Fig. 5.8 shows this exciton-phonon correlation number for the ground state of a $L = 99$ site Frenkel-Holstein model, for several values of the phonon energy, $\hbar\omega$. As expected, this quantity satisfies $N_{\text{ex-ph}} = 1$ in the anti-adiabatic limit (i.e., as $\hbar\omega / \langle J \rangle \to \infty$, the exciton-phonon correlations become entirely local) with the quantity increasing as the adiabatic limit is then approached (i.e., as $\hbar\omega / \langle J \rangle \to 0$, the exciton-phonon correlations become 'long-ranged'). Also shown in this figure is the exciton-phonon correlation number for the steady state solution, given by the solid blue curve. The exciton-phonon correlation number, $N_{\text{ex-ph}}$, shows the same trend with $\hbar\omega$ for both the steady state solution and the ground state, where in both cases the values of this quantity are very similar. As the VRSs of the Frenkel-Holstein model exhibit exciton-polaron character (see Section 2.5), this confirms that the steady state also exhibits this

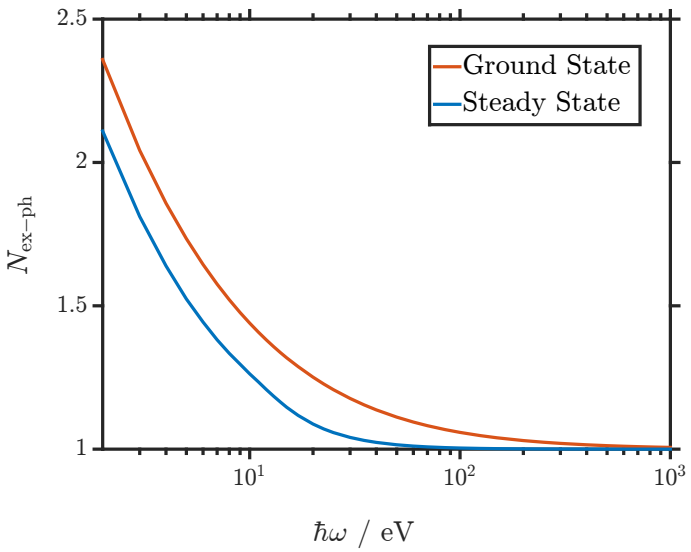


Figure 5.8: The dependence of the steady state exciton-phonon correlation number, $N_{\text{ex-ph}}$, on the harmonic oscillator phonon energy, $\hbar\omega$, for a $L = 99$ site Frenkel-Holstein model (given by the solid blue curve). Additionally, the ground state exciton-phonon correlation number, $N_{\text{ex-ph}}$, is given by the solid orange curve in this figure.

property as well. This explains why the LFS approach is able to converge the steady state solution so efficiently, as only basis states with short ranged exciton-phonon correlations are needed to accurately describe the steady state, which can be included through only a few generation steps within the LFS scheme.

We now compare the steady state exciton-phonon correlation function to the corresponding correlation function obtained from the TEBD dynamics (discussed in Section 4.2.1). The solid blue curve in Fig. 5.9 corresponds to the exciton-phonon correlation function at $t = 60$ fs, associated with the TEBD dynamics of an initial QEES given in Fig. 4.2. A $L = 99$ site Frenkel-Holstein model was used for this simulation, with $\hbar\omega = 0.2$ eV and $\lambda = 1.6$ eV. In addition, the dashed black curve corresponds to the steady state exciton-phonon correlation function, within the same Frenkel-Holstein model. Both results show good agreement with one another, confirming that using perturbation theory to obtain the steady state solution of the dynamics is valid for this parameter set

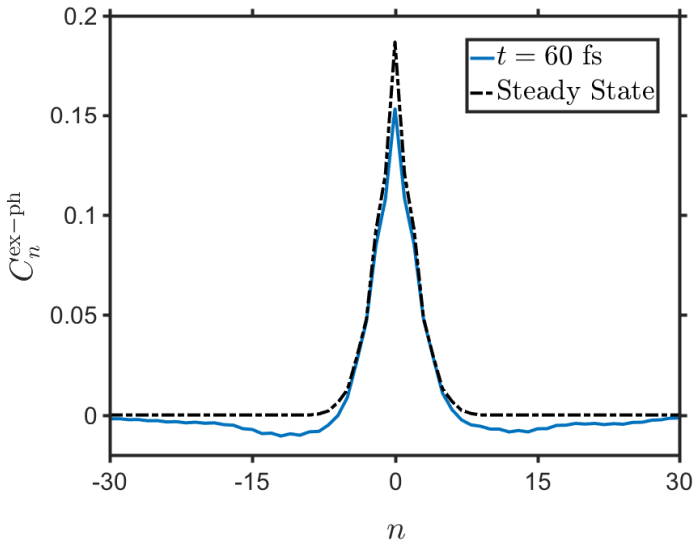


Figure 5.9: The exciton-phonon correlation function, $C_n^{\text{ex-ph}}$, at $t = 60$ fs obtained using the TEBD technique (given by the solid blue curve), for an initial QEES given in Fig. 4.2. The parameters $\hbar\omega = 0.2$ eV and $\lambda = 1.6$ eV were used. Additionally the corresponding steady state exciton-phonon correlation function is given by the dashed black curve.

(indeed, the agreement is better than was found between this TEBD correlation function and the ground state quantity, as was compared in Section 4.2.1 (see Fig. 4.7)). This agreement is also to be expected, as the exciton-polaron formation time scale (∼10 fs, as found in Section 4.2.1) is much less than the $t = 60$ fs for which the TEBD dynamics were obtained, suggesting that this quantity has already reached its equilibrium value during the dynamics. Slight deviations between the two results do however appear in the exciton-phonon correlation function at small values of n. This arises because the TEBD dynamics were performed with a phonon cut-off of $n_{\text{max}} = 2$, therefore reducing the size of the nuclear displacements which are able to be described within this basis. In addition, deviations within the 'tail' of the correlation function arise due to the presence of persistent oscillations in the dynamical quantity, as has already been discussed in Section 4.2.1.

5.5.2 Exciton Decoherence

The range of exciton coherences between different site/moieties in the model can be quantified by the exciton coherence correlation function [115, 116]:

$$C_n^{\mathrm{coh}} = \sum_m |\langle m|\hat{\rho}_{\mathrm{ex}}|m+n\rangle| \tag{5.79}$$

which corresponds to the average magnitude of the exciton coherences between sites a distance n apart. Within this expression, $|m\rangle$ is the state corresponding to the exciton residing on site m and $\hat{\rho}_{\mathrm{ex}}$ is the exciton reduced density matrix:

$$\hat{\rho}_{\mathrm{ex}} = \sum_v \langle v|\hat{\rho}|v\rangle \tag{5.80}$$

which is obtained by taking the trace of the system density matrix over the nuclear degrees of freedom (characterised by the quantum number v). As in Section 4.2.2, the exciton coherence number can be defined as follows:

$$N_{\mathrm{coh}} = \sum_n C_n^{\mathrm{coh}} \tag{5.81}$$

which corresponds to the average number of sites/moieties over which exciton coherences persist.

As discussed in Section 4.2.2, the decay in the exciton coherence number during the dynamics is dominated by the decay in the vibrational overlap factors arising from exciton-polaron formation. As the time scale for exciton decoherence is approximately equal to that for exciton-polaron formation, we would therefore expect the steady state exciton coherence correlation function to show good agreement with the TEBD result at $t =$

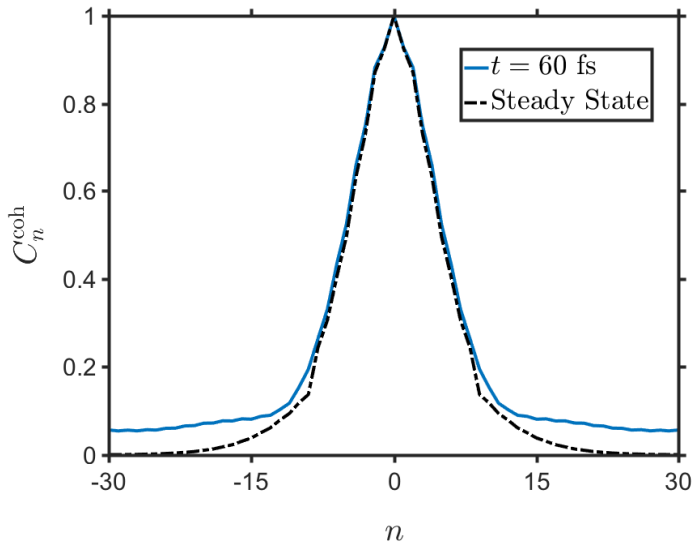


Figure 5.10: The exciton coherence correlation function, C_n^{coh}, at $t = 60$ fs obtained using the TEBD technique (given by the solid blue curve), for an initial QEES given in Fig. 4.2. The parameters $\hbar\omega = 0.2$ eV and $\lambda = 1.6$ eV were used. Additionally the corresponding steady state coherence correlation function is given by the dashed black curve.

60 fs. The solid blue curve in Fig. 5.10 corresponds to the exciton coherence correlation function at $t = 60$ fs, associated with the TEBD dynamics of an initial QEES given in Fig. 4.2. In addition, the dashed black curve corresponds to the steady state coherence correlation function, within the same Frenkel-Holstein model. Both results again show good agreement with one another, confirming that this correlation function has indeed reached its equilibrium value during the dynamics, as expected.

5.5.3 Exciton Density Localisation

In Section 4.2.3, it was found that the exciton density associated with the TEBD dynamics contained additional peaks which did not correspond to VRSs on the polymer chain (see Fig. 4.9). It was unclear whether these peaks were also present in the steady state or arose because the exciton density had not reached its equilibrium value for the times

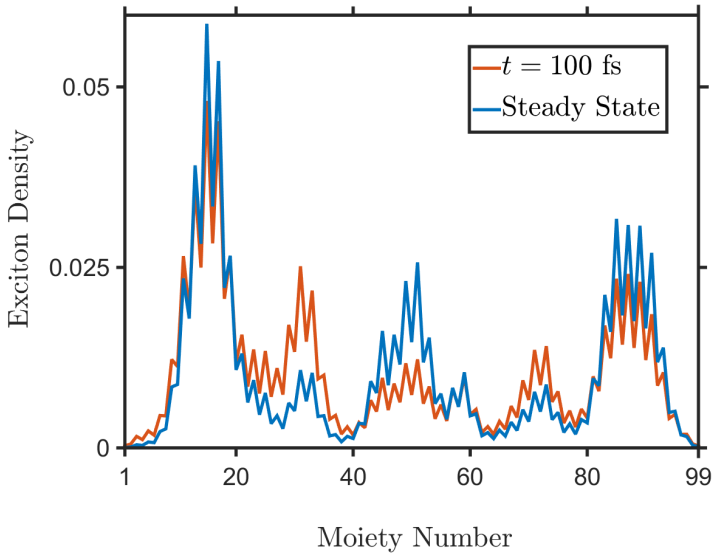


Figure 5.11: The exciton density at $t = 100$ fs, given by the solid orange curve, for an initial QEES given in Fig. 4.2. The parameters $\hbar\omega = 0.2$ eV and $\lambda = 1.6$ eV were used. Additionally the exciton density associated with the steady state solution is given by the solid blue curve.

considered. The solid orange curve in Fig. 5.11 corresponds to this exciton density at $t = 100$ fs during the TEBD dynamics, for an initial QEES given in Fig. 4.2. A $L = 99$ site Frenkel-Holstein model was used for this simulation, with $\hbar\omega = 0.2$ eV and $\lambda = 1.6$ eV. In addition, the solid blue curve corresponds to the steady state exciton density, within the same Frenkel-Holstein model. The fact that the steady state exciton density also contains these additional peaks confirms that the steady state does not solely consist of the VRSs of the model, for this realistic parameter set corresponding to a PPV polymer chain. This is not surprising, as earlier in Section 5.5 it was shown that the steady state solution only corresponds to the VRSs of the model in the adiabatic limit. This therefore means that the chromophore states described in this model are more complicated than initially thought (i.e., they do not just correspond to the low energy eigenstates of the Frenkel-Holstein model).

We now compare the exciton localisation correlation function, obtained for the same

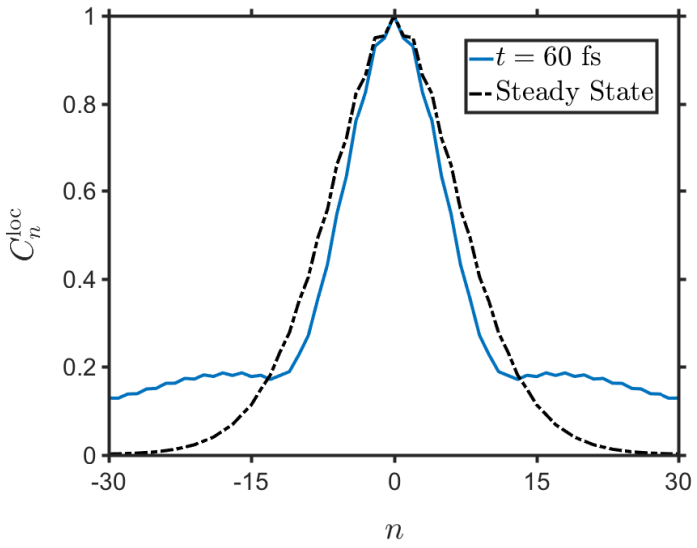


Figure 5.12: The exciton localisation correlation function, C_n^{loc}, at $t = 60$ fs obtained using the TEBD technique (given by the solid blue curve), for an initial QEES given in Fig. 4.2. The parameters $\hbar\omega = 0.2$ eV and $\lambda = 1.6$ eV were used. Additionally the corresponding steady state exciton localisation correlation function is given by the dashed black curve.

TEBD dynamics, with the identical quantity for the corresponding steady state solution. The exciton localisation correlation function can be used to quantify the spatial extent of the exciton and is given by [117, 118]:

$$C_n^{\mathrm{loc}} = \frac{\sum_m |\langle m, 0|\hat{\rho}|m+n, 0\rangle|}{\sum_m |\langle m, 0|\hat{\rho}|m, 0\rangle|} \tag{5.82}$$

where ket $|m,\, 0\rangle$ corresponds to the exciton being on site/moiety m, with the L harmonic oscillators in their ground state, signified by the '0' index. In Section 4.2.3, it was shown that this correlation function physically corresponds to the average magnitude of the exciton wavefunction overlap between sites/moieties a distance n apart. The solid blue curve in Fig. 5.12 corresponds to the exciton localisation correlation function at $t = 60$ fs, associated with the TEBD dynamics of an initial QEES given in Fig. 4.2. Additionally,

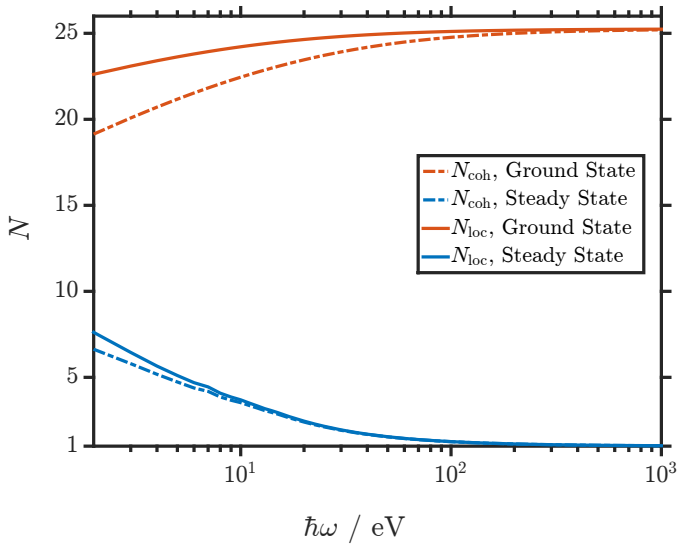


Figure 5.13: The dependence of the steady state coherence number, N_{coh} (given by the dashed blue curve) and the steady state localisation number, N_{loc} (given by the solid blue curve) on the harmonic oscillator phonon energy, $\hbar\omega$, for a $L = 99$ site Frenkel-Holstein model with $\lambda = 1.6$ eV. Additionally the ground state coherence number, N_{coh} (given by the dashed orange curve) and the ground state localisation number, N_{loc} (given by the solid orange curve) are also included.

the dashed black curve corresponds to the steady state exciton localisation correlation function, within the same Frenkel-Holstein model. These two results are significantly different, which is consistent with the exciton localisation correlation function having not yet reached its equilibrium value during the dynamics. This is to be expected, as the time scale associated with exciton density localisation is much longer compared to the ultra-fast exciton-polaron formation and exciton decoherence time scales, while also being considerably longer than the time for which the TEBD dynamics were performed (see Section 4.2.3).

As stated previously, for the chromophore states of the model to be physically realistic, they must have an associated short ranged exciton localisation length. To quantify the spatial extent of the exciton, the exciton localisation number can be defined as in

Section 4.2.3 [118]:

$$N_{\mathrm{loc}} = \sum_{n} C_{n}^{\mathrm{loc}} \tag{5.83}$$

which physically corresponds to the average number of moieties over which the exciton wavefunction overlap remains non-zero. The phonon energy dependence of the exciton localisation number is given by the solid curves in Fig. 5.13, for both the ground state (solid orange curve) and steady state (solid blue curve) of a $L = 99$ Frenkel-Holstein model. Also shown in this figure is the exciton coherence number, N_{coh}, defined by Eq. (5.81), for both the ground state (dashed orange curve) and the steady state (dashed blue curve). Firstly, we note that the exciton coherence number is always less than the corresponding exciton localisation number. This arises because the exciton coherence number contains an additional vibrational overlap contribution, which always acts to decrease its value relative to the corresponding exciton localisation number (see Sections 4.2.2 and 4.2.3). Despite this difference, the figure shows that both quantities display the same dependence on the phonon energy, for both the ground and steady state, and hence can be analysed together. Secondly, the value of the steady state exciton localisation number is always smaller than the corresponding value for the ground state (i.e., one of the VRSs of the polymer). The same is equally true for the exciton coherence number. This means that the concept of a chromophore (i.e., an exciton localised to a particular subset of a polymer chain, with short ranged exciton coherences) is still retained within the theory, even though the steady state solution does not correspond to the VRSs of the model. Indeed for the steady state solution, the exciton is most localised in the anti-adiabatic limit, where from this figure it is shown that $N_{\mathrm{loc}} = N_{\mathrm{coh}} = 1$ and hence the chromophores correspond to the sites/moieties of the model. However, this is also the limit for which the steady state solution is most different from the ground state (i.e., it corresponds to

an 'infinite temperature' exciton state).

In conclusion, there are therefore two factors which determine the properties associated with the chromophores defined within our model. Firstly, the Frenkel-Holstein parameters determine the properties associated with the energy eigenstates, which enter the steady state solution via the diagonal density matrix elements, $\rho_{k,k}$. In the adiabatic limit, it is solely this factor which determines the properties of the chromophores (i.e., the size of the chromophores in this limit are determined by the spatial extent of the VRSs, which is in turn controlled by the disorder within the model). Secondly, away from the adiabatic limit, the dissipation of the internal nuclear degrees of freedom by the environment also alters the properties associated with these chromophore states. In other words, the system-environment coupling is accounted for in this theory through the Lindblad master equation, the form of which directly determines the steady state solutions. This can be further understood by considering the dynamics of a single quantum trajectory within the quantum jump trajectory technique (as discussed in Section 4.2.3). In this section, it was shown that 'quantum jumps' lead to an immediate localisation of the exciton density for a particular quantum trajectory, which therefore results in a reduction of the chromophore size within the model. Hence physically, the system-environment coupling is able to effect the size of a chromophore through a 'wavefunction collapse' process, where local environment interactions with the internal phonon degrees of freedom act as a quantum measurement.

6

Correcting Ehrenfest Dynamics

So far in this thesis, we have solely considered the exciton-phonon dynamics induced by the coupling of the exciton to the high frequency C-C bond oscillations within a polymer. The time evolution of these nuclear degrees of freedom can be well described by using a truncated and static harmonic oscillator eigenstate basis within the time evolving block decimation (TEBD) technique, as illustrated in Chapter 4. From experiment, it is known that the coupling of the polymer's low frequency torsional modes are also important in describing the exciton relaxation dynamics within these systems [5]. However, nuclear degrees of freedom close to the classical limit are hard to describe within our current framework, as a large number of harmonic oscillator eigenstates must be retained, leading to an unmanageably large Hilbert space basis. While using Ehrenfest trajectories seems a more sensible approach to describe such nuclear degrees of freedom, their inability to describe the branching of a trajectory on passing through a conical intersection leads to unphysical dynamics, as discussed in Section 4.1 [22, 23].

In this chapter we introduce two methods, developed by us, which correct the unphysical properties of Ehrenfest dynamics, such that the nonadiabatic dynamics of nuclei close to the classical limit can be accurately obtained. The underlying theory associated with each method is outlined and its validity is then demonstrated by applying the methods to the Frenkel-Holstein and the two-level conical intersection models, both of which were introduced in Chapter 2.

6.1 TEBD-Ehrenfest

The harmonic oscillator eigenstates, $|n\rangle$, used in this thesis as the nuclear basis within the TEBD technique, can be written as follows:

$$|n\rangle = \frac{1}{\sqrt{n!}} \left(\sqrt{\frac{2\lambda}{\hbar\omega}}\, \hat{b}'^{\dagger} \right)^{n} |0\rangle \tag{6.1}$$

where the dimensionless harmonic oscillator creation operator, $\hat{b}'^{\dagger}$, is defined as:

$$\hat{b}'^{\dagger} = \sqrt{\frac{\hbar\omega}{2\lambda}}\, \hat{b}^{\dagger} \tag{6.2}$$

so that taking the classical limit (where $\hbar\omega \to 0$) of a Hamiltonian represented in this basis is well defined, as discussed in Section 2.5. For these eigenstates, the ground state, $|0\rangle$, is a minimum uncertainty Gaussian wavepacket, with an average nuclear displacement and momentum of zero (i.e., $\langle \hat{Q}' \rangle = 0$ and $\langle \hat{P}' \rangle = 0$). From the definition given in Eq. (6.1), the excited states then correspond to a number of phonon excitations, n, about this ground state.

All of the harmonic oscillator eigenstates are associated with $\langle \hat{Q}' \rangle = 0$ and $\langle \hat{P}' \rangle = 0$. These states can therefore be generalised as follows:

$$|n,\, \alpha'\rangle = \frac{1}{\sqrt{n!}} \left(\sqrt{\frac{2\lambda}{\hbar\omega}}\, \hat{\bar{b}}'^{\dagger} \right)^{n} |\alpha'\rangle \tag{6.3}$$

and are referred to as generalised coherent states [129–131]. Now the 'ground state' corresponds to a coherent state $|\alpha'\rangle$; a minimum uncertainty Gaussian wavepacket with $\langle \hat{Q}' \rangle = \sqrt{2}\mathrm{Re}[\alpha']$ and $\langle \hat{P}' \rangle = \sqrt{2}\mathrm{Im}[\alpha']$, where the prime signifies that the coherent state parameter is scaled as in Eq. (6.2). In addition, the 'excited states' now correspond to

a number of phonon excitations, n, about this coherent state. These phonon excitations are created by:

$$\hat{\bar{b}}'^{\dagger} = \hat{b}'^{\dagger} - (\alpha')^{*} \tag{6.4}$$

which is the shifted harmonic oscillator creation operator.

The time evolving block decimation Ehrenfest technique (TEBD-Ehrenfest) proceeds as follows. We represent the time evolving state of our system in a basis of generalised coherent states:

$$|\psi\rangle = \sum_{j,\, n_1,..,\, n_L} C_{j,\, n_1,..,\, n_L}\, |j\rangle \otimes |n_1,\, \alpha'_1\big(\tilde{t}\,\big)\rangle \otimes \cdots \otimes |n_L,\, \alpha'_L\big(\tilde{t}\,\big)\rangle \tag{6.5}$$

where $|j\rangle$ is the exciton site basis. In addition, the coherent state parameters, α'_m, evolve so that the centre of each generalised coherent state always lies on the average nuclear displacement and momentum associated with the time evolving state, $|\psi\rangle$. In other words:

$$\alpha'_m = \frac{1}{\sqrt{2}} \Big(\langle\psi|\hat{Q}'_m|\psi\rangle + i\, \langle\psi|\hat{P}'_m|\psi\rangle \Big) \tag{6.6}$$

This means that phonon excitations in this technique now purely describe quantum fluctuations of the nuclear wavefunction about its average. Within this state representation, the time dependence of the probability amplitude tensor, $C_{j,\, n_1,..,\, n_L}$, can be obtained from a time-dependent Schrödinger like equation, which involves an effective Hamiltonian, $\hat{H}_{\text{eff}}$:

$$\dot{C}_{j,\, n_1,..,\, n_L} = -\frac{i}{\hbar\omega} \sum_{j',\, n'_1,..,\, n'_L} \langle j,\, n_1,..,\, n_L|\hat{H}_{\text{eff}}|j',\, n'_1,..,\, n'_L\rangle\, C_{j',\, n'_1,..,\, n'_L} \tag{6.7}$$

where:

$$|j,\, n_1,..,\, n_L\rangle = |j\rangle \otimes |n_1,\, \alpha'_1\big(\tilde{t}\,\big)\rangle \otimes \cdots \otimes |n_L,\, \alpha'_1\big(\tilde{t}\,\big)\rangle \tag{6.8}$$

This effective Hamiltonian accounts for the fact that the basis states are now time dependent. Finally, Eq. (6.7) is solved using the time evolving block decimation technique (TEBD), which was outlined in Section 3.3.

To implement this technique, expressions for the effective Hamiltonian, $\hat{H}_{\text{eff}}$ and the time derivative of the coherent state parameters, $\dot{\alpha}'_m$, need to be obtained. This is achieved as follows.

6.1.1 The Effective Hamiltonian

The parameters within the TEBD-Ehrenfest ansatz, given by Eq. (6.5), must be evolved such that the time-dependent Schrödinger equation is satisfied:

$$\frac{d\left|\psi\right\rangle}{d\tilde{t}} = -\frac{i}{\hbar\omega}\hat{H}\left|\psi\right\rangle \tag{6.9}$$

Inserting Eq. (6.5) into Eq. (6.9) gives the following expression for the time derivative of the probability amplitude tensor:

$$\begin{aligned}&\sum_{j,\,n_1,..,\,n_L} \dot{C}_{j,\,n_1,..,\,n_L}\left|j,\,n_1,..,\,n_L\right\rangle = \\ &-\sum_{j,\,n_1,..,\,n_L} C_{j,\,n_1,..,\,n_L}\left(\sum_m \left|j\right\rangle \otimes \left|n_1,\,\alpha'_1\right\rangle \otimes \cdots \otimes \left|n_m,\,\dot{\alpha}'_m\right\rangle \otimes \cdots \otimes \left|n_L,\,\alpha'_L\right\rangle + \frac{i}{\hbar\omega}\hat{H}\left|j,\,n_1,..,\,n_L\right\rangle\right)\end{aligned} \tag{6.10}$$

To proceed, the time derivative of a generalised coherent state can be written in the following compact form:

$$\left|n_m,\,\dot{\alpha}'_m\right\rangle = \frac{2\lambda}{\hbar\omega}\left[\tfrac{1}{2}\left(\left(\alpha'_m\right)^*\dot{\alpha}'_m - \left(\dot{\alpha}'_m\right)^*\alpha'_m\right) + \dot{\alpha}'_m\hat{\bar{b}}'^{\dagger}_m - \left(\dot{\alpha}'_m\right)^*\hat{\bar{b}}'_m\right]\left|n_m,\,\alpha'_m\right\rangle \tag{6.11}$$

where $\hat{\bar{b}}'^{\dagger}_m$ is the shifted harmonic oscillator creation operator for site m, defined in Eq. (6.4). The derivation of this expression is included in Appendix D. Inserting Eq. (6.11) into Eq. (6.10) and comparing the resulting expression to Eq. (6.7) leads to the following equation for the effective Hamiltonian:

$$\hat{H}_{\text{eff}} = \hat{H} - 2i\lambda \sum_m \left[\tfrac{1}{2} \left((\alpha'_m)^* \, \dot{\alpha}'_m - (\dot{\alpha}'_m)^* \, \alpha'_m \right) + \dot{\alpha}'_m \hat{\bar{b}}'^{\dagger}_m - (\dot{\alpha}'_m)^* \, \hat{\bar{b}}'_m \right] \tag{6.12}$$

6.1.2 Generalised Coherent State Evolution

The coherent state parameters within the TEBD-Ehrenfest technique are evolved so that the centre of the generalised coherent states always lie on the average nuclear displacements and momenta associated with the time evolving state, $|\psi\rangle$. Defining shifted nuclear displacement and momenta operators as follows:

$$\begin{aligned} \hat{\bar{Q}}'_m &= \hat{Q}'_m - \sqrt{2}\text{Re}\left[\alpha'_m\right] \\ \hat{\bar{P}}'_m &= \hat{P}'_m - \sqrt{2}\text{Im}\left[\alpha'_m\right] \end{aligned} \tag{6.13}$$

means that $\langle \hat{\bar{Q}}'_m \rangle = 0$ and $\langle \hat{\bar{P}}'_m \rangle = 0$ must be satisfied throughout the whole time evolution. In other words, using the shifted harmonic oscillator destruction operator, defined as:

$$\hat{\bar{b}}'_m = \frac{1}{\sqrt{2}} \left(\hat{\bar{Q}}'_m + i \hat{\bar{P}}'_m \right) \tag{6.14}$$

the following expression must be satisfied:

$$\frac{d}{d\tilde{t}} \langle \psi | \hat{\bar{b}}'_m | \psi \rangle = 0 \tag{6.15}$$

if the starting values of the parameters α'_m are chosen so that $\langle \hat{\bar{b}}'_m \rangle = 0$ at the start of the dynamics.

Working in the time evolving generalised coherent state basis, the time derivative in Eq. (6.15) can be performed using Eq. (6.7), to give:

$$\langle \psi | \left[\hat{\bar{b}}'_m, \hat{H}_{\text{eff}} \right] | \psi \rangle = 0 \tag{6.16}$$

Inserting the expression for the effective Hamiltonian, $\hat{H}_{\text{eff}}$, given in Eq. (6.12) and rearranging leads to the following expression for the time dependence of the coherent state parameters, α'_m:

$$\frac{d\alpha'_m}{d\tilde{t}} = -\frac{i \langle \psi | \left[\hat{\bar{b}}'_m, \hat{H} \right] | \psi \rangle}{\hbar\omega \left(1 - \langle \psi | \hat{\mathbb{P}}_m | \psi \rangle \right)} \tag{6.17}$$

where we have used the commutation relation for the shifted harmonic oscillator creation/destruction operators in a truncated basis, which contains the $n_{\max} + 1$ generalised coherent states with the smallest quantum numbers:

$$\left[\hat{\bar{b}}'_m, \hat{\bar{b}}'^{\dagger}_j \right] = \frac{\hbar\omega}{2\lambda} \left(1 - \hat{\mathbb{P}}_m \right) \delta_{m,\,j} \tag{6.18}$$

In addition, $\hat{\mathbb{P}}_m$ is a projection operator defined as follows:

$$\hat{\mathbb{P}}_m = (n_{\max} + 1) \, | n_{\max},\, \alpha'_m \rangle \, \langle n_{\max},\, \alpha'_m | \tag{6.19}$$

Therefore, the TEBD-Ehrenfest technique amounts to iteratively solving Eqs. (6.7), (6.12) and (6.17). To illustrate the procedure, we now apply this technique to the Frenkel-Holstein Hamiltonian.

6.1.3 The Frenkel-Holstein Model

The Frenkel-Holstein Hamiltonian, introduced in Section 2.5, has the following form [32, 57, 58]:

$$\hat{H}_{\mathrm{FH}} = \hat{H}_{\mathrm{F}} - \sqrt{2}\lambda \sum_m \hat{a}_m^\dagger \hat{a}_m \left(\hat{b}_m'^\dagger + \hat{b}_m'\right) + 2\lambda \sum_m \hat{b}_m'^\dagger \hat{b}_m' \tag{6.20}$$

where $\hat{H}_{\mathrm{F}}$ is the Frenkel Hamiltonian and λ is an exciton-phonon coupling parameter, which must remain constant when the classical limit is taken. This coupling parameter is given by:

$$\lambda = \frac{A^2 \hbar \omega}{2} \tag{6.21}$$

where A is the dimensionless exciton-phonon coupling parameter. Using the definition for the shifted harmonic oscillator creation operator given in Eq. (6.4), the Frenkel-Holstein Hamiltonian can be written as:

$$\begin{aligned}\hat{H}_{\mathrm{FH}} = \hat{H}_{\mathrm{F}} - \sqrt{2}\lambda \sum_m \left(\hat{a}_m^\dagger \hat{a}_m \left(\hat{\tilde{b}}_m'^\dagger + \hat{\tilde{b}}_m'\right) + \left((\alpha_m')^* + \alpha_m'\right) \hat{a}_m^\dagger \hat{a}_m\right) \\ + 2\lambda \sum_m \left(\hat{\tilde{b}}_m'^\dagger \hat{\tilde{b}}_m' + \alpha_m' \hat{\tilde{b}}_m'^\dagger + (\alpha_m')^* \hat{\tilde{b}}_m' + |\alpha_m'|^2\right)\end{aligned} \tag{6.22}$$

Inserting this expression for the Hamiltonian into Eq. (6.17) then leads to the following equation for the time dependence of the coherent state parameters, α_m':

$$\frac{d\alpha_m'}{d\tilde{t}} = -i\alpha_m' + \frac{i \langle \hat{a}_m^\dagger \hat{a}_m \rangle}{\sqrt{2}} + \frac{i\left(\langle \hat{a}_m^\dagger \hat{a}_m \rangle \langle \hat{\mathbb{P}}_m \rangle - \langle \hat{a}_m^\dagger \hat{a}_m \hat{\mathbb{P}}_m \rangle\right)}{\sqrt{2}\left(1 - \langle \hat{\mathbb{P}}_m \rangle\right)} \tag{6.23}$$

where we have used the commutation relation for the shifted harmonic oscillator creation/destruction operators given in Eq. (6.18), as well as the following relation involving

the phonon number operator:

$$\left[\hat{\bar{b}}'_m, \hat{\bar{b}}'^{\dagger}_j \hat{\bar{b}}'_j\right] = \frac{\hbar\omega}{2\lambda} \hat{\bar{b}}'_m \delta_{m,j} \tag{6.24}$$

From Eq. (6.23), we notice the following. Firstly, in the case when there are no phonons present in the generalised coherent state basis (i.e., $n_{\max} = 0$), $\langle \hat{\mathbb{P}}_m \rangle = 1$ from Eq. (6.19) and the equation for the time dependence of the coherent state parameters becomes undefined. This arises because our imposed requirement that $\langle \hat{\bar{b}}'_m \rangle = 0$ during the dynamics is satisfied for any evolution of the coherent state parameters, α'_m, in this case.

Secondly, to obtain accurate results within the TEBD-Ehrenfest technique, the number of phonons included within the generalised coherent state basis must be large enough, such that the population of the generalised coherent states with quantum number $n_{\max}$ is small (i.e., the expectation values $\langle \hat{a}_m \hat{a}_m \hat{\mathbb{P}}_m \rangle$ and $\langle \hat{\mathbb{P}}_m \rangle$ are approximately zero during the dynamics). Assuming that this is the case, a simplified expression for the time dependence of the coherent state parameters can be obtained, by setting these expectation values to zero in Eq. (6.23):

$$\frac{d\alpha'_m}{d\tilde{t}} = -i\alpha'_m + \frac{i \langle \hat{a}^{\dagger}_m \hat{a}_m \rangle}{\sqrt{2}} \tag{6.25}$$

This expression is identical to the analogous one used in Ehrenfest dynamics, as given in Section 3.2. Treating the coherent state parameters as encoding a classical nuclear displacement and momentum:

$$\alpha'_m = \frac{1}{\sqrt{2}} \left(q'_m + i p'_m\right) \tag{6.26}$$

illustrates that Eq. (6.25) is also equivalent to Newton's equations of motion for the

nuclear degrees of freedom in the Frenkel-Holstein model:

$$\begin{aligned} \frac{dq'_m}{d\tilde{t}} &= p'_m \\ \frac{dp'_m}{d\tilde{t}} &= \langle \hat{a}_m^\dagger \hat{a}_m \rangle - q'_m \end{aligned} \tag{6.27}$$

Hence the evolution of the coherent state parameters under Eq. (6.25) is more physically motivated, while also being well defined when there are no phonons present in the generalised coherent state basis.

Finally, inserting Eq. (6.25) into Eq. (6.12) gives the following expression for the effective Hamiltonian:

$$\begin{aligned} \hat{H}_{\text{eff}} = \hat{H}_{\text{F}} - 2\lambda \sum_m q'_m \hat{a}_m^\dagger \hat{a}_m - \sqrt{2}\lambda \sum_m \left(\hat{a}_m^\dagger \hat{a}_m - \langle \hat{a}_m^\dagger \hat{a}_m \rangle \right) \left(\hat{\bar{b}}_m'^\dagger + \hat{\bar{b}}'_m \right) \\ + 2\lambda \sum_m \hat{\bar{b}}_m'^\dagger \hat{\bar{b}}'_m + \lambda \sum_m \langle \hat{a}_m^\dagger \hat{a}_m \rangle \, q'_m \end{aligned} \tag{6.28}$$

where the last term is a constant and can be neglected. In the case where there are no phonons present in the generalised coherent state basis, only the first two terms in Eq. (6.28) are non-zero. These two terms are identical to the electronic Hamiltonian used in Ehrenfest dynamics, as given in Section 3.2.

Therefore, in the limit when no phonons are included in the basis, TEBD-Ehrenfest as outlined above is entirely equivalent to Ehrenfest dynamics. Adding phonons to the TEBD-Ehrenfest ansatz hence aids to correct Ehrenfest dynamics, by introducing fluctuations of the nuclear wavefunction about its average.

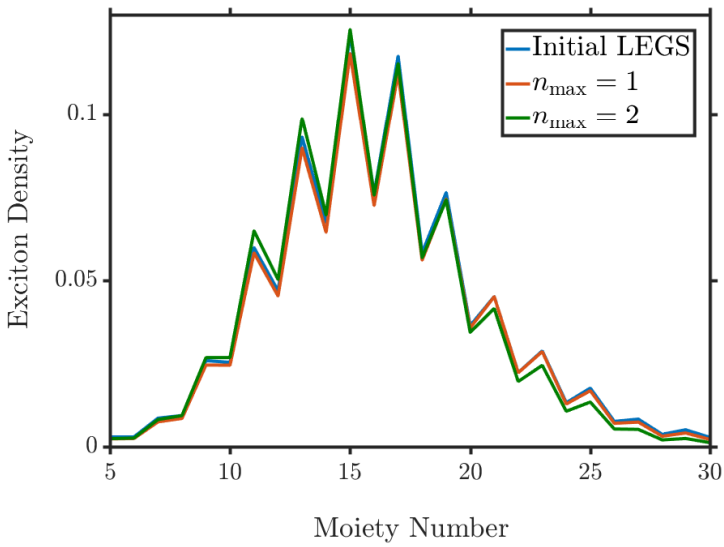


Figure 6.1: The exciton density at $t = 2$ ps associated with the exciton relaxation dynamics, for a $L = 99$ Frenkel-Holstein model. The dynamics were obtained using the standard TEBD technique, with parameters $\hbar\omega = 0.01$ eV and $\lambda = 1.6$ eV. The initial LEGS is given by the solid blue curve, while the other curves correspond to different phonon 'cut-offs', $n_{\max}$, used for the calculation.

6.1.4 Numerical Results

To test the method, we now apply it to calculate the exciton relaxation dynamics within a $L = 99$ site/moiety Frenkel-Holstein model. The parameters used for this model correspond to a PPV polymer chain (values of which are given in Table 2.2) with $\hbar\omega = 0.01$ eV and $\lambda = 1.6$ eV. These parameters were chosen so that the oscillator frequency corresponds to the torsional modes within the system and so that the exciton-phonon coupling parameter is consistent with the parameters $A = 4$ and $\hbar\omega = 0.2$ eV, as used in Chapter 4.

We first consider the exciton relaxation dynamics of an initial LEGS, given by the solid blue curve in Fig. 6.1. Also given in this figure is the exciton density at $t = 2$ ps, obtained using the standard TEBD technique for different values of the phonon 'cut-off', $n_{\max}$. For these low frequency nuclear modes, the standard TEBD technique with a site basis containing only a few phonons is completely unable to describe the dynamics correctly,

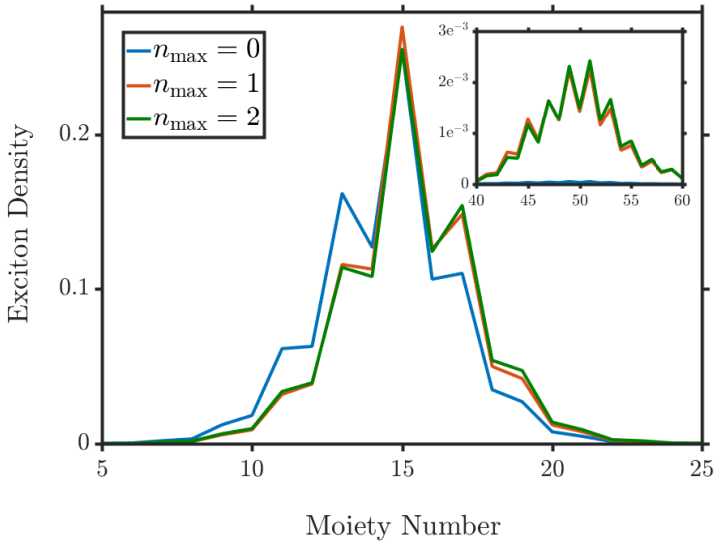


Figure 6.2: The exciton density at $t = 2$ ps associated with the exciton relaxation dynamics, for a $L = 99$ Frenkel-Holstein model. The parameters $\hbar\omega = 0.01$ eV and $\lambda = 1.6$ eV were used. The dynamics were obtained using the TEBD-Ehrenfest technique, for an initial LEGS given by the solid blue curve in Fig. 6.1. The different curves correspond to different phonon 'cut-offs', $n_{\max}$, used for the calculation. Additionally, the inset of the figure shows the exciton density peak located at the position of the central VRS of the model.

with the associated exciton density essentially unchanged from that of the starting LEGS.

In contrast, the TEBD-Ehrenfest technique is able to give essentially "exact" results for the relaxation dynamics of an initial LEGS, with a site basis containing only a few phonons. Figure 6.2 gives the exciton density at $t = 2$ ps calculated using this method, for several values of the phonon 'cut-off'. The results given in this figure have essentially converged for $n_{\max} = 1$, showing that only small quantum fluctuations about the average displacements and momenta of the nuclei are needed to correctly describe the nuclear wavefunction for this relaxation process. Indeed, the relaxation dynamics of an initial LEGS essentially corresponds to 'Born-Oppenheimer' like dynamics on a single adiabatic potential energy surface, as discussed in Section 4.2.4.

Comparing the exciton density at $t = 2$ ps to that of the initial LEGS (given by the

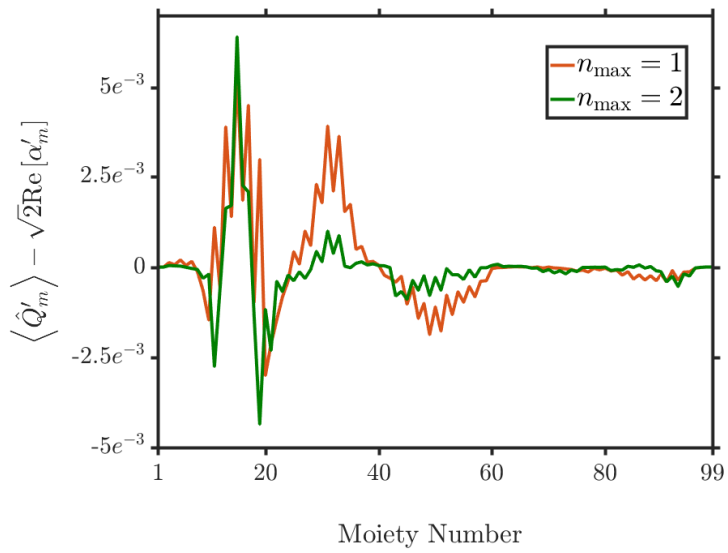


Figure 6.3: The difference between the average nuclear displacements of the system (given by $\langle \hat{Q}'_m \rangle$) and the displacements associated with the generalised coherent states (given by $\sqrt{2}\mathrm{Re}[\alpha'_m]$), for several values of the phonon 'cut-off', $n_{\max}$. This quantity was calculated at $t = 2$ ps during the exciton relaxation dynamics, for an initial LEGS.

solid blue curve in Fig. 6.1) shows that the dynamics have resulted in a large localisation of the exciton density. This is to be expected, as the coupling of the exciton to 'classical' nuclei results in the formation of a highly localised Landau polaron (see Section 2.5.1). However, one effect of adding 'phonons' to the Ehrenfest dynamics within the TEBD-Ehrenfest technique is the introduction of a non-zero transition probability for the system to transfer to a neighbouring chromophore. This can be seen in the inset of Fig. 6.2, where a peak appears in the exciton density located at the position of the central VRS of the model, which is completely absent in the Ehrenfest dynamics calculation (given by the solid blue curve).

We can also use the relaxation of an initial LEGS to ascertain whether evolving the coherent state parameters using Ehrenfest dynamics (i.e., by Eq. (6.25)) is sensible. Figure 6.3 shows the difference between the average nuclear displacements of the system (given by $\langle \hat{Q}'_m \rangle$) and the displacements associated with the generalised coherent states

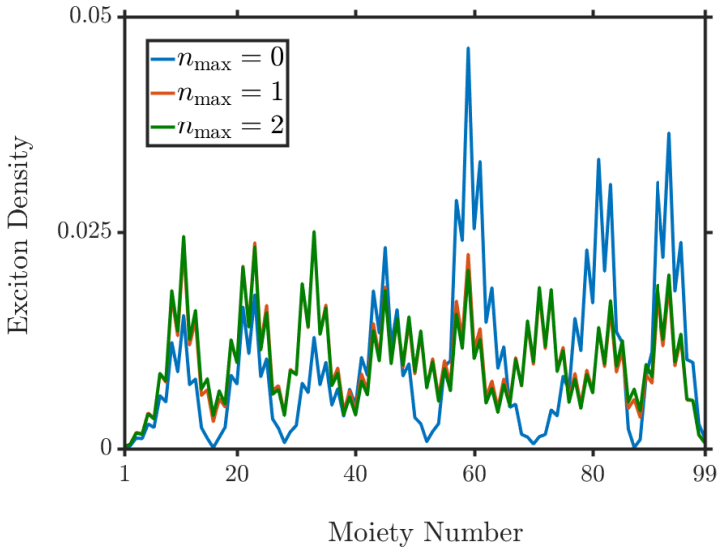


Figure 6.4: The exciton density at $t = 0.2$ ps associated with the exciton relaxation dynamics, for a $L = 99$ Frenkel-Holstein model. The parameters $\hbar\omega = 0.01$ eV and $\lambda = 1.6$ eV were used. The dynamics were obtained using the TEBD-Ehrenfest technique, for an initial QEES given by Fig. 4.2. The different curves correspond to different phonon 'cut-offs', $n_{\max}$, used for the calculation.

(given by $\sqrt{2}\mathrm{Re}[\alpha'_m]$), for several values of the phonon 'cut-off', $n_{\max}$. If the coherent state parameters were evolved using Eq. (6.23), then the quantity $(\langle \hat{Q}'_m \rangle - \sqrt{2}\mathrm{Re}[\alpha'_m])$ would necessarily be zero and the basis states would definitely be evolved correctly. However in this figure, it is shown that the values of this quantity remain small when the coherent state parameters are instead evolved using Eq. (6.25), confirming that this approximate expression also correctly evolves the basis states so that they well describe the average nuclear displacements associated with the system, as originally designed.

Finally, the TEBD-Ehrenfest technique is applied to the exciton relaxation dynamics of an initial QEES. This calculation was much more difficult to perform, as the entanglement between sites was found to increase much more rapidly than compared to the analogous dynamics for an initial LEGS. This meant that it was only feasible to obtain the dynamics for much shorter times of $t = 0.2$ ps. The exciton density associated with this time is given

in Fig. 6.4, for several values of the phonon 'cut-off'. These results have again converged for $n_{\max} = 1$, showing that the TEBD-Ehrenfest technique is able to accurately describe the relaxation dynamics for these extremely short times (i.e., for times significantly less than the vibrational time period of the nuclear degrees of freedom, which is ≈ 0.4 ps). However, the growth of the entanglement within the calculation means that the technique is ill-suited to describe the relaxation dynamics of a QEES over any useful time scale.

The reason that the TEBD-Ehrenfest technique struggles to efficiently describe the relaxation dynamics of an initial QEES can be understood by considering how the system behaves on passing through a conical intersection. Figure 6.5 shows the probability distribution for the x' nuclear displacement within the two-level conical intersection model (introduced in Section 2.1) as a function of the dimensionless time, $\tilde{t}$. In this model, the conical intersection is positioned at $x' = 0$. Before the conical intersection is reached (i.e., for $x' > 0$), the x' nuclear coordinate is well described by a single classical trajectory and the TEBD-Ehrenfest technique can efficiently describe the dynamics. However, after the conical intersection is passed (i.e., for $x' < 0$), the dynamics are no longer well described by a single classical trajectory and a large number of phonons are needed within the TEBD-Ehrenfest technique to describe the resulting branching process. As the initial QEES corresponds to a high energy surface of the Frenkel-Holstein model, the exciton relaxation dynamics will therefore involve passing through many conical intersections. In the next section, we consider how the exciton relaxation dynamics of an initial QEES could be efficiently obtained, for nuclei close to the classical limit.

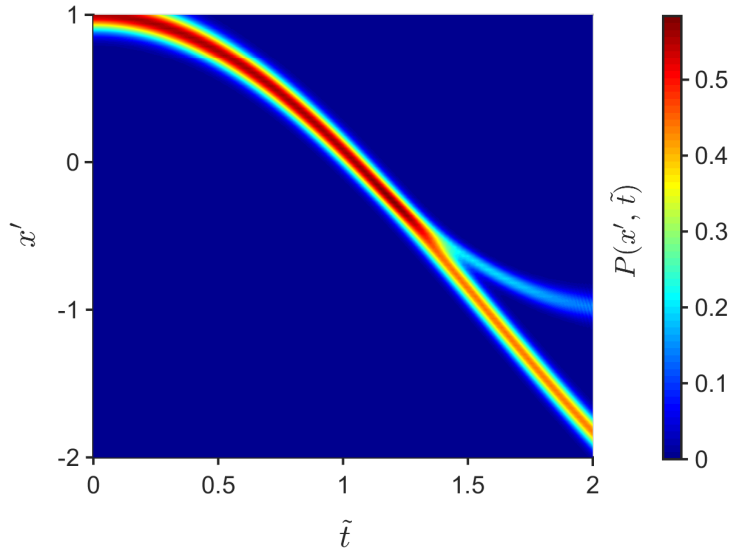


Figure 6.5: The probability distribution associated with the harmonic oscillator having a displacement x', $P\big(x', \tilde{t}\,\big)$, as a function of the dimensionless time, $\tilde{t} = \omega t$, after the photoexcitation process has occurred. This quantity was calculated within the two-level conical intersection model (introduced in Section 2.1) with $\lambda = 0.5$ eV and $\hbar\omega = 0.01$ eV.

6.2 Bundle Trajectories

While the nuclear dynamics close to a conical intersection are not described by a single Ehrenfest trajectory (i.e., a single average nuclear displacement and momentum) even in the classical limit, the branching process illustrated by Fig. 6.5 can be described by multiple trajectories. This is the basic idea behind bundle trajectory techniques [37].

In other words, consider a quantum state of the system, which at time $\tilde{t} = 0$ has the following form:

$$|\psi\big(\tilde{t} = 0\big)\rangle = |\psi_{\text{el}}\rangle \otimes |\alpha'_1\rangle \otimes \cdots \otimes |\alpha'_L\rangle \tag{6.29}$$

where $|\psi_{\text{el}}\rangle$ is a quantum state involving the electronic degrees of freedom and $|\alpha'_m\rangle$ is a coherent state for the nuclear coordinate m. The prime signifies that the coherent states

have been scaled as follows:

$$\alpha'_m = \sqrt{\frac{\hbar\omega}{2\lambda}}\,\alpha_m \tag{6.30}$$

so that they are well defined in the classical limit. Within a bundle trajectory technique, observables associated with the subsequent dynamics are given as an average over N_{traj} trajectories:

$$\langle\hat{O}\rangle = \frac{1}{N_{\text{traj}}}\sum_{j=1}^{N_{\text{traj}}}\langle\psi_j|\hat{O}|\psi_j\rangle \tag{6.31}$$

where each trajectory, $|\psi_j\rangle$, has a mean-field ansatz and is evolved using Ehrenfest dynamics:

$$|\psi_j(\tilde{t})\rangle = |\psi_{\text{el},j}\rangle \otimes |\alpha'_{1,j}\rangle \otimes \cdots \otimes |\alpha'_{L,j}\rangle \tag{6.32}$$

The time evolution for each trajectory differs, as the nuclear displacements and momenta at time $\tilde{t} = 0$ (i.e., $x'_m = \sqrt{2}\text{Re}\left[\alpha'_{m,j}\right]$ and $p'_m = \sqrt{2}\text{Im}\left[\alpha'_{m,j}\right]$) are sampled from the following Gaussian probability distributions:

$$\begin{aligned} P(x'_m) &= \sqrt{\frac{2\lambda}{\pi\hbar\omega}}\exp\left[\frac{-2\lambda\left(x'_m - \sqrt{2}\text{Re}\left[\alpha'_m\right]\right)^2}{\hbar\omega}\right] \\ P(p'_m) &= \sqrt{\frac{2\lambda}{\pi\hbar\omega}}\exp\left[\frac{-2\lambda\left(p'_m - \sqrt{2}\text{Im}\left[\alpha'_m\right]\right)^2}{\hbar\omega}\right] \end{aligned} \tag{6.33}$$

which correspond to the quantum uncertainty associated with the nuclear coordinates of the starting coherent states given in Eq. (6.29). Sampling the nuclear coordinates from these distributions is entirely equivalent to sampling from the corresponding Classical Wigner distribution [132]:

$$P(x'_m)P(p'_m) = \frac{2\lambda}{\pi\hbar\omega}\int_{-\infty}^{\infty}\langle x'_m + z'|\alpha'_m\rangle^*\,\langle x'_m - z'|\alpha'_m\rangle\exp\left[\frac{4i\lambda p'_m z'}{\hbar\omega}\right]dz' \tag{6.34}$$

where $|x'_m - z'\rangle$ is the position eigenstate at nuclear displacement $x'_m - z'$.

To obtain exact quantum dynamics (i.e., dynamics that is an exact solution to the time-dependent Schrödinger equation) the equations of motion for the electronic degrees of freedom for each trajectory must be coupled. This gives rise to the multi-configurational Ehrenfest technique [133]. Such equations of motion are unstable when N_{traj} is large, because the overlap matrix between trajectories becomes singular when the Hilbert space basis becomes overcomplete. As we are only interested in obtaining the quantum dynamics in the classical limit, we postulate that using uncoupled trajectories will be sufficient in this case. Indeed, it is known that in the absence of conical intersections, the exact dynamics in the classical limit corresponds to uncoupled trajectories evolving adiabatically on a potential energy surface under Born-Oppenheimer dynamics [134, 135]. Additionally we find that uncoupled trajectories are also in principle sufficient to exactly describe the nonadiabatic dynamics at a conical intersection in the classical limit, as we will now illustrate.

6.2.1 A Conical Intersection in the Classical Limit

The quantum dynamics about a conical intersection can be described using the two-level conical intersection model, introduced previously in Section 2.1. The Hamiltonian for this model is given by [36, 37]:

$$\hat{H}_{\text{CI}} = \lambda \left(\hat{P}'_x\right)^2 + \lambda \left(\hat{P}'_y\right)^2 + \hat{H}_{\text{el}}(\hat{x}', \hat{y}') \tag{6.35}$$

where $\hat{P}'_x$ and $\hat{P}'_y$ are the momentum operators for the x and y nuclear degrees of freedom, scaled according to Eq. (6.30). Additionally, $\hat{H}_{\text{el}}(\hat{x}', \hat{y}')$ is the electronic Hamiltonian:

$$\hat{H}_{\text{el}}(\hat{x}', \hat{y}') = 2\lambda \begin{pmatrix} \hat{x}' & \hat{y}' \\ \hat{y}' & -\hat{x}' \end{pmatrix} + \lambda \left(\hat{x}'\right)^2 + \lambda \left(\hat{y}'\right)^2 \tag{6.36}$$

where $\lambda = A^2\hbar\omega/2$ is the electron-phonon coupling constant and $\hat{x}'$ and $\hat{y}'$ are the nuclear displacement operators for the two nuclear degrees of freedom.

Within this model, the mean-field trajectories take the form:

$$|\psi_j(\tilde{t})\rangle = (\psi_{1,j}\,|1\rangle + \psi_{2,j}\,|2\rangle) \otimes |\alpha'_{x,j}\rangle \otimes |\alpha'_{y,j}\rangle \tag{6.37}$$

where $|1\rangle$ and $|2\rangle$ are the diabatic electronic basis states and correspond to the basis used to represent the electronic Hamiltonian in Eq. (6.36). The parameters within this ansatz are evolved so that they solve the time-dependent self-consistent field equations, introduced in Section 3.2. For the two-level conical intersection model, this means that the time dependence of the coherent state parameters are given by:

$$\begin{aligned} \frac{d\alpha'_{x,j}}{d\tilde{t}} &= -i\alpha'_{x,j} - \frac{i}{\sqrt{2}}\left(|\psi_{1,j}|^2 - |\psi_{2,j}|^2\right) \\ \frac{d\alpha'_{y,j}}{d\tilde{t}} &= -i\alpha'_{y,j} - \frac{i}{\sqrt{2}}\left(\psi^*_{1,j}\psi_{2,j} + \psi^*_{2,j}\psi_{1,j}\right) \end{aligned} \tag{6.38}$$

while the time dependence of the electronic probability amplitudes are given by the following time-dependent Schrödinger like equation:

$$\frac{d}{d\tilde{t}} \begin{pmatrix} \psi_{1,j} \\ \psi_{2,j} \end{pmatrix} = -\frac{2i\lambda}{\hbar\omega} \begin{pmatrix} x'_j & y'_j \\ y'_j & -x'_j \end{pmatrix} \begin{pmatrix} \psi_{1,j} \\ \psi_{2,j} \end{pmatrix} \tag{6.39}$$

where $x'_j = \sqrt{2}\text{Re}\left[\alpha'_{x,j}\right]$ and $y'_j = \sqrt{2}\text{Re}\left[\alpha'_{y,j}\right]$. Together, these equations of motion

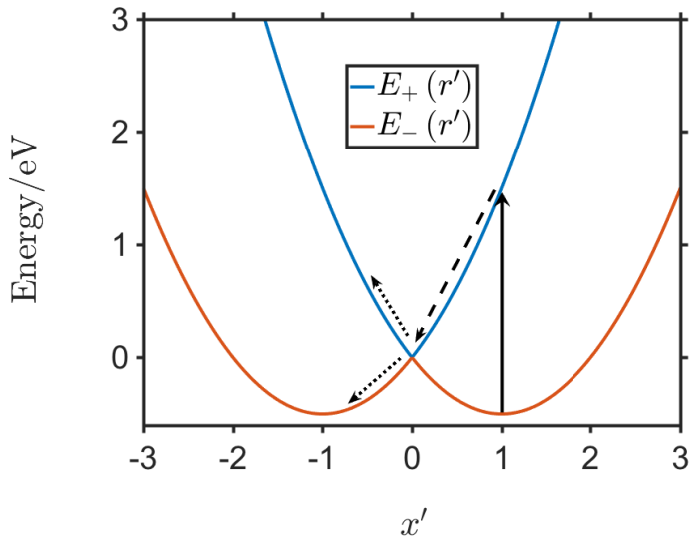


Figure 6.6: The potential energy surfaces for the two-level conical intersection model for $\lambda = 0.5$ eV, as a function of the x' nuclear displacement, with $y' = 0$. The solid arrow illustrates the photoexcitation process considered from the energy minimum of the lower E_- surface to the upper E_+ surface, from which the resulting quantum dynamics of interest occur. The resulting dynamics before the conical intersection is reached is labelled by the dashed line, while the dynamics after passing through the conical intersection is labelled by the dotted lines.

correspond to Ehrenfest dynamics for this model.

We again consider the following scenario, first introduced in Section 2.1. As illustrated in Fig. 6.6, the starting quantum state, which is formed by photoexcitation of the system from a minimum of the lower E_- surface, is given by:

$$|\psi(\tilde{t}=0)\rangle = |1\rangle \otimes |\alpha'_x = \tfrac{1}{\sqrt{2}}\rangle \otimes |\alpha'_y = 0\rangle \tag{6.40}$$

where the nuclear degrees of freedom are in coherent states, centred at $x' = 1$ and $y' = 0$, while the electron occupies the $|1\rangle$ diabatic state, which to a very good approximation corresponds to the $|\psi_+\rangle$ surface at this nuclear geometry. The gradient of the $|\psi_+\rangle$ surface at this initial nuclear geometry results in the subsequent dynamics passing through the

conical intersection at $x' = 0$, as shown in Fig. 6.6.

To show that the resulting dynamics around the conical intersection can be described by independent trajectories, we consider the time evolution of each degree of freedom within the model in turn.

6.2.1.1 The x Coordinate

Away from the conical intersection and in the classical limit, the nuclear degrees of freedom evolve on a single potential energy surface under Born-Oppenheimer dynamics. For the two-level conical intersection model, the adiabatic potential energies are obtained as the eigenvalues of the electronic Hamiltonian, given in Eq. (6.36) [37]:

$$E_+(r') = \lambda\,(r')^2 + 2\lambda r', \quad E_-(r') = \lambda\,(r')^2 - 2\lambda r' \tag{6.41}$$

where r is the distance from the conical intersection:

$$r' = \sqrt{(x')^2 + (y')^2} \tag{6.42}$$

For the starting quantum state given in Eq. (6.40), $\langle \hat{y}' \rangle = 0$ throughout the dynamics and we can therefore replace r' with $|x'|$ in the potential energy expressions.

At $\tilde{t} = 0$, the system initially populates the $|\psi_+\rangle$ surface. Hence the dimensionless force associated with the x nuclear coordinate, $F_{+,x}$, can be obtained from the gradient of the E_+ potential energy:

$$F_{+,\,x} = -\frac{1}{2\lambda}\frac{\partial E_+}{\partial x'} \simeq \begin{cases} -x' - 1, & \text{for} \quad x' \geq 0 \\ -x' + 1, & \text{for} \quad x' < 0 \end{cases} \tag{6.43}$$

which gives rise to Newton's equations of motion for the x nuclear coordinate evolving on

this surface:

$$\frac{d^2x_+}{d\tilde{t}^2} \simeq \begin{cases} -x'_+ - 1, & \text{for} \quad x'_+ \geq 0 \\ -x'_+ + 1, & \text{for} \quad x'_+ < 0 \end{cases} \tag{6.44}$$

As the x nuclear displacement initially satisfies $x' \geq 0$, we first solve the equations of motion for this situation. Using the initial conditions $x' = x'|_{\tilde{t}=0}$ and $p'_x = 0$, the following expression for the time evolution of the x coordinate on the $|\psi_+\rangle$ surface is obtained:

$$x'_+\big(\tilde{t}\,\big) = (x'|_{\tilde{t}=0} + 1)\cos\big(\tilde{t}\,\big) - 1, \qquad \text{for} \quad x'_+ \geq 0 \tag{6.45}$$

and is shown by part of the solid blue curve in Fig. 6.7 for $\lambda = 0.5$ eV and $x'_+ \geq 0$. Knowing that the conical intersection is located at $x' = y' = 0$, from Eq. (6.45) we can then obtain the time at which the system passes through the conical intersection, $\tilde{t}_{\rm c}$:

$$\tilde{t}_{\rm c} = \cos^{-1}\left[\frac{1}{x'|_{\tilde{t}=0} + 1}\right] \tag{6.46}$$

After passing through the conical intersection, the x nuclear displacement now satisfies $x' < 0$. Hence we can now solve the equations of motion, given by Eq. (6.44), for this situation as well. Requiring that the trajectory is continuous on passing through the conical intersection (i.e., $x' = 0$ and $p'_x = p'_x|_{\tilde{t}=\tilde{t}_{\rm c}}$ at time $\tilde{t} = \tilde{t}_{\rm c}$), the complementary expression to Eq. (6.45) for the time evolution of the x coordinate on the $|\psi_+\rangle$ surface is obtained:

$$x'_+\big(\tilde{t}\,\big) = -\cos\big(\tilde{t} - \tilde{t}_{\rm c}\,\big) + p'_x|_{\tilde{t}=\tilde{t}_{\rm c}}\sin\big(\tilde{t} - \tilde{t}_{\rm c}\,\big) + 1, \qquad \text{for} \quad x'_+ < 0 \tag{6.47}$$

and is shown by the remainder of the solid blue curve in Fig. 6.7. At $\tilde{t} = \tilde{t}_{\rm c}$, the conical

intersection induces a nonadiabatic partial population transfer to the $|\psi_-\rangle$ surface, as discussed in Section 2.1. Hence at times after $\tilde{t}_c$, there exist two x coordinate trajectories, which evolve independently on each surface. From the expression for the E_- potential energy given in Eq. (6.41), the Newton's equations of motion for the x coordinate evolving on this surface can be obtained:

$$\frac{d^2x'_-}{d\tilde{t}^2} = -x'_- - 1, \qquad \text{for} \quad x'_- < 0 \tag{6.48}$$

As the trajectories x_+ and x_- must have the same displacement and momentum at the crossing time, the conditions $x' = 0$ and $p'_x = p'_x|_{\tilde{t}=\tilde{t}_c}$ at time $\tilde{t} = \tilde{t}_c$ must be satisfied. Hence, the time evolution of the x coordinate on the $|\psi_-\rangle$ surface is given by:

$$x'_-\big(\tilde{t}\,\big) = -\left(x'|_{\tilde{t}=0} + 1\right)\cos\big(\tilde{t}\,\big) - 1, \qquad \text{for} \quad x'_- < 0 \tag{6.49}$$

and is shown by the solid orange curve in Figure 6.7, for $\lambda = 0.5$ eV. These classical trajectories reproduce the paths seen in the "exact" quantum probability distribution for the x nuclear coordinate, given in Figure 6.5.

6.2.1.2 The y Coordinate

The y nuclear coordinate enters into the model through the off-diagonal elements of the electronic Hamiltonian, given in Eq. (6.36). Therefore, the evolution of the probability distribution associated with this y nuclear displacement is important in determining the nonadiabatic electronic transition probability on passing through the conical intersection. The "exact" probability distribution associated with the y nuclear displacement is given in Fig. 6.8, as a function of the dimensionless time, $\tilde{t}$. The width of this distribution at

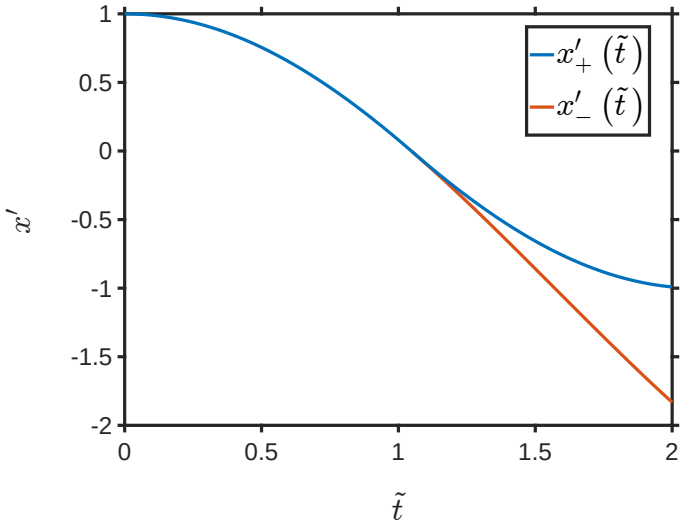


Figure 6.7: The time dependence of the x nuclear displacement associated with the evolution of the nuclei on the two adiabatic potential energy surfaces within the two-level conical intersection model, for $\lambda = 0.5$ eV. The solid blue curve corresponds to the dynamics on the $|\psi_+\rangle$ surface, while the solid orange curve corresponds to the dynamics on the $|\psi_-\rangle$ surface, starting at the crossing time $\tilde{t}_c$.

time $\tilde{t} = 0$ is determined by the harmonic oscillator frequency through the initial coherent state, given by Eq. (6.40). From Fig. 6.8, we see that this distribution narrows as the conical intersection is approached at $\tilde{t} = \pi/3$, which is induced by the electron-nuclear coupling term in the electronic Hamiltonian.

The narrowing of this y coordinate probability distribution can be understood from considering the dimensionless classical force acting on the y nuclear degree of freedom, when evolving on the $|\psi_+\rangle$ surface. Using the expression for the E_+ potential energy, given in Eq. (6.36), the force can be obtained as follows:

$$F_{+,y} = -\frac{1}{2\lambda}\frac{\partial E_+}{\partial y'} = -y' - \frac{y'}{\sqrt{(x')^2 + (y')^2}} \tag{6.50}$$

Hence the electron-nuclear coupling term in the model Hamiltonian leads to an additional

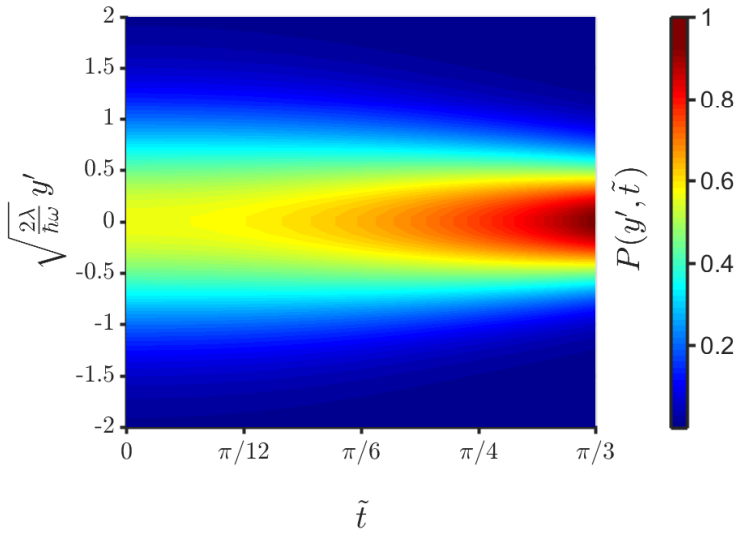


Figure 6.8: The probability distribution for the harmonic oscillator having a displacement y', $P\big(y',\,\tilde{t}\,\big)$, as a function of the dimensionless time, $\tilde{t} = \omega t$, after the photoexcitation process has occurred. This quantity was calculated within the two-level conical intersection model, introduced in Section 2.1, with parameters $\lambda = 0.5$ eV and $\hbar\omega = 0.01$ eV. The dynamics are shown up to the crossing time, $\tilde{t}_{\mathrm{c}} = \pi/3$.

restoring force, which pulls classical trajectories towards $y' = 0$. Such classical trajectories can be obtained by solving Newton's equations of motion for the y nuclear displacement evolving on the $|\psi_+\rangle$ surface, given by:

$$\frac{d^2 y'_+}{d\tilde{t}^2} = -y'_+ - \frac{y'_+}{\sqrt{\left(x'_+\right)^2 + \left(y'_+\right)^2}} \tag{6.51}$$

where x'_+ is given by Eq. (6.45) for $x'_+ \geq 0$ and the initial y nuclear displacement and momentum are sampled from the following Gaussian distributions:

$$\begin{aligned} P(y') &= \sqrt{\frac{2\lambda}{\pi\hbar\omega}}\exp\left[\frac{-2\lambda\left(y'\right)^2}{\hbar\omega}\right] \\ P\left(p'_y\right) &= \sqrt{\frac{2\lambda}{\pi\hbar\omega}}\exp\left[\frac{-2\lambda\left(p'_y\right)^2}{\hbar\omega}\right] \end{aligned} \tag{6.52}$$

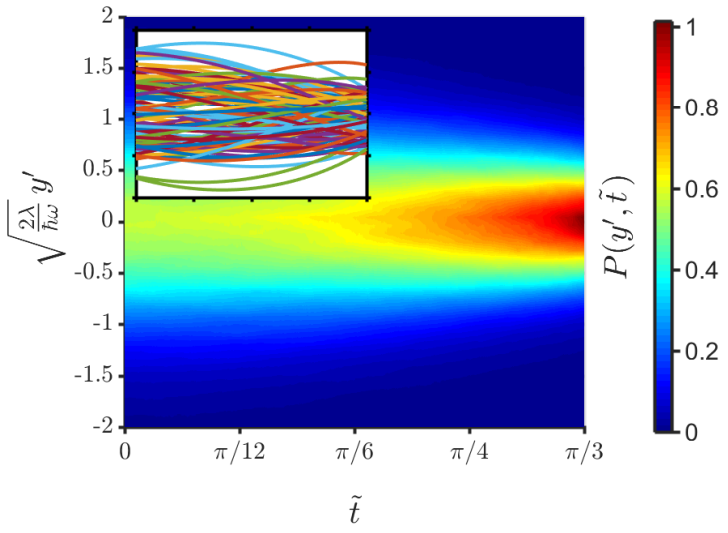


Figure 6.9: A histogram of the nuclear displacement, y', for a set of trajectories generated within the bundle trajectory technique, as a function of the dimensionless time. The inset gives some example trajectories that were used to obtain the histogram in the main figure. The parameters $\lambda = 0.5$ eV and $\hbar\omega = 0.01$ eV were used, while the dynamics are shown up to the crossing time, $\tilde{t}_c = \pi/3$.

Example trajectories generated in this way are given by the inset in Fig. 6.9. A classical probability distribution for the y nuclear displacement can then be obtained as a histogram of these classical trajectories. This classical probability distribution is given in Fig. 6.9 and is seen to reproduce the "exact" quantum result given in Fig. 6.8.

6.2.1.3 The Nonadiabatic Transition

On passing through the conical intersection at $r' = 0$, a nonadiabatic electronic transition occurs. As $y' \to 0$ during the dynamics in the classical limit, the diabatic and adiabatic basis states coincide (i.e., $|\psi_1\rangle = |\psi_+\rangle$ and $|\psi_2\rangle = |\psi_-\rangle$ for $x' > 0$, while $|\psi_1\rangle = |\psi_-\rangle$ and $|\psi_2\rangle = |\psi_+\rangle$ for $x' < 0$, as shown in Section 2.1). This means that the nonadiabatic transition can be quantified by $P_1\left(\tilde{t}\right)$, the probability that the system occupies the diabatic state $|1\rangle$. Figure 6.10 gives $P_1\left(\tilde{t}\right)$ for $\lambda = 0.5$ eV and several values of $\hbar\omega$, confirming that

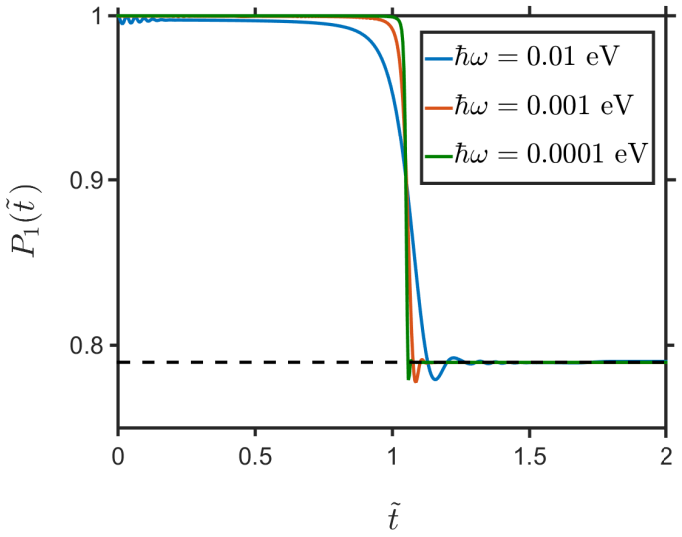


Figure 6.10: The probability of the system being in the $|1\rangle$ diabatic electronic state, $P_1\left(\tilde{t}\right)$, during the dynamics, for $\lambda = 0.5$ eV. The solid curves correspond to the "exact" quantum dynamics, for several values of $\hbar\omega$, while the dashed black line corresponds to the transition probability calculated using Eq. (6.55).

the nonadiabatic transition probability remains finite when the classical limit is taken.

From Fig. 6.10, the nonadiabatic transition is seen to occur almost instantaneously at the crossing time, $\tilde{t}_c$. Hence the expression for the time dependence of the exciton probability amplitudes, given by Eq. (6.39), should be well approximated by Taylor expanding the x and y nuclear displacements about the crossing time and retaining the first non-zero terms. Doing so leads to the following expression:

$$\frac{d}{d\tilde{t}}\begin{pmatrix}\psi_{1,j}\\ \psi_{2,j}\end{pmatrix} \simeq -\frac{2i\lambda}{\hbar\omega}\begin{pmatrix}p'_{x,j}|_{\tilde{t}=\tilde{t}_c}\left(\tilde{t}-\tilde{t}_c\right) & y'_j|_{\tilde{t}=\tilde{t}_c}\\ y'_j|_{\tilde{t}=\tilde{t}_c} & -p'_{x,j}|_{\tilde{t}=\tilde{t}_c}\left(\tilde{t}-\tilde{t}_c\right)\end{pmatrix}\begin{pmatrix}\psi_{1,j}\\ \psi_{2,j}\end{pmatrix} \tag{6.53}$$

which has the same form as the equation of motion for the Landau-Zener problem [136]. This model has an analytical expression for the nonadiabatic transition probability, given by:

$$P_{\text{trans}}(y') = \exp\left[-\frac{2\pi\lambda\left(y'\right)^2}{\hbar\omega p'_x}\right] \tag{6.54}$$

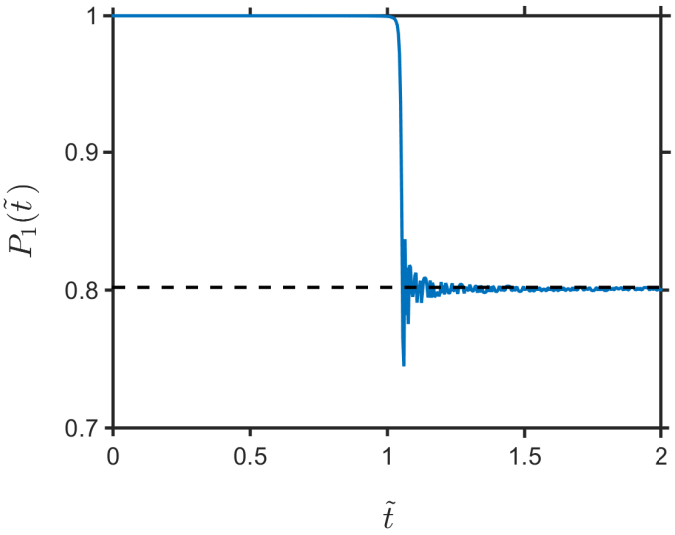


Figure 6.11: The probability of the system being in the $|1\rangle$ diabatic electronic state, $P_1\left(\tilde{t}\right)$, for a single typical Ehrenfest trajectory, given by the solid blue curve. The dashed black line corresponds to the transition probability for this trajectory calculated using the Landau-Zener formula given in Eq. (6.54). Additionally, the parameters $\lambda = 0.5$ eV and $\hbar\omega = 0.0001$ eV were used.

where y' and p'_x in this expression correspond to the value of these quantities at $\tilde{t} = \tilde{t}_c$. Figure 6.11 compares the nonadiabatic transition probability for a single typical bundle trajectory, evolved using Eqs. (6.38) and (6.39), with the Landau-Zener transition probability, given in Eq. (6.54). The agreement is essentially exact, confirming that the Taylor expansion used to obtain Eq. (6.54) is valid in the classical limit [137].

To obtain the nonadiabatic transition probability for the conical intersection model, given in Fig. 6.10, the Landau-Zener transition probability must be averaged over the probability distribution associated with the y nuclear displacement at the crossing time, $\tilde{t}_c$. This probability distribution at the crossing time is given in Fig. 6.12 for $\lambda = 0.5$ eV and several values of $\hbar\omega$. This figure shows that as the classical limit is taken, the distribution at the crossing point becomes Gaussian. Hence, the conical intersection

transition probability is given as follows:

$$P_{\text{Conical}} = \sqrt{\frac{2\lambda}{\hbar\omega\pi\sigma^2}} \int_{-\infty}^{\infty} P_{\text{trans}}(y') \exp\left[-\frac{2\lambda\,(y')^2}{\hbar\omega\sigma^2}\right] dy' = \left(1 + \frac{\pi\sigma^2}{p'_x}\right)^{-\frac{1}{2}} \tag{6.55}$$

where σ is the dimensionless standard deviation for this Gaussian distribution associated with the y nuclear displacement. Such an expression has already been obtained in the literature, but additionally assumed that $\sigma = 1$ [138]. However we know from the previous subsection that this distribution actually narrows as the crossing point is approached, meaning that $\sigma < 1$. The exact value of σ in the classical limit can be obtained from Fig. 6.12. Inserting this value for σ into Eq. (6.55) results in a value for the classical conical intersection transition probability, given by the dashed black line in Fig. 6.10. Indeed, this quantity coincides with the transition probabilities obtained from the "exact" quantum dynamics, for several values of $\hbar\omega$ close to the classical limit, given by the solid curves in this figure.

In conclusion, a classical treatment of the nuclear degrees of freedom in the two-level conical intersection model can well describe all the features of the associated dynamics in the classical limit. The problem with the bundle trajectory technique, however, is that Ehrenfest dynamics does not correctly describe the evolution of the nuclei after the conical intersection has been crossed. This is illustrated in Fig. 6.13, which gives the time dependent classical probability distribution associated with the x nuclear displacement, calculated using the standard bundle trajectory technique with $\lambda = 0.5$ eV and $\hbar = 0.01$ eV. After the nonadiabatic transition, the nuclei described by Ehrenfest dynamics evolve on the average potential energy associated with that trajectory, rather than evolving on each adiabatic potential energy surface independently. This means that the two distinct trajectories seen in the "exact" result given in Fig. 6.5 are not reproduced.

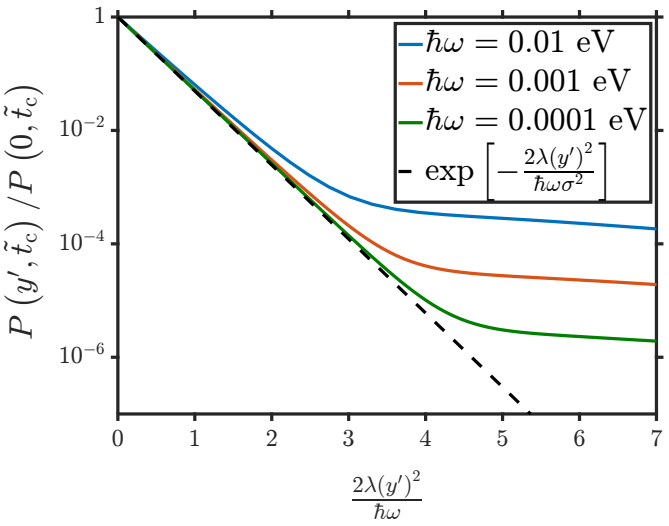


Figure 6.12: The probability distribution associated with the harmonic oscillator having a displacement y, $P\left(y', \tilde{t}\right)$, at the crossing time, $\tilde{t}_c$, for $\lambda = 0.5$ eV. The solid curves correspond to this probability distribution obtained for several values of $\hbar\omega$, while the dashed black line corresponds to a Gaussian distribution, with a dimensionless variance given by $\sigma^2 = 0.333$.

To correct for this, we will now allow each trajectory to branch at the crossing point.

6.2.2 Branching Bundle Trajectories

Within the branching bundle trajectory technique, the ansatz used for the quantum state of each trajectory changes as the conical intersection is passed. The conical intersection crossing time for trajectory j is determined as the time at which $x'_j = 0$. For times $\tilde{t} < \tilde{t}_c$, each trajectory has a mean-field ansatz, given by Eq. (6.37), and the technique becomes identical to the standard bundle trajectory technique introduced earlier. However after the conical intersection has been passed for $\tilde{t} \geq \tilde{t}_c$, each trajectory is allowed to 'branch',

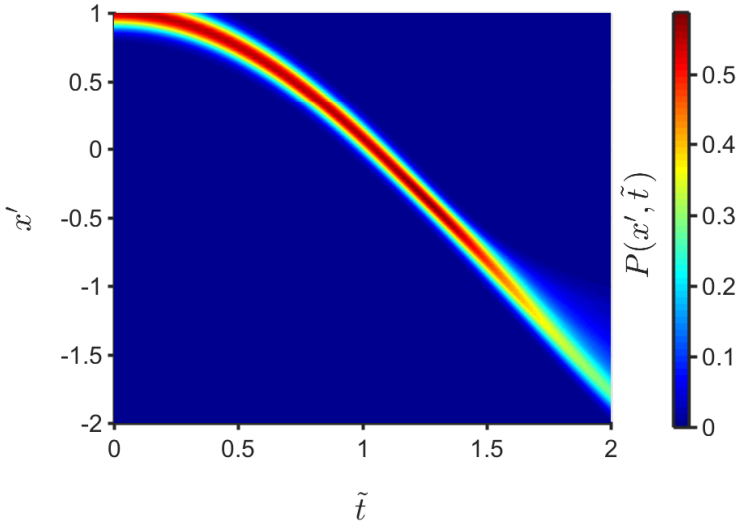


Figure 6.13: A histogram of the nuclear displacement, x', for a set of trajectories generated within the standard bundle trajectory technique, as a function of the dimensionless time. The parameters $\lambda = 0.5$ eV and $\hbar\omega = 0.01$ eV were used.

by now having an ansatz which is a linear combination of two mean-field states:

$$|\psi_j(\tilde{t})\rangle = (\psi_{1,1j}|1\rangle + \psi_{2,1j}|2\rangle) \otimes |\alpha'_{x,1j}\rangle \otimes |\alpha'_{y,1j}\rangle + (\psi_{1,2j}|1\rangle + \psi_{2,2j}|2\rangle) \otimes |\alpha'_{x,2j}\rangle \otimes |\alpha'_{y,2j}\rangle \tag{6.56}$$

The initial conditions for the parameters in this ansatz are chosen so that the dynamics associated with each trajectory is continuous as it passes through the crossing point. Thus, the coherent state parameters are chosen to be the same in the two ansatzes at time $\tilde{t} = \tilde{t}_c$ and the electronic probability amplitudes in the new ansatz at this time are given by:

$$\begin{aligned} |\psi_{\mathrm{el},1j}(\tilde{t} = \tilde{t}_c)\rangle &= |\psi_+\rangle \langle\psi_+|\psi_{\mathrm{el},j}(\tilde{t} = \tilde{t}_c)\rangle \\ |\psi_{\mathrm{el},2j}(\tilde{t} = \tilde{t}_c)\rangle &= |\psi_-\rangle \langle\psi_-|\psi_{\mathrm{el},j}(\tilde{t} = \tilde{t}_c)\rangle \end{aligned} \tag{6.57}$$

i.e., the $1j$ sub-trajectory is chosen to correspond to the $|\psi_+\rangle$ surface and the $2j$ sub-trajectory is chosen to correspond to the $|\psi_-\rangle$ surface at $\tilde{t} = \tilde{t}_c$. This choice therefore allows the nuclei corresponding to the $1j$ and $2j$ sub-trajectories to evolve independently on the two adiabatic surfaces, meaning that together both sub-trajectories should reproduce the two distinct 'paths' seen in the "exact" quantum dynamics after the crossing, given in Fig. 6.5.

The equations of motion for the coherent state parameters in the branched trajectory ansatz are chosen to be of a similar form to the Ehrenfest equations for the unbranched case:

$$\begin{aligned} \frac{d\alpha'_{x,\,1j}}{d\tilde{t}} &= -i\alpha'_{x,\,1j} - \frac{i}{\sqrt{2}}\Phi_{x,\,1j} \\ \frac{d\alpha'_{y,\,1j}}{d\tilde{t}} &= -i\alpha'_{y,\,1j} - \frac{i}{\sqrt{2}}\Phi_{y,\,1j} \end{aligned} \tag{6.58}$$

where $\Phi_{x,\,1j}$ and $\Phi_{y,\,1j}$ are effective densities, which determine the strength of the linear force acting on the x and y nuclear degrees of freedom for the $1j$ sub-trajectory. Possible expressions for these effective density terms will be given later. Inserting the branched trajectory ansatz, given by Eq. (6.56), into the time-dependent Schrödinger equation, while also using the time dependence of the coherent state parameters given by Eq. (6.58), leads to the following expression for the time evolution of the electronic probability amplitudes:

$$\begin{aligned} \frac{d}{d\tilde{t}}\begin{pmatrix}\psi_{1,\,1j}\\ \psi_{2,\,1j}\end{pmatrix} = -\frac{2i\lambda}{\hbar\omega}\Bigg[&\begin{pmatrix}T_{x,\,1j} & T_{y,\,1j}\\ T_{y,\,1j} & -T_{x,\,1j}\end{pmatrix}\begin{pmatrix}\psi_{1,\,1j}\\ \psi_{2,\,1j}\end{pmatrix} \\ &+\frac{\langle\alpha'_1|\alpha'_2\rangle}{\sqrt{2}\left(1-|\langle\alpha'_1|\alpha'_2\rangle|^2\right)}\begin{pmatrix}\Delta\alpha'_{x,\,j} & \Delta\alpha'_{y,\,j}\\ \Delta\alpha'_{y,\,j} & -\Delta\alpha'_{x,\,j}\end{pmatrix}\begin{pmatrix}\psi_{1,\,2j}\\ \psi_{2,\,2j}\end{pmatrix} - D_{1j}\begin{pmatrix}\psi_{1,\,1j}\\ \psi_{2,\,1j}\end{pmatrix}\Bigg] \end{aligned} \tag{6.59}$$

The right-hand side of this expression contains three terms. The first term involves the coupling of the probability amplitudes associated with the $1j$ sub-trajectory to its own

nuclear degrees of freedom. The strength of this coupling term is determined by the following parameter:

$$T_{x,\,1j} = x'_{1j} + \frac{\Delta\alpha'_{x,\,1j}\,|\langle\alpha'_1|\alpha'_2\rangle|^2}{\sqrt{2}\left(1-|\langle\alpha'_1|\alpha'_2\rangle|^2\right)} \tag{6.60}$$

where:

$$\begin{aligned}\Delta\alpha'_{x,\,1j} &= \alpha'_{x,\,1j} - \alpha'_{x,\,2j}\\ \langle\alpha'_1|\alpha'_2\rangle &= \langle\alpha'_{x,\,1j}|\alpha'_{x,\,2j}\rangle\,\langle\alpha'_{y,\,1j}|\alpha'_{y,\,2j}\rangle\end{aligned} \tag{6.61}$$

Additionally, the second term involves the coupling of the two sub-trajectories, while the last term is a phase factor, given by:

$$D_{1j} = \left(T_{x,\,1j} - \frac{x'_{1j}}{2}\right)\Phi_{x,\,1j} + \left(T_{y,\,1j} - \frac{y'_{1j}}{2}\right)\Phi_{y,\,1j} + \frac{\langle\alpha'_1|\alpha'_2\rangle\left(\Delta\alpha'_{x,\,1j}\Phi_{x,\,2j} + \Delta\alpha'_{y,\,1j}\Phi_{y,\,2j}\right)}{\sqrt{2}\left(1-|\langle\alpha'_1|\alpha'_2\rangle|^2\right)} \tag{6.62}$$

In the limit that the two sub-trajectories are far apart in space, $\langle\alpha'_1|\alpha'_2\rangle \to 0$ and, up to a phase factor, Eq. (6.59) reduces to the independent evolution of each sub-trajectory under the Ehrenfest equations of motion, given by Eq. (6.39). Therefore the sub-trajectory dynamics only differ from the standard bundle trajectory technique, for the time evolution close to the conical intersection. Additionally for $\tilde{t} \simeq \tilde{t}_{\mathrm{c}}$, $(1-|\langle\alpha'_1|\alpha'_2\rangle|^2) \simeq 0$ and the equation of motion for the electronic probability amplitudes given in Eq. (6.59) diverges. To keep this equation of motion stable, we introduce a tolerance factor, δ, so that terms which have a $1/\left(1-|\langle\alpha'_1|\alpha'_2\rangle|^2\right)$ factor are only included when $1-|\langle\alpha'_1|\alpha'_2\rangle|^2 > \delta$. Practically, the value of δ in our simulations is reduced until the dynamics converge.

To use this technique, we now need to find a sensible expression for the effective densities. We first consider the case where the chosen effective densities result in the equations of motion for the coherent state parameters, given by Eq. (6.38), becoming

identical to Ehrenfest dynamics for each sub-trajectory:

$$\begin{aligned}\Phi_{x,\,1j} &= \left(\frac{|\psi_{1,\,1j}|^2 - |\psi_{2,\,1j}|^2}{|\psi_{1,\,1j}|^2 + |\psi_{2,\,1j}|^2}\right) \\ \Phi_{y,\,1j} &= \left(\frac{\psi^*_{1,\,1j}\psi_{2,\,1j} + \psi^*_{2,\,1j}\psi_{1,\,1j}}{|\psi_{1,\,1j}|^2 + |\psi_{2,\,1j}|^2}\right)\end{aligned} \tag{6.63}$$

Figure 6.14 shows the time-dependent probability distribution associated with the x nuclear displacement for $\lambda = 0.5$ eV and $\hbar\omega = 0.01$ eV, calculated by this branching bundle trajectory technique. While the dynamics now correctly show two distinct classical trajectories that form after the conical intersection has been passed, these trajectories do not match those from the "exact" dynamics given in Fig. 6.5. Also, the nonadiabatic electronic transition probability obtained from the branching bundle trajectory technique, given by the solid orange curve in Fig. 6.15, is significantly different from the "exact" result, given by the solid blue curve in the same figure. The reason for this failure is because even though at time $\tilde{t} = \tilde{t}_{\rm c}$ the two sub-trajectories correspond to the two adiabatic surfaces, the evolution of the electronic probability amplitudes by Eq. (6.59) does not keep this the case.

One arbitrary way to fix the nuclear trajectories is to choose the effective densities such that the nuclei are forced to evolve on a single adiabatic surface:

$$\Phi_{x,1j} = \begin{cases} -\frac{x'_{1j}}{r'_{1j}}, & \text{for} \quad |\langle\psi_+|\psi_{\text{el},\,1j}\rangle|^2 \geq \frac{1}{2}\,|\langle\psi_{\text{el},\,1j}|\psi_{\text{el},\,1j}\rangle|^2 \\ \frac{x'_{1j}}{r'_{1j}}, & \text{for} \quad |\langle\psi_-|\psi_{\text{el},\,1j}\rangle|^2 < \frac{1}{2}\,|\langle\psi_{\text{el},\,1j}|\psi_{\text{el},\,1j}\rangle|^2 \end{cases} \tag{6.64}$$

i.e., the nuclei for a given sub-trajectory are evolved on the adiabatic surface for which that sub-trajectory has the greatest overlap. Forcing the nuclei to evolve correctly in this way gives a much improved nonadiabatic electronic transition probability, given by the solid green curve in Fig. 6.15. Indeed, this nonadiabatic electronic transition probability

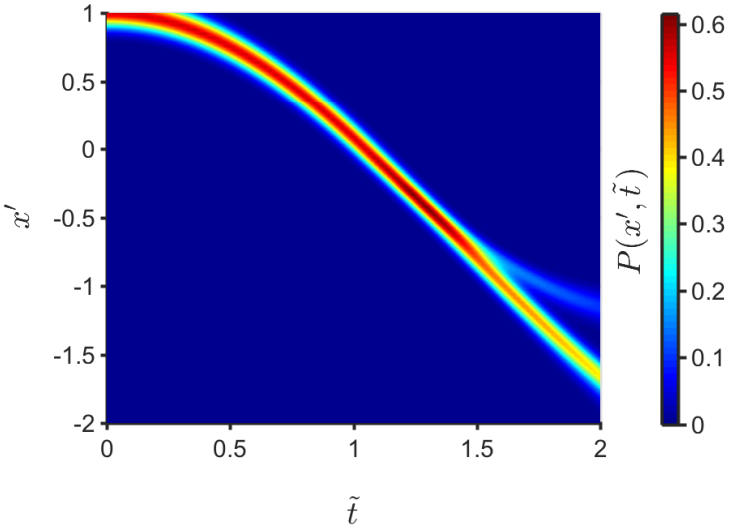


Figure 6.14: A histogram of the nuclear displacement, x', for a set of trajectories generated within the new branching bundle trajectory technique, as a function of the dimensionless time. After the crossing point, the nuclei associated with each sub-trajectory are evolved using Ehrenfest dynamics. Additionally the parameters $\lambda = 0.5$ eV and $\hbar\omega = 0.01$ eV were used.

becomes exact when the classical limit is taken.

In conclusion, the dynamics obtained using the branched bundle trajectory technique are sensitive to the equations of motion used to evolve the nuclei within the branched trajectory ansatz. Ehrenfest dynamics is insufficient to correctly evolve the nuclei and thus we suspect that a variational theory is probably needed, such as the variational multi-configurational Gaussian method (vMCG) [139]. While this technique still needs further development before it can be applied to more complicated models, such as the Frenkel-Holstein model, it does act to highlight the basic ingredients needed to describe the dynamics within systems containing conical intersections, for which the nuclear degrees of freedom are close to the classical limit.

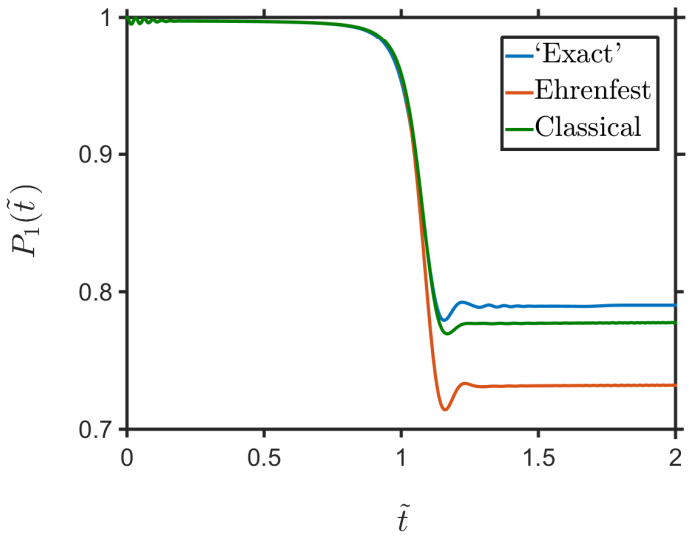


Figure 6.15: The probability of the system being in the $|1\rangle$ diabatic electronic state, $P_1\left(\tilde{t}\right)$, during the dynamics, for $\lambda = 0.5$ eV and $\hbar\omega = 0.01$ eV. The solid blue curve corresponds to the "exact" quantum dynamics. In addition, the solid orange curve corresponds to the branching bundle trajectory technique, where the nuclei associated with each sub-trajectory are evolved using Ehrenfest dynamics, while the solid green curve corresponds to the same technique, but where the nuclei from each sub-trajectory are now evolved on a single adiabatic surface.

7

Conclusion

A theory for the exciton relaxation dynamics within polymer systems has been developed and then applied to the specific case of PPV. This theory is consistent with experimental findings and offers new insight into the associated mechanisms involved within the dynamics.

In this thesis, the important nuclear and electronic degrees of freedom associated with the polymer chain are described using a parametrised Frenkel-Holstein model. Within this model, the sites correspond to the moieties of the polymer chain, the low energy excited electronic states are described by a single Frenkel exciton and the site harmonic oscillators are parametrised to describe a high frequency stretching mode for each moiety. The dynamics associated with the model are then described by a Lindblad master equation, which includes damping of the internal nuclear degrees of freedom by the polymer environment.

Firstly, the short time dynamics associated with this theory were obtained using the quantum jump trajectory and time evolving block decimation techniques, for realistic initial electronic excitation energies. The dynamics resulted in a decrease in the system energy, confirming that the dissipative terms in the Lindblad master equation were having the desired effect. Two distinct time scales arose from the time evolution: an ultra-fast time scale that depends on the Frenkel-Holstein parameters and corresponds to energy transfer from the exciton to the internal nuclear degrees of freedom, as well as a longer external dissipation time scale that corresponds to the damping of the internal nuclear

degrees of freedom by the environment. Several processes were found to be present within our model dynamics, all of which are consistent with the system relaxing into the low energy chromophore states of the polymer. Of these, polaron formation and exciton decoherence were found to occur on the ultra-fast time-scale ($\sim$ 10 fs) within half a vibrational time period of the internal harmonic oscillators. Indeed the mechanism for exciton decoherence within our model was found to correspond to the decay in the vibrational overlaps as a result of polaron formation, showing that these two processes are intrinsically linked. Exciton density localisation in contrast was found to occur on the much longer external dissipation time scale via a 'wavefunction collapse' process, which is driven by instantaneous system-environment interactions. Therefore for the relaxation dynamics involving the coupling of the exciton to the high frequency stretching modes within the polymer, our results showed that exciton decoherence and exciton density localisation (terms which are often used interchangeably in the literature) are distinct processes that occur on considerably different time scales. These results were then compared to experiment by calculating the decay in the fluorescence anisotropy during the dynamics. The decay of this quantity was shown to be a measure of the exciton decoherence process, with the associated time scale in good agreement with the ultra-fast time scale observed within the corresponding experiment.

Secondly, the long time dynamics associated with the model were investigated. The steady state solution of the Lindblad master equation was obtained using a Lindblad perturbation theory developed by us, in which the external dissipation parameter was treated as a perturbation to the model. An analytical solution for this steady state was obtained in the adiabatic and anti-adiabatic limits using this theory. In the adiabatic limit, the steady state solution was shown to consist entirely of the vibrationally relaxed

states of the polymer, such that relaxation to the ground state is complete in this limit. In contrast, the steady state solution in the anti-adiabatic limit was shown to correspond to a 'high temperature Boltzmann state'. Numerical results were obtained using variants of the limited functional space approach and were shown to be consistent with the previously obtained analytical solutions, as well as the time evolving block decimation dynamics. These numerical results confirmed that the steady state solution contains all the properties associated with the chromophores of a real polymer chain, such as exciton-polaron character and short ranged exciton coherence and exciton localisation lengths. Away from the adiabatic limit, the exciton localisation length associated with the steady state was found to be much smaller than that of the VRSs, showing that to correctly describe the chromophore states of a polymer chain requires the effects of the external dissipation to be taken into account, as well as the disorder within the polymer chain itself.

Finally, we noted that one experimental time scale (~ 100 fs) was absent in our model, which we postulated arose from the coupling of the exciton to the low frequency torsional modes of the polymer. Describing these 'classical' nuclear modes was unfeasible in our current framework, so computational techniques developed by us were introduced that were better suited to this task. The TEBD-Ehrenfest technique was firstly introduced, which corresponds to representing the nuclear degrees of freedom using a generalised coherent state basis. In other words, the average nuclear positions and momenta of the system are described by classical variables, which are evolved using the Ehrenfest equations of motion, while quantum fluctuations about this average in the nuclear quantum state are described by adding phonons to the basis. The probability amplitude tensor in the TEBD-Ehrenfest ansatz is then evolved using the time evolving block decimation

technique. This technique was shown to be effective for obtaining the exciton relaxation dynamics of an initial local exciton ground state in the classical limit, but was less well suited to describing the analogous dynamics associated with an initial high energy quasi-extended exciton state. The branching bundle trajectory technique was then motivated by considering the branching process which results from passing through a conical intersection. We showed that a bundle of non-interacting classical trajectories was in principle able to "exactly" describe the dynamics associated with a conical intersection in the classical limit, as long as these classical trajectories can 'branch' at the conical intersection. Such a method was able to "exactly" reproduce the dynamics associated with the two-level conical intersection model in the adiabatic limit, as long as an "exact" theory was used to evolve the nuclear coherent state basis.

Possible future work consists of the following. We would like to include the torsional modes into our model to ascertain whether both experimental time scales of $\lesssim 50$ fs and ~ 100 fs can be simultaneously accounted for. This could be achieved for an initial local exciton ground state using the TEBD-Ehrenfest technique. For initial quasi-extended exciton states, the branching bundle trajectory technique would need to be developed further, so that it can be applied to models with multiple conical intersections (i.e., developed into a 'black box' method, where prior knowledge of the conical intersection locations are not required). To make better comparison to experiment, calculation of more complicated experimental quantities associated with the dynamics, such as 2D electronic spectra, would be advantageous. Finally, theories for more complicated dynamics, such as exciton migration/transport along a polymer chain, could be developed using a similar model to that outlined in this thesis.

Bibliography

[1] J. H. Burroughes, D. D. C. Bradley, A. R. Brown, R. N. Marks, K. Mackay, R. H. Friend, P. L. Burn, A. B. Holmes, Light-Emitting-Diodes Based on Conjugated Polymers, *Nature* **347**, 539–541 (1990).

[2] W. Barford, *Electronic and optical properties of conjugated polymers*, OUP, (2013).

[3] A. Ruseckas, P. Wood, I. D. W. Samuel, G. R. Webster, W. J. Mitchell, P. L. Burn, V. Sundstrom, Ultrafast depolarization of the fluorescence in a conjugated polymer, *Phys. Rev. B* **72**, 115214 (2005).

[4] M. M. L. Grage, Y. Zaushitsyn, A. Yartsev, M. Chachisvilis, V. Sundström, T. Pullerits, Ultrafast excitation transfer and trapping in a thin polymer film, *Phys. Rev. B* **67**, 205207 (2003).

[5] T. E. Dykstra, E. Hennebicq, D. Beljonne, J. Gierschner, G. Claudio, E. R. Bittner, J. Knoester, G. D. Scholes, Conformational Disorder and Ultrafast Exciton Relaxation in PPV-family Conjugated Polymers, *J. Phys. Chem. B* **113**, 656–667 (2009).

[6] J. Sperling, A. Nemeth, P. Baum, F. Sanda, E. Riedle, H. F. Kauffmann, S. Mukamel, F. Milota, Exciton dynamics in a disordered conjugated polymer: Three-pulse photon-echo and transient grating experiments, *Chem. Phys.* **349**, 244–249 (2008).

[7] T. E. Dykstra, V. Kovalevskij, X. Yang, G. D. Scholes, Excited state dynamics of a conformationally disordered conjugated polymer: A comparison of solutions and film, *Chem. Phys.* **318**, 21–32 (2005).

[8] X. Yang, T. E. Dykstra, G. D. Scholes, Photon-echo studies of collective absorption and dynamic localization of excitation in conjugated polymers and oligomers, *Phys. Rev. B* **71**, 045203 (2005).

[9] C. Consani, F. Koch, F. Panzer, T. Unger, A. Köhler, T. Brixner, Relaxation dynamics and exciton energy transfer in the low-temperature phase of MEH-PPV, *J. Chem. Phys.* **142**, 212429 (2015).

[10] I. Hwang, G. D. Scholes, Electronic Energy Transfer and Quantum-Coherence in pi-Conjugated Polymers, *Chem. Mater.* **23**, 610–620 (2011).

[11] W. Barford, E. R. Bittner, A. Ward, Exciton Dynamics in Disordered Poly(p-phenylenevinylene). 2. Exciton Diffusion, *J. Phys. Chem. A* **116**, 10319–10327 (2012).

[12] W. Barford, O. R. Tozer, Theory of exciton transfer and diffusion in conjugated polymers, *J. Chem. Phys.* **141** (2014).

[13] O. R. Tozer, W. Barford, Intrachain exciton dynamics in conjugated polymer chains in solution, *J. Chem. Phys.* **143** (2015).

[14] J. E. Poole, D. A. Damry, O. R. Tozer, W. Barford, Charge mobility induced by Brownian fluctuations in pi-conjugated polymers in solution, *Phys. Chem. Chem. Phys.* **18**, 2574–2579 (2016).

[15] O. R. Tozer, W. Barford, Exciton Dynamics in Disordered Poly(p-phenylenevinylene). 1. Ultrafast Interconversion and Dynamical Localization, *J. Phys. Chem. A* **116**, 10310–10318 (2012).

[16] F. Sterpone, P. J. Rossky, Molecular Modelling and Simulation of Conjugated Polymer Oligomers: Ground and Excited State Chain Dynamics of PPV in the Gas Phase, *J. Phys. Chem. B* **112**, 4983–4993 (2008).

[17] S. Tretiak, A. Saxena, R. L. Martin, A. R. Bishop, Conformational Dynamics of Photoexcited Conjugated Molecules, *Phys. Rev. Lett.* **89**, 097402 (2002).

[18] D. G. Truhlar, *Decoherence in Combined Quantum Mechanical and Classical Mechanical Methods for Dynamics as Illustrated for Non–Born—Oppenheimer Trajectories*, Springer Berlin Heidelberg, (2007), 227–243.

[19] E. R. Bittner, P. J. Rossky, Quantum Decoherence in Mixed Quantum-Classical Systems - Nonadiabatic Processes, *J. Chem. Phys.* **103**, 8130–8143 (1995).

[20] H. Hwang, P. J. Rossky, Electronic decoherence induced by intramolecular vibrational motions in a betaine dye molecule, *J. Phys. Chem. B* **108**, 6723–6732 (2004).

[21] M. J. Bedard-Hearn, R. E. Larsen, B. J. Schwartz, Mean-field dynamics with stochastic decoherence (MF-SD): A new algorithm for nonadiabatic mixed quantum/classical molecular-dynamics simulations with nuclear-induced decoherence, *J. Chem. Phys.* **123**, 234106 (2005).

[22] E. R. Bittner, P. J. Rossky, Decoherent histories and nonadiabatic quantum molecular dynamics simulations, *J. Chem. Phys.* **107**, 8611–8618 (1997).

[23] O. V. Prezhdo, P. J. Rossky, Mean-field molecular dynamics with surface hopping, *J. Chem. Phys.* **107**, 825–834 (1997).

[24] F. Dorfner, L. Vidmar, C. Brockt, E. Jeckelmann, F. Heidrich-Meisner, Real-time decay of a highly excited charge carrier in the one-dimensional Holstein model, *Phys. Rev. B* **91** (2015).

[25] C. Brockt, F. Dorfner, L. Vidmar, F. Heidrich-Meisner, E. Jeckelmann, Matrix-product-state method with a dynamical local basis optimization for bosonic systems out of equilibrium, *Phys. Rev. B* **92** (2015).

[26] R. Borrelli, M. F. Gelin, Simulation of Quantum Dynamics of Excitonic Systems at Finite Temperature: an efficient method based on Thermo Field Dynamics, *Sci. Rep.* **7**, 9127 (2017).

[27] J. Ren, Z. Shuai, G. Kin-Lic Chan, Time-Dependent Density Matrix Renormalization Group Algorithms for Nearly Exact Absorption and Fluorescence Spectra of Molecular Aggregates at Both Zero and Finite Temperature, *J. Chem. Theory Comput.* **14**, 5027–5039 (2018).

[28] L. P. Chen, Y. Zhao, Y. Tanimura, Dynamics of a One-Dimensional Holstein Polaron with the Hierarchical Equations of Motion Approach, *J. Phys. Chem. Lett.* **6**, 3110–3115 (2015).

[29] T. C. Berkelbach, M. S. Hybertsen, D. R. Reichman, Microscopic theory of singlet exciton fission. I. General formulation, *J. Chem. Phys.* **138**, 114102 (2013).

[30] J. Zheng, Y. Xie, S. Jiang, Z. Lan, Ultrafast Nonadiabatic Dynamics of Singlet Fission: Quantum Dynamics with the Multilayer Multiconfigurational Time-Dependent Hartree (ML-MCTDH) Method, *J. Phys. Chem. C* **120**, 1375–1389 (2016).

[31] R. Binder, D. Lauvergnat, I. Burghardt, Conformational Dynamics Guides Coherent Exciton Migration in Conjugated Polymer Materials: First-Principles Quantum Dynamical Study, *Phys. Rev. Lett.* **120** (2018).

[32] W. Barford, M. Marcus, Theory of optical transitions in conjugated polymers. I. Ideal systems, *J. Chem. Phys.* **141**, 164101 (2014).

[33] M. Marcus, O. R. Tozer, W. Barford, Theory of optical transitions in conjugated polymers. II. Real systems, *J. Chem. Phys.* **141** (2014).

[34] M. Marcus, J. D. Milward, A. Kohler, W. Barford, Structural Information for Conjugated Polymers from Optical Modeling, *J. Phys. Chem. A* **122**, 3621–3625 (2018).

[35] J. D. Milward, M. Marcus, A. Kohler, W. Barford, Extracting structural information from MEH-PPV optical spectra, *J. Chem. Phys.* **149** (2018).

[36] G. A. Hagedorn, Molecular Propagation through Electron-Energy Level-Crossings, *Mem. Am. Math. Soc.* **111**, 1–130 (1994).

[37] C. Schütte, F. A. Bornemann, Computational Molecular Dynamics: Challenges, Methods, Ideas, 380–395.

[38] R. J. Glauber, Coherent and Incoherent States of the Radiation Field, *Phys. Rev.* **131**, 2766–2788 (1963).

[39] E. C. G. Sudarshan, Equivalence of Semiclassical and Quantum Mechanical Descriptions of Statistical Light Beams, *Phys. Rev. Lett.* **10**, 277–279 (1963).

[40] P. Atkins, R. Friedman, *Molecular Quantum Mechanics*, OUP, (2010).

[41] E. Schrödinger, Der stetige Übergang von der Mikro- zur Makromechanik, *Naturwissenschaften* **14**, 664–666 (1926).

[42] C. W. Gardiner, P. Zoller, *Quantum Noise*, Springer-Verlag, (1991).

[43] W. Barford, Excitons in Conjugated Polymers: A Tale of Two Particles, *J. Phys. Chem. A* **117**, 2665–2671 (2013).

[44] M. Chandross, S. Mazumdar, S. Jeglinski, X. Wei, Z. V. Vardeny, E. W. Kwock, T. M. Miller, Excitons in poly(para-phenylenevinylene), *Phys. Rev. B* **50**, 14702–14705 (1994).

[45] W. Barford, N. Paiboonvorachat, Excitons in conjugated polymers: Wavefunctions, symmetries, and quantum numbers, *J. Chem. Phys.* **129**, 164716 (2008).

[46] J. Frenkel, On the Transformation of light into Heat in Solids. I, *Phys. Rev.* **37**, 17–44 (1931).

[47] J. Frenkel, On the Transformation of Light into Heat in Solids. II, *Phys. Rev.* **37**, 1276–1294 (1931).

[48] E. Moore, B. Gherman, D. Yaron, Coulomb screening and exciton binding energies in conjugated polymers, *J. Chem. Phys.* **106**, 4216–4227 (1997).

[49] W. Barford, D. Trembath, Exciton localization in polymers with static disorder, *Phys. Rev. B* **80**, 165418 (2009).

[50] G. Grosso, P. Parravicini, *Solid State Physics*, Elsevier, (2014).

[51] P. W. Anderson, Absence of Diffusion in Certain Random Lattices, *Phys. Rev.* **109**, 1492–1505 (1958).

[52] A. V. Malyshev, V. A. Malyshev, Statistics of low energy levels of a one-dimensional weakly localized Frenkel exciton: A numerical study, *Phys. Rev. B* **63**, 195111 (2001).

[53] A. V. Malyshev, V. A. Malyshev, F. Domínguez-Adame, On the Low-Temperature Diffusion of Localized Frenkel Excitons in Linear Molecular Aggregates, *J. Phys. Chem. B* **107**, 4418–4425 (2003).

[54] A. Malyshev, V. Malyshev, F. Domínguez-Adame, Low-temperature quenching of one-dimensional localized Frenkel excitons, *Chem. Phys. Lett.* **371**, 417 – 425 (2003).

[55] D. V. Makhov, W. Barford, Local exciton ground states in disordered polymers, *Phys. Rev. B* **81**, 165201 (2010).

[56] W. Barford, M. Marcus, Perspective: Optical spectroscopy in pi-conjugated polymers and how it can be used to determine multiscale polymer structures, *J. Chem. Phys.* **146**, 130902 (2017).

[57] T. Holstein, Studies of Polaron Motion .1. The Molecular-Crystal Model, *Ann. Phys. (N. Y.)* **8**, 325–342 (1959).

[58] T. Holstein, Studies of Polaron Motion .2. The Small Polaron, *Ann. Phys. (N. Y.)* **8**, 343–389 (1959).

[59] W. Barford, M. Marcus, O. R. Tozer, Polarons in pi-Conjugated Polymers: Anderson or Landau?, *J. Phys. Chem. A* **120**, 615–620 (2016).

[60] O. R. Tozer, W. Barford, Localization of large polarons in the disordered Holstein model, *Phys. Rev. B* **89**, 155434 (2014).

[61] U. Schollwöck, The density-matrix renormalization group in the age of matrix product states, *Ann. Phys. (N.Y.)* **326**, 96–192 (2011).

[62] M. Hoffmann, Z. G. Soos, Optical absorption spectra of the Holstein molecular crystal for weak and intermediate electronic coupling, *Phys. Rev. B* **66**, 024305 (2002).

[63] A. H. Romero, D. W. Brown, K. Lindenberg, Electron-phonon correlations, polaron size, and the nature of the self-trapping transition, *Phys. Lett. A* **266**, 414–420 (2000).

[64] E. Jeckelmann, S. R. White, Density-matrix renormalization-group study of the polaron problem in the Holstein model, *Phys. Rev. B* **57**, 6376–6385 (1998).

[65] E. Rashba, Theory of Strong Interactions of Electron Excitations with Lattice Vibrations in Molecular Crystals .1., *Opt. Spektrosk.* **2**, 75–87 (1957).

[66] E. Rashba, Theory of Strong Interactions of Electron Excitations with Lattice Vibrations in Molecular Crystals .2., *Opt. Spektrosk.* **2**, 88–98 (1957).

[67] L. D. Landau, *Z. Phys* **3**, 664 (1933).

[68] D. K. Campbell, A. R. Bishop, K. Fesser, Polarons in quasi-one-dimensional systems, *Phys. Rev. B* **26**, 6862–6874 (1982).

[69] G. D. Mahan, *Many-particle Physics*, Plenum Press, New York, (1990).

[70] I. G. Lang, Y. A. Firsov, *Zh. Eksp. Teor. Fiz.* **16**, 1301 (1963).

[71] M. Hohenadler, H. G. Evertz, W. von der Linden, Quantum Monte Carlo and variational approaches to the Holstein model, *Phys. Rev. B* **69**, 024301 (2004).

[72] L. Mandel, E. Wolf, *Optical Coherence and Quantum Optics*, Cambridge, (1995).

[73] M. Chakraborty, A. N. Das, A. Chakrabarti, Study of the one-dimensional Holstein model with next-nearest-neighbor hopping, *J. Phys. Condens. Matter* **23**, 025601 (2011).

[74] O. S. Barišić, S. Barišić, Phase diagram of the Holstein polaron in one dimension, *Eur. Phys. J. B* **64**, 1–18 (2008).

[75] J. E. Campbell, On a Law of Combination of Operators (Second Paper)*, *Proc. Lond. Math. Soc.* **s1-29**, 14–32 (1897).

[76] H. F. Baker, Alternants and Continuous Groups, *Proc. Lond. Math. Soc.* **s2-3**, 24–47 (1905).

[77] G. Lindblad, On the generators of quantum dynamical semigroups, *Comm. Math. Phys.* **48**, 119–130 (1976).

[78] V. Gorini, A. Kossakowski, E. C. G. Sudarshan, Completely positive dynamical semigroups of N-level systems, *J. Math. Phys.* **17**, 821–825 (1976).

[79] H.-P. Breuer, F. Petruccione, *The theory of open quantum systems*, OUP, (2002).

[80] J. Binney, D. Skinner, *The Physics of Quantum Mechanics*, Oxford, (2014).

[81] A. Barchielli, B. Vacchini, Quantum Langevin equations for optomechanical systems, *New J. Phys.* **17**, 083004 (2015).

[82] R. Horn, C. Johnson, *Matrix Analysis*, Cambridge University Press, (1994).

[83] T. F. Havel, Robust procedures for converting among Lindblad, Kraus and matrix representations of quantum dynamical semigroups, *J. Math. Phys.* **44**, 534–557 (2003).

[84] M. Am-Shallem, R. Kosloff, N. Moiseyev, Exceptional points for parameter estimation in open quantum systems: analysis of the Bloch equations, *New J. Phys.* **17**, 113036 (2015).

[85] M. Am-Shallem, R. Kosloff, N. Moiseyev, Parameter estimation in atomic spectroscopy using exceptional points, *Phys. Rev. A* **93**, 032116 (2016).

[86] J. Dalibard, Y. Castin, K. Mølmer, Wave-function approach to dissipative processes in quantum optics, *Phys. Rev. Lett.* **68**, 580–583 (1992).

[87] R. Dum, A. S. Parkins, P. Zoller, C. W. Gardiner, Monte Carlo simulation of master equations in quantum optics for vacuum, thermal, and squeezed reservoirs, *Phys. Rev. A* **46**, 4382–4396 (1992).

[88] K. Mølmer, Y. Castin, J. Dalibard, Monte Carlo wave-function method in quantum optics, *J. Opt. Soc. Am. B* **10**, 524–538 (1993).

[89] B. M. Garraway, P. L. Knight, Comparison of quantum-state diffusion and quantum-jump simulations of two-photon processes in a dissipative environment, *Phys. Rev. A* **49**, 1266–1274 (1994).

[90] A. J. Daley, Quantum trajectories and open many-body quantum systems, *Adv. Phys.* **63**, 77–149 (2014).

[91] A. García-Vela, R. B. Gerber, Three-dimensional quantum wave packet study of the Ar–HCl photodissociation: A comparison between time-dependent self-consistent-field and exact treatments, *J. Chem. Phys.* **103(9)**, 3463–3473 (1995).

[92] R. B. Gerber, V. Buch, M. A. Ratner, Time-dependent self-consistent field approximation for intramolecular energy transfer. I. Formulation and application to dissociation of van der Waals molecules, *J. Chem. Phys.* **77**, 3022–3030 (1982).

[93] F. A. Bornemann, P. Nettesheim, C. Schütte, Quantum-classical molecular dynamics as an approximation to full quantum dynamics, *J. Chem. Phys.* **105**, 1074–1083 (1996).

[94] P. Ehrenfest, Bemerkung über die angenäherte Gültigkeit der klassischen Mechanik innerhalb der Quantenmechanik, *Zeitschrift für Physik* **45**, 455–457 (1927).

[95] U. Schollwöck, The density-matrix renormalization group, *Rev. Mod. Phys.* **77**, 259–315 (2005).

[96] C. Zhang, E. Jeckelmann, S. R. White, Density Matrix Approach to Local Hilbert Space Reduction, *Phys. Rev. Lett.* **80**, 2661–2664 (1998).

[97] A. J. Daley, C. Kollath, U. Schollwöck, G. Vidal, Time-dependent density-matrix renormalization-group using adaptive effective Hilbert spaces, *J. Stat. Mech.: Theory Exp.* , P04005 (2004).

[98] G. Vidal, Efficient Classical Simulation of Slightly Entangled Quantum Computations, *Phys. Rev. Lett.* **91**, 147902 (2003).

[99] G. Vidal, Efficient simulation of one-dimensional quantum many-body systems, *Phys. Rev. Lett.* **93**, 040502 (2004).

[100] I. Bengtsson, K. Kzyczkowski, *Geometry of Quantum States*, Cambridge University Press, (2007).

[101] R. Orús, A practical introduction to tensor networks: Matrix product states and projected entangled pair states, *Ann. Phys.* **349**, 117 – 158 (2014).

[102] I. P. McCulloch, From density-matrix renormalization group to matrix product states, *J. Stat. Mech.* **2007**, P10014 (2007).

[103] K.-L. G. Chan, J. J. Dorando, D. Gosh, J. Hachmann, E. Neuscamman, H. Wang, T. Yanai, Frontiers in Quantum Systems in Chemistry and Physics. Progress in Theoretical Chemistry and Physics, 49–65.

[104] U. Schollwöck, S. R. White, Effective Models for Low-Dimensional Strongly Correlated Systems, 155.

[105] M. A. Nielson, I. L. Chuang, *Quantum Computation and Quantum Information*, Cambridge University Press, (2000).

[106] E. M. Stoudenmire, S. R. White, Minimally entangled typical thermal state algorithms, *New J. Phys.* **12**, 055026 (2010).

[107] S. R. White, A. E. Feiguin, Real-Time Evolution Using the Density Matrix Renormalization Group, *Phys. Rev. Lett.* **93**, 076401 (2004).

[108] J. Bonča, S. A. Trugman, I. Batistić, Holstein polaron, *Phys. Rev. B* **60**, 1633–1642 (1999).

[109] J. Bonča, S. Maekawa, T. Tohyama, P. Prelovšek, Spectral properties of a hole coupled to optical phonons in the generalized $t-J$ model, *Phys. Rev. B* **77**, 054519 (2008).

[110] L.-C. Ku, S. A. Trugman, J. Bonča, Dimensionality effects on the Holstein polaron, *Phys. Rev. B* **65**, 174306 (2002).

[111] D. Golež, J. Bonča, L. Vidmar, S. A. Trugman, Relaxation Dynamics of the Holstein Polaron, *Phys. Rev. Lett.* **109**, 236402 (2012).

[112] L. Vidmar, J. Bonča, S. A. Trugman, Emergence of states in the phonon spectral function of the Holstein polaron below and above the one-phonon continuum, *Phys. Rev. B* **82**, 104304 (2010).

[113] L. Vidmar, J. Bonča, M. Mierzejewski, P. Prelovšek, S. A. Trugman, Nonequilibrium dynamics of the Holstein polaron driven by an external electric field, *Phys. Rev. B* **83**, 134301 (2011).

[114] S. Al-Assam, S. R. Clark, D. Jaksch, The tensor network theory library, *J. Stat. Mech. Theor. Exp.* , 093102 (2017).

[115] O. Kuhn, V. Sundstrom, Pump-probe spectroscopy of dissipative energy transfer dynamics in photosynthetic antenna complexes: A density matrix approach, *J. Chem. Phys.* **107**, 4154–4164 (1997).

[116] C. Smyth, F. Fassioli, G. D. Scholes, Measures and implications of electronic coherence in photosynthetic light-harvesting, *Philos. Trans. R. Soc. A.* **370**, 3728–3749 (2012).

[117] F. C. Spano, S. C. J. Meskers, E. Hennebicq, D. Beljonne, Using circularly polarized luminescence to probe exciton coherence in disordered helical aggregates, *J. Chem. Phys.* **129**, 024704 (2008).

[118] R. Tempelaar, F. C. Spano, J. Knoester, T. L. C. Jansen, Mapping the Evolution of Spatial Exciton Coherence through Time-Resolved Fluorescence, *J. Phys. Chem. Lett.* **5**, 1505–1510 (2014).

[119] W. Barford, I. Boczarow, T. Wharram, Ultrafast Dynamical Localization of Photoexcited States in Conformationally Disordered Poly(p-phenylenevinylene), *J. Phys. Chem. A* **115**, 9111–9119 (2011).

[120] J. Lakowicz, *Principles of Fluorescence Spectroscopy*, Plenum Press, New York, (1983).

[121] T. S. Rahman, R. S. Knox, V. M. Kenkre, Theory of Depolarization of Fluorescence in Molecular Pairs, *Chem. Phys.* **44**, 197–211 (1979).

[122] J. Cornil, D. Beljonne, C. M. Heller, I. H. Campbell, B. K. Laurich, D. L. Smith, D. D. C. Bradley, K. Mullen, J. L. Bredas, Photoluminescence spectra of oligo-paraphenylenevinylenes: a joint theoretical and experimental characterization, *Chem. Phys. Lett.* **278**, 139–145 (1997).

[123] E. del Valle, M. J. Hartmann, Correlator expansion approach to stationary states of weakly coupled cavity arrays, *J. Phys. B: At. Mol. Opt. Phys.* **46**, 224023 (2013).

[124] A. C. Y. Li, F. Petruccione, J. Koch, Perturbative approach to Markovian open quantum systems, *Sci. Rep.* **4**, 4887 (2014).

[125] A. C. Y. Li, F. Petruccione, J. Koch, Resummation for Nonequilibrium Perturbation Theory and Application to Open Quantum Lattices, *Phys. Rev. X* **6**, 021037 (2016).

[126] E. A. Gómez, J. D. Castaño-Yepes, S. P. Thirumuruganandham, Perturbation theory for open quantum systems at the steady state, *Results Phys.* **10**, 353 – 355 (2018).

[127] F. Benatti, A. Nagy, H. Narnhofer, Asymptotic entanglement and Lindblad dynamics: a perturbative approach, *J. Phys. A: Math. Theor.* **44**, 155303 (2011).

[128] F. Marsiglio, Pairing in the Holstein model in the dilute limit, *Physica C: Superconductivity* **244**, 21 – 34 (1995).

[129] I. R. Senitzky, Harmonic Oscillator Wave Functions, *Phys. Rev.* **95**, 1115–1116 (1954).

[130] M. Boiteux, A. Levelut, Semicoherent states, *J. Phys. A: Math. Nucl. Gen.* **6**, 589 (1973).

[131] S. M. Roy, V. Singh, Generalized coherent states and the uncertainty principle, *Phys. Rev. D* **25**, 3413–3416 (1982).

[132] E. Wigner, On the Quantum Correction For Thermodynamic Equilibrium, *Phys. Rev.* **40**, 749–759 (1932).

[133] D. V. Shalashilin, Quantum mechanics with the basis set guided by Ehrenfest trajectories: Theory and application to spin-boson model, *J. Chem. Phys.* **130**, 244101 (2009).

[134] M. Born, R. Oppenheimer, Zur Quantentheorie der Molekeln, *Ann. Phys.* **389**, 457–484 (1927).

[135] G. A. Hagedorn, A time dependent Born-Oppenheimer approximation, *Commun. Math. Phys.* **77**, 1–19 (1980).

[136] C. Zener, R. H. Fowler, Non-adiabatic crossing of energy levels, *Proc. R. Soc. London* **137**, 696–702 (1932).

[137] G. A. Hagedorn, Proof of the Landau-Zener formula in an adiabatic limit with small eigenvalue gaps, *Commun. Math. Phys.* **136**, 433–449 (1991).

[138] G. A. Hagedorn, Electron energy level crossings in the time-dependent Born-Oppenheimer approximation, *Theor. Chim. Acta* **77**, 163–190 (1990).

[139] G. Richings, I. Polyak, K. Spinlove, G. Worth, I. Burghardt, B. Lasorne, Quantum dynamics simulations using Gaussian wavepackets: the vMCG method, *Int. Rev. Phys. Chem.* **34**, 269–308 (2015).

A

Superoperators in Liouville Space

In a Hilbert space of size N, the system density matrix, $\hat{\rho}$, which contains all known information about the state of the system, takes the form of a $N \times N$ matrix. Operators, $\hat{A}$, which correspond to observables associated with the system and are also represented by $N \times N$ matrices, can be applied to the system density matrix to calculate useful quantities, such as expectation values.

Often it is beneficial to represent these quantities in Liouville space, where the system density matrix becomes a N^2 column vector:

$$|\vec{\rho}\rangle = \begin{pmatrix} \rho_{1,1} \\ \rho_{2,1} \\ \rho_{3,1} \\ \vdots \end{pmatrix} \tag{A.1}$$

where $\rho_{i,j}$ are the various matrix elements of the system density matrix. In Liouville space, any operators that act on the system density matrix, $\hat{A}$, are represented by superoperators of size $N^2 \times N^2$. It will become apparent that expressions for these superoperators can be written in terms of Kronecker products of Hilbert space operators, where a Kronecker product of two matrices $\mathbf{A}$ and $\mathbf{B}$ is defined as follows:

$$\mathbf{A} \otimes \mathbf{B} = \begin{pmatrix} A_{1,1}\mathbf{B} & \cdots & A_{1,N}\mathbf{B} \\ \vdots & \ddots & \vdots \\ A_{N,1}\mathbf{B} & \cdots & A_{N,N}\mathbf{B} \end{pmatrix} = \begin{pmatrix} A_{1,1}B_{1,1} & A_{1,1}B_{1,2} & \cdots & A_{1,N}B_{1,N} \\ A_{1,1}B_{2,1} & A_{1,1}B_{2,2} & \cdots & A_{1,N}B_{2,N} \\ \vdots & \vdots & \ddots & \vdots \\ A_{N,1}B_{N,1} & A_{N,1}B_{N,2} & \cdots & A_{N,N}B_{N,N} \end{pmatrix} \tag{A.2}$$

for a Hilbert space of size N. Here, $A_{i,j} = \langle\psi_i|\hat{A}|\psi_j\rangle$ corresponds to the various matrix elements of operator $\hat{A}$. We now consider the following cases for Hilbert space operators acting on a system density matrix and obtain expressions for their corresponding superoperator representations in Liouville space:

- $\underline{\hat{\rho}' = \hat{A}\hat{\rho}\hat{B}:}$

To proceed, we consider the matrix elements of the above equation involving the system density matrices $\hat{\rho}$ and $\hat{\rho}'$:

$$\langle m|\hat{\rho}'|n\rangle = \sum_{r,\,s} \langle m|\hat{A}|r\rangle \langle r|\hat{\rho}|s\rangle \langle s|\hat{B}|n\rangle \tag{A.3}$$

where we have used that $\hat{\mathbb{1}} = \sum_r |r\rangle\langle r|$ is the unit operator. As an illustrative case, consider a Hilbert space of dimension 2. Writing the density matrices $\hat{\rho}$ and $\hat{\rho}'$ as N^2 column vectors, corresponding to their representation in Liouville space, the matrix elements in

Eq. (A.3) can be reproduced from the following matrix equation:

$$\begin{pmatrix} \rho'_{1,1} \\ \rho'_{2,1} \\ \rho'_{1,2} \\ \rho'_{2,2} \end{pmatrix} = \begin{pmatrix} B_{1,1}A_{1,1} & B_{1,1}A_{1,2} & B_{2,1}A_{1,1} & B_{2,1}A_{1,2} \\ B_{1,1}A_{2,1} & B_{1,1}A_{2,2} & B_{2,1}A_{2,1} & B_{2,1}A_{2,2} \\ B_{1,2}A_{1,1} & B_{1,2}A_{1,2} & B_{2,2}A_{1,1} & B_{2,2}A_{1,2} \\ B_{1,2}A_{2,1} & B_{1,2}A_{2,2} & B_{2,2}A_{2,1} & B_{2,2}A_{2,2} \end{pmatrix} \begin{pmatrix} \rho_{1,1} \\ \rho_{2,1} \\ \rho_{1,2} \\ \rho_{2,2} \end{pmatrix} \tag{A.4}$$

where we identify the middle 4×4 matrix as the superoperator representation in this two-dimensional Hilbert space. Using the definition of the Kronecker product given by Eq. (A.2), the superoperator representation for the case when $\hat{A}$ is applied to the left of the system density matrix and $\hat{B}$ is applied to the right can then be seen to be given by the following expression:

$$\hat{A}\hat{\rho}\hat{B} \rightarrow \hat{B}^T \otimes \hat{A} \left|\vec{\rho}\right\rangle \tag{A.5}$$

where $\hat{B}^T$ corresponds to the transpose of the operator $\hat{B}$.

As introduced in Section 2.6, the Lindblad master equation has the following Hilbert space representation:

$$\frac{\partial \hat{\rho}}{\partial \tilde{t}} = -\frac{i}{\hbar\omega}\left[\hat{H}, \hat{\rho}\right] - \frac{\tilde{\gamma}}{2}\sum_m \left(\hat{b}_m^\dagger \hat{b}_m \hat{\rho} + \hat{\rho}\hat{b}_m^\dagger \hat{b}_m - 2\hat{b}_m \hat{\rho} \hat{b}_m^\dagger\right) \tag{A.6}$$

Writing this equation in Liouville space, we define the Lindblad superoperator $\hat{\hat{L}}$ as follows:

$$\frac{d\left|\vec{\rho}\right\rangle}{d\tilde{t}} = -i\hat{\hat{L}}\left|\vec{\rho}\right\rangle \tag{A.7}$$

Hence comparing Eqs. (A.6) and (A.7), while using the result given by Eq.(A.5), leads to the following expression for the Lindblad superoperator:

$$\hat{\hat{L}} = \frac{1}{\hbar\omega}\left(\hat{\mathbb{1}} \otimes \hat{H} - \hat{H}^T \otimes \hat{\mathbb{1}}\right) - \frac{i\tilde{\gamma}}{2}\sum_m \left(\hat{\mathbb{1}} \otimes \hat{b}_m^\dagger \hat{b}_m + \left(\hat{b}_m^\dagger \hat{b}_m\right)^T \otimes \hat{\mathbb{1}} - 2\left(\hat{b}_m^\dagger\right)^T \otimes \hat{b}_m\right) \tag{A.8}$$

where $\hat{\mathbb{1}}$ is the unit operator. This is indeed the same result that was stated in Section 2.6.1.

A.1 Matrix Elements of Superoperators

For the Lindblad perturbation theory introduced in Section 5.1, the expressions derived for the perturbative corrections to the Lindblad superoperator eigenvalues involve calculating matrix elements in Liouville space. In this subsection, we derive simplified expressions for these perturbative corrections, for two different situations:

1. Off-Diagonal Zeroth-Order Eigenstates:

For the off-diagonal zeroth-order eigenstates, non-degenerate perturbation theory is used to derive expressions for the various perturbative corrections. As shown in Section 5.1.2, the first-order correction to the Lindblad superoperator eigenvalues is given by the fol-

lowing expectation value:

$$\lambda^{(1)}_{l,\,j} = \langle \vec{\rho}_{l,\,j} | \hat{\hat{V}} | \vec{\rho}_{l,\,j} \rangle \,, \quad \text{for} \quad l \neq j \tag{A.9}$$

where $\hat{\hat{V}}$ is the perturbation superoperator, defined as follows:

$$\hat{\hat{V}} = \tilde{\gamma} \left[\frac{1}{\hbar\omega} \left(\hat{\mathbb{1}} \otimes \hat{H}_\Delta - \hat{H}^T_\Delta \otimes \hat{\mathbb{1}} \right) - \frac{i}{2} \sum_m \left(\hat{\mathbb{1}} \otimes \hat{b}^\dagger_m \hat{b}_m + \left(\hat{b}^\dagger_m \hat{b}_m \right)^T \otimes \hat{\mathbb{1}} - 2 \left(\hat{b}^\dagger_m \right)^T \otimes \hat{b}_m \right) \right] \tag{A.10}$$

The matrix representation of $\hat{B}^T \otimes \hat{A}$ for a two-dimensional Hilbert space is given by Eq. (A.4). Looking at the diagonal elements of this matrix, the following relation for the superoperator matrix elements is shown to hold:

$$\langle \vec{\rho}_{l,\,j} | \hat{B}^T \otimes \hat{A} | \vec{\rho}_{l,\,j} \rangle = \langle \psi_l | \hat{A} | \psi_l \rangle \langle \psi_j | \hat{B} | \psi_j \rangle \,, \quad \text{for} \quad l \neq j \tag{A.11}$$

where $|\psi_j\rangle$ are the eigenstates of the Frenkel-Holstein Hamiltonian with quantum number j. Therefore, inserting Eqs. (A.10) and (A.11) into Eq. (A.9) leads to the following simplified expression for the first-order corrected eigenvalues associated with the off-diagonal zeroth-order eigenstates:

$$\begin{aligned} \lambda^{(1)}_{l,\,j} = \tilde{\gamma} \Bigg[& \frac{1}{\hbar\omega} \left(\langle \psi_l | \hat{H}_\Delta | \psi_l \rangle - \langle \psi_j | \hat{H}_\Delta | \psi_j \rangle \right) \\ & - \frac{i}{2} \sum_m \left(\langle \psi_l | \hat{b}^\dagger_m \hat{b}_m | \psi_l \rangle + \langle \psi_j | \hat{b}^\dagger_m \hat{b}_m | \psi_j \rangle - 2 \langle \psi_l | \hat{b}_m | \psi_l \rangle \langle \psi_j | \hat{b}_m | \psi_j \rangle \right) \Bigg] \end{aligned} \tag{A.12}$$

which is identical to the stated expression used in Section 5.1.2.

2. Diagonal Zeroth-Order Eigenstates:

As the diagonal zeroth-order eigenstates are degenerate (see Section 5.1.1), the various perturbative corrections must be derived using degenerate perturbation theory in this case. This involves calculating the perturbation superoperator within the basis of the degenerate states. The matrix representation of $\hat{B}^T \otimes \hat{A}$ for a two-dimensional Hilbert space, given by Eq. (A.4), can be used to obtain the following relation for the perturbation superoperator matrix elements in the degenerate subspace:

$$\langle \vec{\rho}_{l,\,l} | \hat{B}^T \otimes \hat{A} | \vec{\rho}_{j,\,j} \rangle = \langle \psi_l | \hat{A} | \psi_j \rangle \langle \psi_j | \hat{B} | \psi_l \rangle \tag{A.13}$$

Using the expression for the perturbation superoperator given in Eq. (A.10), Eq. (A.13) can then be used to obtain the following formula for the diagonal matrix elements of this superoperator, involving the degenerate states $|\vec{\rho}_{j,j}\rangle$:

$$\langle \vec{\rho}_{j,\,j} | \hat{\hat{V}} | \vec{\rho}_{j,\,j} \rangle = -i\tilde{\gamma} \sum_m \left(\langle \psi_j | \hat{b}^\dagger_m \hat{b}_m | \psi_j \rangle - \left| \langle \psi_j | \hat{b}_m | \psi_j \rangle \right|^2 \right) \tag{A.14}$$

Using the same equations also gives a similar expression for the off-diagonal matrix elements:

$$\langle \vec{\rho}_{l,l} | \hat{\hat{V}} | \vec{\rho}_{j,j} \rangle = i\tilde{\gamma} \sum_m \left| \langle \psi_l | \hat{b}_m | \psi_j \rangle \right|^2 \tag{A.15}$$

where $|\psi_j\rangle$ are the eigenstates of the Frenkel-Holstein Hamiltonian with quantum number j and $\langle \psi_l | \psi_j \rangle = \delta_{l,j}$ (i.e., these states are orthonormal). Both these results are indeed identical to those stated in Section 5.1.3.

B

The TEBD Parameters

In this appendix, the values of the TEBD parameters used in this thesis are justified. For simplicity, all results presented in this section correspond to the case with no external dissipation (i.e., $\tilde{\gamma} = 0$). We now consider each parameter in turn:

- $\underline{n_{\max}}$:

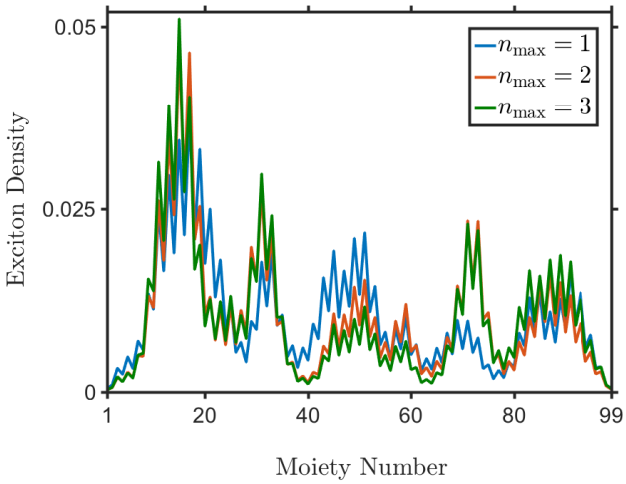


Figure B.1: The exciton density at $t = 100$ fs for a 99 site Frenkel-Holstein model parametrised for PPV. Each curve corresponds to a different value for the phonon 'cut-off', $n_{\max}$.

In this figure, the exciton density at $t = 100$ fs for the TEBD dynamics is given, for several values of the phonon cut off, $n_{\max}$. The dimensionless time step $\delta\tilde{t} = 5\,\mathrm{e}^{-4}$ was chosen by comparing TEBD simulations to "exact" results obtained from diagonalising the Hamiltonian matrix for small system sizes of $L \sim 5$. The value of χ was chosen to be large, while the singular value ratio S_{ratio} was chosen to be small, so the effect of truncation was minimal. Within this figure, the $n_{\max} = 1$ result appears to be significantly different from the others, while the $n_{\max} = 2$ and $n_{\max} = 3$ results seem qualitatively similar. Hence to reduce the computational expense of the calculation, $n_{\max} = 2$ is chosen for the simulations in this thesis. The other TEBD parameters are then chosen so that the largest error in our results arises from this choice of $n_{\max}$.

- $\underline{\delta\tilde{t}}$:

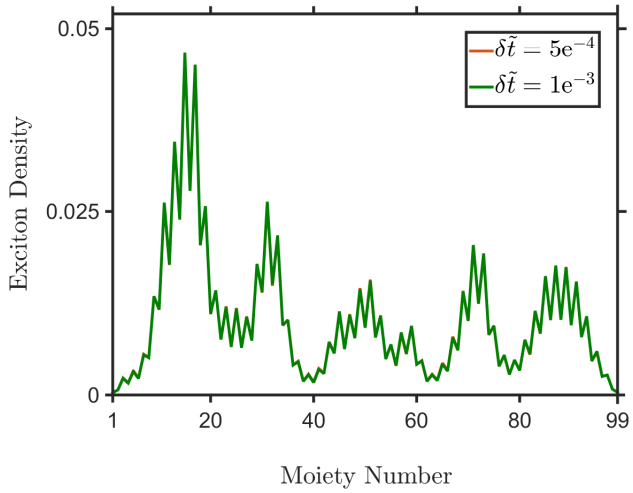


Figure B.2: The exciton density at $t = 100$ fs for a 99 site Frenkel-Holstein model parametrised for PPV. Each curve corresponds to a different value for the dimensionless time step, $\delta\tilde{t}$.

With $n_{\max} = 2$, we now confirm whether $\delta\tilde{t} = 5\,e^{-4}$ is indeed a suitable value for a Frenkel-Holstein model containing a much greater number of sites. As the correct value of S_{ratio} to choose for the simulation depends on the chosen time step, we again keep this parameter small so that the effect of truncation is minimised. The curves in this figure lie on top of one another, confirming that this value for the time step produces accurate results.

- S_{ratio} and χ:

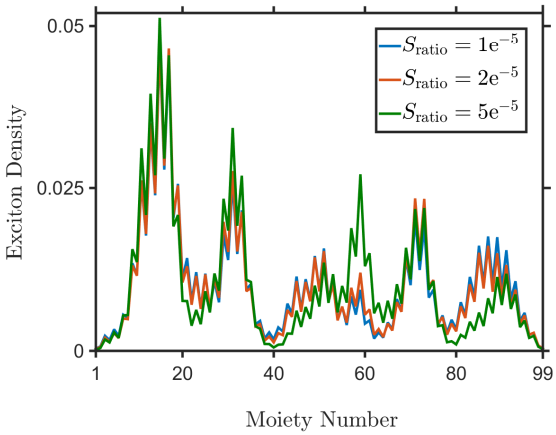


Figure B.3: The exciton density at $t = 100$ fs for a 99 site Frenkel-Holstein model parametrised for PPV. Each curve corresponds to a different value of S_{ratio}.

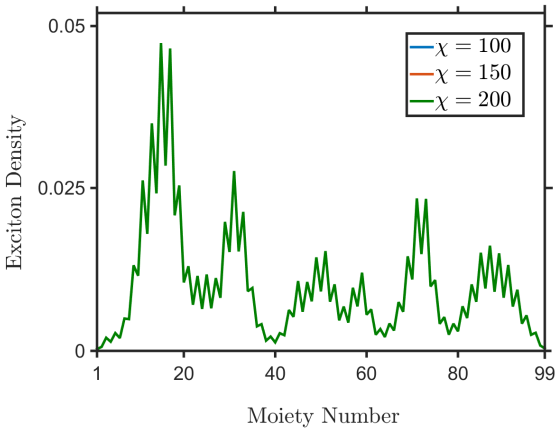


Figure B.4: The exciton density at $t = 100$ fs for a 99 site Frenkel-Holstein model parametrised for PPV. Each curve corresponds to a different value of χ.

Finally, the truncation parameters are tuned so that the computational cost of the calculation is made as small as possible. Firstly, the singular value ratio, S_{ratio}, is tuned while keeping a large value of $\chi = 150$. In Fig. B.3, we see that the calculation with $S_{\text{ratio}} = 5\,\text{e}^{-5}$ has a large associated truncation error, while the results with $S_{\text{ratio}} = 2\,\text{e}^{-5}$ and $S_{\text{ratio}} = 1\,\text{e}^{-5}$ are largely the same, with any error much less than that associated with the choice of the phonon cut off, $n_{\text{max}} = 2$. Therefore, using $S_{\text{ratio}} = 2e^{-5}$ seems an optimum choice. Figure B.4 confirms that the value of $\chi = 150$ used is large, so that altering its value does not change the obtained dynamics. This large value of χ is retained so that any trajectories that become strongly correlated within the quantum jump trajectory technique can still be well described within this parameter set.

On using these TEBD parameters to evolve trajectories within the quantum jump trajectory technique, the accuracy of the results can be tested by comparing the discarded singular values at each time step with the same quantity associated with these results. We find that the discarded singular values have similar magnitudes in both cases, meaning that we can be confident in the accuracy of our calculations when external dissipation is included. Finally the number of trajectories used within the quantum jump trajectory technique was chosen so that the associated observables become converged.

C

Nonadiabatic Derivative Coupling Vector

The nonadiabatic derivative coupling vector between two surfaces (corresponding to quantum numbers β and β' at a nuclear geometry $\mathbf{Q}'_{\mathbf{0}}$) is given by:

$$d_m(\boldsymbol{\beta},\, \mathbf{Q}'_{\mathbf{0}}) = \left\langle \psi_{\beta',\,\mathrm{ex}} \left| \frac{\partial \psi_{\beta,\,\mathrm{ex}}}{\partial Q'_m} \right\rangle \right|_{\mathbf{Q}'=\mathbf{Q}'_{\mathbf{0}}} \tag{C.1}$$

where $|\psi_{\beta,\,\mathrm{ex}}(\mathbf{Q}')\rangle$ is the quantum state corresponding to the adiabatic surface β, which is an eigenstate of the Born-Oppenheimer Hamiltonian for the Frenkel-Holstein model:

$$\hat{H}_{\mathrm{BO}}\, |\psi_{\beta,\,\mathrm{ex}}(\mathbf{Q}')\rangle = E_\beta(\mathbf{Q}')\, |\psi_{\beta,\,\mathrm{ex}}(\mathbf{Q}')\rangle \tag{C.2}$$

In addition, $E_\beta(\mathbf{Q}')$ are the associated adiabatic surface energies. To obtain the derivative of the quantum state $|\psi_{\beta,\,\mathrm{ex}}(\mathbf{Q}')\rangle$, which appears in Eq. (C.1), we write the Born-Oppenheimer Hamiltonian as an expansion about the nuclear coordinate $\mathbf{Q}'_{\mathbf{0}}$:

$$\hat{H}_{\mathrm{BO}} = \hat{H}_0 + \sum_m \left(Q'_m - Q'_{0,\,m}\right) \hat{V}_m \tag{C.3}$$

where $\hat{H}_0$ is the Born-Oppenheimer Hamiltonian at this nuclear coordinate (except for the quadratic potential) and $\hat{V}_m$ includes the corrections to the linear coupling term:

$$\begin{aligned} \hat{H}_0 &= \hat{H}_{\mathrm{F}} - 2\lambda \sum_m Q'_{0,\,m} \hat{a}^\dagger_m \hat{a}_m + \lambda \sum_m \left(Q'_m\right)^2 \\ \hat{V}_m &= -2\lambda \hat{a}^\dagger_m \hat{a}_m \end{aligned} \tag{C.4}$$

Written in this way, the eigenstates of the Born-Oppenheimer Hamiltonian can then be obtained as a perturbative expansion:

$$|\psi_{\beta,\,\mathrm{ex}}(\mathbf{Q}')\rangle \simeq |\psi^{(0)}_{\beta,\,\mathrm{ex}}\rangle + \sum_m \left(Q'_m - Q'_{0,\,m}\right) |\psi^{(1,\,m)}_{\beta,\,\mathrm{ex}}\rangle + \cdots \tag{C.5}$$

where $|\psi^{(0)}_{\beta,\,\mathrm{ex}}\rangle$ is an eigenstate of the unperturbed Hamiltonain $\hat{H}_0$ (i.e., $|\psi_{\beta,\,\mathrm{ex}}(\mathbf{Q}'_{\mathbf{0}})\rangle$) and $|\psi^{(1,\,m)}_{\beta,\,\mathrm{ex}}\rangle$ is the first-order correction to the eigenket associated with the perturbative term $\hat{V}_m$:

$$|\psi^{(1,\,m)}_{\beta,\,\mathrm{ex}}\rangle = \sum_{\beta' \neq \beta} \frac{\langle \psi_{\beta',\,\mathrm{ex}}(\mathbf{Q}'_{\mathbf{0}}) | \hat{V}_m | \psi_{\beta,\,\mathrm{ex}}(\mathbf{Q}'_{\mathbf{0}}) \rangle}{E_\beta(\mathbf{Q}'_{\mathbf{0}}) - E_{\beta'}(\mathbf{Q}'_{\mathbf{0}})}\, |\psi_{\beta',\,\mathrm{ex}}(\mathbf{Q}'_{\mathbf{0}})\rangle \tag{C.6}$$

Expanding $|\psi_{\beta,\,\mathrm{ex}}(\mathbf{Q}')\rangle$ as a Taylor expansion about the nuclear geometry $\mathbf{Q}'_{\mathbf{0}}$ results in the following analogous expression:

$$|\psi_{\beta,\,\mathrm{ex}}(\mathbf{Q}')\rangle \simeq |\psi_{\beta,\,\mathrm{ex}}(\mathbf{Q}'_{\mathbf{0}})\rangle + \sum_m \left(Q'_m - Q'_{0,\,m}\right) \left|\frac{\partial \psi_{\beta,\,\mathrm{ex}}}{\partial Q'_m}\right\rangle\Big|_{\mathbf{Q}'=\mathbf{Q}'_{\mathbf{0}}} + \cdots \tag{C.7}$$

Comparing Eqs. (C.5) and (C.7) gives $|\psi^{(1,\,m)}_{\beta,\,\mathrm{ex}}\rangle = \left|\frac{\partial \psi_{\beta,\,\mathrm{ex}}}{\partial Q'_m}\right\rangle\Big|_{\mathbf{Q}'=\mathbf{Q}'_{\mathbf{0}}}$. Therefore inserting Eq. (C.6) into Eq. (C.1) leads to the following exact expression for the nonadiabatic derivative coupling vector:

$$d_m(\boldsymbol{\beta},\, \mathbf{Q}'_{\mathbf{0}}) = \frac{-2\lambda \psi^*_{\beta',\,m}\psi_{\beta,\,m}}{E_\beta(\mathbf{Q}'_{\mathbf{0}}) - E_{\beta'}(\mathbf{Q}'_{\mathbf{0}})} \qquad \text{for} \quad \beta' \neq \beta \tag{C.8}$$

where $\psi_{\beta,\,m}$ is the probability amplitude for site m, associated with the state $|\psi_{\beta,\,\mathrm{ex}}(\mathbf{Q}'_{\mathbf{0}})\rangle$.

D

Generalised Coherent States

A generalised coherent state can be defined as follows:

$$|n,\, \alpha'\rangle = \frac{1}{\sqrt{n!}} \left(\sqrt{\frac{2\lambda}{\hbar\omega}}\, \hat{\bar{b}}'^{\dagger} \right)^{n} |\alpha'\rangle \tag{D.1}$$

where the shifted harmonic oscillator creation operator, $\hat{\bar{b}}'^{\dagger}$, is given by:

$$\hat{\bar{b}}'^{\dagger} = \hat{b}'^{\dagger} - (\alpha')^{*} \tag{D.2}$$

Within Eq. (D.1), $|\alpha'\rangle$ is a coherent state; a minimum uncertainty Gaussian wavepacket, with an average nuclear displacement and momentum of $\langle \hat{Q}' \rangle = \sqrt{2}\mathrm{Re}[\alpha']$ and $\langle \hat{P}' \rangle = \sqrt{2}\mathrm{Im}[\alpha']$. Such a coherent state can be written as:

$$|\alpha'\rangle = e^{-\lambda|\alpha'|^2/\hbar\omega} \sum_{q=0}^{\infty} \frac{1}{\sqrt{q!}} \left(\sqrt{\frac{2\lambda}{\hbar\omega}}\, \alpha' \right)^{q} |q\rangle \tag{D.3}$$

where $|q\rangle$ is a harmonic oscillator eigenstate, with quantum number q.

We now consider a generalised coherent state, for which only the parameter α' is time dependent. Using Eqs. (D.1) and (D.3), the time derivative of such a generalised coherent state is given by:

$$\begin{aligned} |n,\, \dot{\alpha}'\rangle = &-\frac{\lambda}{\hbar\omega} \left((\alpha')^{*}\, \dot{\alpha}' + (\dot{\alpha}')^{*}\, \alpha' \right) |n,\, \alpha'\rangle \\ &+ \dot{\alpha}' \sqrt{\frac{2\lambda}{\hbar\omega}} e^{-\lambda|\alpha'|^2/\hbar\omega} \sum_{q=0}^{\infty} \frac{q}{\sqrt{q!n!}} \left(\sqrt{\frac{2\lambda}{\hbar\omega}}\, \alpha' \right)^{q-1} \left(\sqrt{\frac{2\lambda}{\hbar\omega}}\, \hat{\bar{b}}'^{\dagger} \right)^{n} |q\rangle \\ &- (\dot{\alpha}')^{*} \sqrt{\frac{2\lambda}{\hbar\omega}} \frac{n}{\sqrt{n!}} \left(\sqrt{\frac{2\lambda}{\hbar\omega}}\, \hat{\bar{b}}'^{\dagger} \right)^{n-1} |\alpha'\rangle \end{aligned} \tag{D.4}$$

We proceed by considering each term in turn.

1. Term 2:

From Eq. (D.4), this second term can be first simplified to give:

$$\dot{\alpha}' \sqrt{\frac{2\lambda}{\hbar\omega}} e^{-\lambda|\alpha'|^2/\hbar\omega} \sum_{q=1}^{\infty} \sqrt{\frac{q}{(q-1)!n!}} \left(\sqrt{\frac{2\lambda}{\hbar\omega}}\, \alpha' \right)^{q-1} \left(\sqrt{\frac{2\lambda}{\hbar\omega}}\, \hat{\bar{b}}'^{\dagger} \right)^{n} |q\rangle \tag{D.5}$$

Using the definition of the harmonic oscillator creation operator:

$$\sqrt{\frac{2\lambda}{\hbar\omega}}\,\hat{b}'^{\dagger}\,|q-1\rangle = \sqrt{q}\,|q\rangle \tag{D.6}$$

the expression given in Eq. (D.5) can be rewritten as follows:

$$\frac{2\lambda\dot{\alpha}'\hat{b}'^{\dagger}}{\hbar\omega}e^{-\lambda|\alpha'|^2/\hbar\omega}\sum_{q=1}^{\infty}\frac{1}{\sqrt{(q-1)!n!}}\left(\sqrt{\frac{2\lambda}{\hbar\omega}}\,\alpha'\right)^{q-1}\left(\sqrt{\frac{2\lambda}{\hbar\omega}}\,\hat{\bar{b}}'^{\dagger}\right)^{n}|q-1\rangle \tag{D.7}$$

Performing the substitution $p = q-1$ converts the right-hand side of Eq. (D.7) back into a generalised coherent state, leading to the following compact expression for term 2:

$$\frac{2\lambda\dot{\alpha}'\hat{b}'^{\dagger}}{\hbar\omega}\,|n,\,\alpha'\rangle \tag{D.8}$$

2. Term 3:

From Eq. (D.4), this third term can be first simplified to give:

$$-\,(\dot{\alpha}')^{*}\sqrt{\frac{2\lambda}{\hbar\omega}}\sqrt{\frac{n}{(n-1)!}}\left(\sqrt{\frac{2\lambda}{\hbar\omega}}\,\hat{\bar{b}}'^{\dagger}\right)^{n-1}|\alpha'\rangle \tag{D.9}$$

Using the definition for a generalised coherent state given in Eq. (D.1), we can simplify the expression in Eq. (D.9) as follows:

$$-\,(\dot{\alpha}')^{*}\sqrt{\frac{2\lambda}{\hbar\omega}}\sqrt{n}\,|n-1,\,\alpha'\rangle \tag{D.10}$$

Using the definition of the shifted harmonic oscillator destruction operator:

$$\sqrt{\frac{2\lambda}{\hbar\omega}}\,\hat{\bar{b}}'\,|n,\,\alpha'\rangle = \sqrt{n}\,|n-1,\,\alpha'\rangle \tag{D.11}$$

leads to the following compact expression for term 3:

$$-\,\frac{2\lambda\,(\dot{\alpha}')^{*}\,\hat{\bar{b}}}{\hbar\omega}\,|n,\,\alpha'\rangle \tag{D.12}$$

Combining Eqs. (D.8) and (D.12) into Eq. (D.4) leads to the following expression for the time derivative of a generalised coherent state:

$$|n,\,\dot{\alpha}'\rangle = \frac{2\lambda}{\hbar\omega}\left[\tfrac{1}{2}\left((\alpha')^{*}\,\dot{\alpha}' - (\dot{\alpha}')^{*}\,\alpha'\right) + \dot{\alpha}'\hat{\bar{b}}'^{\dagger} - (\dot{\alpha}')^{*}\,\hat{\bar{b}}'\right]|n,\,\alpha'\rangle \tag{D.13}$$

where we have also used the definition for the shifted harmonic oscillator creation operator, given in Eq. (D.2).